INVESTIGATION OF NATURAL GAS HYDRATE POTENTIAL OF THE
SOUTH CASPIAN SEA

A THESIS SUBMITTED TO
THE GRADUATE SCHOOL OF NATURAL AND APPLIED SCIENCES
OF
MIDDLE EAST TECHNICAL UNIVERSITY

BY
ZHALA MUSTAFAYEVA

IN PARTIAL FULFILLMENT OF THE REQUIREMENTS
FOR
THE DEGREE OF MASTER OF SCIENCE
IN
PETROEUM AND NATURAL GAS ENGINEERING

SEPTEMBER 2018

Approval of the thesis:

INVESTIGATION OF NATURAL GAS HYDRATE POTENTIAL OF THE SOUTH CASPIAN SEA

Submitted by **ZHALA MUSTAFAYEVA** in partial fulfillment of the requirements for the degree of **Master of Science in Petroleum and Natural Gas Engineering Department, Middle East Technical University** by,

Prof. Dr. Halil KALIPÇILAR
Dean, Graduate School of **Natural and Applied Sciences** ⎯⎯⎯⎯

Prof. Dr. Serhat AKIN
Head of Department, **Petroleum and Natural Gas Engineering** ⎯⎯⎯⎯

Prof. Dr. Mahmut PARLAKTUNA
Supervisor, **Petroleum and Natural Gas Engineering Dept., METU** ⎯⎯⎯⎯

Examining Committee Members:

Prof. Dr. Günay ÇİFÇİ
The Institute of Marine Sciences and Technology,
Dokuz Eylul Univeristy ⎯⎯⎯⎯⎯⎯

Prof. Dr. Mahmut PARLAKTUNA
Petroleum and Natural Gas Engineering Dept., METU ⎯⎯⎯⎯⎯⎯

Assoc. Prof. Dr. Çağlar SINAYUÇ
Petroleum and Natural Gas Engineering Dept., METU ⎯⎯⎯⎯⎯⎯

Date:

I hereby declare that all information in this document has been obtained and presented in accordance with academic rules and ethical conduct. I also declare that, as required by these rules and conduct, I have fully cited and referenced all material and results that are not original to this work.

Name, Last name: ZHALA MUSTAFAYEVA

Signature:

ABSTRACT

INVESTIGATION OF NATURAL GAS HYDRATE POTENTIAL OF THE SOUTH CASPIAN SEA

MUSTAFAYEVA, Zhala

M.S., Department of Petroleum and Natural Gas Engineering

Supervisor: Prof. Dr. Mahmut PARLAKTUNA

September 2018, 176 Pages

Considering the improved technology, increase in demand on energy and limited conventional hydrocarbon resources make researchers look for new clean energy alternatives. Existence of large amount of gas hydrates in continental margins and permafrost regions shows that methane in gas hydrates may be the next clean energy supply of the world. The energy potential of gas hydrates has been encouraged researhers from all around the world to understand conditions for occurrence of gas hydrate and estimate the amount of methane in them.

The Caspian Sea, especially the South Caspian Sea, is a convenient environment for generation of gas hydrates. Low geothermal gradient, rapid sedimentation, a great number of mud volcanoes, suitable temperature and pressure conditions and actively generation of hydrocarbons are some unique characteristics of the region which make it worth for exploration.

The targeted area lies within the coordinates 39°N, 50°E - 40°N, 50°E and 39°N, 52°E - 40°N, 52°E, which includes Apsheron area and several mud volcanoes but excluding

the parts shallower than 100 m water depth. The total area is subdivided into three sections based on the following characteristics: i) Existence of bottom simulating reflections (BSRs) is observed in Apsheron area from Chevron's exploration in 1998. This area is studied as gas hydrate concentrated zone at 200-600 m water depths. ii) Since suitable conditions for gas hydrate occurrence spread to a very large area in the Caspian Sea, another area is specified and named as gas hydrate bearing zones between 100-1000 m water depths. iii) 17 mud volcanoes are studied on their gas hydrate potential although more than 60 mud volcanoes show suitable conditions for hydrate formation in the South Caspian Sea. Salinity, gas compositions, and geothermal gradients obtained from literature are utilized in the estimation of gas hydrate potential of all three sections through Monte Carlo simulation.

Area, thickness, hydrate saturation, porosity, cage occupancy and volume ratio parameters are needed for volumetric calculations. Area of the gas hydrate concentrated zone is 7.30×10^8 km^2 and area of gas hydrate bearing zone is 1.68×10^{10} km^2. Radii of craters of mud volcanoes are assumed as large as twice of their original radii and their total area is calculated as 5.94×10^7 km^2. Thickness of gas hydrate stability zone (GHSZ) for each zone is determined by temperature-depth diagrams. Hydrate saturation, porosity, cage occupancy and volume ratio are determined from analog studies and literature.

The mean of accessible resource volume is estimated as 1.50×10^{12}, 1.48×10^{13}, 1.65×10^{10} Sm^3 of gas for concentrated zone, bearing zone and in and around of craters of mud volcanoes, respectively. The mean of total accessible resource volume of targeted areas is estimated as 1.64×10^{13} Sm^3. The results show that the area has great potential of gas hydrates and clean energy supply for future.

Keywords: Natural Gas Hydrates, Caspian Sea, South Caspian Sea, Mud Volcanoes, Monte Carlo Method

ÖZ

GÜNEY HAZAR DENİZİ'NİN DOĞAL GAZ HİDRAT POTANSİYELİNİN İNCELENMESİ

MUSTAFAYEVA, Zhala

Yüksek Lisans Tezi, Petrol ve Doğal Gaz Mühendisliği Bölümü

Tez Yöneticisi: Prof. Dr. Mahmut PARLAKTUNA

Eylül 2018, 176 sayfa

Gelişen teknoloji ile enerjiye olan talebin artması ve geleksel hidrokarbon kaynaklarının sınırlı olması, araştırmacıları yeni temiz enerji kaynaklarının keşfine yöneltmektedir. Derin deniz sedimanlarında ve permafrost bölgelerde bulunan yüksek miktarlardaki gaz hidratları, bunların içindeki metanın dünyanın gelecekteki temiz enerji kaynağı olabileceğini göstermektedir. Gaz hidratların içindeki enerji potansiyeli, dünyanın yer yanından araştırmacıları bunların oluşum şartlarını ve içindeki metan miktarını araştırmaya teşvik etmektedir.

Hazar Denizi özellikle Güney Hazar Denizi kısmı gaz hidratların oluşumu için uygun şartlara sahip bir çevre oluşturmaktadır. Düşük jeotermal gradyan, süratli sedimentasyon, çok sayıda çamur volkanları, uygun sıcaklık ve basınç ve aktif bir şekilde devam eden hidrokarbon oluşumu gibi kendine mahsus özellikleri, bölgeyi araştırmaya değer kılmaktadır.

39°N, 50°E - 40°N, 50°E and 39°N, 52°E - 40°N, 52°E arasında yerleşen hedef alan, Apşeron bölgesini ve birkaç çamur volkanı içermektedir. Fakat su derinliği 100 m'den az olan bölgeler araştırma alanının dışında tutulmaktadır. Toplam alan paragrafın

devamında belirtilecek olan özelliklerine göre üç kısma ayrılmıştır. i) Chevron tarafından 1998'de yapılmış olan araştırmaya göre, tabana benzeyen yansımalar gözlemlenmiş olan kısım 200-600 m arası su derinliğinde olup, gaz hidratların yoğun olduğu bölge olarak çalışılmıştır. ii) Gaz hidratların oluşumu için uygun olan koşullar Hazar Denizi'nde geniş bir alana yayılmıştır. Bu bağlamda, 100-1000 m su derinliğinde diğer bir bölge belirtilmiş ve gaz hidrat içeren bölge olarak adlandırılmıştır. iii) Gaz hidratların oluşumu için gerekli koşulları sağlayan 60'tan fazla çamur volkanı olduğu olduğu halde, bunların 17 adeti gaz hidrat potansiyelleri göz önünde bulundurularak çalışmaya dahil edilmiştir. Literatürden elde edilmiş olan tuzluluk, gaz compozisyonu ve jeotermal gradyan verileri Monte Carlo simulasyonu kullanılarak bu üç bölgenin gaz hidrat potansiyelini tahmin etmede kullanılmıştır.

Hacimsel hesaplamalar için alan, kalınlık, hidrat doymuşluğu, gözeneklilik, kafes doluluk oranı ve hacim oranı parametreleri gerekmektedir. Gaz hidrat yoğun bölgenin alanı 7.30×10^8 km^2 ve gaz hidrat içeren bölgenin alanı 1.68×10^{10} km^2'dir. Çamur volkanı kraterlerinin yarıçapları belirlenen özgün değerlerinin iki katı olarak varsayılmış ve toplam alanları 5.94×10^7 km^2 olarak hesaplanmıştır. Her bir bölge için gaz hidrat kararlılık zonu kalınlığı sıcaklık-derinlik grafikleri doğrultusunda belirlenmiştir. Hidrat doymuşluğu, gözeneklilik, kafes doluluk oranı ve hacim oranı parametreleri yayınlar ve benzer çalışmalarda kullanılan değerler doğrultusunda kararlaştırılmıştır.

Ortalama erişilebilir kaynak hacmi, gaz hidrat yoğun bölge için 1.50×10^{12} Sm^3; gaz hidrat içeren bölgeler için 1.48×10^{13} Sm^3; ve çamur volkanı kraterlerinin içi ve çevresi için 1.65×10^{10} Sm^3 olarak tahmin edilmiştir. Hedef bölge için toplam erişilebilir kaynak hacminin ortalaması 1.64×10^{13} Sm^3 olarak hesaplanmıştır. Elde edilen sonuçlara göre çalışma alanı yüksek gaz hidrat ve temiz enerji potansiyeline sahiptir.

Anahtar Kelimeler: Doğal Gaz Hidratları, Hazar Denizi, Güney Hazar Denizi, Çamur Volkanları, Monte Carlo Yöntemi

To my family

ACKNOWLEDGEMENT

TABLE OF CONTENTS

LIST OF TABLES

TABLES

FIGURES

FIGURES

FIGURES

FIGURES

LIST OF ABBREVIATIONS

BGHSZ	Base of Gas Hydrate Stability Zone
BSR	Bottom Simulating Reflection
DSDP	Deep Sea Drilling Project
GHSZ	Gas Hydrate Stability Zone
High GG	High Geothermal Gradient
ISC	International Seismological Centre
Low GG	Low Geothermal Gradient
Mbsf	Meter Below Seafloor
MV	Mud Volcano
ODP	Ocean Drilling Program
PDF	Probability Density Function
S_h	Hydrate Saturation
sH	Structure H
sI	Structure I
sII	Structure II

CHAPTER 1

INTRODUCTION

Natural gas hydrates are solid, ice-like crystalline substances, composed of water molecules as host in which low molecular weight hydrocarbon molecules are enclosed. Under low temperature and high pressure conditions, the constituents come into contact and form gas hydrates. Thus, it can be deduced that formation of gas hydrates strongly depend on gas composition, pressure and temperature. Suitable conditions for their occurrence exist in oil and gas wells and pipelines. However, in the natural environment, gas hydrates occur in oceanic sediment of continental and insular slopes and rises of active and passive margins, in deep-water sediment of inland lakes and seas, and in polar sediment on both continents and continental shelves.

In oceanic sediments, gas hydrates may occur at water depths of deeper than 300 m where water temperature at the seafloor is almost 0°C. Gas hydrate stability zone (GHSZ) may extend from seafloor to sediment depths of about 1,100 m. In permafrost regions, gas hydrates may exist in sediments depths from 150 m to 2,000 m. Existing in shallow geosphere, they may effect physical and chemical properties of sediments near to surface (Kvenvolden and Lorenson, 2001).

Gas hydrates are surveyed by geophysical, geochemical, and geological methods. Bottom simulating reflections (BSRs) from seismic investigations is important for interpreting presence of gas hydrates in oceanic sediments. They mostly coincide with the bottom of GHSZ (Hyndman and Spence, 1992).

In one m^3 of gas hydrate, approximately 164 m^3 of methane may be contained at standard conditions. By this means, in early 1970s and following years, estimated amount of methane in gas hydrate deposits are ranged from 10^{17} to 10^{18} m^3. However, in years, estimations have been decreased. The reason behind this is that more information about gas hydrates is known, but still need progress. The consensus value is estimated as 2.1×10^{16} m^3 by Kvenvolden, 1999. Therefore, the global volume of methane in gas hydrates deposits is 2 to 10 times greater than the overall proved gas reserves in the world. According to BP Statistical Review of World Energy (2017), it is estimated as 1.866×10^{14} Sm^3 of proved gas reserves. These estimations make researchers consider gas hydrates as potential clean energy supply for future.

The Caspian Sea is one of the oldest regions that petroleum industry is actually established. Recently, the region is under question as being gas hydrate province as well as being oil and gas province. Some unique properties of the region, like low geothermal gradient, rapid sedimentation, a great number of mud volcanoes, suitable temperature and pressure conditions, and actively generation of hydrocarbons make it attention grabbing (Buryakovsky et al., 2001).

Under Deep Sea Drilling Project (DSDP) and Ocean Drilling Program (ODP), seismic, geological, and geophysical investigations are conducted and analyzed that the Caspian Sea has all essential conditions for formation of gas hydrates especially in the southern part.

In the study of Gerivani and Gerivani, 2015, a rough estimation of amount of methane is done. According to their calculation in GHSZ in Apsheron region, which is 100 km away from Baku, with thickness of 200 m extending for 10 km and only 5% of the sediments volume being composed of gas hydrates is assumed. Around 1 billion cubic meters of methane hydrate is estimated. Since one m^3 of solid hydrate can contain 160 Sm^3 of methane has around 160 standard billion cubic meter of hydrocarbon gas.

For mud volcanoes, an estimation is done by Muradov, 2002. In that study, resources of hydrocarbon gases in hydrates saturate sediments up to a depth of 100 m and are estimated at $0.2\cdot10^{15}$–$8\cdot10^{15}$ m^3. The amount of hydrocarbon gases concentrated in them is 10^{11}–10^{12} Sm^3 (Huseynov and Guliyev, 2004).

In this study, natural gas hydrate potential in the South Caspian Sea is investigated. The targeted area is taken almost within the coordinates 39°N, 50°E - 40°N, 50°E and 39°N, 52°E - 40°N, 52°E, excluding the parts shallower than 100 m. The area is divided by three according to hydrate saturation in sediments.

Three gas compositions are adapted from Diaconescu and Knapp, 2000. Pure and saline water environments are considered and compared regarding the gas compositions and related zones. Pressure values are obtained by CSMHYD program (CSMHYD, 2017). Pressure-temperature and temperature-depth diagrams are obtained accordingly.

Mud volcanoes in the region experiences very high geothermal gradient values and intensive gas seepage. Different gas compositions and geothermal gradient values from mud volcanoes of the South Caspian Sea are available in the study of Ginsburg et al., 1992. CSMHYD is used to obtain hydrate formation pressure values. Pressure-temperature and temperature-depth diagrams are obtained for three of the mud volcanoes, Buzdag, Elm, and unnamed one on the Abikha bank.

Calculations are done by volumetric method. Estimations are calculated by Monte Carlo method using @RISK. Parameters are obtained from literature and other studies from different fields in the world. Accessible resource volumes are obtained from all three parts within the field of interest. Total accessible resource volume is reached finally. Although these estimations are done under lots of uncertainties, unique geologic and stratigraphic features make gas hydrates of the South Caspian Sea worth for researching.

CHAPTER 2

NATURAL GAS HYDRATES

2.1. Clathrates

Clathrates are inclusion compounds, composed of host and guest molecules. Host molecules build a crystal lattice and guest molecules reside in the cavities within this crystal lattice structure. Guest molecules may comprise of more than one kind of compound and less commonly, host molecules may do so as well (IUPAC, 1997). When suitable molecules are present, clathrates occur spontaneously in certain pressure and temperature conditions (Max, 2003). In general, higher pressure and lower temperature conditions promote clathrate stability (Ors, 2012).

Many clathrates have a framework backbone sustained by hydrogen bonds. Guest molecules need to be smaller than the voids of this framework to fit physically in these voids. Moreover, molecular configuration of host molecules and interactions between host and guest atoms must not disrupt this framework. In fact, certain interactions between host and guest molecules are mandatory for a stable structure. One of the defining properties of clathrates is that there is no chemical bonding between host and guest molecules. Therefore, a clathrate is not a single compound but a complex of different compounds (Max, 2003).

Clathrate properties were not understood for nearly 170 years after their discovery. Emerging theories on chemical structure of compounds and atoms were not applying to these inclusion compounds. H. M. Powell was a pioneer in understanding their true nature. In his work "Clathrate Compounds" in 1948, Powell brought insight on the

structure, principle arrangement, and terminology of a novel branch of chemistry, nowadays known as "Inclusion Chemistry". The term clathrate was also proposed by H. M. Powell. This name was derived from the Latin word "clathratus", which means "with bars" or "lattice" (Dyadin et al., 1999). Until 1976, it was believed that clathrates occur only in solid phase (Mayes, 1963). However, a wide range of clathrates has been discovered, even liquid clathrates that are known to be stable in room temperature (Christie et al. 1991).

In Figure 2.1, clathrate structure of urea and 1,6-dichlorohexane is displayed as an example. Urea serves as the host molecule and forms hexagonal complexes. Dominant intermolecular interaction between urea molecules occurs via hydrogen bonding. 1,6-dichlorohexane molecules act as the guest molecules. They are placed inside the hexagonal framework (Clathrate Compound, 2017).
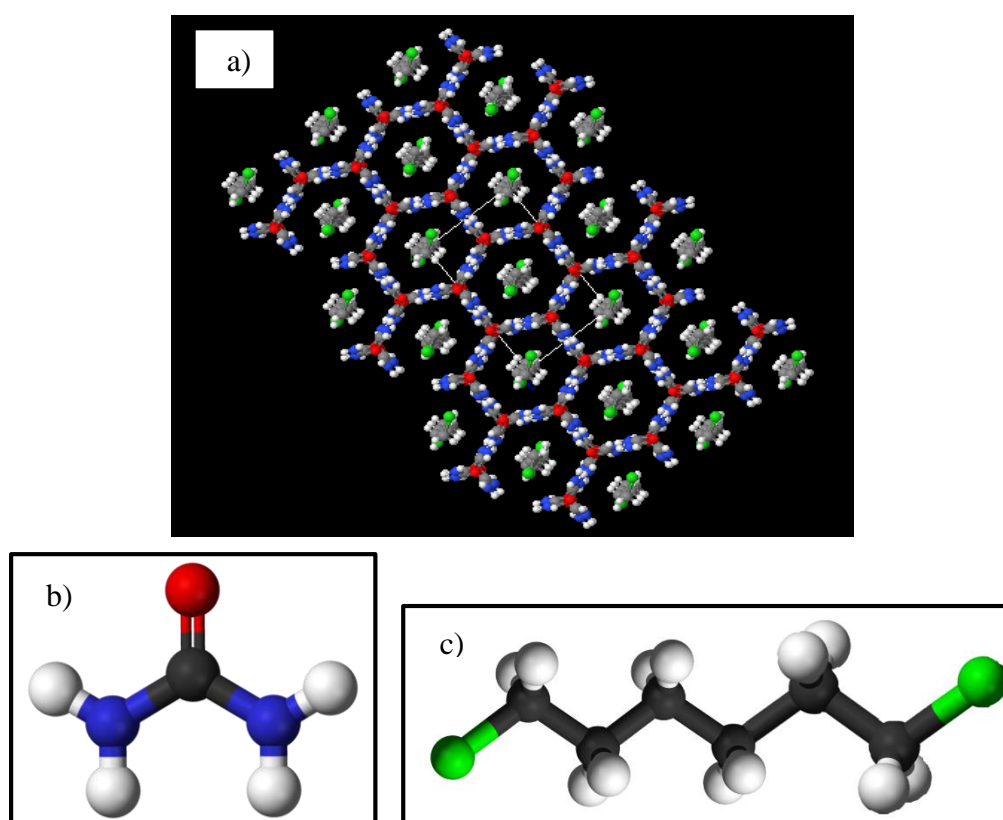
Figure 2.1: Example to a clathrate structure: (a) Clathrate structure of Urea and 1,6-dichlorohexane (b) Urea (Carbonic diamide - $CO(NH_2)_2$) molecule, ball and stick model. (c) 1,6-Dichlorohexane ($C_6H_{12}Cl_2$) molecule, ball and stick model. Atoms' color scheme: carbon-grey; hydrogen-white; oxygen-red; nitrogen-blue, chlorine-green (adapted from Clathrate Compound, 2018; Urea, 2018)

Some examples of clathrates, formed by combination of host and guest substances, are listed in Table 2.1 (Max, 2003).

Table 2.1: Examples of clathrate forming combinations of substances (adapted from Max, 2003)

Host substances	Guest Substances
Urea	Straight chain hydrocarbons
Thiourea	Branched chain and cyclic hydrocarbons
Dinitrodiphenyl	Derivatives of diphenyl
Phenol	Hydrogen chloride, sulphur dioxide, acetylene
Water (ice)	Halogens, noble gases, sulphur hexaflouride, low molecular weight hydrocarbons, CO_2, SO_3, N_2, etc.
Nickel dicyanobenzene	Benzene, chloroform
Clay minerals (molecular sieves)	Hydrophilic substances
Zeolites	Wide range of adsorbed substances
Graphite	Oxygen, hydrocarbons, alkali metals (in sheet-like cavities and Buckminsterfullerenes)
Cellulose	Water, hydrocarbons, dyes, iodine

2.2. Clathrate Hydrates

Clathrate hydrates constitute a subset of clathrates. A clathrate where the host molecule is water is said to be a "clathrate hydrate" or simply, a "hydrate". Water molecules that interact by hydrogen bonds form the crystal lattice structure. Varieties of molecules qualify as possible guests. The list includes but is not limited to methane (CH_4), oxygen (O_2), nitrogen (N_2), carbon dioxide (CO_2), ethane (C_2H_6), propane (C_3H_8), butane (C_4H_{10}) and hydrogen sulfide (H_2S). As noticeable, common guest molecules are gases of small size. Hence, hydrates are commonly referred as gas hydrates. In general, chemical expression of a hydrate is shown as $M \cdot nH_2O$ where M stands for the guest molecules formula and n represents number of water molecules (Ye and Liu, 2013).

Hydrates are crystalline, non-stoichiometric host-guest compounds. Here, non-stoichiometry means that the combination of substances does not follow a fixed amount ratio. Cavities must be occupied with guest molecules to some extent but not all the cavities require to be filled. There are no strong directional interactions between guests and hosts (Sum et al., 2009). The guest independently vibrates and rotates but is confined in the cavity and exhibit limited translational motion. Typically common hydrates incorporate 85 mol% water and 15 mol% guest(s), when all the cavities are filled (Sloan, 2003). As an example, methane and water molecules being connected by hydrogen bonds forms a common type of clathrate hydrate in Figure 2.2 (Mahajan et al., 2007).
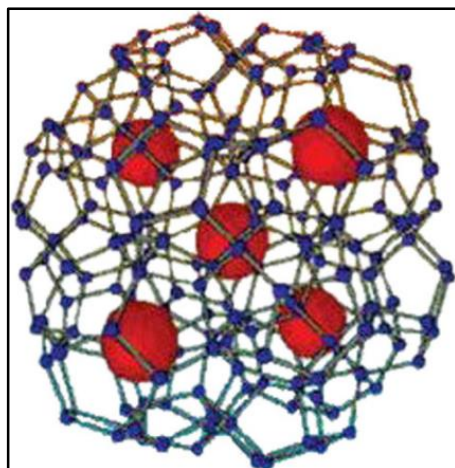
Figure 2.2: Schematic drawing of methane and water clathrate, a common hydrate. Red spheres: methane molecules; blue spheres: water molecules; grey rods: hydrogen bonds (adapted from Mahajan et al., 2007)

2.3. Historical Milestones

Clathrates are known to humankind for more than two centuries. First reported observance of a clathrate is suspected to be of sulphur dioxide (SO_2) and water. Between 1777 and 1778, Joseph Priestley experimented on mixtures of such substances and reported that at -8.33 °C (17 °F) the mixture was found in a frozen state. On the other hand, hydrogen chloride (HCl) gas and tetrafluorosilane (SiF_4) gas did not freeze under the same conditions. This solid state of mixture might be very well attributed to clathrate formation or to the below 0 °C temperature. This observance of clathrates is debatable but Sir Humphrey Davy's comments on chlorine and water mixture in the Bakerian lecture to the Royal Society, in 1810, is considered an unequivocal report of a clathrate. He noted that such mixture froze at a higher temperature than both pure water and pure chlorine gas in his experiments. Until then, frozen material was thought to be pure chlorine. This is widely considered the discovery of clathrates in literature. In 1823, more light was shed on the matter as Michael Faraday assigned the formula $Cl_2 \cdot 10H_2O$ to this clathrate. More experiments, like Ditte's in 1882, Mauméné's in 1883 and Roozeboom's in 1884, were conducted to refine its composition. In 1829, A. de la Rive amended Priestley's efforts and defined $SO_2 \cdot 10H_2O$ hydrate (Sloan and Koh, 2008).

Larger host molecules were found to form clathrates too, with the first report about the quinol (hydroquinone). Wohler prepared first non-hydrate clathrate with quinol as host

8

and H$_2$S as guest and found compositions of 4(quinol)·H$_2$S and 3(quinol)·H$_2$S, which are not so different from modern calculations. SO$_2$ was found to be a guest as well by Clemm in 1859. Later on, Mylius prepared carbon monoxide (CO), hydrogen cyanide (HCN) and formic acid (HCOOH) clathrates and proposed possible enclosure of these molecules by quinol, without chemical combination. Discovery of the first tunnel (channel) inclusion complex was possibly as early as 1874, when Nencki reported he found 2(thiourea)·diethyl oxalate complex. Paul Pfeiffer's compilation of scientific data in his book "Organische Molekulverbindungen" in 1927 was a noteworthy contribution to clathrate chemistry for that time. Second quarter of twentieth century witnessed use of X-ray diffraction methods and determination of key crystal structures. Since 1950's crystal structure, analysis methods revealed much information on inclusion compounds and complexity of synthesized inclusion compounds greatly increased. In addition, two distinct hydrate crystal structures are defined, namely structure I and structure II. Research is currently directed towards mechanics of physical behavior including electrical conductivity, energetics, and thermodynamics of interactions between the components (Herbstein, 2005; Sloan and Koh, 2008).

As for clathrates that are relevant for petroleum industry, hydrates of natural gases are extensively studied in the 20th century. Hydrates of natural gases were discovered including methane, ethane, and propane hydrates, which are prepared by P. Villard in 1888. G. Hammerschmidt detected that hydrates are clogging oil and gas pipelines in 1934, directing research interest into thermodynamic properties of hydrates. Initial efforts were primarily focused on avoiding hydrate formation inside pipelines. In 1960s, gas hydrates are found belonging to the class of compounds, named clathrates. Around the same time, their energy source potential is also recognized. Y. F. Makogon found gas hydrates in the Siberian permafrost region in 1965 and C. Bily and J.W.L. Dick reported the presence of hydrates in a core extracted from the MacKenzie Delta in 1974 (Bily and Dick, 1974; Sloan and Koh, 2008).

2.4. Natural Gas Hydrates

Natural gas hydrates are ice-like crystalline structures, made up of light hydrocarbon molecules that are attached and encaged by water molecules under sufficiently low temperature and high pressure. In this study, natural gas hydrates is mentioned as gas

hydrates to simplify. Although it was known that gas hydrates are formed by hydrocarbon molecules in gas phase and water in aqueous phase, Verma determined that they could also form from the mixtures of the liquid hydrocarbons and water (Sloan, 1991).

In the 21st century, among primary energy sources, natural gas usage is the most rapidly increasing one in the world. Natural gas burn is the cleanest among the petroleum fuels. Natural gas can be extracted from gas hydrates. Gas hydrates are an attractive economic target as a potential energy source for near future, especially when it is feasible for producing in the areas relatively close to the Earth's or seabed surface (Max, 2003).

They also have massive storage capacity. In the sediments, less than 1500 m under surface, unit volume of gas hydrate contains more methane molecules than unit volume of free gas contains (Kvenvolden, 1993). To be specific, 164 volumes of methane and 0.8 volume of water are stored in one volume of hydrate. Schematic drawing of volumetric relationship between gas hydrate, methane, and water is shown in Figure 2.3. Hydrates form when roughly 90% of the cages are filled. This corresponds to 150 volume of methane per one volume of hydrate at standard conditions (Sloan, 1991).
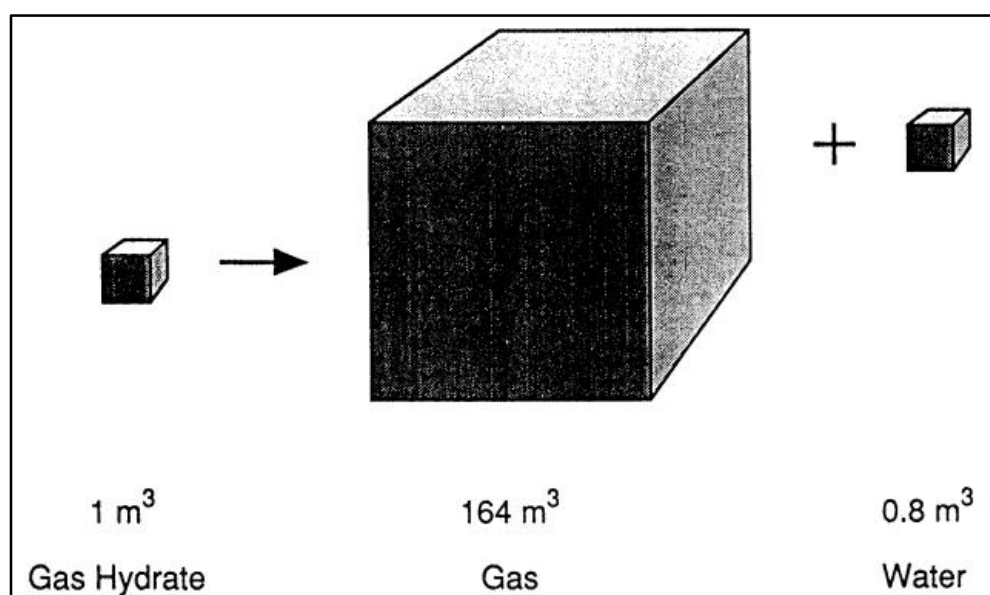
Figure 2.3: Schematic representation of volumetric relationship between methane gas hydrate and its constituents. One cubic meter of gas hydrate yields 0.8 m^3 H$_2$O and 164 m^3 free CH$_4$ gas at standard temperature and pressure (adapted from Kvenvolden, 1993)

This high storage capacity makes gas hydrates one of the largest unexploited energy sources in the world and is the main reason behind hydrate's current significance in petroleum industry. Energy equivalent being held in hydrates is at least twice as large as that of all other fossil fuels in the world (Tohidi et al., 2012; Chatti et al., 2005). Amount of organic carbon in different sources are listed in Table 2.2. Methane hydrate is in the center of the global organic carbon cycle.

Table 2.2: Worldwide amounts of organic carbon sources (adapted from Kvenvolden, 2002)

Source of organic carbon	Amount (gigatons)
Gas hydrates (onshore and offshore)	10,000
Recoverable and non-recoverable fossil fuels (oil, coal, gas)	5,000
Soil	1,400
Dissolved organics	980
Biota	830
Peat	500
Atmosphere	3.6

Some projections estimate that this amount of energy could provide the world's energy needs for a millennium. Hydrate reserves are located under continental shelves and on land under permafrost. Unfortunately, current technology has refined to extract fluid resources from such depths of Earth. Due to the solid nature of hydrates, conventional petroleum and gas recovery methods cannot be used to recover hydrates. Current recovery techniques are based on in situ dissociation of hydrates on their reservoir and retrieving extracted methane. Heating the reservoir or lowering the reservoir pressure is used to disassociate hydrates (Sloan and Koh, 2008).

2.4.1. Structural Characterization of Gas Hydrates

Gas hydrates are combination of water molecules aligned to form a cage and non-polar or insignificantly polar guest molecules. The first requirement for a guest molecule is the size and this is dictated by 3-dimensional structure of crystal lattice structure. The ideal ratio of diameters of cage and guest molecule is found to be 0.76 (Jeffrey, 1984). Slightly larger guest molecules may deform the cavity and fit in. Secondly, guest molecule must have hydrophobic moieties that will not disrupt water's cage-like organization. In a gas hydrate, the overall structure is maintained by weak interactions. Between water molecules, the dominating attraction force is hydrogen bonds. Guest molecules are hold in place via van der Waals forces. Guest molecules are vital for the

crystal structure since their absence disarrange the metastable structure. Specifically, hydrate is the inevitable result of interactions between host and guest compounds. Water molecules are forced to organize in cages and these cages have pentagonal and hexagonal faces due to angles of hydrogen bonds. Combination of these planes results in different polyhedra and consequently different types of hydrate structures. All known natural gas hydrates observed in nature show three main types of structures. They are structure I (sI), structure II (sII) and much less commonly structure H (sH). A variety of compounds including bromine (Br), dimethyl ether (C_2H_6O), and ethanol (C_2H_6O) form less common clathrate hydrate structures (such as Jeffrey's structures III–VII, structure T, complex layer structures). In addition, high pressure hydrate phases are also in different structural configuration. However, of more than 130 compounds as well as natural gas compounds form either sI, sII, or sH hydrate (Sloan and Koh, 2008).

All of three hydrate structures comprise nearly 85% water on a molecular basis. Thus, many physical properties of hydrates resemble ice, or more specifically hexagonal ice. Hexagonal ice, depicted as Ih, is one of the 17 known solid crystalline phases of water, and the most common form of ice. In fact, virtually all-existing ice in nature is Ih. Each water molecule bonds with four others via tetrahedral angled hydrogen bonds. This angle and distance between water nuclei are very similar to the values measured in hydrates. For example, hydrogen bond angle differs by only 1.5° in pentagonal faces of hydrates.

The cavities of hydrates are enclosed within polyhedra. In sI, sII and sH, five distinct polyhedra are described. Jeffrey propounded a naming system for such polyhedra as $n_i^{m_i}$, where n_i represents the number of edges in the face type "i" and m_i is the number of faces with n_i edges (Sloan, 1991; Makogon, 1997).

Structure I

Structure I is formed when guest molecules have a diameter between 0.42 and 0,6 nm, such as methane (CH_4), ethane (C_2H_6), carbon dioxide (CO_2), and hydrogen sulfide (H_2S). sI consists of two pentagonal dodecahedrons ($5^{12}6^2$) and six tetrakaidecahedrons ($5^{12}6^2$). In the final organization, a cubic arrangement is achieved.

One cubic cell contains 46 water molecules and 8 possible guest molecules (Sloan, 1991; Makogon, 1997; Strobel et al., 2009).

Structure II

Nitrogen (N_2) and small molecules including hydrogen (H_2) (d < 4.2 Å) are organized in structure II as single guests. sII takes shape in case of larger (6 Å < d < 7 Å) single guest molecules such as propane (C_3H_8) or 2-methylpropane (C_4H_{10}) as well. sII is cubic, like sI and consists of sixteen pentagonal dodecahedrons (5^{12}) and eight hexakaidecahedron ($5^{12}6^4$). One cubic cell contains 136 water molecules and 24 possible guest molecules (Sloan, 1991; Makogon, 1997; Strobel et al., 2009).

Structure H

Even larger molecules (typically 7 Å < d < 9 Å) such as 2-methylbutane (C_5H_{12}) or neohexane (2,2-dimethylbutane) can be found in hydrates when accompanied by smaller molecules such as methane, hydrogen sulfide, or nitrogen. In this case, a third structure takes shape, which is defined much later than other hydrates, in 1987 by Ripmeester (Ripmeester et al., 1987). This structure was named structure H because it forms hexagonal crystals, unlike cubic structure of sI and sII hydrates. Unit of sH includes three pentagonal dodecahedrons (5^{12}), irregular dodecahedron ($4^3 5^6 6^3$) and one icosahedron ($5^{12}6^8$). One cubic cell contains 34 water molecules and 6 possible guest molecules (Sloan, 1991; Makogon, 1997; Strobel et al., 2009).

3D drawing of five basic polyhedra and their corresponding names are shown in Figure 2.4. Corresponding names are from left to right, 5^{12}-pentagonal dodecahedron, $5^{12}6^2$-tetrakaidecahedron, $5^{12}6^4$-hexakaidecahedron, $5^{12}6^8$-icosahedron, $4^3 5^6 6^3$-irregular dodecahedron. Combination of 2 5^{12} and 6 $5^{12}6^2$ makes up type I structure, combination of 16 5^{12} and 8 $5^{12}6^4$ makes up type II structure, and combination of 3 5^{12}, 1 $5^{12}6^8$ and 2 $4^3 5^6 6^3$ makes up type H structure.
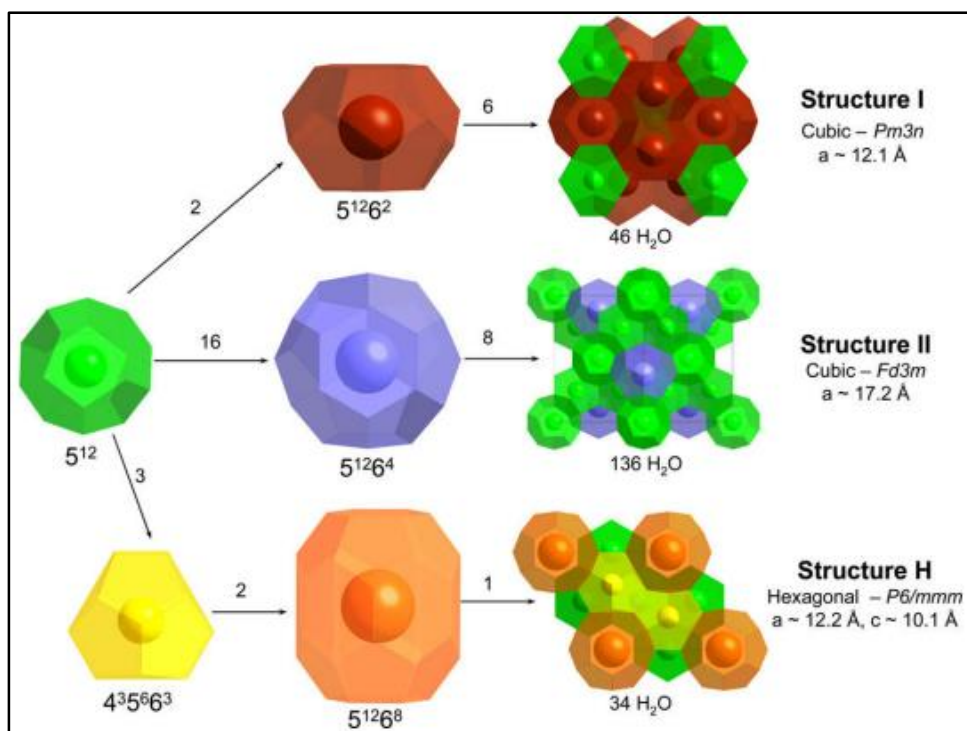
Figure 2.4: On the 3D drawing of five basic polyhedra and their corresponding names (adapted from Strobel et al., 2009)

Cavity geometries between gas hydrate crystal structures (sI, sII, sH) is compared in Table 2.3.

Table 2.3: Comparison of cavity geometries between gas hydrate crystal structures (adapted from Ye and Liu, 2013)

Crystal structure of gas hydrate	sI		sII		sH		
Cavity description	Small	Large	Small	Large	Small	Medium	Large
Crystal lattice structure	5^{12}	$5^{12}6^2$	5^{12}	$5^{12}6^4$	5^{12}	$4^35^66^3$	$5^{12}6^8$
Number of cavities in one unit	2	6	16	8	3	2	1
Average cavity radius[a], Å	3.91	4.33	3.902	4.683	3.91	4.06	5.71
Varying rate of radius[b], %	3.4	14.4	5.5	1.73	4.0[c]	8.5[c]	15.1[c]
Cavity coordinate number[d]	20	24	20	28	20	20	36

a: Average radius of cavity is dependent on temperature, pressure, and guest molecule.
b: Variation in distance of oxygen atoms from the center of a cage. A smaller variation in radius reflects a more symmetric cage.
c: This value is obtained by dividing the difference between the longest and shortest distances by the longest distance.
d: Cavity coordinate number depicts the number of oxygen atoms at the periphery of each cavity and also corresponds to the number of water molecules involved in the cavity

2.4.2. Gas Hydrate Occurrence Conditions

Major ingredients of systems in nature that bear gas hydrate deposits contain adequate water and gas, majority in methane (99%). Along with these substances, the

occurrence of gas hydrates still demands relatively low temperature, high pressure, appropriate hydrocarbon gas composition and ionic strength of environment which itself is affected by salinity and pH. These favorable conditions can be found both below the permafrost and off the coasts on the continental margins (Kvenvolden, 1993).

In oceanic sediments, bottom water temperature and the geothermal gradient keep the temperature in line while water depth provides the needed pressure. Natural gas hydrates form from seafloor to sediment depth of around 1,100 m (Amundsen et al., 2013), where bottom water temperature is around 0 °C and water depth exceeds approximately 300 m.

In the continental slopes, temperature generally increases downward by 3-4 °C per 100 m. Pressure, depth and temperature conditions suitable for hydrates are generally found just below the slope break of continental regions. Whereas in continental polar regions where temperature gradients are much less than that in the oceanic environments, temperature and pressure caused by the thickness of permafrost discovered methane hydrate deposits occur from 150 m below the surface to 2000 m, whose temperature is typically less than 0 °C (Max, 2003; Amundsen et al., 2013).

2.4.3. Accumulation Types for Natural Gas Hydrates in Sediments

Gas hydrate accumulations are grouped into three as they occur in sediments. These are structural accumulation, stratigraphic accumulation, and combination of the first two types of accumulation that are distinguished according to the mode of fluid migration and gas hydrate concentration in the GHSZ. A gas hydrate province occurs when several gas hydrate accumulations are present within a basin (Milkov and Sassen, 2002).

Structural accumulations exist in high fluid flux settings where fault systems, mud volcanoes and other geological structures are encountered. Gas hydrates are found near and at the seafloor. Hydrocarbon gas seepages also occur from the seafloor to the water column. Since gas is rapidly transported from great depth to highly permeable fractured channels, gas hydrate concentration is comparatively high in sediments.

These sediments are host for both sI and sII gas hydrates crystallized from thermogenic, biogenic and mixed origin of gas (Milkov and Sassen, 2002).

In stratigraphic accumulations, low fluid flux settings or diffusion-controlled settings are observed. Gas hydrates occur from bacterial gas reproduced in situ or slowly supplied from great depth. They are encountered well beneath the seafloor as distributed in a wide area within the GHSZ with low concentrations. Mostly, sI gas hydrates from bacterial methane are noted. Considering the great areal extend of stratigraphic accumulations, BSRs and the presence of free gas are examined at under the GHSZ (Milkov and Sassen, 2002).

Combination accumulations occur in sediments where relatively permeable strata and rapid gas supply are present. In Figure 2.5, cross-sectional views of three types of gas hydrate accumulations are shown. In (a) and (b), structural accumulations are presented with a fault and mud volcano systems. In (c) and (d), stratigraphic and combination accumulations are displayed (Milkov and Sassen, 2002).
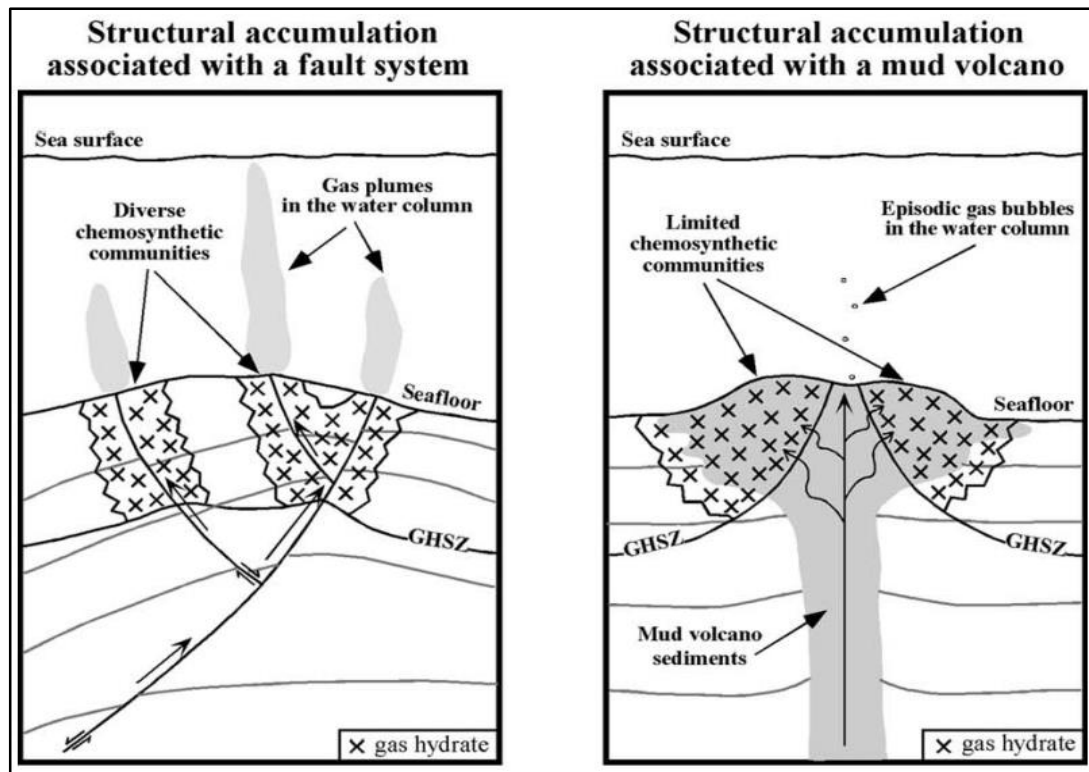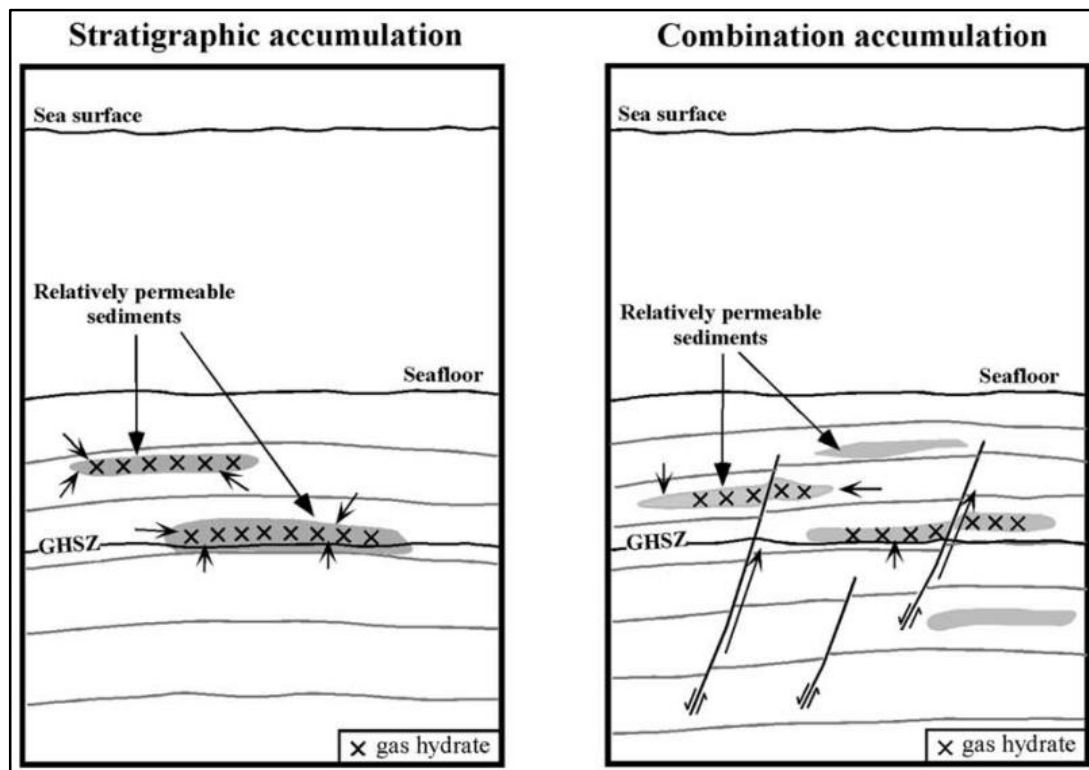
Figure 2.5: Cross-sectional views of three types of gas hydrate accumulations (adapted from Milkov and Sassen, 2002)

Besides accumulation, microstructural distribution of gas hydrate in sands is also need to understood and modelled. Correlation between seismic data (seismic characteristics such as attribute) and well data (thickness of hydrate stability zone, saturation etc.) is very important (Tsuji, 2003). Figure 2.6 shows microstructural models of gas hydrate bearing sediments. These models are classified into six types depending on the microstructural relationship between gas hydrates and the bearing sediment. They occur as cement at grain contacts, coat around grains, support material between grains, filling in pores of grains, an inclusion element, and filling in fractures (Dai et al., 2008).
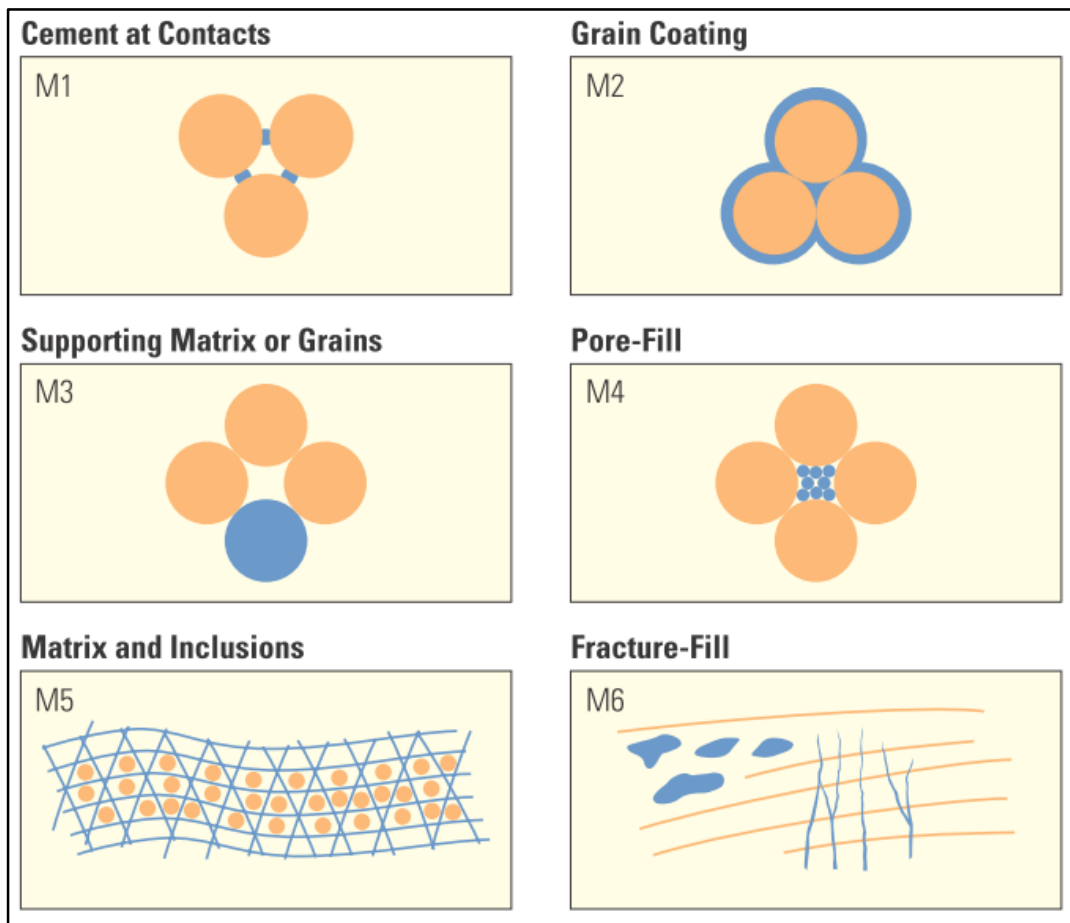
Figure 2.6: Microstructural models of gas hydrate bearing sediments (adapted from Birchwood et al., 2010)

In order to assess the amount of methane in gas hydrates, the volume of hydrated zone and the percentage of that volume filled by hydrates, more precisely hydrate saturation in sands, must be evaluated (MacDonald, 1990).

According to occurrence of gas hydrates in sediments, hydrate accumulations in them may be grouped as follows:

1. Solid masses type of accumulations is mostly encountered at or very near surface in association with vents.
2. Pore-filling type of gas hydrate accumulation demonstrate low hydrate saturation, $S_h \sim 10\%$ or less in fine-grained sediments, whereas hydrate saturation is much higher in coarser grained sediments like coarse silts and sands, $S_h \sim 50\%\text{-}90\%$.
3. In grain displacing type of accumulations $S_h \sim 5\%\text{-}40\%$ or more (Boswell et al., 2012).

2.4.4. Origin of Methane

The most common guest found in natural gas hydrates is methane. Methane hydrates collect their methane moiety via two distinct processes. First and the dominant way of generation are biogenic, while the second is thermogenic. Biogenic methane generation takes place when organic matter decays in oxygen deficient environment. Anaerobic microorganisms (archaea- 'single-celled microorganisms') produce methane gas as they degrade organic matter. Such microorganisms are termed "methanogens" and the process is named methanogenesis. When descending organic matter reach the seafloor, firstly aerobic bacteria degrades it, releasing carbon dioxide. They also convert sulfates to sulfides, depleting sulfates. Anaerobic archaea located in the sediments processes the remaining organic matter and generate methane. Organic matter with a composition of carbon, nitrogen, and phosphorus in a ratio of 106:16:1 may decompose to generate methane as follows:

$$(CH_2O)_{106}(NH_3)_{16}(H_3PO_4) \rightarrow 53CO_2 + 53CH_4 + 16NH_3 + H_3PO_4$$
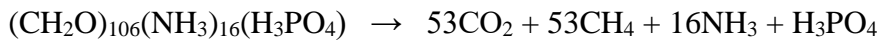
Acetate fermentation also takes place during decomposition yielding methane and carbon dioxide, which can be further reduced to more methane.

$$CH_3COOH \rightarrow CH_4 + CO_2$$
$$CO_2 + 4H_2 \rightarrow CH_4 + 2H_2O$$

19
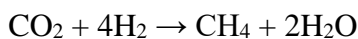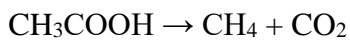
Outside the hydrate stability zone, large volumes of methane may occur as free gas in the sediments. Alternatively, thermal cracking of organically derived materials produces methane as well as other petroleum and natural gas components. This process is called thermogenic and it occurs in substantially deeper sedimentary basins. At higher depths, thermal degradation of oil or maturation of coal produces methane as well.

Once methane is generated in the sediments, it may flow as free gas, dissolved in pore water and move with it or dissipate by molecular diffusion. If moving methane encounters suitable conditions along with sufficient water molecules, hydrates will form inside sediment pore spaces. The temperature required for thermogenic process inhibits hydrate formation. Hence, thermogenic methane has to ascend to hydrate stability zone in order to be deposited in hydrate. Biogenic methane on the other hand, either may move up from its origin to reach hydrate stability zone or may form inside hydrate stability zone. Hydrate progressively fills and cements fractures and pore spaces in the sediments inside hydrate stability zone, producing vein-type and massive hydrate deposits (Sloan and Koh, 2008; Max, 2003).

2.4.5. Gas Hydrate Life Span

Hydrate life span can be divided into three segments that are nucleation, growth, and dissociation. Hydrate formation and dissociation are first-order thermodynamic phase transitions. When a hydrate forms from its constituents, it releases energy as heat to the environment. Hence, the formation is exothermic. On the other hand, dissociation of hydrate to its ingredients is endothermic. The energy in question is equal in absolute magnitude in both transitions. The sign however is opposite naturally.

Nucleation is the stage where hydrate occurs for the first time. In an environment where gas and water are present, on a microscopic scale, water and gas clusters grow and disperse continuously. Nucleation is the process that a cluster of gas-water reaches the critical size for continuous growth. This process may involve several thousands of molecules. There are two prominent hypotheses on this matter. One hypothesis is centered on labile clusters. Water molecules around a dissolved gas molecule happen to have a correct coordination number for hydrate structure and produce labile clusters.

Labile clusters may agglomerate and reach the critical size. Another hypothesis proposes guest molecules are locally ordered in correct structure for hydrate formation, at a size comparable to critical size. Without going into more detail, more uniformly accepted points of nucleation could be summarized as follows. Nucleation happens heterogeneously in mixture but most usually at the gas-water interface. Induction process is stochastic and highly variable according to the experimental setup. This stochastic property is less pronounced at higher driving forces with constant cooling. Induction times correlate with the degree of sub cooling but vary with a number of other factors, some of them being guest size and composition, geometry, surface area, contaminant substances other than host and guests, degree of agitation and history of the sample. Prior hydrate formation brings along a memory effect, which causes separated host and guest to reform hydrate more easily.

Crystal growth is the phase where microscopic water and gas clusters develop further to achieve a macroscopic size. This phase is better understood and modelled. Like nucleation, this phase is also dependent on sub cooling, surface area, agitation, and history of the sample. Moreover, mass and heat transfer substantially affects growth. Mass transfer is related to the rate of guests diffuse to the hydrate surface. The hydrate contains up to 15 mol% gas and this is more than 100 times higher than methane gas solubility in water. Heat transfer is related to the dissipation of exothermic heat of its formation from the hydrate. According to the system, crystal grows in four distinct processes.

- **Single crystal growth:** Under low driving forces, hydrates may form a unitary crystal in the solution
- **Hydrate film/shell growth at the gas-water interface:** Hydrate film occurs at the water-gas boundary. In the water phase, shells take shape in the periphery of hydrocarbon droplets. If the driving force is low, then the shell surface will be smooth. If the driving force is high, then the crystal surface will have protuberances of long thin crystals.
- **Multiple crystal growth in an agitated system:** In this process, each crystal takes shape in a quite close manner as single crystal growth process. Modelling this process is a more faithful demonstration of actual hydrocarbon-water systems in the nature although results are apparatus dependent.

- **Growth of metastable phases:** The observation of metastable phases during hydrate growth is possible by Raman and NMR spectroscopy along with neutron and X-ray diffraction. For example, during formation of sI hydrates, coexistence of sI and sII structures is reported (Moudrakovski et al., 2001; Uchida et al., 2003). Observations of such metastable phases are useful in resolving molecular processes and thermodynamics of hydrate growth.

Existing models of growth only works under their own parameters. In addition, these parameters may not resemble real life conditions in question. Driving force behind a substantial fraction of hydrate formation data is hydrate clogs in gas pipelines. sI hydrates are investigated more than sII, which occurs more commonly in pipelines due to higher hydrocarbons.

Hydrate dissociation phase is the final phase of hydrate lifespan. Revealing its mechanics is crucial to produce gas from hydrate reservoirs and to resolve pipeline plugs. This process is endothermic. For instance, methane hydrate's heat of dissociations is 500 J/gm-water. Three basic requirements of hydrate formation, namely pressure, temperature, and molecules in the system, can be exploited to disrupt their concordance. Depressurization is the removal of external pressure to hydrate crystal. Thermal stimulation is the applications of external heat. Injection of thermodynamic inhibitors is another method and alters the substance composition of hydrate system.

During the dissociation phase, some hydrates have a tendency to retain a portion of its volume for extended periods even though they are exposed to conditions out of hydrate stability limits. This unexpected condition is documented in literature on numerous accounts and termed anomalous self-preservation. Self-preservation phenomenon may be of use in gas storage applications where higher and prolonged hydrate stability is essential (Sloan and Koh, 2008).

When methane hydrate is rapidly depressurized at a constant temperature between 242 K and 271 K, initially, it loses 5-20% of its volume. However, it retains its remaining quantity in a metastable state. This preservation may continue for up to 3 weeks depending on temperature. sI hydrates of CO_2 also exhibit preservation whereas sII

hydrates of ethane-methane do not display such characteristic. In Figure 2.7, average time to reach 50% dissociation for methane gas hydrates at 0.1 MPa methane pressure is shown. Destabilization is triggered by rapid depressurization. The anomalous self-preservation is observed between 242 K and 271 K. In addition, hollow squares where pressure is kept at 2 MPa and hollow diamonds where sII methane-ethane hydrate is studied are shown (Sloan and Koh, 2008).
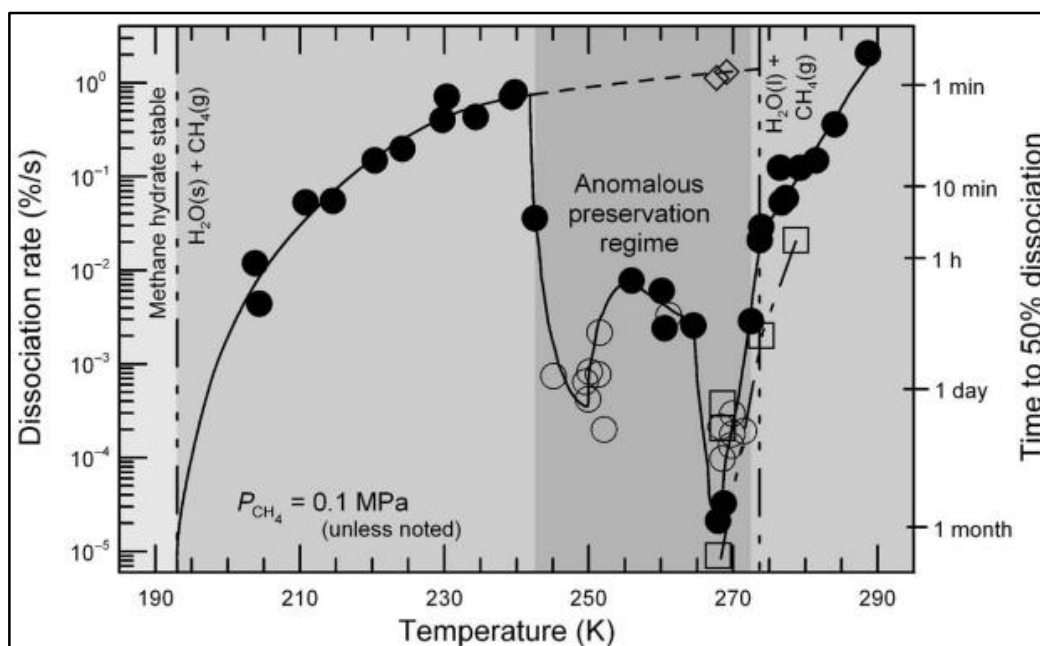
Figure 2.7: Average time to reach 50% dissociation for methane gas hydrates at 0.1 MPa methane pressure (adapted from Sloan and Koh, 2008)

2.5. Gas Hydrate Stability Zone

Problems related to hydrates in petroleum and petrochemical industry inspired the development of methods aiming to predict the gas hydrate stability zone (GHSZ), which is the region on the temperature-depth diagram reflecting the pressure-temperature phase diagram of gas hydrates. In this hydrate stability zone, thermodynamical stability of hydrates is achieved compared with ice, natural gas, and liquid water (Kvenvolden, 1993, Kvenvolden, 1988 (a)).

Even though methane is the major ingredient, hydrates in nature hold CO_2, H_2S, and N_2 gases as well. The pressure-temperature phase diagram for pure methane and pure water is shown in Figure 2.8. Addition of NaCl into the system shifts the phase boundary to the left and shrinks the GHSZ. Presence of N_2 also does the same effect.

However, CO_2, H_2S, C_2H_6, and C_3H_8 shift the curve to the right and enlarge the GHSZ. Lithostatic and hydrostatic pressure gradients are assumed 10.1 kPa m^{-1} (Kvenvolden, 1993, Kvenvolden, 1988 (b)).
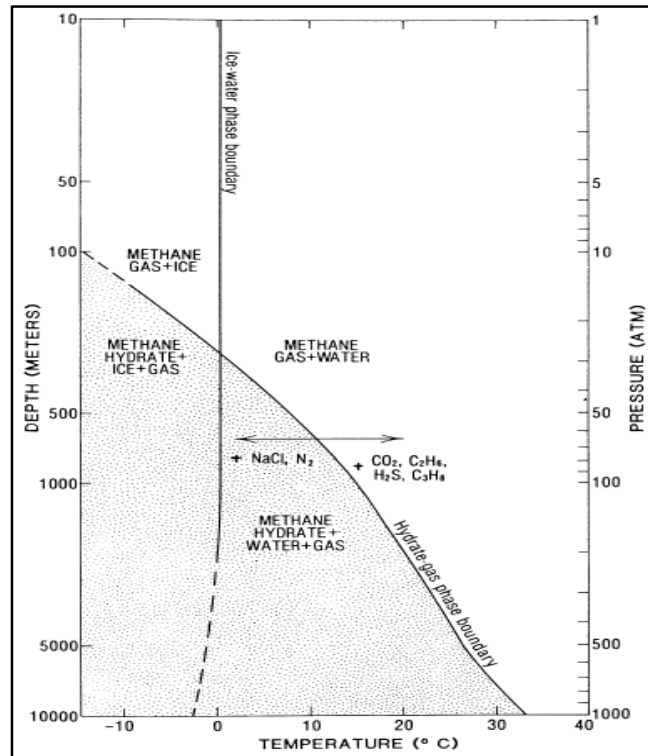
Figure 2.8: The pressure-temperature phase diagram for pure methane and pure water and change with adding chemicals into the system (adapted from Kvenvolden, 1993)

Considering its massive area, oceanic seabed harbors the majority of hydrates on Earth. In open oceans, surface waters are typically warmer than seafloor waters. Hydrothermal gradient refers to the change in water temperature with depth. This is affected by heat input mechanisms of the local body of water such as latitude, weather conditions, and streams. Ordinarily, fall of temperature is faster with increasing depth near the surface. At some depth point, this steep fall will be slowed and this point is referred as thermocline. Thermocline is more pronounced in summer and it may disappear in winter. In polar waters, surface temperature is very low and thermocline is not observed. Hydrate stability zone is at much lower depths due to low temperature as well. Exceptions also include closed bodies of waters. For example, Mediterranean Sea has warmer waters at the seabed and hydrates require much higher pressure-depths (Kvenvolden, 1993, Kvenvolden, 1988 (b); Max).

Gas hydrate stability zone as found in marine environments and in permafrost regions are displayed in Figure 2.9 and Figure 2.10 defined by temperature and depth.
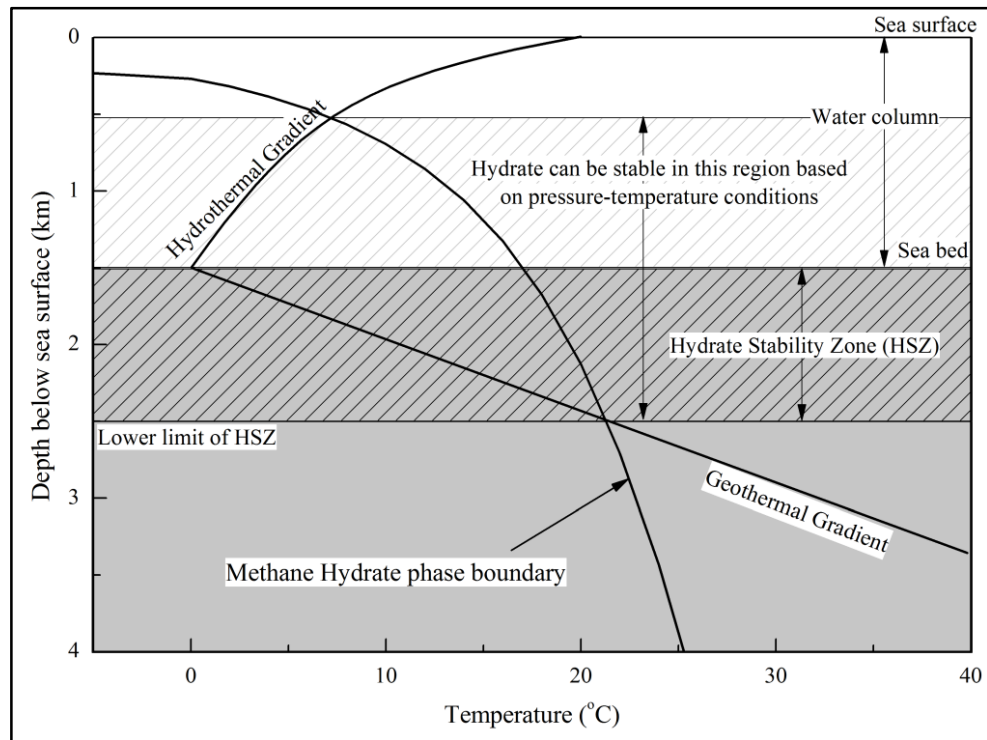
Figure 2.9: Gas hydrate stability zone in marine environments, defined by temperature and depth (adapted from Kvenvolden, 1993)
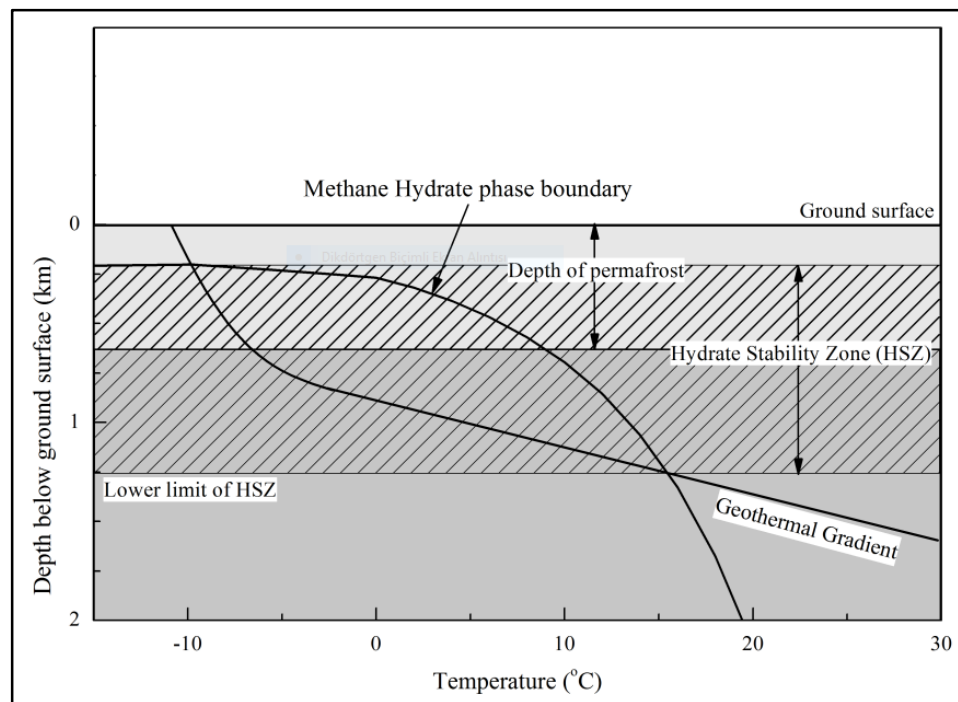
Figure 2.10: Gas hydrate stability zone in permafrost environments, defined by temperature and depth (adapted from Kvenvolden, 1993)

2.6. Gas Hydrates Investigation Techniques

For the purpose of determining and evaluating gas hydrates, seismic and acoustic techniques (Multibeam Bathymetry and Side Scan Sonar) are employed depending upon the depth and purpose. Beside these seismic and acoustic techniques, well logging, Ocean Bottom Seismograms (OBS), Electromagnetic (EM), Direct Current Resistance (DCR), and Controlled Source Electromagnetic (CSEM) are also utilized to determine gas hydrates and their distribution. Some other properties of gas hydrates such as temperature, gas composition, pore water analysis are specified by geologic sampling methods (i.e. gravity core, piston core), drilling ships, remote control devices and mini submarines (Akarsu, 2012).

Core sampling is a helpful method for observing hydrates and their reservoir characteristics. Preserving the in situ pressure and temperature and preventing dissociation of hydrates while traveling the core sample to the surface are important to acquire integrated and quantitative information about hydrates (Yamamoto, 2014). For this purpose, pressure retaining core barrels have been developed. Core sampling method is used together with seismic and well logging to specify the exact location for a better sample (Ye and Liu, 2013).

Wire line well logging tools can be used for finding and assessing geophysical information on gas hydrates. These well logging tools i.e., caliper, gamma ray, spontaneous potential, resistivity, sonic velocity, and neutron porosity are utilized in different combinations with each other (Kvenvolden, 1988). In Figure 2.11, well log data of a NW Eileen State 2 well, situated on the North Slope of Alaska, is depicted. This well is found to pass through a hydrate deposit. Hydrate bearing interval is also shown in the figure.
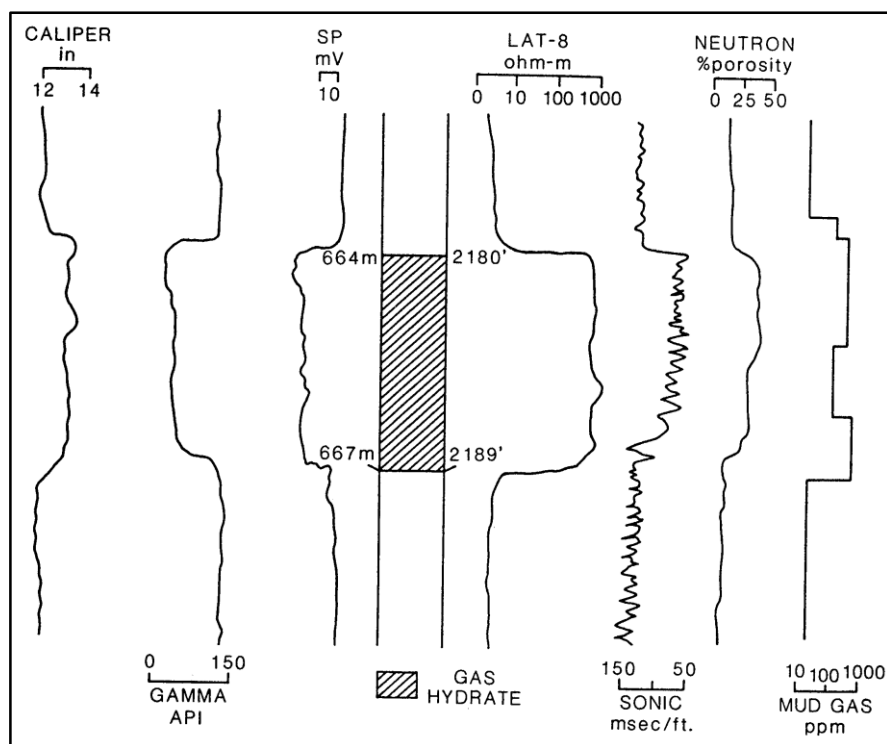
Figure 2.11: Well log responses of wire line of a NW Eileen State 2 well's hydrate bearing interval. Hydrate is identified between 664 m and 667 m. (adapted from Kvenvolden, 1993)

Out of 445 wells that were studied on the North Slope of Alaska 50 wells were found to drill through six distinct hydrate bearing zones. A comprehensive analysis of this data and logs from a Deep Sea Drilling Project hole located in Guatemala showed that resistivity and sonic velocity measurements are the most helpful tools to detect hydrate presence and as a whole, well log data is able to determine gas hydrate zones clearly (Mathews, 1986). Well logs may also be useful tools for estimating gas amount in gas hydrates.

Geophysical well log methods take advantage of gas hydrates' differing properties from surrounding unconsolidated, water-saturated sediments. Gas hydrates have cementing effect and decrease porosity and permeability of the sediments and increase bulk resistivity of formation. Well logs measure electrical resistivity and compressional velocity of sediments in the area of interest and an increase in both values suggests gas hydrate existence (Collett, 2001; Collett et al., 2012; Guerin et al., 1999). Moreover, gas hydrates have higher acoustic velocity readings. Combined with high electrical resistivity and increased acoustic velocity indicate gas hydrate existence (Hyndman et al., 1999). These measurements and other data extracted from well logs

are also helpful in characterizing unconsolidated sediment and sedimentary rock in the periphery of gas hydrate deposits (Kim et al., 2007).

Seismic and geophysical well log methods are the most widely used approach for detecting gas hydrates and their reservoirs in marine sediments (Akarsu, 2012). Presence of bottom simulating reflection (BSR), acoustic blanking, and seismic chimney/vent on seismic data all indicate gas hydrate presence. On seismic data, -BSR, which will be discussed further under its own heading, is the main indicator of the base of gas hydrate stability zone (BGHSZ) (Ryu et al., 2009). Seismic blanking zone on seismic data is defined as a decrease in vertical seismic reflection under the hydrate zone. They are thought being related to cold-water flow and gas outlet (Riedel et al., 2002).

Alterations in certain geochemical properties suggest the presence of gas hydrates residing inside sediment layers. Therefore, several geochemical measurements are utilized for discovery and determination of gas hydrates. Principal methods are observations of hydrocarbon gas contents, inconsistencies of ion concentrations in pore waters, aberrations in geochemical isotopes, and detection of indicator minerals. Hesse and Harrison (1981) were the first scientists to identify the abnormalities of chlorine concentration in pore water specimens from hydrate harboring sediments. Characterization of Chloride ion (Cl-) concentration in addition to upward and downward trends in Carbon, Hydrogen, Oxygen, and Chlorine isotopes were carried out in the Blake Ridge area. Almost all sites where hydrates are formed bear authigenic minerals. This suggests authigenic minerals are tightly associated with hydrate occurrence. Other indicator minerals include bitumen, natural aluminum, amorphous sulphur, and pyrite (Ye and Liu, 2013).

2.6.1. Bottom Simulating Reflection

In oceanic sediments, presence of gas hydrates is believed to relate to bottom simulating reflection (BSR). BSRs are believed to be located at the interface between base of methane hydrate zone and free gas zone beneath it. Therefore, they can be used to predict the depth of the gas hydrate stability zone. BSRs generally follow geothermal gradient and are parallel to ocean floor, which is why they are named as bottom simulating reflection. Depth of BSR increases as the depth of the ocean

increases and follow the temperature pressure equilibrium (Hyndman and Spence, 1992).

High amplitude reflector is the characteristic sign of gas hydrates. This high amplitude reflector is almost parallel to seafloor and deepens with increasing water depth. As a result, it generates a BSR. BSRs are associated with a strong negative polarity reflection and have higher reflection coefficient. Such negative reflection coefficient proves that there is a reflective interface between a higher velocity layers on top of a lower velocity layer. The velocity of P wave is increased by hydrate bearing sediments and decreased by free gas zone. This creates acoustic impedance difference in wave velocity at the interface of hydrates and free gas zone (Mackay et al., 1994).

2.7. Worldwide Distribution and Energy Resource Potential of Gas Hydrates

Geological formations suitable for hydrate occurrence, continental margins and polar permafrost, occupy a very large area on Earth. Studies indicate many of them harbors gas hydrates (Figure 2.12). A global evaluation on the matter reveals an immense energy potential lies in these fields. Although most approximations of total amount of energy stored in gas hydrates have a high degree of uncertainty, they range between 2.8×10^{15} and 8×10^{18} m^3. However, even most cautious estimate points to a huge potential of natural gas presence in hydrates.
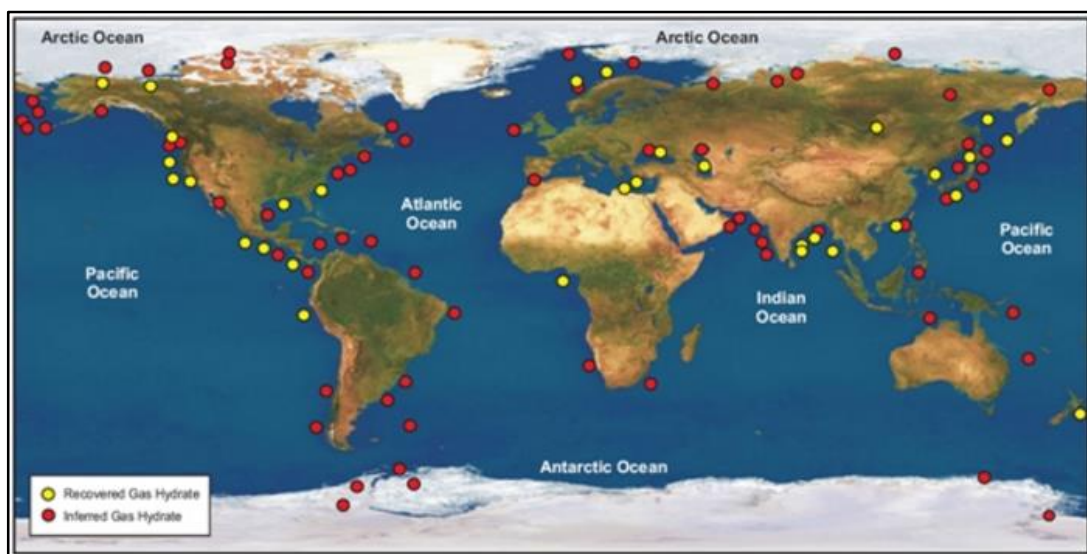
Figure 2.12: Distribution of known methane hydrates accumulations (adapted from Krey et al., 2009)

Currently, it is reasonable to estimate 3×10^{15} m^3 of methane is stored in hydrates. It is accepted that 98% of gas hydrates are in seafloor sediments, and remaining 2% are under continental and polar permafrost (Zou, 2014).

Onshore hydrates are only found under permafrost of Arctic, Antarctic, and Tibetan Plateau and they have total surface area of 1.1×10^7 km^2. Gas hydrate potential in permafrost regions are thought to be between 1.4×10^{13} m^3 and 3.4×10^{16} m^3 (Trofimuk et al., 1977). The permafrost part of Tibet plateau has a surface area of 1.59×106 km^2, which corresponds to 61% of the total area of Tibet Plateau and 7% of the world permafrost. The Qiangtang and terrestrial Hoh Xil Basins, and the Qilian permafrost regions have favorable conditions for hydrate formation and for exploration (Zou, 2014).

As for offshore, continental margins include passive and active margins and total estimations being from 0.2×10^{15} to 7.6×10^{18} m^3 of gas hydrate is stored in seafloor sediments (Zou, 2014; Kvenvolden and Claypool, 1988). These resources of gas hydrates are mostly found in separated offshore tracts, including active or passive continental margins, deep lakes, and inner oceanic plates. Table 2.4 shows broader estimations of the amount of gas within gas hydrates in the world (Zou, 2014; Sloan and Koh, 2008). However, amount of methane in gas hydrates is estimated 2.1×10^{16} m^3 by Kvenvolden, 1999 and accepted as the consensus value in the literature.

Table 2.4: Worldwide estimations of the amount of methane within gas hydrates (adapted from Sloan and Koh, 2008)

CH$_4$ amount Sm^3	Citations	Year
3.053×10^{18}	Trofimuk et al.	1973
1.135×10^{18}	Trofimuk et al.	1977
1.573×10^{18}	Cherskiy et al.	1982
1.20×10^{17}	Trofimuk et al.	1981
3.01×10^{17}	McIver	1981
1.5×10^{16}	Makogon	1974/1981
1.5×10^{16}	Trofimuk et al.	1982
4.0×10^{16}	Kvenvolden and Claypool	1988
2.0×10^{16}	Kvenvolden	1988
2.0×10^{16}	MacDonald	1990
2.64×10^{16}	Gornitz and Fung	1994
4.54×10^{16}	Harvey and Huang	1995
1.0×10^{15}	Ginsburg and Soloviev	1995
6.8×10^{15}	Holbrook et al.	1996
1.5×10^{16}	Makogon	1997
0.2×10^{15}	Soloviev	2002
2.5×10^{15}	Milkov	2004
1.20×10^{17}	Klauda and Sandler	2005

2.8. Estimation of Methane Gas in Natural Gas Hydrate Reservoirs

In order to have a better understanding of the global abundance of gas hydrates and methane potential, field data and advanced numerical simulations have critical importance. Based on these methods, since early 1970's, serious assessments on the amount of methane in gas hydrate accumulations are discussed by several authors. In consequence of these assessments, it is stated that tremendous amount of methane is enclosed in gas hydrates.

Trofimuk, Cherskiy and Tsarev, Soviet geologists, are the first ones to present data and assumptions that can be easily used to make volumetric estimation of submarine gas hydrates. Based on these data and assumptions, global hydrocarbon volume present in gas hydrate reservoirs may be calculated by multiplying the global volume of the GHSZ and gas yield of hydrate bearing sediments. Within this context, global volume of hydrate-bound gas is a function of geologic condition and is commonly formulated as follows:

$$OGIP = A \; x \; h \; x \; \varphi \; x \; S_h \; x \; G \tag{5.1}$$

OGIP: Original CH_4 in-place in gas hydrate reservoirs, Sm^3

A: Cross-sectional area of hydrate zone, m^2

h: Thickness of hydrate zone, m

φ: Porosity, fraction

S_h: Gas hydrate saturation in pore space, fraction

G: Gas hydrate yield (volume of gas at STP in 1 m^3 of gas hydrate), Sm^3/m^3 (Parlaktuna and Erdogmus, 2001; Boswell and Collet, 2011; Milkov, 2004; Merey and Sinayuc, 2016).

Gas hydrate yield, which is stated as volumetric conversion factor (Boswell and Collet, 2011) in some other works, relates to the cage occupancy of the hydrate lattice. It varies from about 140 Sm^3 to 180 Sm^3 according to different researches. However, it is generally stated that one m^3 of gas hydrate yield maximum of 164 m^3 of methane gas (Parlaktuna and Erdogmus, 2001; Boswell and Collet, 2011, Sloan, 1991).

After that, a dynamic model is developed by Trofimuk and his colleagues to make a global estimation in 1975. In this equation, GHSZ is considered separately for continental shelf, continental slope, and abyssal plain, since it is realized that areal extends and thicknesses are considered different for each region. Moreover, that model includes formation, decomposition, migration, and recrystallization of the gas in gas hydrate.

$$OGIP = A \; x \; R = \; (A \; x \; R)_{shelf} + \; (A \; x \; R)_{slope} + \; (A \; x \; R)_{abyssal \; plane} \qquad (5.2)$$

where R is gas hydrate resource density, volume of hydrate-bound gas at STP per square meter of hydrate-bearing area, m^3/m^2 (Milkov, 2004).

In their study, Merey and Sinayuc (2016) use the following formula for methane volume estimation of gas hydrates in the Black Sea. The resulted amount of methane is found by multiplication of Equation (5-3) by sand content.

$$OGIP = A \; x \; h \; x \; \varphi \; x \; CR x \; EF \qquad (5.3)$$
$$EF = \; (MW_{CH4}/(MW_{CH4} + \; N_H MW_{H2O})) \; x \; (V_H \rho_H / \rho_{CH4}) \qquad (5.4)$$

OGIP: Original CH_4 in-place in gas hydrate reservoirs, Sm^3

A: Cross-sectional area of hydrate zone, m^2

h: Thickness of hydrate zone, m

φ: Porosity, fraction

CR: Cavity fill ratio of CH4

EF: Expansion factor of CH_4 in hydrate to surface standard conditions, fraction

MW_{CH4}: Molecular weight of CH_4, g/mol

MW_{H2O}: Molecular weight of H_2O, g/mol

N_H: Hydration number of CH_4 hydrate

V_H: Unit hydrate volume (1 m^3)

ρ_H: CH_4 hydrate density, kg/m^3

ρ_{CH4}: CH_4 gas density at standard conditions (0.717935 kg/m^3 at 0°C and 1atm).

In another study, Senger et al. (2010), the following formula adapted from Equation (5-1) is used to calculate methane volume at the Nyegga gas hydrate prospect.

$$OGIP = GRV \; x \; \varphi \; x \; N/G \; x \; (1 - S_w) \; x \; 1/B_G \qquad (5.5)$$

OGIP: Original CH_4 in-place in gas hydrate reservoirs, Sm^3

GRV: Gross rock volume, m^3

N/G: Net-to-gross ratio, fraction

S_w: Water saturation, fraction

B_G: Formation volume factor, volume at reservoir/volume at STP

Fujii et al. (2008) also adapted the Equation (5-5) to assess methane resources in bcf in gas hydrates concentrated zones at the Nankai Trough. For that purpose, a conversion coefficient is added to the equation and it takes the following form:

$$OGIP = GRV \; x \; \varphi \; x \; N/G \; x \; S_h \; x \; VR \; x \; CO / 28.3 \qquad (5.6)$$

OGIP: Original CH_4 in-place in gas hydrate reservoirs, bcf

GRV: Gross rock volume, MMm^3

N/G: Net-to-gross ratio, fraction

S_h: Gas hydrate saturation in pore space, fraction

VR: Volume ratio, fraction

CO: Cage occupancy, fraction

28.3: Conversion coefficient, 1 bcf = 28.3 MMm^3

The modern technology and recent field explorations improved interpretation of the field data for understanding behavior of gas hydrates. Yet still, all these parameters in above equations have some extend of uncertainties and the probabilistic method is one of the best approaches to uncertainties. In this sense, Monte Carlo method is a good way of modelling complex physical problems (Woller, 1996). It allows users achieving the most optimal outputs when dealing with uncertainties of the input variables over trial runs (Senger et al., 2010). Amount of methane in gas hydrates of the South Caspian Sea, is calculated using volumetric method. Each parameter, such as area, thickness, gas hydrate saturation, porosity, methane hydrate yield are given as probabilistic distribution for Monte Carlo simulation, considering the uncertainties of these evaluations (Fujii et al. 2008).

CHAPTER 3

CASPIAN SEA

3.1. Caspian Sea

The Caspian Sea (Figure 3.1) is the largest body of water on Earth totally enclosed by land. It is located between Europe and Asia and bounded by Azerbaijan, Russia, Kazakhstan, Turkmenistan, and Iran in clockwise order. It has a length of 1,174 km from the north to the south, average width of 326 km from the west to the east, and a surface area of 375,000 km^2 (Buryakovsky et al., 2001). The maximal width of the Caspian Sea is 566 km. Average depth is 184 m with maximal depth of 1,025 m in the Caspian Sea (Croissant and Aras, 1999; Aladin and Plotnikov, 2004).

Some 50-60 million years ago, the Caspian Sea was a part of Thetis Ocean. To state more precisely, it is a remnant of the Thetis Ocean's gulf, Paratethys (Aladin and Plotnikov, 2004). In the location of the Caspian Sea, a vast body of water named Paratethys Sea lied during late Jurassic and Cretaceous periods. 14 million years ago, it became landlocked, lost most of its water and gave birth to present day of the Caspian Sea, Black Sea, Aral Lake, and Lake Urmia among others (Esin et al., 2016). However, it took the last form of it some 5-7 thousand years ago, in the beginning of the Holocene (Aladin and Plotnikov, 2004).

Figure 3.1: The Caspian Sea and neighborhood countries (retrieved from Map of the Caspian Sea with the Neighboring States, 2018)

Around the Caspian Sea, the major land formations are Caucasus Mountains to the west, Central Asian steppes and Karakum Desert to the east, and Elburz mountains to the south. In the north, there is Caspian Depression, which is even below Caspian Sea level in parts. Even though its surface level fluctuates, the Caspian Sea itself is about 28 m below ocean level (Buryakovsky et al., 2001). More than 130 rivers feed the sea to a total volume of 80,000 km^3 (Croissant and Aras, 1999). This figure corresponds to 44% of all lacustrine waters in the world (Ibrayev et al., 2009).

The Caspian Sea basin is an endorheic basin with a catchment area of nearly 3.5 MMkm^2 (Croissant and Aras, 1999). River runoff is the main water inflow to the Caspian Sea accompanied by groundwater flow and rainfall over the sea. The river runoff makes up 79% of total inflow while rainfall makes up 20% and groundwater flow makes up 1%. Majority of the surface water inflow comes from the Volga River, which covers for 80% of river runoff. The Ural, Kura, Terek, and Emba rivers combine to account for almost all of remaining 20% (Rodionov, 1994). All these major rivers

drain to the north and west of the basin. East and south shores are occupied by Iran and Turkmenistan. Both countries have scarce rivers. Small amount of water passes from the Caspian Sea to its detached lagoon Karabogaz-Gol through a narrow strait. This flow is the only liquid outflow from Caspian Sea and the only surface water inflow to the Karabogaz-Gol lagoon. As a whole, the Caspian Sea and Karabogaz-Gol lagoon systems' only mean of outflow is evaporation. Evaporation makes up 97% of outflow from Caspian Sea while water flux through the strait accounts for the rest (Klige and Myagkov, 1992).

Contour line bathymetry and color bathymetry of the Caspian Sea can be seen in Figure 3.2 and in Figure 3.3, respectively. Based on its physico-geographical conditions and the character of the bottom topography (Kosarev, 2005), the Caspian Sea is divided into four geographical divisions, namely, North, Middle and South Caspian together with the Karabogaz-Gol lagoon.

The North Caspian, the shallowest part, has average depth of 6 m and its maximum depth does not exceed 10 m. It consists of 29% of the area and only 1% of water volume of the entire sea. Almost 20% of the North Caspian has depth less than 1 m (Rodionov, 1994; Aladin and Plotnikov, 2004). An abrupt depth transition at the Mangyshlak Swell separates it from the Derbent Basin of the Middle Caspian Sea (Kosarev, 2005).

The Middle Caspian has average depth of 175 m with maximum depth of 790 m. Its area and water volume are 36% and 35% of the whole sea, respectively. The Middle and South Caspian are separated by underwater Apsheron Swell, a saddle depth of about 200 m (Rodionov, 1994; Aladin and Plotnikov, 2004; Kosarev, 2005).

The South Caspian is the deepest division with average depth of 300 m and the maximum depth of 1,025 m. It is also the largest one in volume, 64% of total volume and covers 35% of total area of the sea (Rodionov, 1994, Aladin and Plotnikov, 2004).

Karabogaz-Gol, the fourth part of the Caspian Sea, is a shallow lagoon with depth not exceeding 10 m. It has area of 15,000 km^2. It is connected to Middle Caspian by a narrow strait (Rodionov, 1994, Aladin and Plotnikov, 2004).
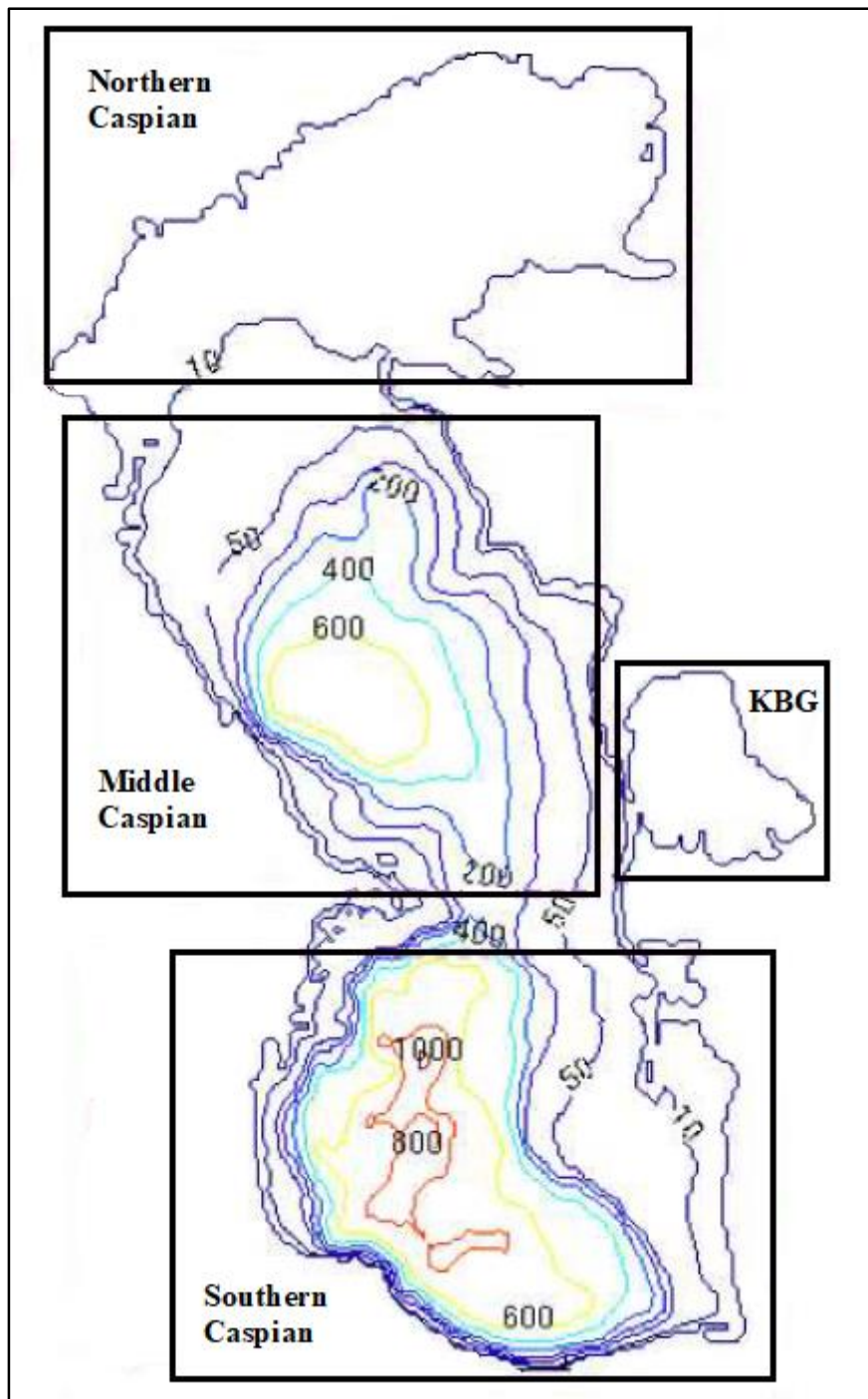
Figure 3.2: Contour line bathymetry of the Caspian Sea in meters (adapted from Tamura-Wicks, 2015)
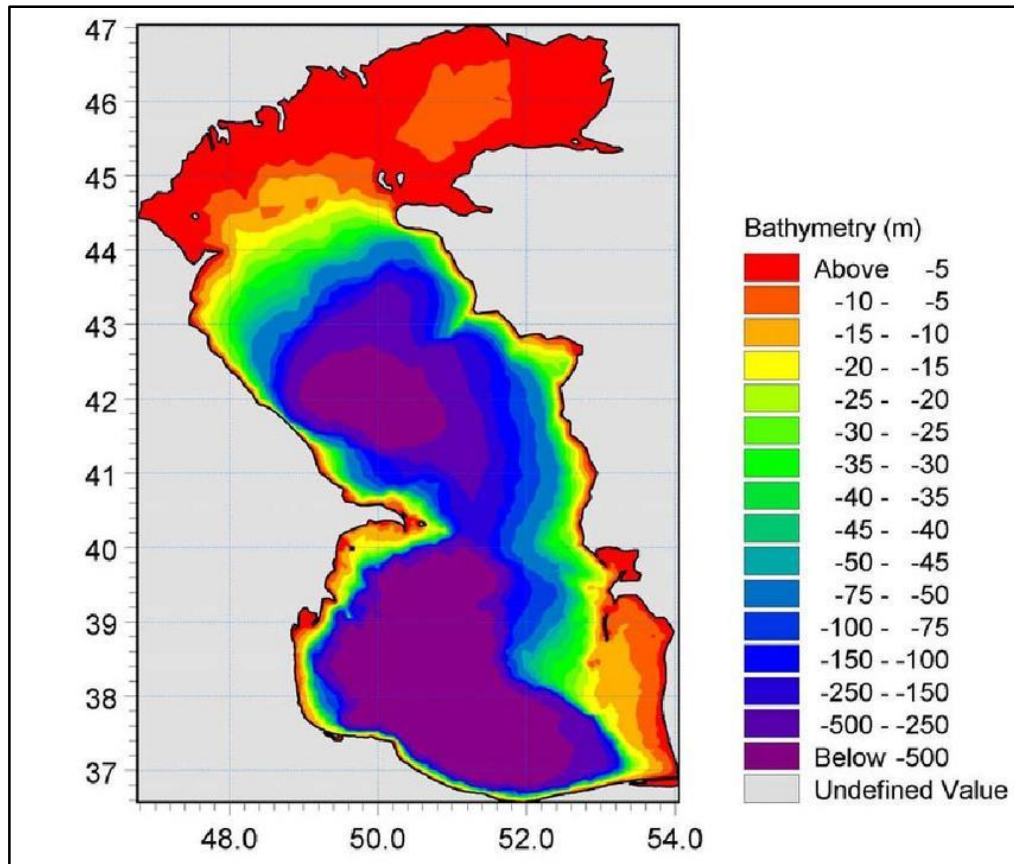
Figure 3.3: Color bathymetry of the Caspian Sea in meters (adapted from Allahdadi et al., 2004)

3.1.1. Salinity

Salt content of the Caspian Sea is inherited from the ancient Paratethys Sea. Roughly, 50-60 million years ago, Paratethys Sea had connections to Atlantic and Pacific Oceans. Eventually, it was isolated from Pacific Ocean and later on from Atlantic Ocean. While isolated, Paratethys' salinity varied with climatic events. During hot and dry periods, when rainfall is low, Paratethys Sea shrank and broke down to smaller lakes with higher salinity than world's ocean. In cool and humid periods with abundant precipitation, these smaller bodies of water would overflow and unite as a single sea with lower salinity. Melting of glaciers resulted in accumulation of huge amounts of freshwater in the sea and reduction in salinity to current level. Today, Caspian Sea has a distinct basin and isolated from other seas and oceans comparable to other lakes. Due to its lake characteristics, water circulation, temperature, and salinity are independent of global oceanic conditions but affected from atmospheric events over the sea and drainage basin (Aladin and Plotnikov, 2004). As a result, Caspian Sea is the world's largest salt-lake (Buryakovsky et al., 2001) with salinity around 13 psu where psu is

practical salinity unit and equals to 1,000 ppm. This amount is roughly one third of ocean salinity.

The Northern, Middle, Southern and the gulf, Karabogaz-Gol, little vary with water salinity. In Figure 3.4, thermohaline characteristics of the Caspian Sea are shown where every dot represents unit volume of water in its corresponding depth. On all three represented layers, dominating water volume has a salinity value around 13 psu. In part (a), on the left side few dots represent the waters of the North Caspian Sea. These waters have vast freshwater influx through Volga River and other rivers but have a small volume. They do not have a representation on parts (b) and (c) due to shallowness of Northern Caspian. Thermohaline values of deeper parts do not exceed the limits set by shallower layers (Tuzhilkin and Kosarev, 2005).
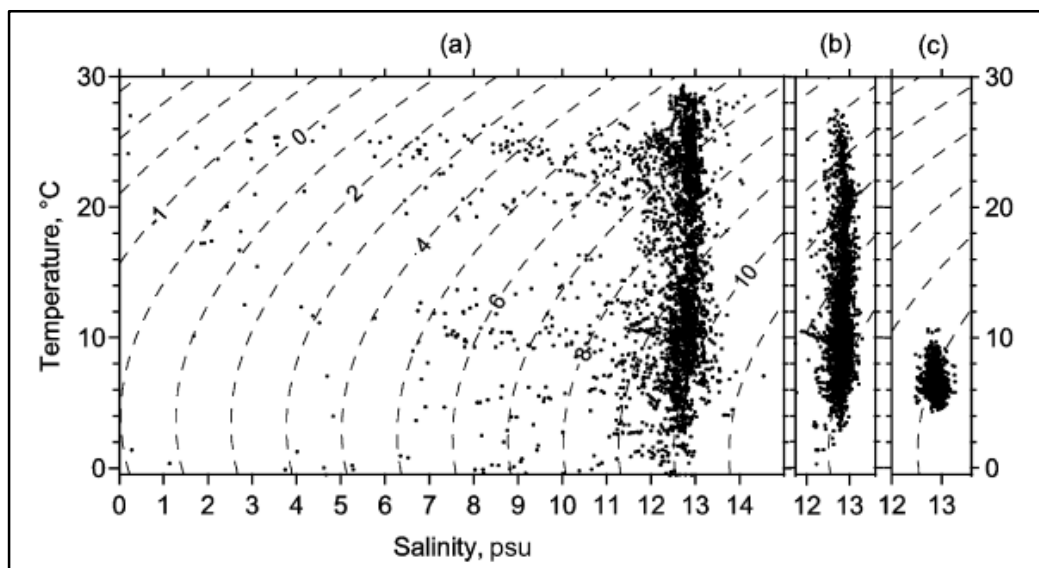
Figure 3.4: Climatic temperature–salinity diagrams of the Caspian Sea waters. a) 0–20 m: Surface layer, b) 20–100 m: Intermediate layer c) Deeper than 100 m: Abyssal layer. Dashed lines Sigma-t contours (adapted from Tuzhilkin and Kosarev, 2005)

Salinity can differ in the surface layer of the near-mouth areas of the Caspian Sea from season to season up to 3 to 5 psu. If river mouth neighboring areas are excluded, through a period spanning multiple years, salinity variation of a particular volume of water is less than 0.5 psu. Additionally, the salinity is almost homogeneous through an entire water column extending from the surface to the seabed. This concept is visualized for the Caspian Sea and South Caspian Sea in Figure 3.5 and 3.6, respectively.

40
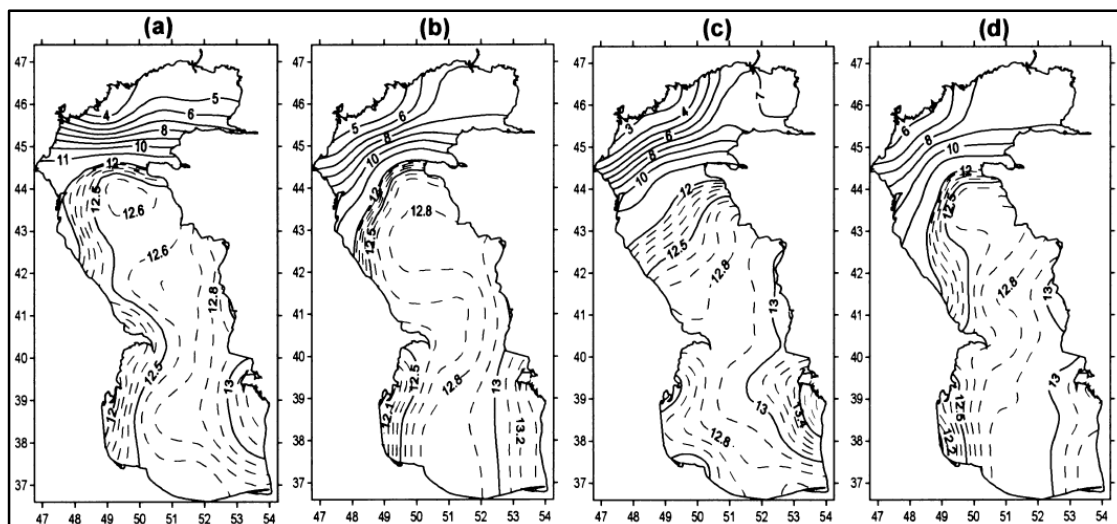
Figure 3.5: Mean water salinity (psu) on the surface of the Caspian Sea (a) February, (b) April, (c) August, (d) November (adapted from Tuzhilkin and Kosarev, 2005)
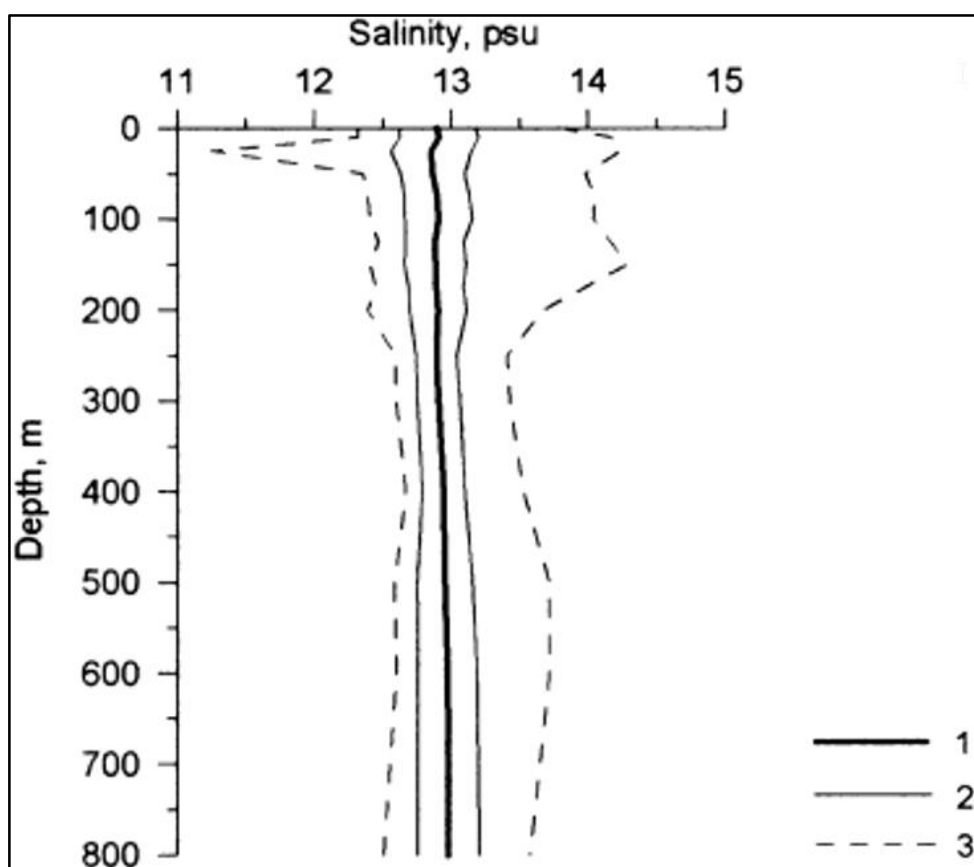
Figure 3.6: Water salinity profile of the deep-water area of the Southern Caspian Sea in August. Lines: 1 mean values, 2 standard deviations, 3 extreme values. ‰ Practical salinity units (adapted from Tuzhilkin and Kosarev, 2005)

It may be inferred that large-scale characteristics of the salinity field are stable yearlong. Positions of reservoirs of fresh water such as river mouths and salt water

41

such as shoal waters off the coast of Turkmenistan are stationary. For depths of deeper than 20 m, amplitudes of the annual harmonic of salinity are not statistically different from zero (Tuzhilkin and Kosarev, 2005).

3.1.2. Temperature

Positioned in the middle latitudes, Caspian Sea is subject to strong inter-annual fluctuations in flux of freshwater and heat. Surface layer of the sea possesses the seasonal character of the time of the year (Figure 3.7). In addition, at any given time, different segments of the sea have different features. Most prominent alterations at sea surface temperature occurs in the Northern Caspian. In summer, temperature reaches a climax of 25-26 °C after falling below freezing point in winter season. In contrast, during summer, Southern Caspian experiences 25-29 °C in terms of maximum sea surface temperature. Lowest temperature observed in wintertime is between 7 and 10 °C. Beneath the surface, thermocline typically takes place at about 20 to 30 meters deeper to the sea level in warmer seasons. In colder months, thermocline can be observed at as deep as 100 m for the Southern Caspian and 200 m for the Middle Caspian (Ibrayev et al. 2009). In deeper parts, temperature shows little variation with respect to time and is stable through a vertical column (Tuzhilkin and Kosarev, 2005).
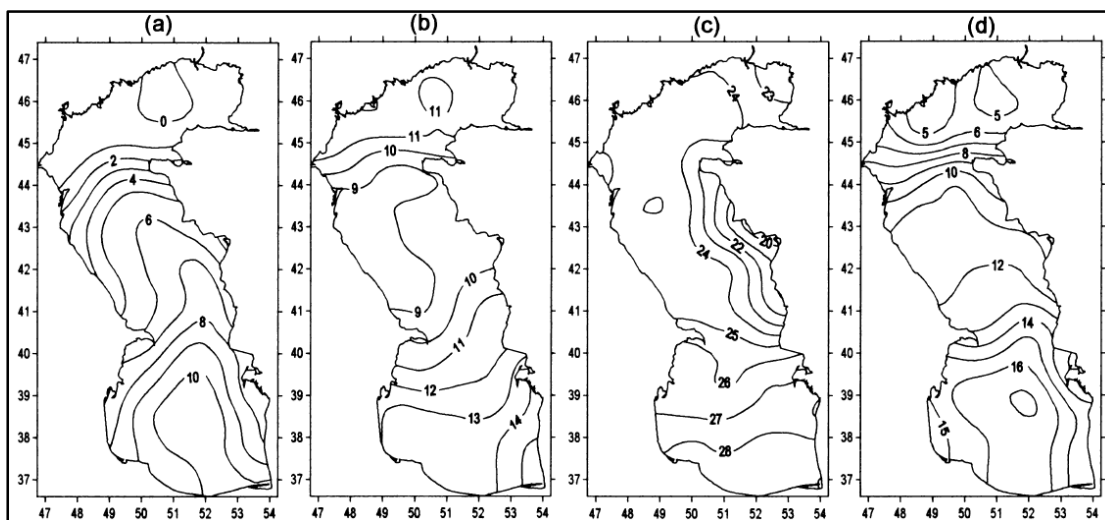
Figure 3.7: Mean water temperature (°C) on the surface of the Caspian Sea (a) February, (b) April, (c) August, (d) November (adapted from Tuzhilkin and Kosarev, 2005)

The amplitude of the yearlong oscillation of water temperature decreases with increasing depth as well and does not statistically differ from zero at depths deeper than 100 m (Tuzhilkin and Kosarev, 2005). Temperature reaches 5.85-6.2 °C at seafloor (Bagirov et al., 1999).

3.1.3. Sea Level

The Caspian Sea which is landlocked since Middle Pliocene experiences the largest regional hydrological cycle variations during the last century. The discharge from the Volga and other rivers as well as precipitation cause increase in sea level of the Caspian Sea. On the other hand, a small amount of groundwater inflow, evaporation and discharge to Karabogaz-Gol decrease the sea level. However, these increasing and decreasing factors are not always balanced. Since the sea level is very sensitive, changes in any one of these factors affect it (Knapp et al., 2005; Arpe et al., 2000; Tamura-Wicks, 2015). It may vary 30-40 cm throughout the year. Sea level reaches to peak values during May-July period due to the spring floods and lower values during the winter (Ibrayev et al., 2009).

Sea level fluctuations are observed at much shorter time scales and much larger amplitudes than other oceans in the world (Knapp et al., 2005). For instance, in the 1930s, 1.7 m drop in the sea level was observed, followed by an unexpected rise by 2.5 m in the 1980s. In Figure 3.8, sea level and height variation diagrams of Caspian Sea is presented. In a), sea level of the Caspian Sea is drawn from 1850 to 2000 based on tide gauge data. The last cycle of Caspian Sea level is noted between 1929 and 1995. In b), height variation of Caspian Sea is displayed from 1992 to 2012 from altimetry satellite data (Kakroodi et al., 2015).
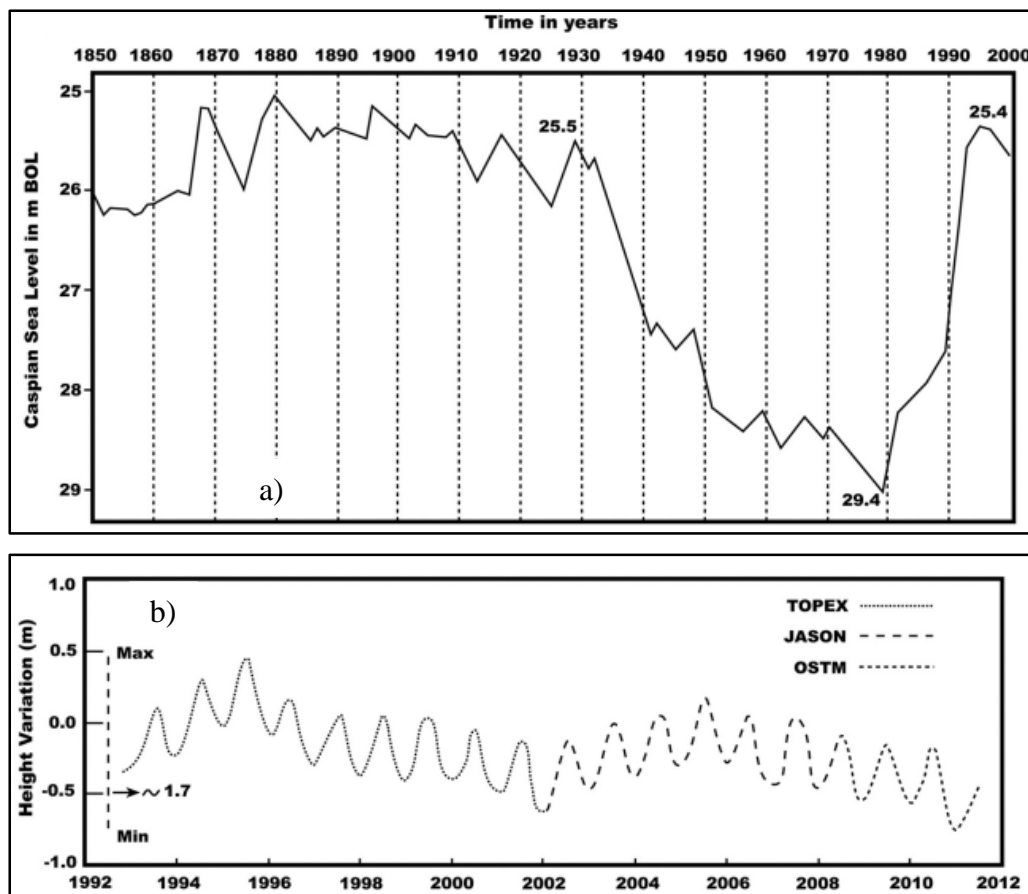
Figure 3.8: Sea level and height variations diagrams of the Caspian Sea. a) Sea level of the Caspian Sea from 1850 to 2000 based on tide gauge data (source: National Iranian Oil Company compiled by A. Jafari). b) Height variation of Caspian Sea from 1992 to 2012 from altimetry satellite data (adapted from Kakroodi et al., 2015)

3.2. The South Caspian Region

The southern portion of the Caspian Sea is situated between Neogene age Greater and Lesser Caucasus and Talysh Mountains in Azerbaijan, Elburz Mountains in Iran and Koped Dag Mountains in Turkmenistan. Although surrounded by high altitude earth formations, seabed of the South Caspian Sea has a complex and irregular topography with a depth of over 1,000 m (Bagirov et al., 1999; Diaconescu et al., 2001; Kosarev, 2005).

The South Caspian Basin takes place within a belt of Tertiary to Holocene compression related to the Alpine-Himalayan orogenic belt. It is surrounded by compressional belts of the earth's crust involved in the formation of mountains. 8-10 km of Plio-Pleistocene clastic sediments are originated in the Kura and Volga rivers and they overlay the

Mesozoic and Paleogene sections. Erosion of Lesser and Greater Caucasus Mountains, due to collision of Arabian Plate and Eurasia, forms a remarkable part of these sediments. The South Caspian Basin's sediments are not deformed as much as the adjacent Caucasus, Kopeh-Dagh, and Elburz fold and thrust belts. However, seafloor bathymetry shows evidence for possible active and recent massive slope failure on the continental shelf. Additionally, according to earthquake seismology, the region is a relatively rigid aseismic block. However, a series of large folds possibly related to gas hydrates may cause the continental slope failure and seafloor deformation, named Apsheron Allochthon, in the region (Devlin et al., 1999; Knapp et al., 2005).

Stratigraphic sections of the South Caspian Sea according to geologic ages are shown in Figure 3.9.
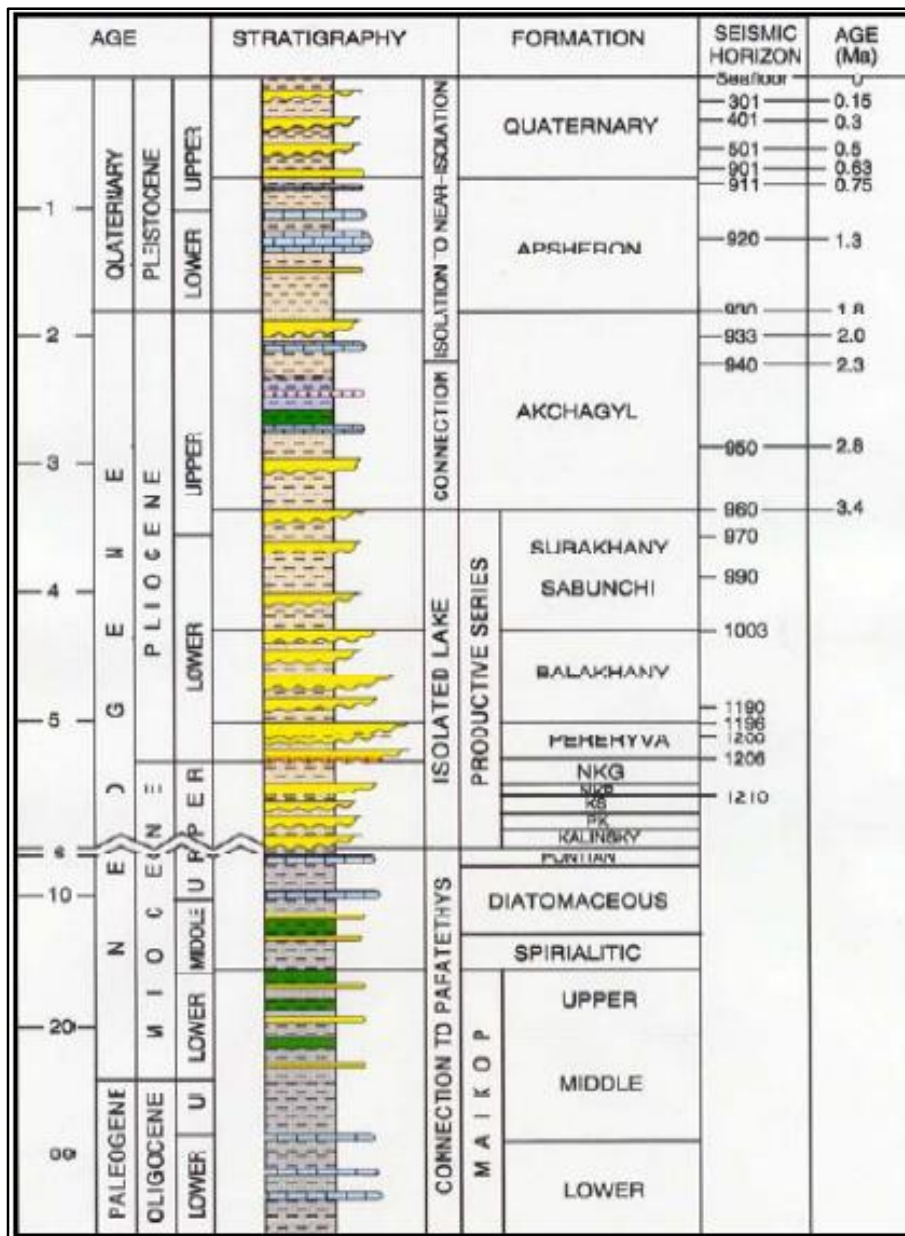
Figure 3.9: Stratigraphic sections of the South Caspian Basin (adapted from Yusifov and Rabinowitz, 2003)

2-D seismic data, almost 23 km long, shows enormous inset anticlinal structures that are buckle folds overlying across a typical formation of the South Caspian Basin (Figure 3.10). The crestal normal faults in the shallow section and the low-angle reverse faults in the lower part of the fold are remarkable. An inferred neutral surface within the lower Surakhany Formation separates these faults. Moreover, the onset of structural growth is indicated by the thinning and on-lap of strata above the top Surakhany Formation, being demonstrated by pink surface (Devlin et al., 1999).
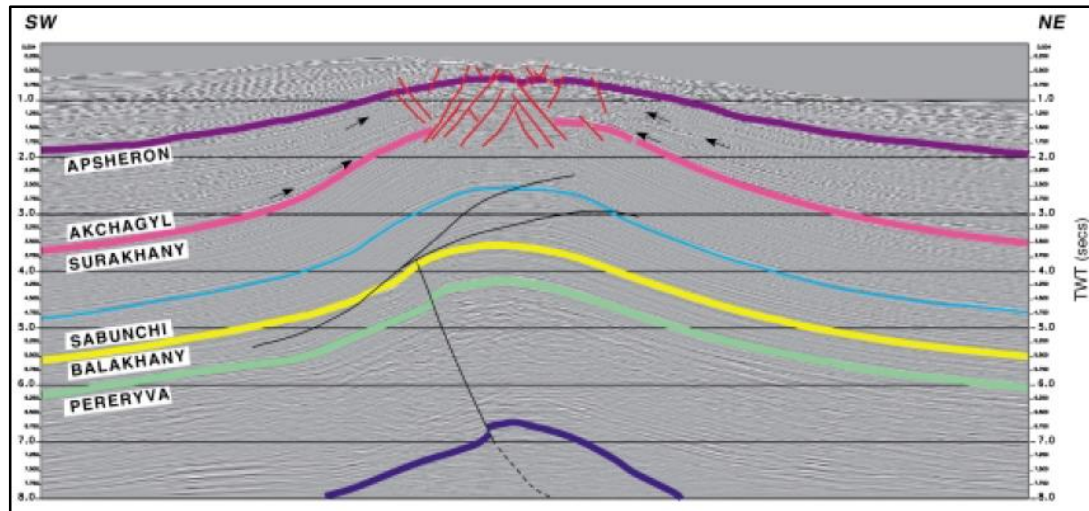
Figure 3.10: Seismic line across a typical South Caspian Basin structure (adapted from Devlin et al., 1999)

Because of the geologic structure of the South Caspian basin, it is among the world's most promising hydrocarbon regions. Sediments have accumulated up to 25 km Mesozoic to Cainozoic (Cenozoic) deposits based on the seismic refraction and reflection profiling. Almost 10 km of these deposits have been created in the last 6 million years during Pliocene–Quaternary interval. The discovered hydrocarbon rich fields are consisted of within siliciclastic reservoirs bounded by structural traps such as anticlinal folds and monoclines with various degrees of reverse faulting and fracturing. Mud diapirs and mud volcanoes penetrate many of these structures (Devlin et al., 1999; Bagirov and Lerche, 1997; Knapp et al., 2005). Presently, active oil and gas seeps are observed in the basin. Plentiful amount of mud volcanoes, active oil and gas seeps, and low temperature gradient (11-17 °C/km) due to the rapid deposition (1.3 km/MA) suggest that hydrocarbons are still actively forming and migrating within the basin. Oil generates at depth of 8 km and gas generates at depth of 13-14 km (Devlin et al., 1999; Knapp et al., 2005).

3.2.1. Hydrocarbon Background of the South Caspian Sea

Producing oil for more than 150 years, South Caspian Basin is one of the world's oldest oil producing regions. Major oil reserves are accumulated during the Middle Pliocene and found in these depositions. Apsheron Peninsula, Gobustan area, Kura lowland, offshore areas of Apsheron and Baku archipelagoes and Apsheron Threshold are the main oil and gas rich regions (Buryakovsky et al., 2001). 11 billion oil-equivalent

barrels of cumulative production and 10 billion oil-equivalent barrels of proven undeveloped reserves are reported. According to the United States Energy Information Administration, natural gas reserves are even larger which is estimated as 236-337 TCF.

After break-up of the Soviet Union, the basin has become a prolific region for global investment of the petroleum companies with new exploration and production opportunities. Thirteen Production Sharing Agreements with diverse national and international companies, 2-D and 3-D seismic acquisition, coring, exploration and production drilling, platform and pipeline construction activities have been held and mostly converged near the Apsheron ridge (Devlin et al., 1999; Diaconescu and Knapp, 2002).

Together with proven hydrocarbon reserves, Southern Caspian was proposed as a gas hydrate site since 1970's by Institute for Geology and Development of Fossil Fuel during a marine geologic exploration. They are encountered broadly in the deep water of the South Caspian Sea mostly as buried deposits under the seafloor. These buried gas hydrates may seriously affect large-scale slope failure and shallow deformation in the area.

Historical documents about the South Caspian Sea also show the area is susceptible to natural hazards, including explosive eruptions of mud volcanoes. Mud volcanoes are known to be associated with hydrate deposits and this poses a threat of explosive eruption offshore and slope failure on the continental shelf (Bagirov et al., 1999; Diaconescu et al., 2001).

In a study of Knapp et al. (2005), it is cited that large-scale slope failure and shallow deformation are mostly encountered with sea level low-stand through massive gas hydrate dissociation. These submarine landslides and deformations generally give rise to turbidity currents, which possibly induce large tsunamis by moving extensive amounts of sediments downslope. All these connections makes the region a natural laboratory to study the relationships among the gas hydrate dissociation, mud volcanism, seismicity, global warming and seafloor deformation, and can be used as a proxy for similar processes in the world's oceans.

3.3. Natural Gas Hydrates in Caspian and South Caspian Sea

In a study of Gerivani and Gerivani (2015), it is said that thermobaric conditions, favorable features of deposits, thick clayey deposits and enough amount of organic substances are essential conditions to drive the process of gas hydrate formation. In the light of this knowledge about hydrates and suitable conditions for their generation, samples of solid gas hydrates are obtained from oceanic sediments by coring under the Deep Sea Drilling Project (DSDP) and later by the Ocean Drilling Program (ODP) from continental margins around the world (Kastner et al., 1998; Kvenvolden and Lorenson, 2001).

Almost all discovered gas hydrates extracted by DSDP and ODP were methane hydrates retrieved from sediments deeper than 100 mbsf. Other sampling methods however, coring with piston, gravity and push cores, dredging, and individual site sampling were used with success in recovery of shallow gas hydrate samples from within 10 m of the seafloor (Kastner et al., 1998; Kvenvolden and Lorenson, 2001).

A majority of oceanic hydrates are concluded to have biogenic origin, which forms sI type of gas hydrates. Naturally, the gas hydrates overlying oil reservoirs are of thermogenic origin and mainly in sII structure. Thermogenic hydrates are observed in the several other parts of the world as well as in the Caspian Sea. These hydrates are able to stabilize at less favorable conditions than pure methane hydrates, which display sI structure, to form. Some have a high content of heavier hydrocarbons and occur in the near surface sediments in association with deep migration, from mud volcanoes in the Caspian Sea (Chong et al., 2016; Laherrere, 2000; Popescu et al., 2006; Merey and Sinayuc, 2016).

Data of 641 locations is taken from World Ocean Database 2005 (WOD05) for evaluating possible distribution of gas hydrates in the Caspian Sea. In Figure 3.11, the resulted maps demonstrate the existence and distribution of gas hydrates in different depths of the seabed. In the figure, red triangles, green circles, and yellow points correspond to high geothermal gradient (17 °C/km), low geothermal gradient (11 °C/km), and the locations with no hydrate potential, respectively. For 20 mbsf, only some parts of the Middle and South Caspian Sea have potential for gas hydrates. At

the depth of 1,000 mbsf, potential for gas hydrates spreads to most of the stations. However, at 1,500 mbsf, potential for gas hydrates decrease to vanish in some stations due to increase in temperature (Gerivani and Gerivani, 2015).
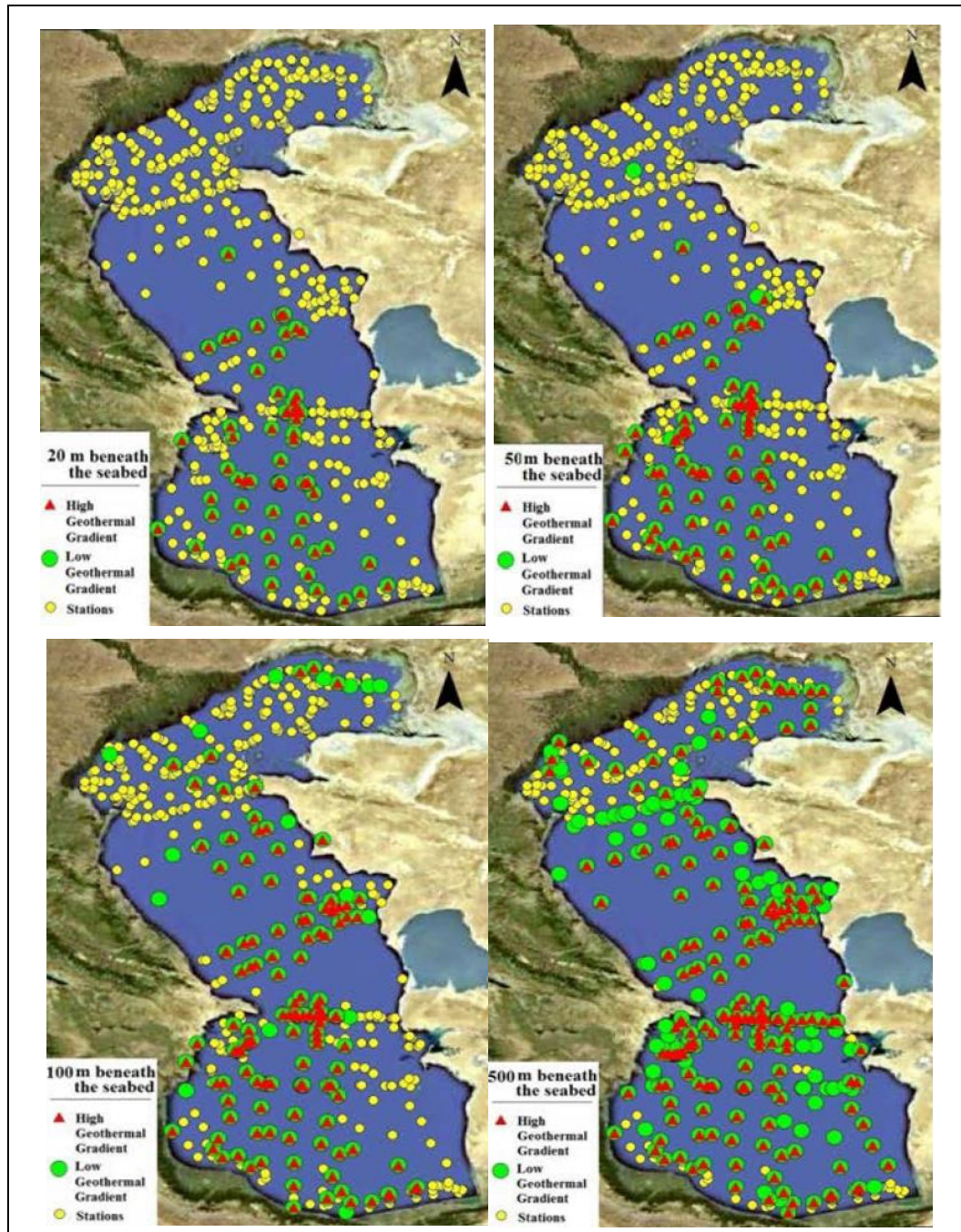
Figure 3.11: Methane hydrate potential and possible distribution in different depths under seabed (adapted from Gerivani and Gerivani, 2015)
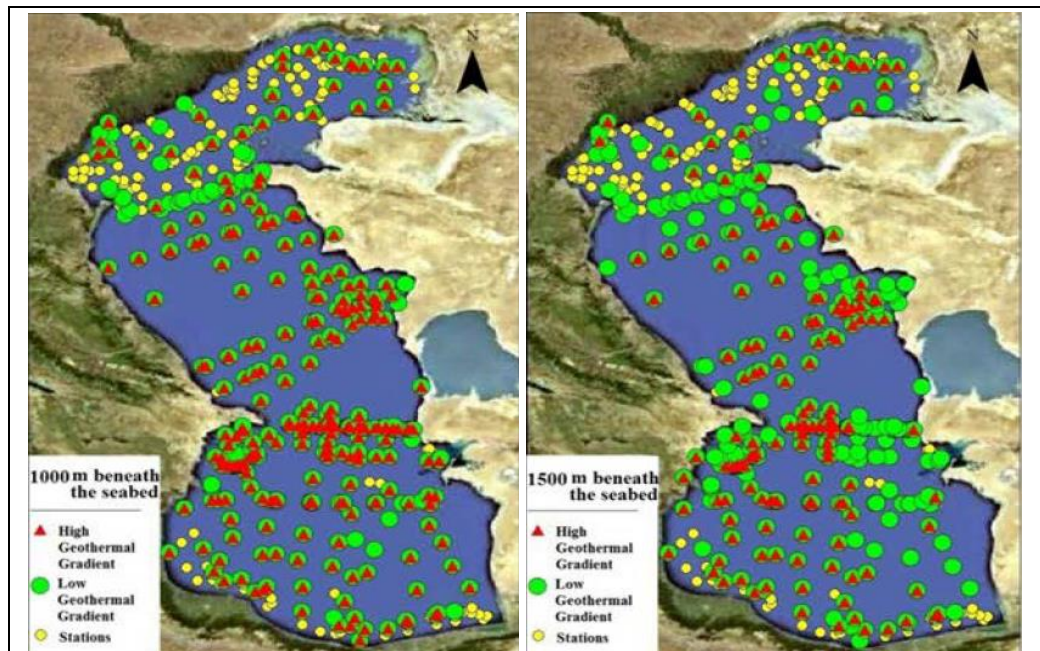
Figure 3.11: (continued) Methane hydrate potential and possible distribution in different depths under seabed (adapted from Gerivani and Gerivani, 2015)

3.3.1. Apsheron Gas Hydrates

Although almost an area of 200 km^2 of the Caspian Sea is stated being covered by gas hydrates, investigations are mostly done in deep water of the South Caspian Sea, especially in offshore areas of the Apsheron Peninsula. Initial researches are done in shallow water, up to 200 m, by Ginsburg and Soloviev (1994), However, in 1998, the first deep water, ~400 - 715 m, geophysical survey is done as part of Chevron's exploration program being conducted concertedly with SOCAR (Azerbaijan) and TotalElfFIna (France) across the Apsheron block. The survey consists of two seismic reflection profiles of approximately 70 km length of each related to gas hydrates (Diaconescu and Knapp, 2002).

The surveyed area harbors gas hydrates in a well-defined, depth restricted ~200 m thick layer. This layer is considerably beneath the seafloor, approximately 300-400 mbsf. Minimum water depth is stated at ~150 m and thickness of the hydrate stability field is ~1,500 m. The area meets the suitable conditions for hydrate occurrence. Hydrostatic pore pressure gradient is assumed 0.1 atm/m. Seafloor temperature was assumed 5.85-6.2℃. Geothermal gradient is reported between 11-17 °C/km. The area contains 80% shale, 10 % sand and 10% limestone (Bagirov et al., 1999). Water

sample from hydrates has salinity between 13.7-23.2 g/l (Diaconescu and Knapp, 2002, Diaconescu et al., 2001, Diaconescu and Knapp, 2000; Knapp et al., 2005).

In Figure 3.12 and Figure 3.13, location map of seismic profiles, Apsheron 1 and Apsheron 2, are shown in offshore Azerbaijan. The inset in the lower left corner displays geographic setting of the Caspian Sea within Central Eurasia and its relation to surrounding countries. The figure displays the relation of the Apsheron exploration block with the Shah Deniz and Oguz structures besides continental slope failure and slides and slumps. Bathymetry of the seafloor (in meters) obtained from the 3-D survey and transition from the shelf edge to deep water, is shown. Stratigraphic constraints are obtained by correlating well log data with the seismic data. Earthquake epicenters that are from the ISC Catalog and mud volcanoes are also shown in the figure. Core on which hydrocarbon gas geochemical analysis performed is obtained on the star labelled C in the Figure 3.13. The interpreted thickness and hydrate stability field are confirmed by the data from thermobaric modelling of gas composition determined from the core sample (Diaconescu et al., 2001; Knapp et al., 2005).
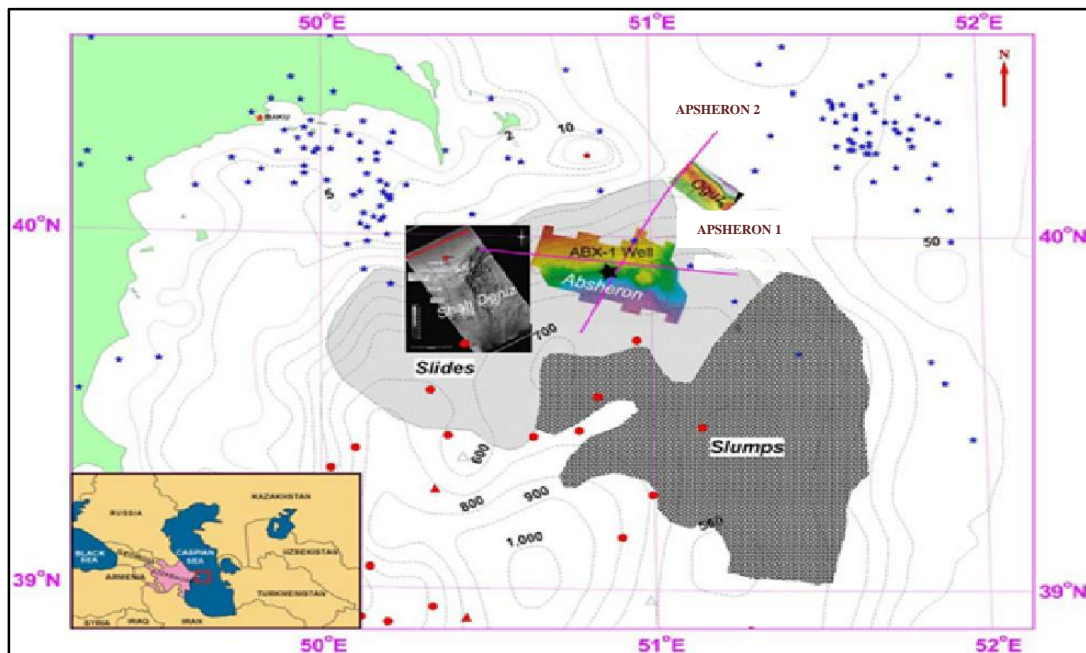
Figure 3.12: Location map of the Apsheron multichannel seismic reflection profiles. Geographic setting of the Caspian Sea within Central Eurasia (inset). Black stars: Stratigraphic constraints. Blue stars: Earthquake epicenters. Red dots and triangles: Mud volcanoes. Bathymetric contours are in meters. (adapted from Knapp et al., 2005)
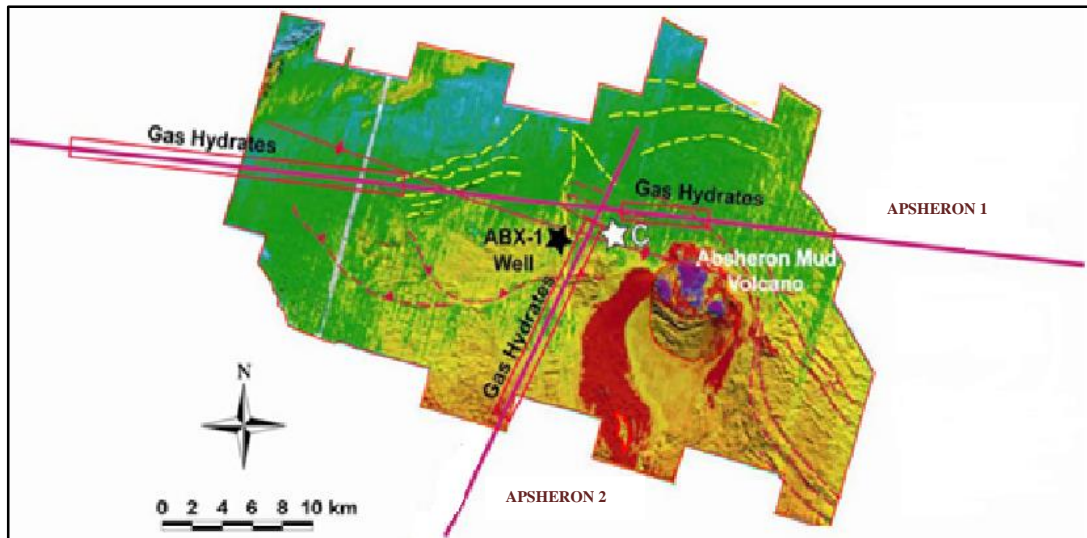
Figure 3.13: Regional 2-D seismic reflection profiles and a 3-D seismic grid from Chevron's exploration program in the deep water (400-715 m) of the South Caspian Sea, offshore Azerbaijan. SF: Shallow Faulting (adapted from Knapp et al., 2005)

High seismic velocity anomalies for Apsheron 1 and 2 are interpreted as gas hydrated zone from the result of the survey and is shown in Figure 3.14. For Apsheron 2, only a 25 km portion is displayed in (a). Its profile, which orients northeast to southwest, the high velocity anomaly starts at a depth around 800 mbsf and continues down to a depth of 1200 mbsf. For the Apsheron 1, a full length, 70 km, seismic data is displayed in (b). Its profile, which orients east to west, two high seismic anomalies are found starting at a depth of 900 to 1350 mbsf. Gas hydrate zone continues for 12 km in Apsheron 2 profile with 300 m of relief and 3 km in Apsheron 1 profile (Diaconescu et al., 2001, Diaconescu and Knapp, 2000).
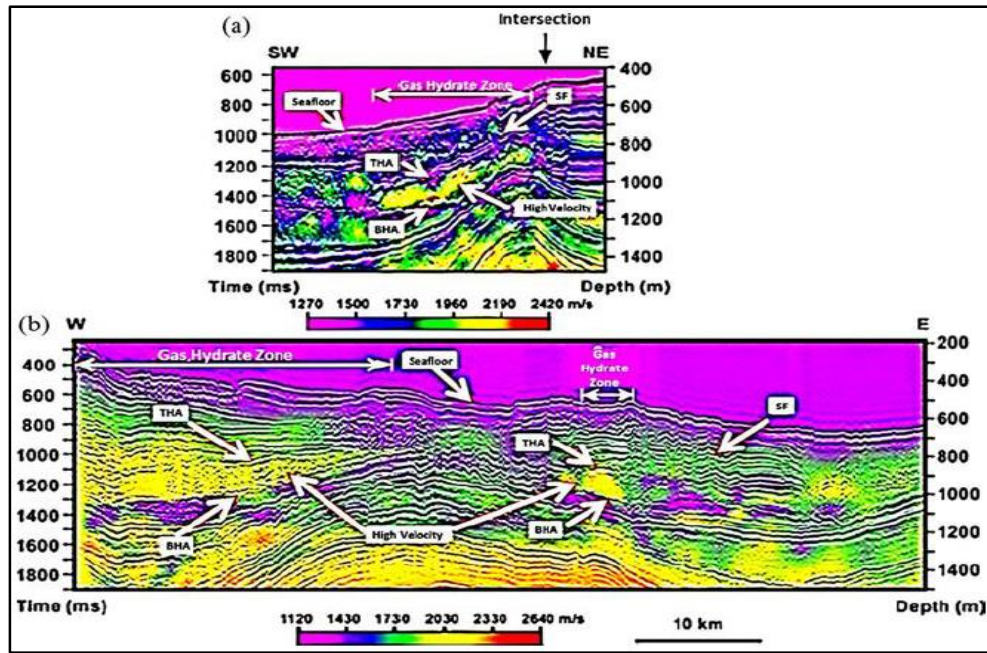
Figure 3.14: Seismic sections of (a) Apsheron 2 and (b) Apsheron 1 in Apsheron Block. TAH: Top Apsheron Hydrate; BAH: Base Apsheron Hydrate; SF: Shallow Faulting (adapted from Knapp et al., 2005)

Theoretical calculations of phase equilibrium can point the possible locations of hydrates. By using van der Waals and Platteeuw's statistical thermodynamics methods for three-phase equilibrium analysis predict hydrate stability pressure-temperature conditions for a certain gas composition and free water (Sloan, 1990). Three theoretical phase equilibrium diagrams and hydrocarbon compositions for each system of gas hydrates regarding the study are shown in Figure 3.15. The system consists of pure water and (a) pure methane, and (b) and (c) thermogenic gas from the area of interest. Gas composition for (b) and (c) are determined from bottom and top part of 55 m long core sample (location C in Figure 3.13). The phase diagrams assume the seafloor depth 475 m as seismic data reports this depth as the up-dip termination of the gas hydrate occurrence. The depth where gas hydrate stability curve and line of geothermal gradients meet shows the base of GHSZ. The point showing the minimum water depth where gas hydrates are stable for a specific gas composition is indicated by the intersection of the gas hydrate stability curves with the seafloor isotherm of 5.85°C (Kvenvolden, 1993). Light grey and dark grey shades show the GHSZ for low (11 °C/km) and high (17 °C/km) geothermal gradient cases. Arrows indicate the direction where the gas hydrate stability curves will be shifted towards if NaCl (left), CO_2 (right) and H_2S (right) are added to the system (Diaconescu et al., 2001, Diaconescu and Knapp, 2000).

54
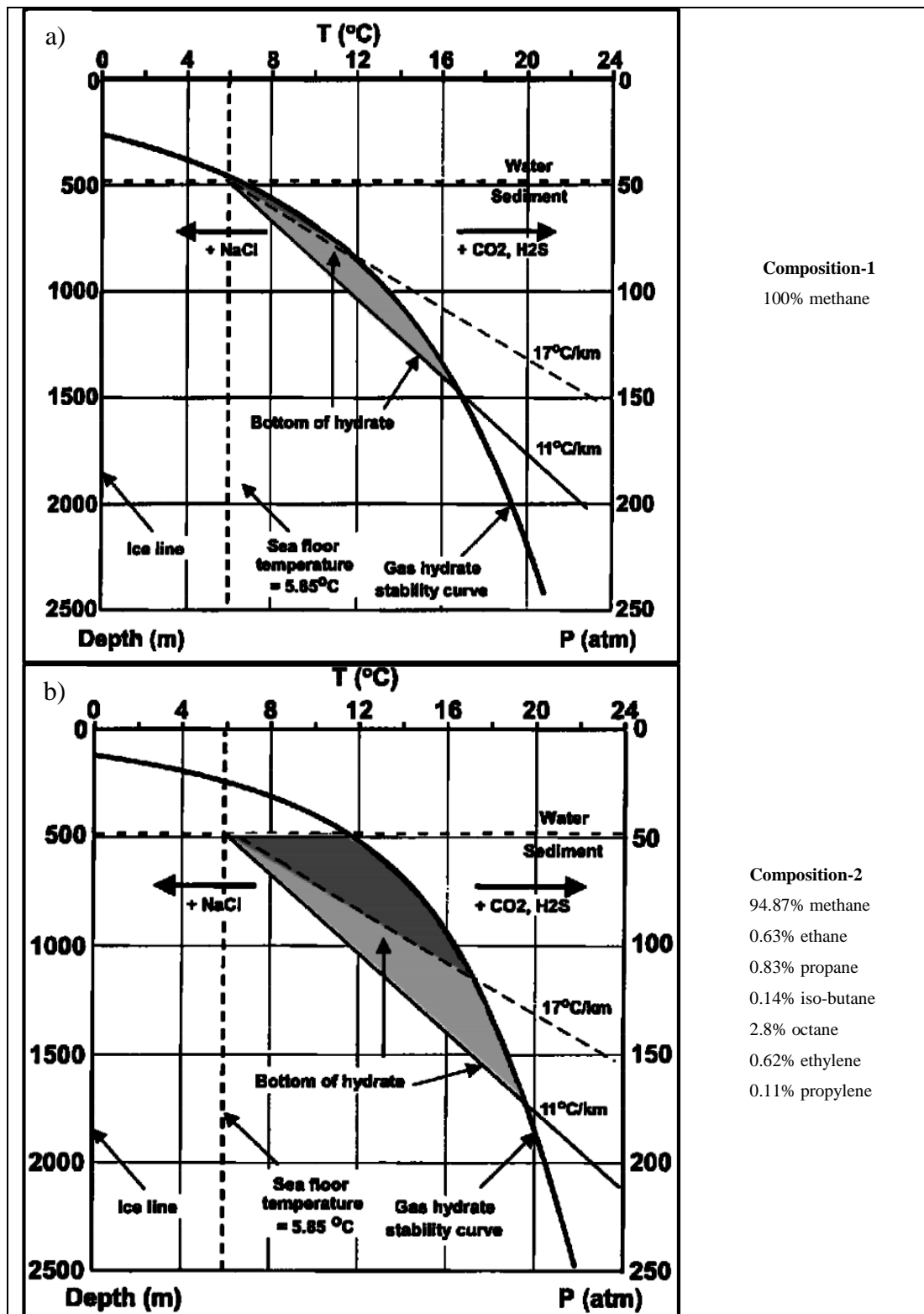
Figure 3.15: GHSZ shown by theoretical phase equilibrium diagrams of different gas compositions from core sample (adapted from Diaconescu and Knapp, 2000)
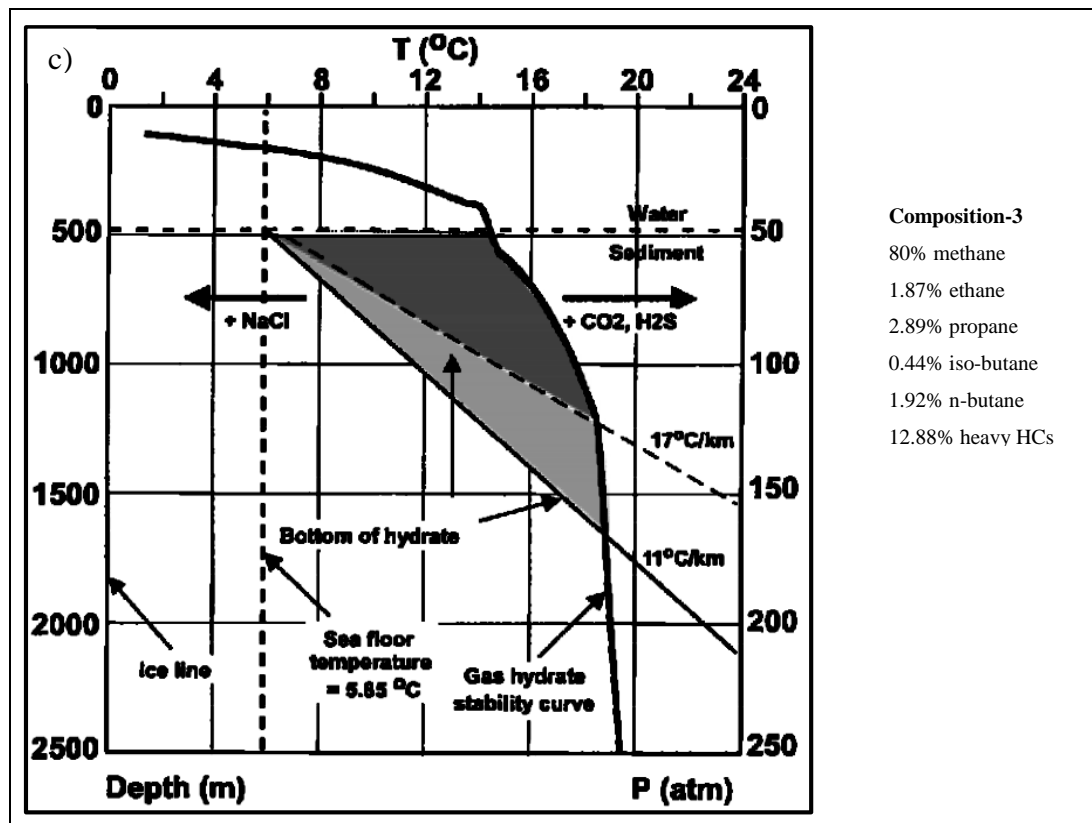
Figure 3.15: (continued) GHSZ shown by theoretical phase equilibrium diagrams of different gas compositions from core sample (adapted from Diaconescu and Knapp, 2000)

3.3.2. Geophysical Evidence for Natural Gas Hydrates in the South Caspian Sea

Researches on gas hydrates note that gas hydrates and surrounding system show notably different seismic characteristics. Acoustic impedance contrast between higher P (compressional)-wave velocity of the hydrate layer and underlying lower P-wave velocity of sediments creates negative polarity of the BSR in relation to seabed reflection. Decrease in acoustic impedances within the gas hydrate cemented sediments causes 'blanking' effect. If gas hydrate layers lie on top of the gas sands, it has a singular AVO (amplitude variation with offset) effect at the BSR. Crosscutting relationship between the BSR and the stratigraphic section on the continental slope is another distinctive property of gas hydrate bearing sediments, which is inferred from 2D seismic data.

Presence of gas hydrates and BSR is clearly visible from multichannel reflection profile of Apsheron area. Gas hydrate zone has high velocity ~2,100 m/s as compared to surrounding sediments, which has velocity of 1,550-1,600 m/s. This zone present

on the seismic data as a depth-limited, ~200 m thick, layer extending down the flanks of Apsheron anticline. Seismic blanking effect is exhibited on the sedimentary section. The top of the gas hydrate layer (TAH- Top Apsheron Hydrate) is recorded having a strong positive-polarity (Rc ≈ 0:123) reflector (Figure 3.12). The base of the hydrate layer (BAH- Base Apsheron Hydrate) is noted having a high-amplitude (Rc ≈ 0.11), negative polarity reflector (Figure 3.12). Moreover, both the top and base of the hydrate zone show a parallel trend to the seabed. They both cut the stratigraphic section adversely which proves that these reflectors are not stratigraphic interfaces but thermobaric. Reduction in amplitude with offset at the base of the gas hydrate zone display the free gas accumulation under it. These results and thermobaric modelling show that the minimum water depth for hydrate formation is ~150 m, and the maximum predicted thickness of the GHSZ is ~1,350 m (Diaconescu and Knapp, 2000).

3.3.3. Formation Characteristics

The South Caspian Basin is a clear example of the young sedimentary basins whose special features are having thick and rapidly accumulated sand and shale sequences. Argillaceous rocks make up 50 to 95% of the section and play a key role in determining the mineralogical, lithological, geochemical, and thermobaric characteristics of the basin. Besides, the South Caspian Basin differs from other basins by its diverse and considerably unique features, which are listed as follows:

(1) Sedimentation rate is notable with a rate up to 1.3 km/Myr since middle Pliocene, whereas other similar basins have 100-200 m/Myr rate of sedimentation (Yusifov and Rabinowitz, 2003, Buryakovsky et al., 2001),

(2) Sedimentary column is very thick, reaching 25 km in certain locations. In the last 6 million years, sediments of Quaternary-Pliocene age, sand-silt-shale, have deposited up to 10 km within this sedimentary column.

(3) The average geothermal gradient is approximately 16 °C/km. The mostly addressed values are between 11 and 17 °C/km. Value of average geothermal gradient on earth is between 25 and 35 °C/km.

(4) Abnormally high pore pressure is observed due to high sedimentation rate.

(5) The hydro-chemical profile of the region is noted to have inverted character. Likely, water is freshening with increasing depth. The chemical composition of water alters with depth from calcium chloride ($CaCl_2$) and magnesium chloride ($MgCl_2$) to sodium bicarbonate ($NaHCO_3$) type.

(6) Maturation of mud volcanism is observed extensively (Buryakovsky et al., 2001; Diaconescu et al., 2001; Diaconescu and Knapp, 2002; Yusifov and Rabinowitz, 2003).

Reason of low geothermal gradient in the South Caspian Basin has explained by Devlin et al. (1999) because of rapid deposition in the last 6 million years, almost 10 km deposition. On the other hand, in a book of Buryakovsky et al. (2001), it has stated that abnormally low temperatures may be related to lack of distinctive clay-mineral transformation. Khitarov and Pugin (1966) and Magara (1982) have taken attention to effect of temperature on montmorillonite degradation and effect of illite degradation on geothermal gradient. Illite-to-montmorillonite transformation releases heat. The process of montmorillonite catagenetic transformation into illite may be driven by increase in temperature. Therefore, it may be said that high geothermal gradient is related to small montmorillonite content. Besides, montmorillonite transformation is decelerated by decrease in temperature. In this sense, low geothermal gradient should be identified by a high montmorillonite content.

For offshore fields of the South Caspian Sea, porosity distribution (Figure 3.16) ranges from 10-30% and mean permeability (Figure 3.17) is approximately ~300 mD (Bagirov et al., 1999; Buryakovsky et al., 2001).
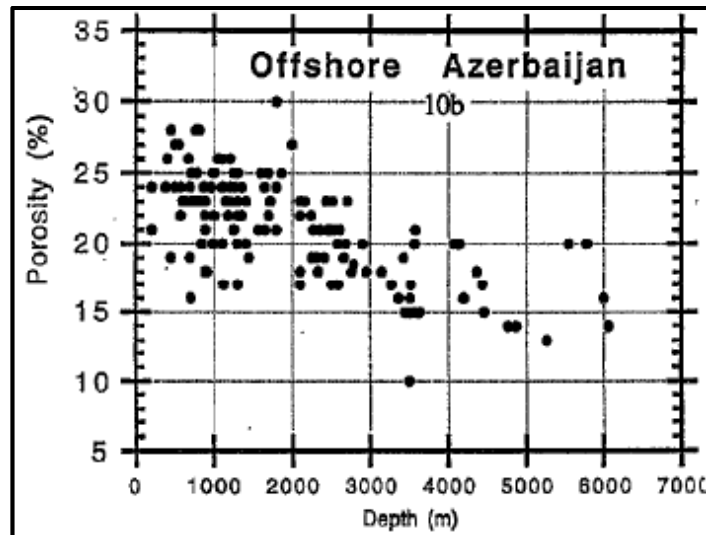
Figure 3.16: Porosity distribution according to depth in the South Caspian Sea (adapted from Bagirov et al., 1999)
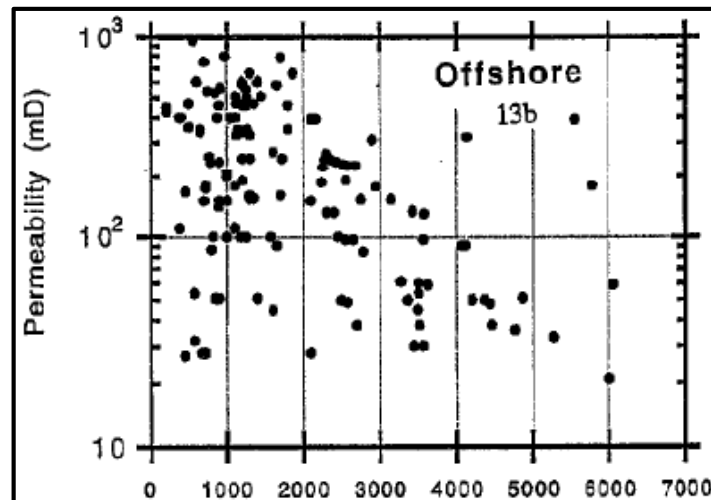
Figure 3.17: Permeability distribution according to depth in the South Caspian Sea (adapted from Bagirov et al., 1999)

3.4. Mud Volcanoes

Mud volcanoes are natural conduits that bring substances and fluid deep from the formation to the surface by overpressure (Kioka and Ashi, 2015). They exist worldwide on shelves, continental and insular slopes and in the abyssal parts of inland seas. The formation of mud volcanoes has been considered as a result of the destruction of deep gas accumulations, the piercing of the surface by shale diapirs, the rise of fluidized mud along faults and the decomposition of gas hydrates (Milkov, 2000).

Submarine mud volcanoes are encountered more broadly than onshore mud volcanoes. When both known and inferred deep-water mud volcanoes are included, total number of mud volcanoes are estimated between 10^3-105 (Milkov, 2000).

Although mud volcanoes have been known for more than 200 years, only since the last decade an extensive research has been made on submarine mud volcanoes with improvement on technology. Wide use of side scan sonar and the increased accuracy of positioning of bottom samplers are key factors of these researches (Milkov, 2000). Global distribution of mud volcanoes are shown in Figure 3.18.
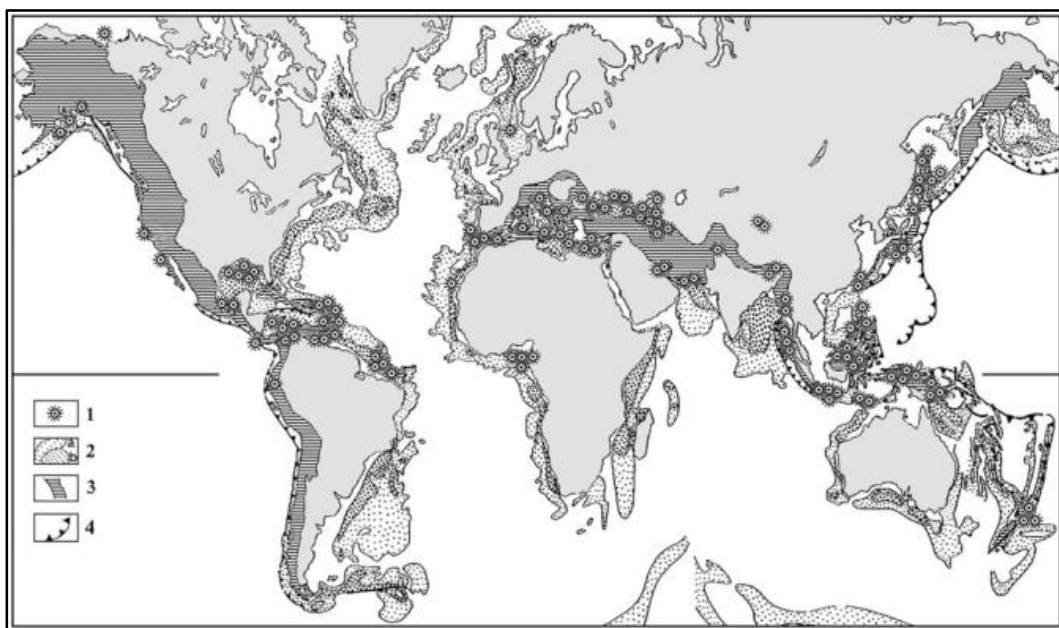
Figure 3.18: Global distribution of mud volcanoes. 1) Single mud volcanoes, separated mud-volcano areas and mud volcano belts; 2) Sediment thickness in the areas out of the continental shelves: a from 1 to 4 km, b more than 4 km. 3) Active compressional areas. 4) Subduction zones (adapted from Dimitrov, 2003)

Research on submarine mud volcanoes is important to petroleum industry in many aspects. Their occurrence is critical for greenhouse effect and climatic change as they are a source of methane flux from lithosphere to hydrosphere and there to atmosphere. Mud volcanic sediments may include useful data about the sedimentary section around it. They may supply evidence of high petroleum potential in the deep subsurface. Gas hydrates are associated with deep-water mud volcanoes and are a potential energy resource. Moreover, drilling operations, rig installations and pipeline routings may be affected by submarine mud volcanic activity (Milkov, 2000).

Although there are different reasons for generation of mud volcanoes in various areas, some causative factors can be used to predict existence of mud volcanoes in targeted areas. These factors may be listed as follow:

Geologic reasons:

- thick sediment layer, from 8 km to 22 km, mostly composed of terrigenous sediments;
- the existence of plastic shale layers in the subsurface;
- a rock density inversion;
- the generation of gas accumulations in deep subsurface;
- remarkably high formation pressure.

Tectonic reasons:

- the rapid deposition of the sediment layer because of the high sedimentation rate or by surpassing thrust sheets;
- the existence of diapiric or anticlinal folds;
- the existence of faults;
- lateral tectonic compression at active continental margins
- seismic activity;
- isostatic processes.

Geochemical reasons:

- formation of hydrocarbons in the deep subsurface;
- the dehydration of clay minerals.

Hydrogeological reasons, i.e. fluid flow through fracture sector (Milkov, 2000).

It is clear that most of above listed causes are closely associated with each other or are necessary for the existence of each other. However, the key factors for generation of submarine mud volcanoes are high sedimentation rate and lateral tectonic compression at active continental margins (Milkov, 2000).

Two basic mechanisms for formation of submarine mud volcanoes are shown in Figure 3.19. These mechanisms are formation of mud volcanoes on top of a seafloor-piercing shale diapir and formation due to the rise of fluidized sediments through faults. (A)-seafloor-piercing shale diapir without a mud volcano, (B)-a mud volcano formed on top of a seafloor-piercing shale diapir, (C)-a seafloor seepage, (D1, D2)-mud volcanoes formed due to the rise of fluidized sediments along faults are symbolized. The migration paths of fluids are shown by arrows (Milkov, 2000).
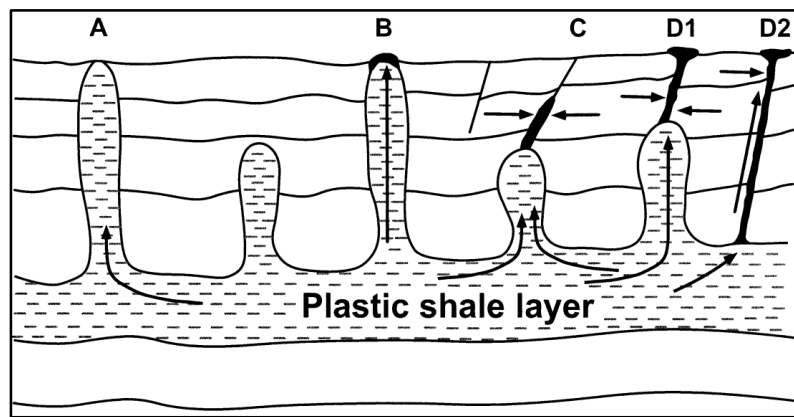
Figure 3.19: Two basic mechanisms for formation of submarine mud volcanoes (adapted from Milkov, 2000)

3.4.1. Gas Hydrates Associated with Mud Volcanoes

Gas hydrates associated with mud volcanoes are first marked by Ginsburg et al. (1984). Since then, these are observed in the Caspian, Black, Mediterranean, Norwegian seas, offshore Barbados, offshore Nigeria and in the Gulf of Mexico (Milkov, 2000).

Some common features of gas hydrates associated with mud volcanoes are having white or grayish-white in color, a plate-like habit and randomly oriented in sediments. Content of gas hydrate in sediments differs from 1–2% to 35% by volume and this may vary through area and depth of a mud volcano (Milkov, 2000). By volumetric method the estimated amount of methane in all gas hydrates associated with submarine mud volcanoes at $10^{10} – 10^{12}$ m^3 at standard pressure and temperature (Milkov, 2000).

In Figure 3.20, the proposed model of the formation of gas hydrates within a mud volcano is presented. According to this model, gas hydrates can form within the mud volcano's crater and hummocky periphery and outside of mud volcano in host marine sediments. In (a), hydrothermal process around the central part of the mud volcano and in (b) metasomatic process at the peripherical part of the mud volcano is demonstrated. To make clear, metasomatism means the alteration of a rock by another with different mineralogy and chemical composition by hydrothermal and other fluids (Milkov, 2000).
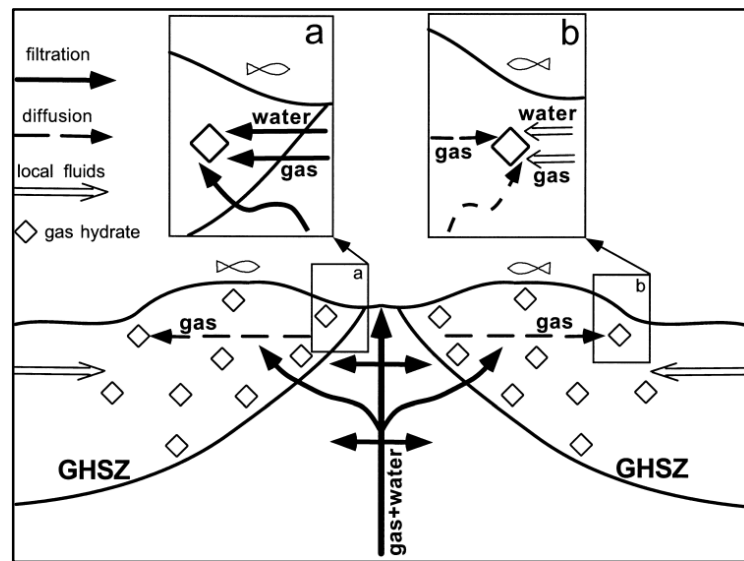
Figure 3.20: The proposed model of the formation of gas hydrates within a mud volcano (adapted from Milkov, 2000)

For formation of gas hydrates, water from both mud volcanic fluid and surrounding sediments are involded. Fluid at the central part of the mud volcano, where mud and fluid flow out, has higher temperature. Since this fluid is warmer than the surrounding sediments likely 15-20 °C, gas hydrates do not form in this part. However, this fluid may contain solution gas and even free gas. When this fluid becomes cold and the solubility of gas decreases, gas hydrates crystallize. However, for formation of gas hydrates with metasomatic process, gas from the central part of the mud volcano is transported in solution by diffusion. In this case, water is the local water coming from the host sediments. Also, some local biochemical gas may involve in formation of gas hydrates. Since the local water is partly changed to gas hydrates, this process is analogous to conventional metasomatic process of mineral formation (Milkov, 2000).

3.4.2. Mud Volcanoes in the South Caspian Sea

Among the abyssal parts of inland seas, the Caspian Sea is one of the main locations for formation of mud volcanoes. According to studies of Azeri and Russian geologists, there are more than 300 mud volcanoes both onshore and offhore Azerbaijan. Mud volcanoes are distributed both in the north and south part of the Caspian Sea but mostly concentrated in the southern part. The South Caspian Sea holds more than 30% of all known mud volcanoes in the world. In the northern part, mud volcanoes are with low relief likely several tens of meters. Whereas, in the southwest part of the sea, mud volcanoes with large vertical relief greater than 200 m are observed. These are relatively large surface features, with an average height of ~400 meters and several kilometers in width (Yusifov and Rabinowitz, 2003, Yusifov and Rabinowitz, 2004).

Previous studies are shown that formation of mud volcanoes within the South Caspian Basin is due to tectonic forces, thermobaric conditions and overpressured sediments (Yusifov and Rabinowitz, 2003). Sedimentary cover of the region is as thick as 25-30 km, which is mostly terrigenous, deposited during Tertiary and recent times under high accumulation rates. Many of the sedimentary sequences are deformed by shale diapirs and faults (Milkov, 2000). Mud volcanoes penetrate most of these structures (Yusifov and Rabinowitz, 2003).

Gas hydrate accumulations associated with mud volcanoes are inferred in more than sixty mud volcanoes of the South Caspian Sea (Ginsburg et al., 1992). In Figure 3.21, distribution of gas hydrate bearing submarine mud volcanoes in the South Caspian is shown. Locations of gas hydrate bearing mud volcanoes (B: Buzdag, E: Elm), clay diapirs for bottom sampling (S: Severnyy, U: unnamed mud volcano on the Abikha bank), other submarine mud volcanoes and boundaries of gas hydrate bearing region are specified on the figure.
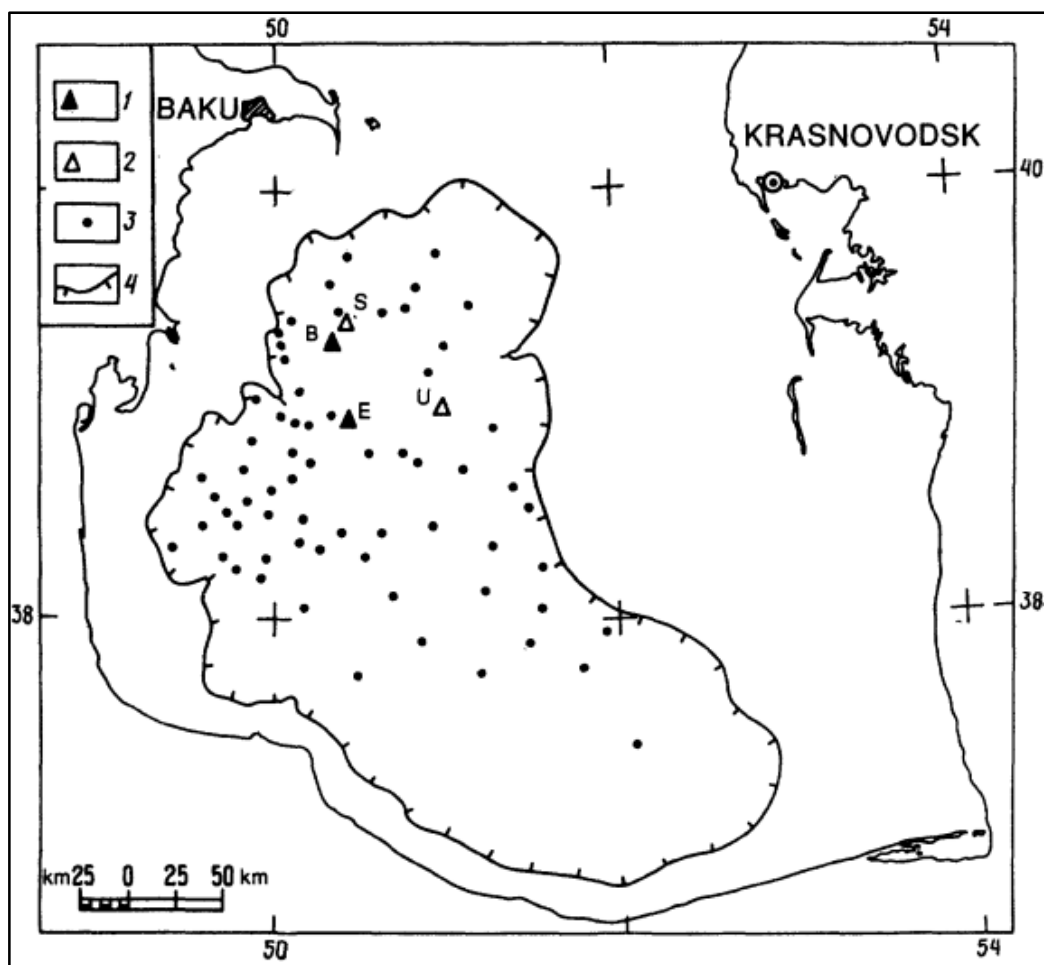
Figure 3.21: Gas hydrates bearing submarine mud volcanoes in the South Caspian. 1) Gas hydrate bearing mud volcanoes (B: Buzdag, E: Elm); 2) clay diapirs for bottom sampling (S: Severnyy, U: unnamed mud volcano on the Abikha bank); 3) submarine mud volcanoes; 4) boundaries of gas hydrate bearing region (adapted from Ginsburg et al., 1992)

Seismic profiling, geothermal measurements, use of bottom sampling apparatus, and a combination of on-board and laboratory gas-hydrate geochemical investigations are done in main mud volcanoes in order to understand and characterize their distribution, host sediments and gas hydrates in them. These investigations are done on the axis of the Vezirov and Azizbekov highs and Abikha bank (Ginsburg et al., 1992). Seismic time sections of the targetted areas are visible on Figure 3.22, Figure 3.23, and Figure 3.24. Samples from mud volcanoes Buzdag on the Vezirov high, Elm on the Azizbekov high and an unnamed one on the Abikha bank are obtained from different stations that is also shown on seismic maps. Results of geothermal measurements and percentages of hydrocarbons and CO_2 in typical gas samples are listed in Chapter 6 (Sectiona 6.2) and used for estimation of methane encapsulated in gas hydrates.

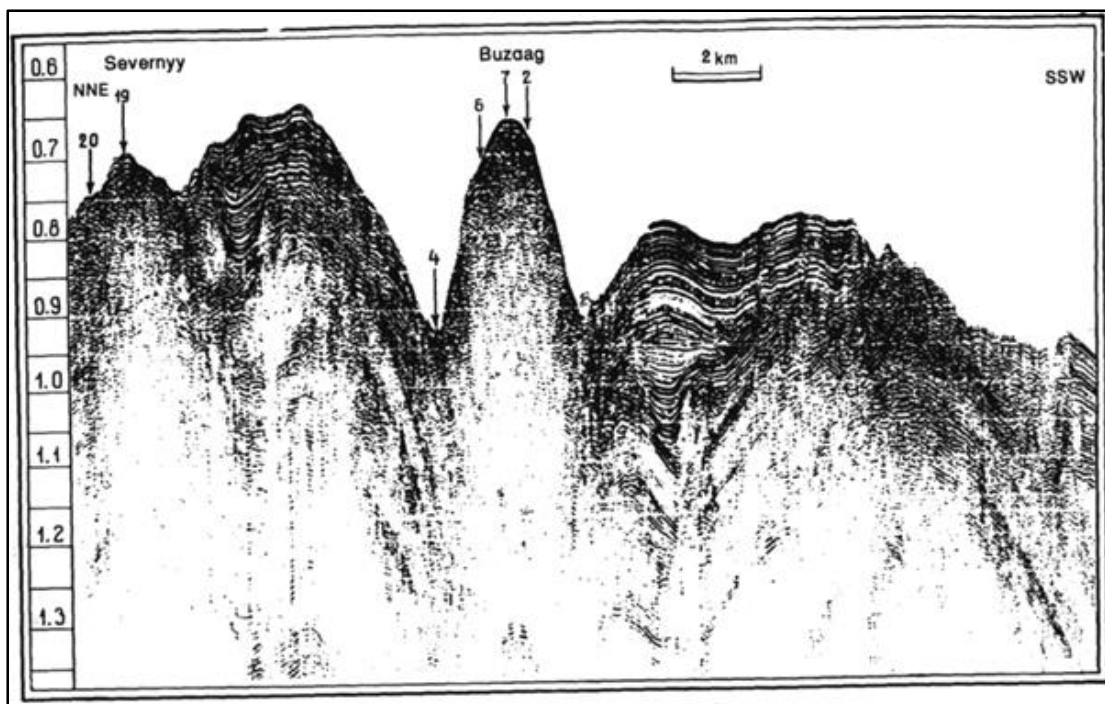Figure 3.22: Two-way section through the Vezirov high, with bottom sampling
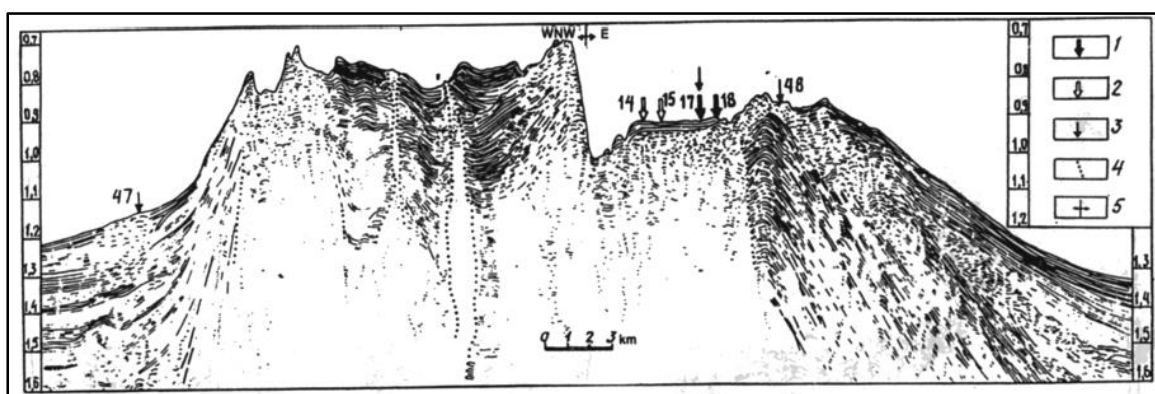stations (adapted from Ginsburg et al., 1992)

Figure 3.23: Interpretted time section through the Azizbekov high. 1) Bottom sampling
stations with gas hydrates in core; 2) Bottom sampling stations without
gas hydrates in core; 3) Geothermal stations; 4) Inferred boundaries of
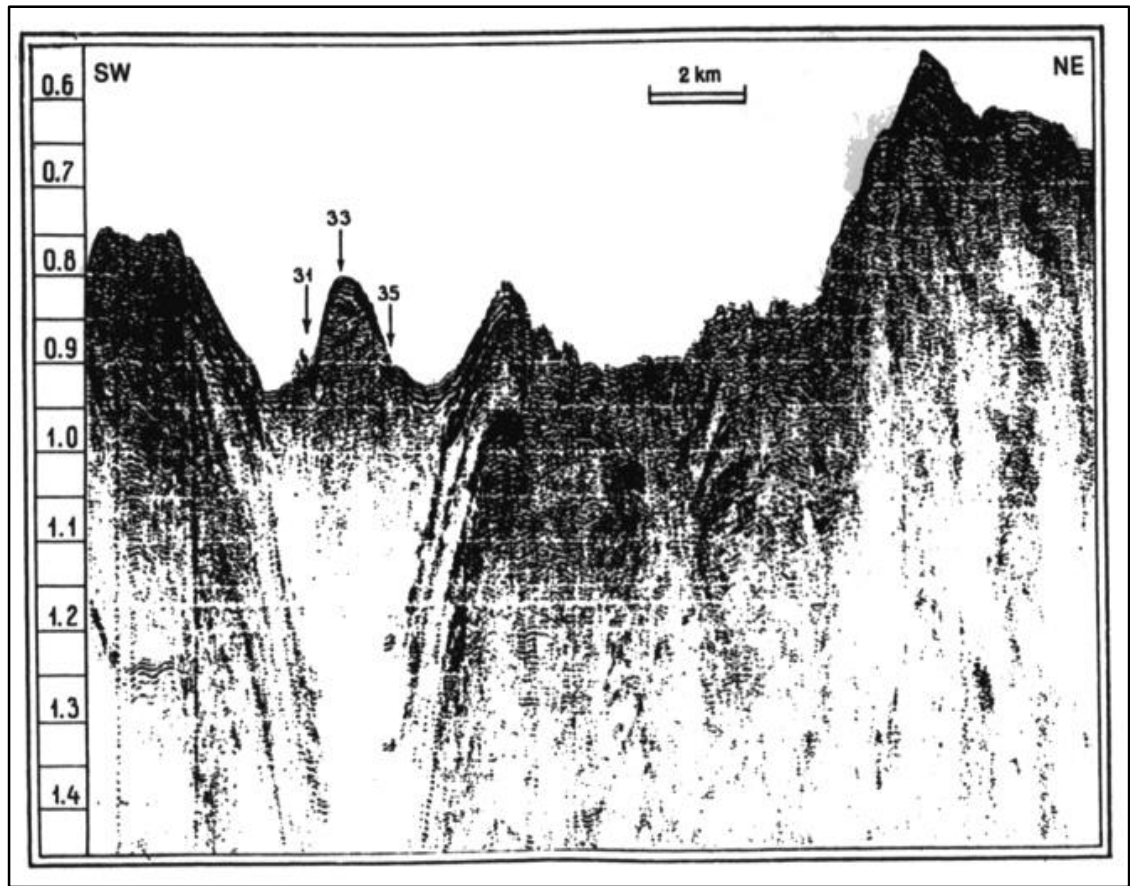diapirs; 5) Band in section (adapted from Ginsburg et al., 1992)

Figure 3.24: Time section through the Abikha bank (adapted from Ginsburg et al., 1992)

The hydrate-bearing Buzdag mud volcano is located on the Vezirov high, in a saddle of a ridge. The coordinates of the center are 39° 18' 37 N and 50° 24' 20 E.. It is 180 m high with base diameter of 2.5 km. Diameter of its slightly convex summit is 0.5 km with an area of 0.2 km^2 and 475 mbsf. Gas hydrates are found in 19 cores out of 20 and average gas hydrate content is obtained as from 2-3 to 35 vol.%. Hydrates occur on Buzdag in the form of ice-like, semi-transparent, matted formations of various shapes and sizes. They are 12x5 cm in area and with a variable thickness up to several millimeters (Ginsburg and Soloviev, 1994; Ginsburg et al., 1992). According to a study of Milkov (2000), for Buzdag, estimated amount of methane is calculated by volumetric method and is obtained as 3×10^8 m^3.

The gas hydrate bearing Elm mud volcano is located on the Azizbekov high. The geographic coordinates of the center are 38° 57' 85 N and 50° 23' 95 E. Its crater is extending for 4 km at water depth of 660 m. Gas hydrates are found in 5 cores out of 7. The appearance of the hydrate-bearing sediments is the same as at Buzdag. The

maximum size of plates has an area of 5 x 2 cm with a thickness of 2-3 mm. Hydrate content is not such high as at Buzdag; the maximum hydrate content is 15-20% (Ginsburg and Soloviev, 1994; Ginsburg et al., 1992).

The unnamed mud volcano on the Abikha bank, located on a saddle, is higher than 75 m with base diameter of 3 km at 530 m of water depth. The geographic coordinates of the center are 38° 59' 96 N, 50° 50' 76 E.This mud volcano is also inferred as hydrate bearing. Because, the content of ethane in the gas hydrates is observed and found to be higher than in associated gases of oil deposits and gases of gas-condensate deposits of the region. This high amount of ethane is probably a consequence of fractionation of the original gas during hydrate formation which suggests that the unnamed mud volcano on the Abikha bank is also hydrate-bearing (Ginsburg et al., 1992). Hydrate content in the sediments reaches 15-20% (Bagirov and Lerche, 1997).

There is no sufficient data to determine the exact depth of occurrence of gas hydrates below the seafloor. Temperature of bottom water on the crater field of the Buzdag and Elm mud volcanoes are measured as ~6°C. According to geothermal data and equilibrium parameters for formation of gas hydrates, hydrate bearing zone may extends a few tens of meter below the seafloor at the Buzdag mud volcano because of high geothermal gradient. Since water depth is 200 m deeper and temperature gradients near the bottom is 3-4 times less than Buzdag, hydrate zone is thicker at the Elm mud volcano.

CHAPTER 4

STATEMENT OF THE PROBLEM

Gas hydrates might be an important hydrocarbon sources for near future. For this reason, a careful consideration and exploration is required even though presently, they cannot be produced with conventional methods and economically are not feasible. Even though, geological uncertainties and technical challenges make it difficult for exact assesment of resources, additional researches are essential for both current petroleum industry and gas hydrates as future energy supply.

The purpose of this thesis is estimating methane amount in gas hydrates of the South Caspian Sea by volumetric method and emphasizing that the region is a gas hydrate province. Monte Carlo method is studied with this purpose by using @RISK. The study area is divided into three parts according to concentration of gas hydrates in the sediments. Parameters of calculations are adapted from literature since there is not enough data for the study area. Drawing attention of researchers is another aim which is essential for more investment on exploration of the region.

CHAPTER 5

METHODOLOGY

5.1. Monte Carlo Method

First, in order to avoid confusion, definitions of the terms like simulation, Monte Carlo method and Monte Carlo simulation need to be specified. A simulation is a figurative representation of reality. Monte Carlo method is a mathematical method to approximate mathematical and statistical problems. However, Monte Carlo simulation is combination of the mathematical (Monte Carlo) method and computational programming (Monte Carlo Method, 2017; Finney et al., 2003).

Monte Carlo simulation is improved year after year and used for problems where theory is not enough to have sufficiently precise solutions in almost all fields such as physics, engineering, computational biology, applied statistics, health, safety and environment (HSE), finance, business, law, etc. (Fathi, 2016; Monte Carlo Method, 2017).

Monte Carlo methods are stochastic techniques. In the widest sense of the term, this method employs random numbers for making consecutive computations to approximate the desired outcome. The simulation requires a mathematical formula to begin with. Input variables in the formula and a domain for each variable are defined. Each variable takes a random value within the domain and the formula is computed deterministically. The outputs are noted for each computation and aggregated (Ayres et al., 2017; Woller, 1996).

5.2. Probability Density Functions

Probability density functions (PDF) are used to describe continuous probability distributions. Continuous random variables are defined over a continuous range of values and are calculated PDF over that domain. Having a domain between a and b, a PDF has the following properties:

- The continuous random variable is defined over a continuous domain.
- The area bounded by the curve of the density function, computed over the defined domain of the variable, and the x-axis is equal to one.
- The probability of a random variable takes a value between a and b. It is equal to the area under the density function bounded by a and b. (Probability Density Function, 2017).

Normal, lognormal, triangular, and beta distribution are some of the probability distribution methods. In this study, triangular and uniform distributions are used in calculations.

Normal distributions are commonly used in natural sciences to have an understanding of unknown distribution of real valued random variables. The PDF for normal distributions are defined by two parameters, μ, location parameter, and σ, scale parameter. The location parameter, μ, is mean where mean, median and mode are equal in normal distributions. The scale parameter, σ, is standard deviation. Normal distributions are symmetric with respect to their mean. To represent variables which are sums or averages of other variables, normal distributions are used. In petroleum industry, normal distributions are used for calculations of field production, reserves of various fields, total cost, and average porosity. Moreover, errors in temperature and pressure measurements are also characterized by normal distributions (Statistical Concepts in Risk Analysis, 2017; Normal Distribution, 2017 (a), (b), (c)).

A lognormal distribution is a continuous probability distribution of a random variable whose logarithm is normally distributed. Lognormal distribution is defined by three parameters σ, shape parameter (or standard deviation), m, scale parameter (or median) and μ, location parameter. To be specific, μ and lognormal distributions are used to

represent variables, which are products of other variables. In petroleum industry, lognormal distributions are used to calculate areas, volumes, production rates, time to reach pseudo steady state. Permeability, annual income within corporation, and ratios of prices are also variables being characterized by lognormal distributions (Log-Normal Distribution, 2017 (a), (b); Statistical Concepts in Risk Analysis, 2017).

A triangular distribution is another type of continuous probability distribution shaped like a triangle. It is based on three-point estimation technique. A minimum value a, a maximum value b, and a peak value c is defined for calculations. It has definite upper and lower limits so that extreme values may be avoided. This distribution is mostly attempted for using when the relationship between variables is known but only limited sample data is available (Triangular Distribution, 2017 (a), (b)).

The uniform distribution defines that every variable has the same probable outcome over a given range for a distribution. For example, when displayed as a bar graph, possibility of happening of different events has almost the same height of each bar. In this way, it typically looks like a rectangle; therefore, is often described as the rectangular distribution. Generating random numbers is a remarkable usage of the uniform distribution. Other random number generators produce random numbers on the (0,1) interval by uniform distribution. For other distributions, some transformation is required to generate uniform random numbers (Uniform Distribution, 2018 (a), (b)).

5.3. Calculation Parameters

The following equation is used to estimate methane amount present in gas hydrate reserves in the South Caspian Sea.

$$OGIP = A \; x \; h \; x \; \varphi \; x \; S_h \; x \; VR \; x \; CO \tag{6.1}$$

Since the field needs further explorations, some data are unavailable in the literature. Estimations from other fields and some assumptions are used for parameters for which are not presently known.

Estimations are run by @RISK program. @RISK is an add-in for Microsoft Excel, which performs risk analysis by using Monte Carlo simulation. @RISK lets users see and analyze all possible outcomes. It presents a range of possible values in a Microsoft Excel spreadsheet that allows making the best choice under uncertainty (@RISK, 2018). So, after determining value range for parameters, probability density functions are used for 10,000 iterations by @Risk. The resulted outcomes give the probability of the minimum, mean, and maximum estimations.

Area

The targeted area of this thesis is determined within the coordinates 39°N, 50°E - 40°N, 50°E and 39°N, 52°E - 40°N, 52°E, excluding the parts shallower than 100 m in the South Caspian Sea (see Figure 5.1). Elm and unnamed mud volcano on the Abikha bank is also added to calculations due to their high probable gas hydrate potential. Planimeter measurements are applied on the available maps to estimate different hydrate bearing areas. The study area makes totally 17576,93 km^2.

While dividing the area into different sections, idea from Fujii et al. (2008) is used to a great effect as a guide. It is divided by three groups according to hydrate saturation. In Figure 5.1, map of the study area is shown. Gas hydrate concentrated zone is bordered by black color. Bearing zones are bordered by blue line. Mud volcanoes are shown by red circles.

The Apsheron (framed with black in Figure 5.1) area includes BSRs, which is determined from seismic investigations and is under Apsheron 1 and 2 lines. Gas hydrates are visible from seismic data and intensively distributed in this zone. Thus, this part is called gas hydrate concentrated zones, whose area is 730,876 km^2. For the second part (framed with blue in Figure 5.1), suitable conditions for generation of gas hydrates are stated by different researchers (Gerivani and Gerivani, 2015; Diaconescu et al., 2001; Knapp et al., 2005; Ginsburg and Soloviev, 1994; Diaconescu and Knapp, 2000 and 2002). It is between 100 m and 1,000 m water depths where gas hydrates are considered partially distributed between layers is called gas hydrate bearing zones. This section covers almost an area of˜17000 km^2. The third part is in and around the sides of crater fields of mud volcanoes where intensively high gas seepage is marked. There are 17 mud volcanoes in the area of interest, Buzdag, Apsheron, Elm and unnamed 14 mud volcanoes.
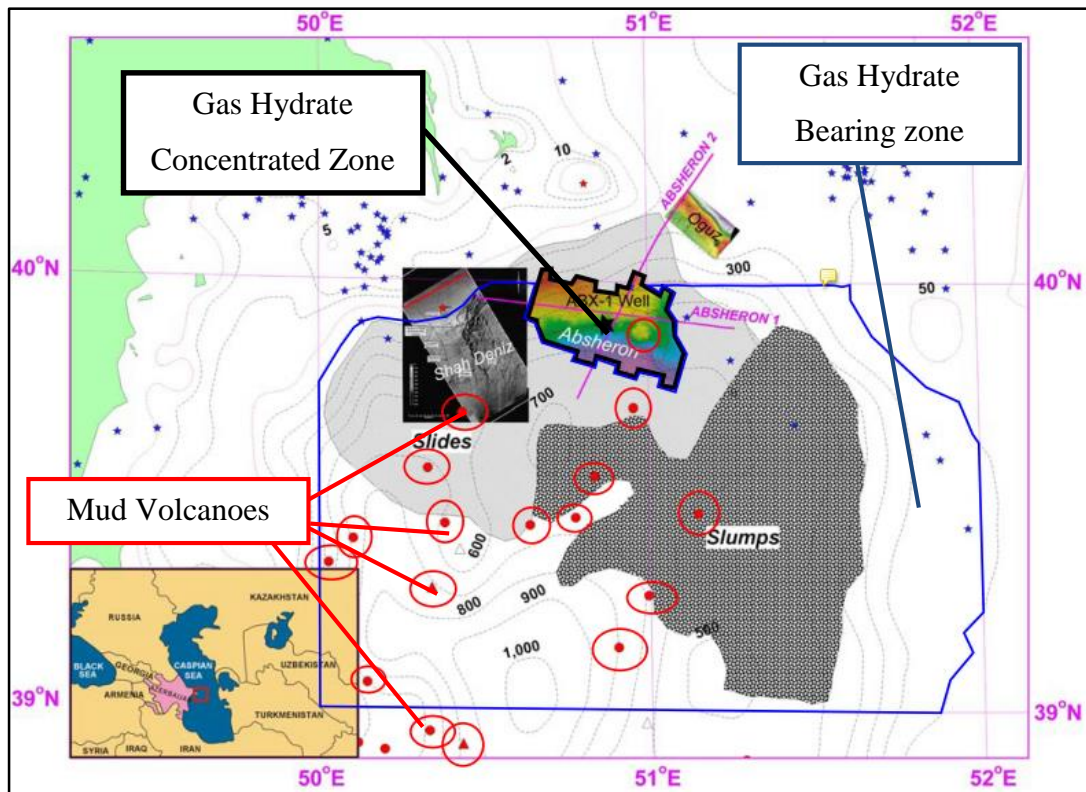

Figure 5.1: Map showing gas hydrate concentrated and bearing zones and mud volcanoes. Black line: gas hydrate concentrated zone; blue line: gas hydrate bearing zone; red circles: mud volcanoes.

To detect the working area in and around of craters of mud volcanoes, radii of Buzdag, Elm, and unnamed mud volcano on the Abikha bank are examined from literature

(Ginsburg et al., 1992; Ginsburg and Soloviev, 1994). However, there is no detailed information for Apsheron mud volcano and the other 13. Radius of them is estimated from known radii of bigger mud volcanoes. Radius of Apsheron mud volcano is taken 0.45 km and other 13 are assumed even smaller and radii of them taken as 0.4 km. In Table 5.1, estimated area including craters of mud volcanoes is listed with extended radius and resulted total area.

Table 5.1: Estimated area for craters of mud volcanoes

Mud Volcanoes	Diameter (km)	Diameter (m)	Radius (m)	Extended Radius (m)	Area (m^2)
				= 2 x Radius	
Elm	4	4000	2000	4000	5.03×10^{07}
Unnamed on Abikha	0.6	600	300	600	1.13×10^{06}
Buzdag	0.5	500	250	500	7.85×10^{05}
Apsheron	0.45	450	225	450	6.36×10^{05}
Unnamed 1	0.4	400	200	400	5.03×10^{05}
Unnamed 2	0.4	400	200	400	5.03×10^{05}
Unnamed 3	0.4	400	200	400	5.03×10^{05}
Unnamed 4	0.4	400	200	400	5.03×10^{05}
Unnamed 5	0.4	400	200	400	5.03×10^{05}
Unnamed 6	0.4	400	200	400	5.03×10^{05}
Unnamed 7	0.4	400	200	400	5.03×10^{05}
Unnamed 8	0.4	400	200	400	5.03×10^{05}
Unnamed 9	0.4	400	200	400	5.03×10^{05}
Unnamed 10	0.4	400	200	400	5.03×10^{05}
Unnamed 11	0.4	400	200	400	5.03×10^{05}
Unnamed 12	0.4	400	200	400	5.03×10^{05}
Unnamed 13	0.4	400	200	400	5.03×10^{05}
Total Area (m^2)					$\mathbf{5.94 \times 10^{07}}$

In the light of Fujii et al. (2008), for area, triangular distribution is chosen since triangular distribution is the best alternative when there is limited data. As practiced in Fujii et al. (2008), -20% and +20% of known area is used as the minimum and maximum input values, respectively.

Thickness

Thickness of gas hydrate concentrated and bearing zones is determined from temperature-depth diagrams, presented in Chapter 6. Average thicknesses for concentrated and bearing zones are 865.4 mbsf and 830 mbsf, respectively where the maximum thickness of GHSZ is restricted to 1400 m. Thickness of GHSZ for mud volcanoes is decided according to a study of Ginsburg et al., 1992. There is insufficient

data to interpret exact thickness. After all, thickness of GHSZ in and around of craters of mud volcanoes is assumed a few tens of meters both with help of studies in literature and temperature-depth diagrams. Triangular distribution is preferred for thickness.

Porosity

For concentrated and bearing zones, porosity data is taken as 10, 20 and 40% for minimum, mean, and maximum values, respectively (Bagirov et al., 1999; Buryakovsky et al., 2001). Porosity for mud volcanoes is estimated from the study of Collet et al., 2009. Triangular distribution is used for porosity.

Hydrate Saturation

In this thesis, hydrate saturation in sands of the area is estimated in correlation with data from several case studies.

A large area of Gulf of Mexico, ~450,000 km^2, is developed for hydrate research by the Minerals Management Service (MMS) of the US department of Interior. Seismic, wellbore, geologic, geochemical, and paleontological data is determined and used to estimate hydrate stability zone and the amount of biogenically developed methane in methane hydrates. A discontinuous high amplitude reflection is found tracking the base of the hydrate stability zone in the Walker Ridge. That high amplitude reflection separates the hydrated zone and free gas zone beneath it, which are mostly found in the sand-rich layers. Gas hydrate saturations for different parts of the Gulf of Mexico are estimated from seismic inversion. At Walker Ridge, hydrate saturation ranges from 0% to 40% whereas at Green Canyon this ranges from 50% to 85% showing high hydrate saturation (Birchwood et al., 2010).

Gas hydrate resources in permafrost of Alaska North Slope are researched by BP Exploration Alaska Inc. by 3D survey over Milne Point. Data and analysis from 3D survey, well logs and reservoir modeling, gas hydrate accumulations are found in the region. Gas hydrates bearing layers are observed being at depths from 550 m to 760 m under surface. From log analysis, 30 m of hydrate bearing zone is discovered with hydrate saturation ranging from 45% to 75% (Birchwood et al., 2010).

Geological Survey of Canada (GSC) is initiated a gas hydrate expedition program in the Mallik field, in the Beaufort Sea, in Canada. As part of this program, a production well and two observation wells are drilled. Drilling, logging, coring, and casing operations are conducted in the production well whereas drilling and casing are done for in the observation wells. Fiber-optic distributed temperature sensors are used in order to observe thermal stimulation and depressurization response of the field. Cross well seismic survey is also another method being used for monitoring the formation through observation wells. According to data obtained and gathered from wells, hydrate saturation varying from 70% to 85% at depths from 890 m to 1,106 m (Birchwood et al., 2010).

China's gas hydrate exploration is developed on eight sites in the Shenhu area of the South China Sea. Pilot holes are drilled and logged at each site. Gas hydrates are discovered at five sites in clay and silt rich sediments filling 20% to 40% of the pore spaces of these fine-grained layers. Thickness of hydrate stability zone is 10-25 m (Birchwood et al., 2010).

Nankai Trough, located off the Pacific Coast of Honshu Island, in Japan, is developed for gas hydrate expedition funded by Japanese government. 2D and 3D seismic surveys are conducted in Eastern Nankai Trough area. Logging-while-drilling (LWD), wireline logging, coring, and using long-term temperature sensors are also included in the program. The aim of these surveys is to specify distribution of BSRs and calculate the amount of methane in methane hydrates. 32 wells are drilled trough BSRs in water depth from 722 to 2,033 m. As a result, high saturation of pore-filling type of methane hydrate is found in turbidity sands. Existence of BSRs, high amplitude reflector and high velocity anomaly and characteristics of the layers above the BSR such as distribution of turbidity sands, mud layers, and channels are determined by 3D seismic survey. Gas hydrates zone in the Nankai Trough is divided into two parts as methane hydrate concentrated zones and methane in hydrate bearing layers with different hydrate saturation characteristics. S_h in concentrated zones ranges between 20%-80% with average 50%. However, in hydrate bearing layers this number is relatively low, S_h~29% (Birchwood et al., 2010; Masuda et al., 2010; Tsuji, 2003).

Besides all these case studies, hydrate saturation estimates from work of several authors are given as an example to help methane volume calculation in gas hydrates. These are listed as follows:

Table 5.2: Hydrate saturation values used in global estimations of methane in gas hydrates (adapted from Milkov, 2004)

Reference, Year	S_h, %
Trofimuk et al., 1973	100
Kvenvolden and Claypool, 1988	10
Kvenvolden, 1988	100
MacDonald, 1990	10
Gornitz and Fung, 1994	5-10
Harvey and Huang, 1995	2.5-10, 5-20, 10-40

Based on the data from other fields mentioned above, hydrate saturation for gas hydrate concentrated zone is taken as 0.45, 0.6 and 0.9 for minimum, mean and maximum values, respectively. For gas hydrate bearing zone, hydrate saturation is taken as 0.21, 0.29 and 0.35 for minimum, mean and maximum values, respectively.

Hydrate saturation for mud volcanoes is estimated from the study of Sha et al. (2015) by considering intensive gas seepage and taken as 0.15, 0.35 and 0.5 for minimum, mean and maximum values, respectively. Hydrate saturation parameter estimated by triangular distribution.

Volume Ratio

Volume ratio is practiced from estimations of Fujii et al. (2008) taken as 166 and 172 for minimum and maximum values, respectively. Uniform distribution is chosen for volume ratio.

Cage Occupancy

Cage occupancy parameter is estimated from the study of Fujii et al. (2008) taken as 0.96, 0.98 and 0.99 as minimum, mean and maximum values, respectively. Triangular distribution is preferred based on the same study.

CHAPTER 6

RESULTS AND DISCUSSION

In this study, natural gas hydrate potential of the South Caspian Sea is investigated. Some rarely seen properties of the region, like low geothermal gradient, a great number of mud volcanoes and suitable temperature-pressure conditions, make it attention grabbing for studying. In order to determine GHSZ, pressure and temperature data at the seafloor, gas composition that made up gas hydrates and geothermal gradient are gathered from literature. Results of the work are presented in this chapter:

6.1. Determination of GHSZ for Concentrated and Bearing Zones

Three gas compositions from Diaconescu and Knapp, 2000 (see Figure 3-15) are studied for gas hydrate concentrated and bearing zones. These gas compositions are obtained from core samples whose location is marked as C in Figure 3.13. Fractions of compounds in each are demonstrated in Table 6.1. Pure and saline water environments are compared regarding the gas compositions and related zones

Table 6.1: List of compounds and their percentages in Composition-1, 2 and 3 (adapted from Diaconescu and Knapp, 2000)

c	Mole Percent (%)		
	Composition-1	Composition-2	Composition-3
methane	100	94.87	80
ethane		0.63	1.87
propane		0.83	2.89
iso-butane		0.14	0.44
n-butane			1.92
octane		2.8	
ethylene		0.62	
propylene		0.11	
heavy hydrocarbons			12.88

6.1.1. Pressure-Temperature Diagrams of Composition-1, 2 and 3 for Pure and Saline Water

CSMHYD is a software developed at Colorado School of Mines by Sloan (1990) that predicts the thermodynamics of stable hydrate structures at given pressure, temperature and composition (CSMHYD, 2017). The program is used to calculate hydrate formation pressure for each temperature values for the three gas compositions. Temperature values are entered from 0 °C to 26 °C by one increment. Salinity is taken as 1.3 weight% (13 psu) from Tuzhilkin and Kosarev, 2005 (Chapter 3) for saline water cases. The resulted pressure-temperature diagrams are shown below.

In Figure 6.1, Figure 6.2, and Figure 6.3, pure and saline water cases are compared for composition-1, 2, and 3. For each composition, it can be inferred that the higher pressure is needed for natural gas hydrate occurrence when saline water is present in the environment.

For composition-1, only sI hydrate structure is formed as expected. For compositon-2, sI and sII hydrate structures are formed. For composition-3, only sII hydrate structure is formed.
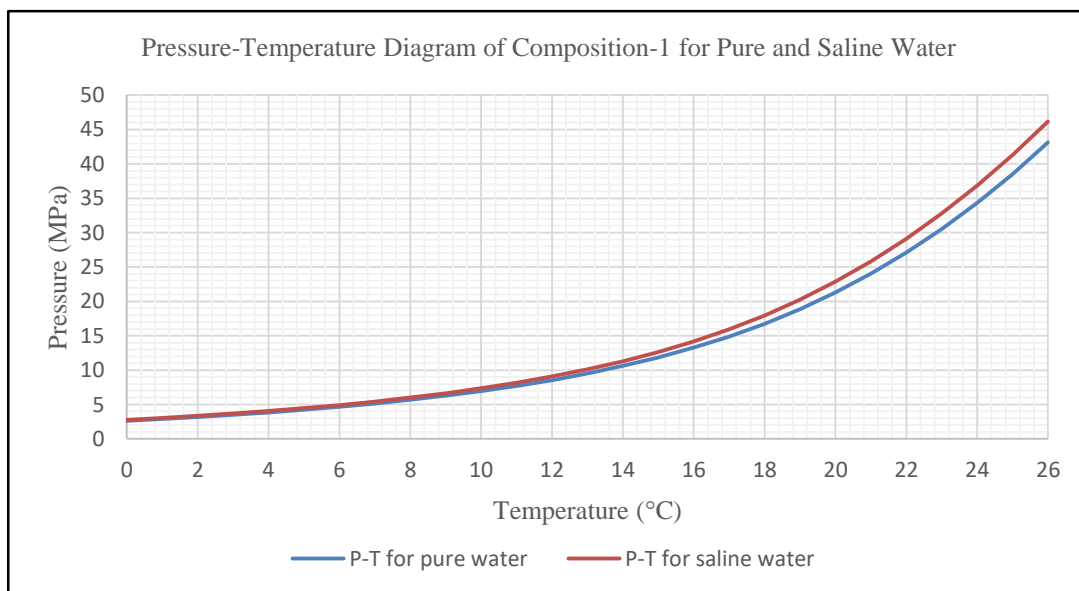
Figure 6.1: Comparison of pressure-temperature diagrams of Composition-1 for pure and saline water

The wavy view in Figure 6.2 is a result of transition from sII hydrate structure to sI hydrate structure and sI to sII for both pure and saline water cases of composition-2.
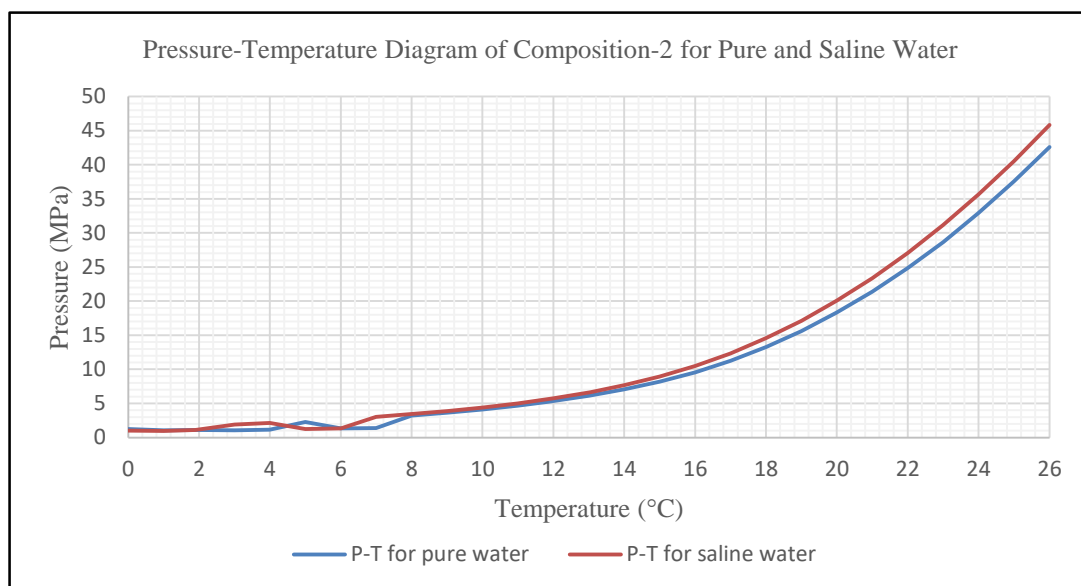
Figure 6.2: Comparison of pressure-temperature diagrams of Composition-2 for pure and saline water

For composition-3, when percentage of heavy hydrocarbons is entered, specific gravity of the composition needs to be specified by the program. Since this information is not available for heavy hydrocarbons, specific gravity of heptane is entered.
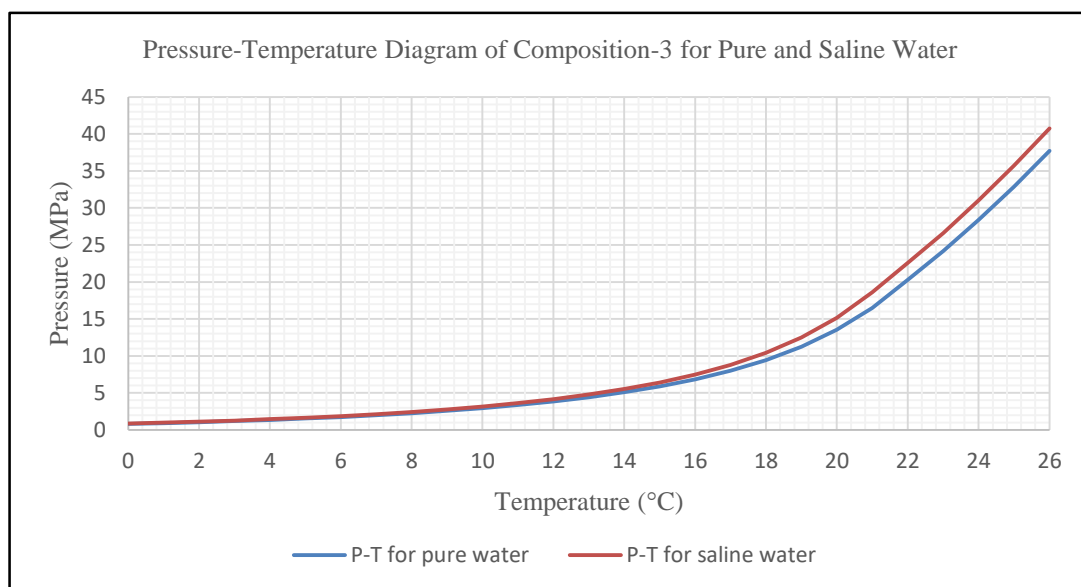
Figure 6.3: Comparison of pressure-temperature diagrams of Composition-3 for pure and saline water

In Figure 6.4, for all the three compositions, the equilibrium lines for natural gas hydrates are compared in the pure water environment.
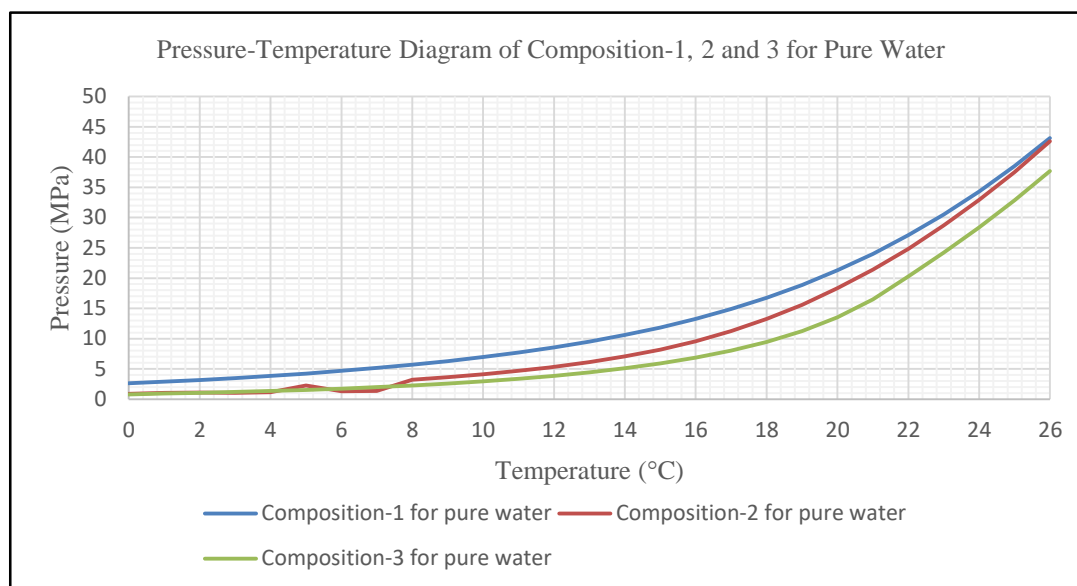
Figure 6.4: Comparison of pressure-temperature diagrams of Composition-1, 2 and 3 for pure water

In Figure 6.5, the equilibrium lines for natural gas hydrate occurrence are compared in the saline water environment for all the three gas compositions.
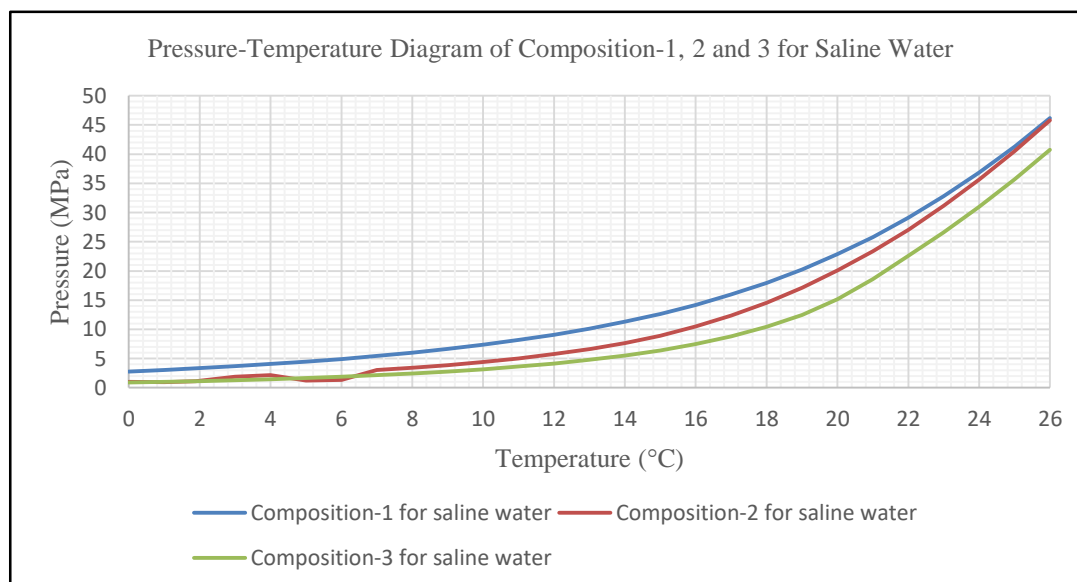
Figure 6.5: Comparison of pressure-temperature diagrams of Composition-1, 2 and 3 for saline water

6.1.2. Temperature-Depth Diagrams of Composition-1, 2 and 3 for Pure and Saline Water

For further calculations, water density requires to be assessed. For this purpose, "Ocean Water Density Calculator" is used (Ocean Water Density Calculator, 2017). The equation used in the background of this calculator is based on the formula in the study of Millero et al. (1980) named as "A new high pressure equation of state for seawater". The calculator determines the density of water as a function of temperature (°C), salinity (psu) and pressure (decibars).

Therefore, density of the seawater is acquired from the calculator. Using these results, depth is determined for each temperature values by the general hydrostatic pressure formula Equation 6.1 as follow:

$$P = \rho \times g \times h \tag{6.1}$$

P: pressure, (N/m^2)
ρ: density, (kg/m^3)
g: acceleration of gravity, 9.8 m/s^2
h: water depth, (m)

Temperature-depth diagrams of the three gas compositions are displayed for pure and saline water cases. Figure 6.6, Figure 6.7, Figure 6.8, Figure 6.9, and Figure 6.10 show the resulted diagrams.

In Figure 6.6, Figure 6.7, and Figure 6.8, pure and saline water cases are studied for each composition separately.
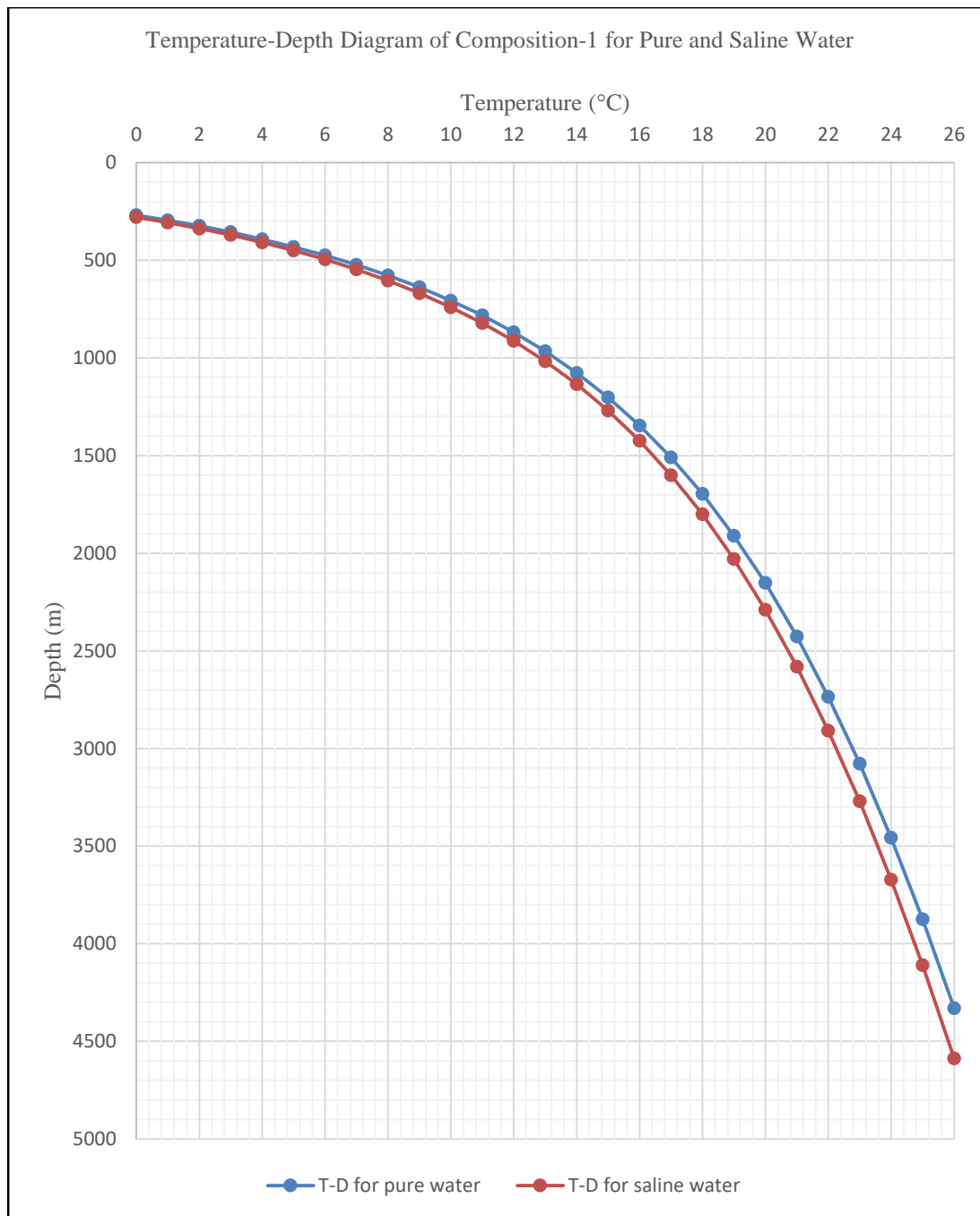
Figure 6.6: Comparison of temperature-depth diagrams of Composition-1 for pure and saline water
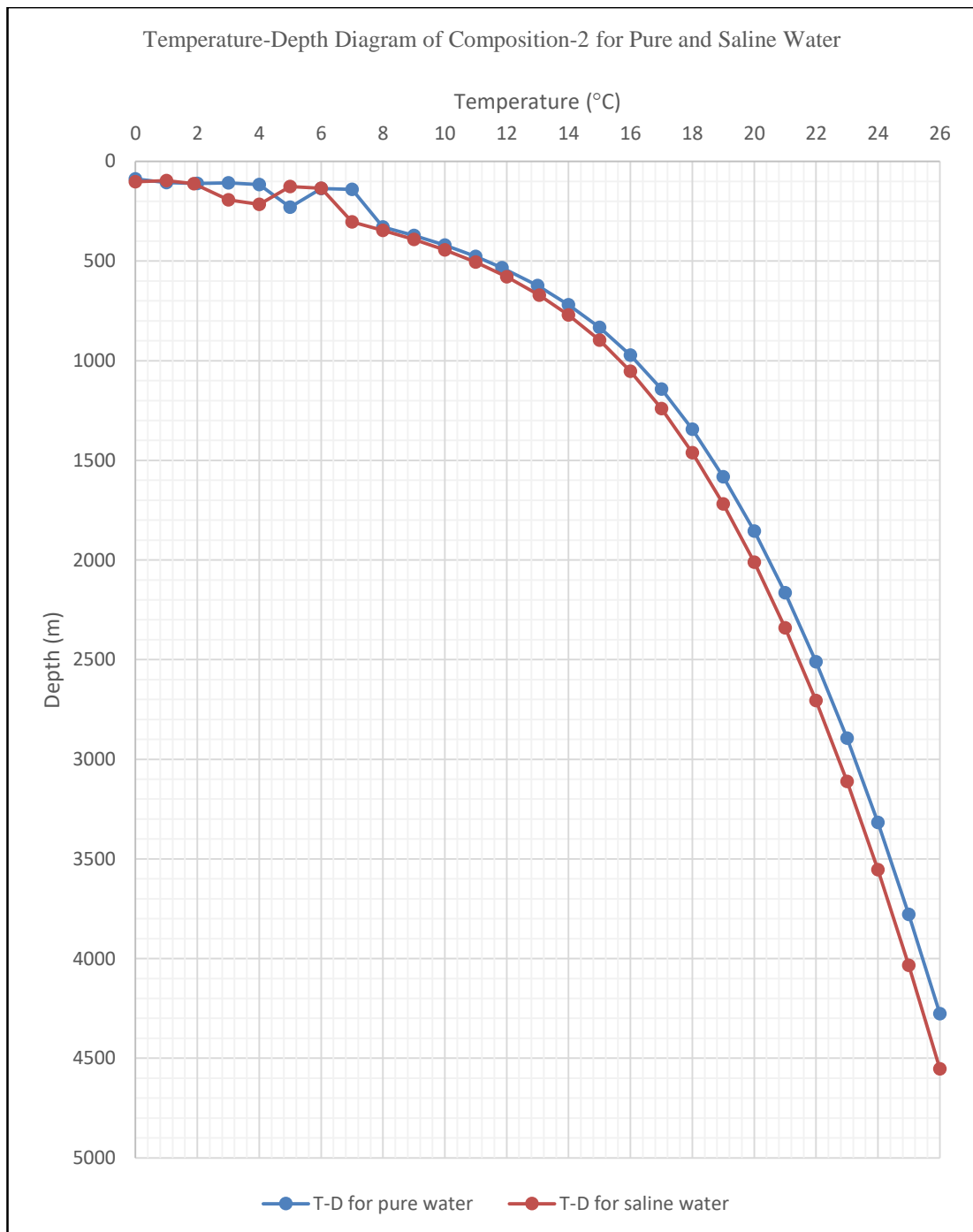
Figure 6.7: Comparison of temperature-depth diagrams of Composition-2 for pure and saline water
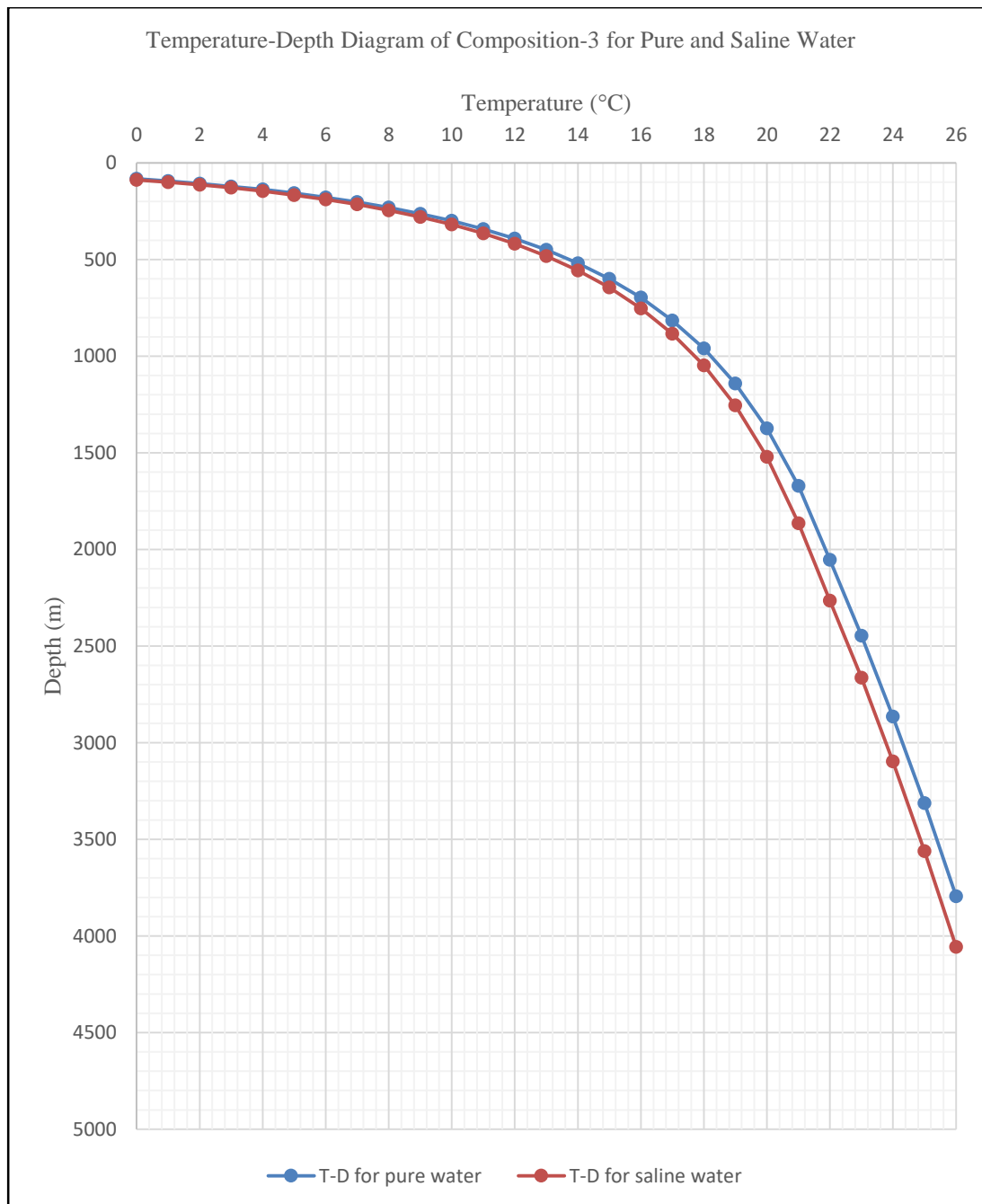
Figure 6.8: Comparison of temperature-depth diagrams of Composition-3 for pure and saline water

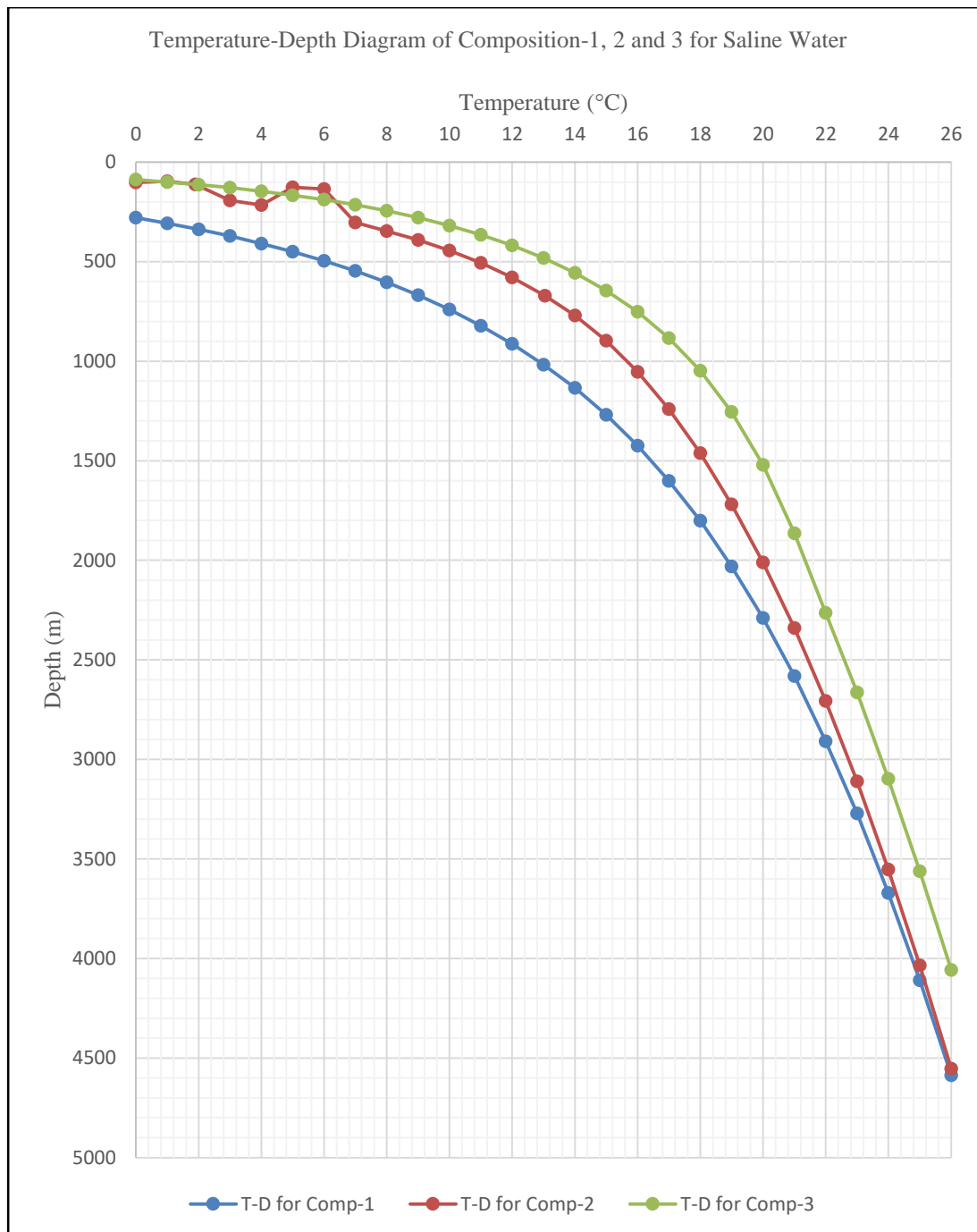In Figure 6.9, temperature-depth diagram of all the three gas compositions are compared together for pure water case.
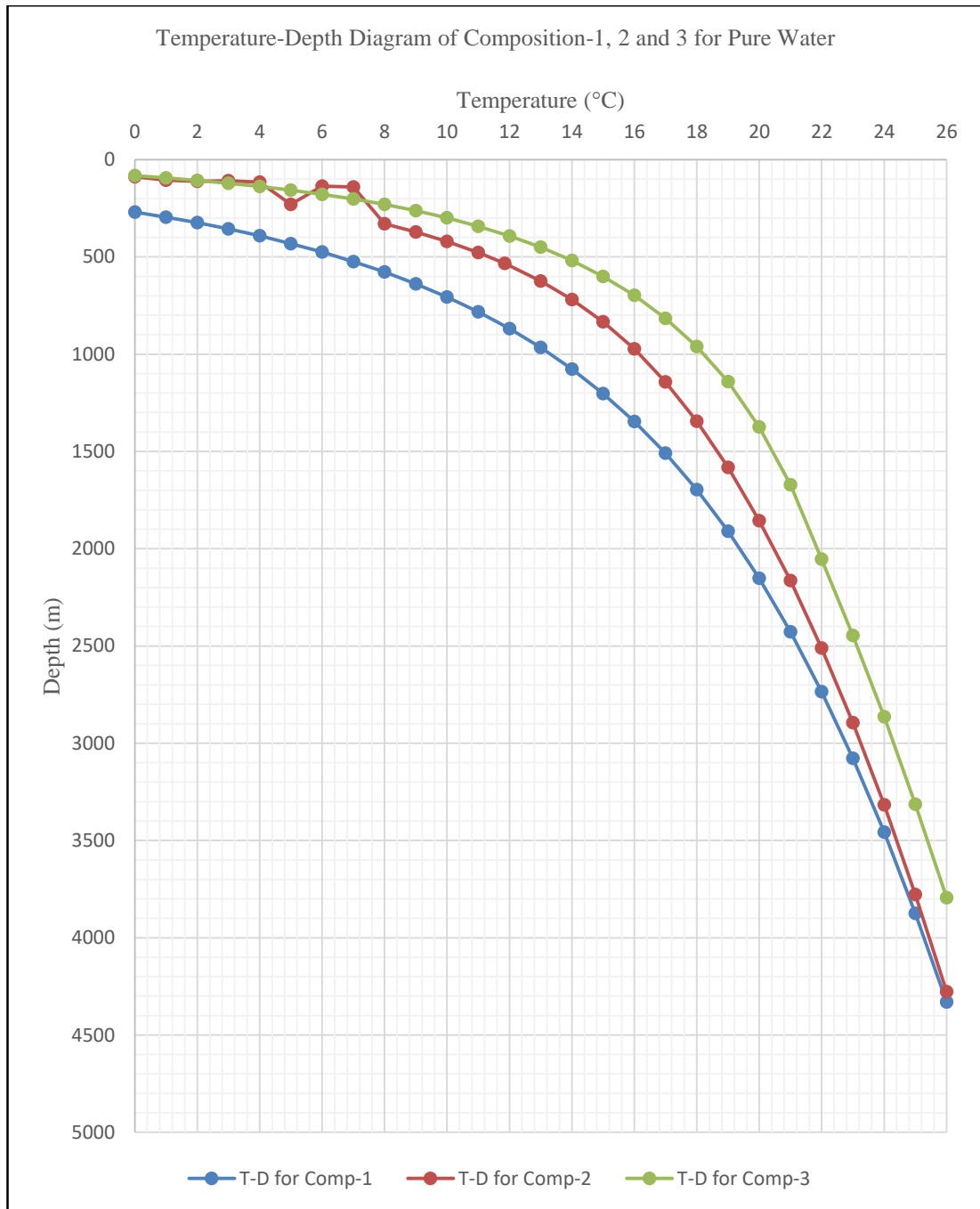
Figure 6.9: Comparison of temperature-depth diagrams of Composition-1, 2 and 3 for pure water case

In Figure 6.10, temperature-depth diagram of all the three gas compositions are compared together for saline water case.

Figure 6.10: Comparison of temperature-depth diagrams of Composition-1, 2 and 3 for saline water

6.1.3. Thickness of GHSZ

In order to understand and estimate thickness of GHSZ, change in geothermal gradient with depth requires to be visualized. The basin of the South Caspian Sea has geothermal gradient between 1.1-1.7 °C/100 m (Chapter-3) (Bagirov et al., 1999). Contour line bathymetry of the Caspian Sea helps to estimate depth of seafloor for

possible gas hydrate zones. Therefore, calculations and diagrams are made for water depth from 100 m to 1,000 m.

According to resulted temperature-depth diagrams for concentrated and bearing zones, gas hydrate occurrence is observed from water depths from 100 m to 1,000 m. Thickness of GHSZ may change from 620 mbsf to 1,900 mbsf for concentrated zones. In bearing zones, it may change from 190 mbsf to 1,420 mbsf. These results are analogous with findings from literature. As reported by Gerivani and Gerivani, 2015 (see Figure 3.11); gas hydrates may even generate and are distributed more than 1500 mbsf. Presence of salt in the environment decrease the stability and thickness of GHSZ gets thinner. List and diagram for thicknesses of GHSZ according to water depth are shown in Table 6.2 and in Figure 6.11.

Table 6.2: Thicknesses of GHSZ according to water depths for concentrated and bearing zones

Water Depth (m)	Composition-1				Composition-2				Composition-3			
	Pure Water		Saline Water		Pure Water		Saline Water		Pure Water		Saline Water	
	Low GG	High GG	Low GG	High GG	Low GG	High GG	Low GG	High GG	Low GG	High GG	Low GG	High GG
100	0	0	0	0	680	0	530	0	1160	430	1080	310
200	0	0	0	0	1050	220	840	0	1320	660	1240	620
300	0	0	0	0	1120	530	1040	470	1360	730	1290	680
400	670	0	440	0	1180	600	1100	550	1400	770	1330	730
500	990	310	900	200	1230	650	1160	600	1420	800	1360	770
600	1080	470	1000	400	1280	690	1200	650	>1400	840	1400	800
700	1170	550	1090	500	1300	720	1250	690	>1400	860	>1300	820
800	1200	610	1150	565	>1200	760	>1200	720	>1400	880	>1300	840
900	>1200	660	>1150	620	>1200	790	>1200	750	>1400	900	>1300	860
1000	>1200	700	>1150	660	>1200	810	>1200	775	>1400	920	>1300	880
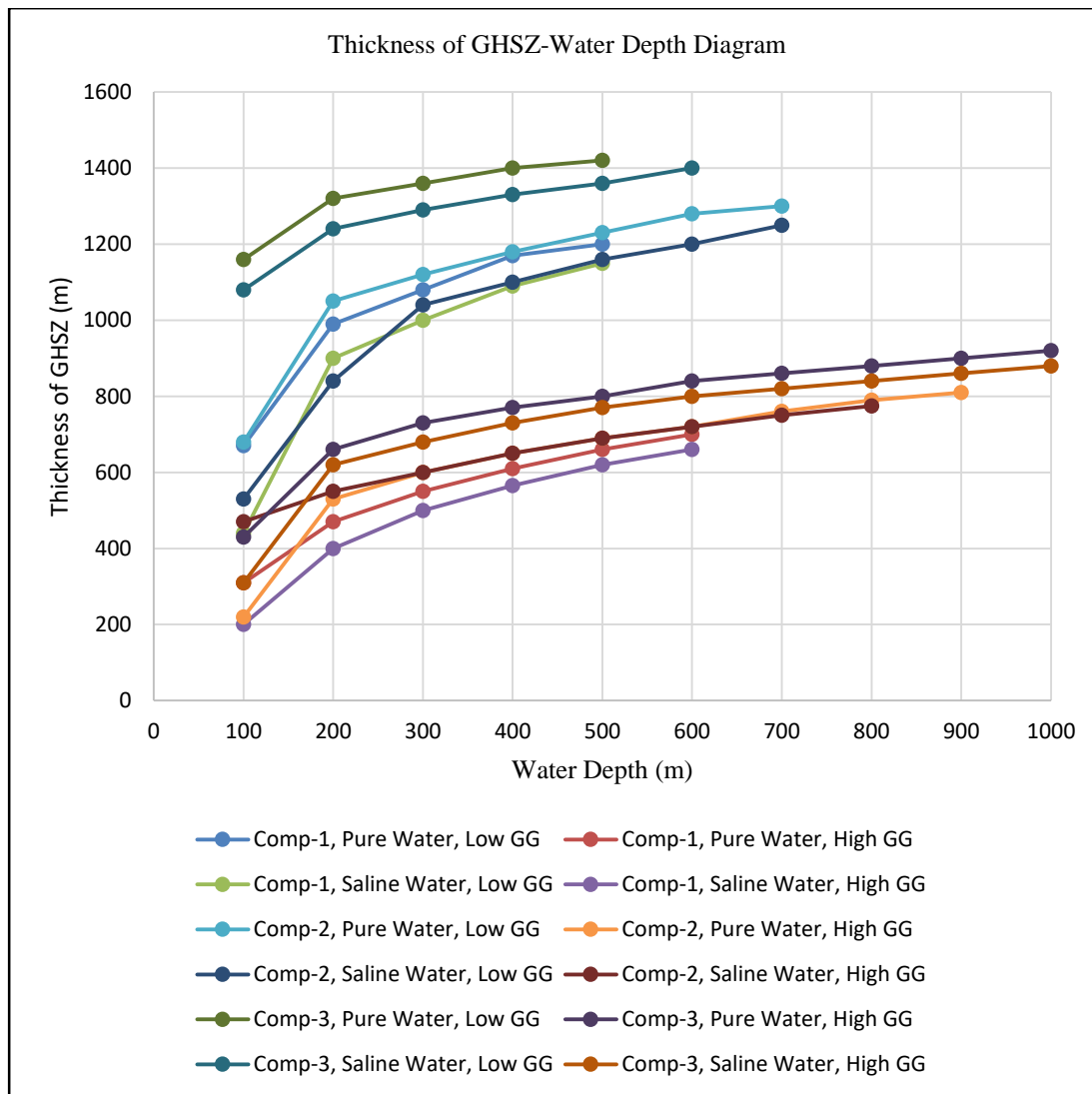
Figure 6.11: Thickness of GHSZ-water depth diagram of composition-1, 2, and 3 for low and high geothermal gradients in pure and saline water environments

Temperature-depth diagram at water depth of 700 m is shown in Figure 6.12 and Figure 6.13 for pure and saline water environments, respectively. Diagrams for other depths are displayed in Appendix A from Figure A-1 to Figure A-18.
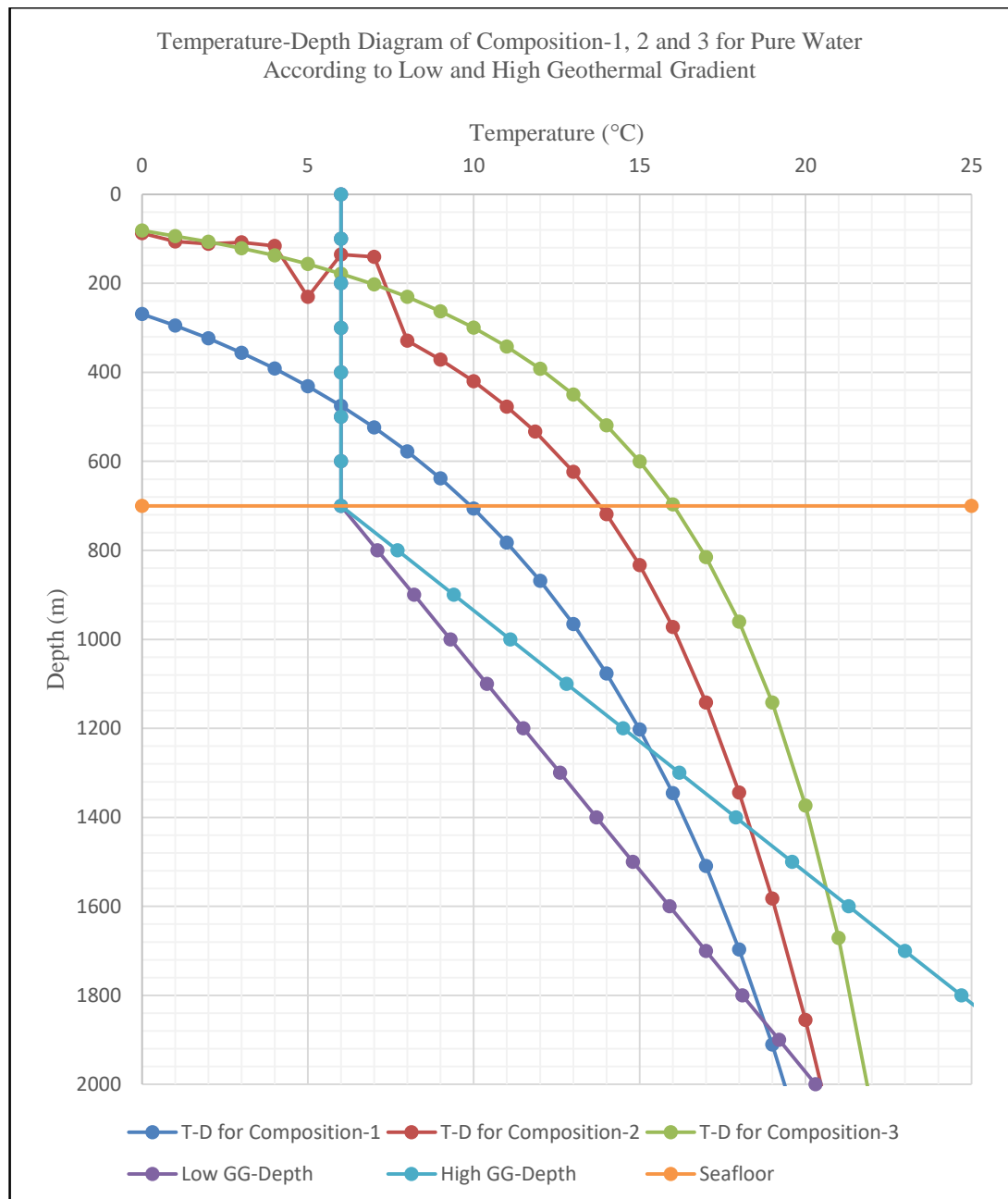
Figure 6.12: Temperature-depth diagram of Composition-1, 2, and 3 for pure water case according to low and high geothermal gradient. Seafloor is at 700 m
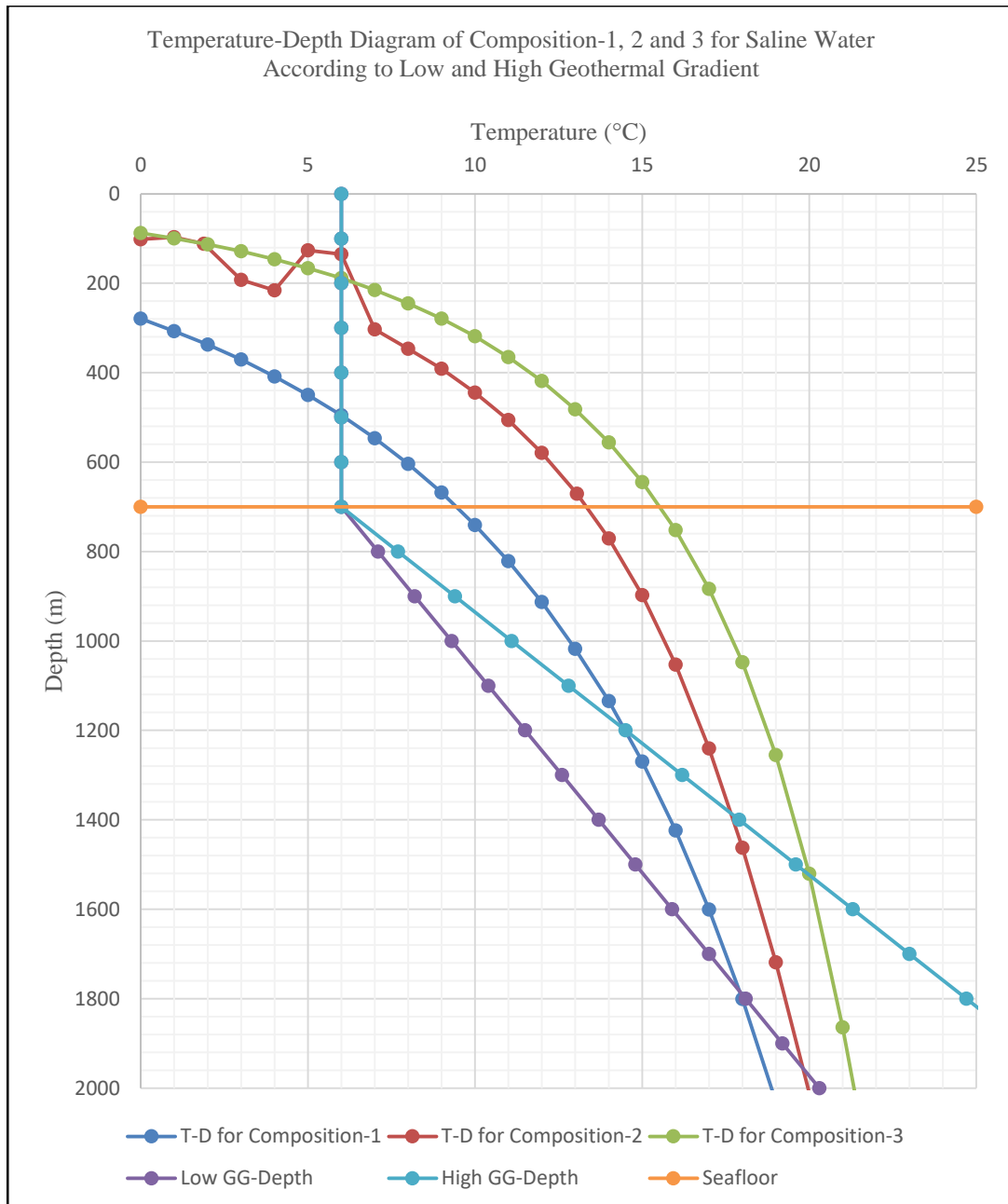
Figure 6.13: Temperature-depth diagram of Composition-1, 2, and 3 for saline water case according to low and high geothermal gradient. Seafloor is at 700 m

6.2. Determination of GHSZ for Mud Volcanoes

As mentioned in Chapter 3, seismic profiling, geothermal measurements, use of bottom sampling apparatus, and a combination of on-board and laboratory gas-hydrate geochemical investigations are conducted on the Vezirov and Azizbekov highs and Abikha bank.

Different gas compositions from mud volcanoes of the South Caspian Sea are available from the study of Ginsburg et al., 1992. All of these compositions are studied in pure water environment. Different gas compositions are obtained from the same station. Some numbers are attributed to these gas compositions for distinguishing them. These numbers are noted in brackets next to station numbers.

Samples are taken from different stations shown on Figure 3.23, Figure 3.24 and Figure 3.25. Percentages of hydrocarbon compositions and CO_2 obtained from these samples are listed in the Table 6.3.

Table 6.3: Percentages of hydrocarbons and CO_2 in typical gas samples (adapted from Ginsburg et al., 1992)

Mud volcano	Station no.	Interval (m)	Percentages of components (%)						
			C1	C2	C3	C4	nC4	C5+	CO2
Buzdag	7s (1)	0.5-0.6	77,115	18,204	2,400	0,400	1,100	0,330	0,450
	7s (2)		74,752	17,412	2,402	0,400	1,101	0,330	3,603
	7s (3)		80,824	13,604	4,201	0,300	0,400	0,020	0,650
	7s (4)		87,035	10,404	1,301	0,100	0,400	0,060	0,700
	7p (1)	0-1.2	74,193	16,998	5,999	0,700	0,900	0,110	1,100
	7p (2)		58,741	19,414	15,811	2,502	2,001	0,680	0,851
	1B + 1C	0-0.6	76,129	19,333	2,404	0,601	0,301	0,050	1,182
Elm	17	0-0.5	95,290	0,600	1,500	1,700	0,000	0,010	0,900
	18A	0-0.4	81,392	15,298	1,600	0,200	0,700	0,000	0,810
Abikha	32	0.3-0.5	87,035	10,050	2,111	0,201	0,201	0,402	0,000

Calculations are done in the light of these results in order to determine pressure-temperature, pressure-temperature-depth, temperature-depth diagrams and GHSZ for Buzdag, Elm and unnamed mud volcano on Abikha bank.

6.2.1. Pressure-Temperature Diagrams for Gas Compositions from Mud Volcanoes

Pressure values for each temperature values are calculated through CSMHYD by introducing gas compositions (Table 6.3) to the software. Both sI and sII hydrates are observed from calculations using CSMHYD. sI type is observed at high temperature values from 23°C to 27°C (note: calculations are done up to 30°C).

In Figure 6.14, the resulted pressure-temperature diagram of Compositions-3, taken from Station 7s on Vezirov high, is shown as a sample. The other gas compositions

and pressure-temperature diagrams are displayed in Appendix B from Figure B-1 to Figure B-9.
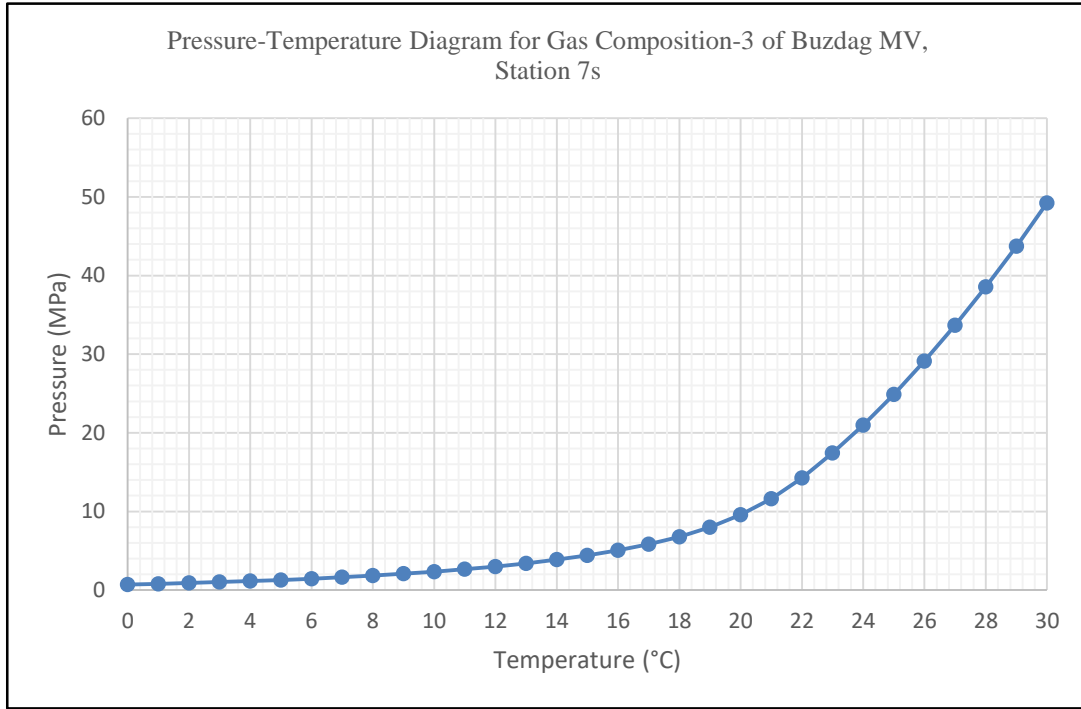
Figure 6.14: Pressure-temperature diagram for gas composition-3 of Buzdag mud volcano, station 7s

6.2.2. Temperature-Depth Diagrams for Gas Compositions from Mud Volcanoes

With the obtained pressure values in previous section, water density and according depth is calculated through Ocean Water Calculator. In Figure 6.15, the resulted temperature-depth diagram of Compositions-3, taken from Station 7s on Vezirov high, is shown as a sample. The other gas compositions and temperature-depth diagrams are displayed in Appendix B from Figure B-10 to Figure B-18 .
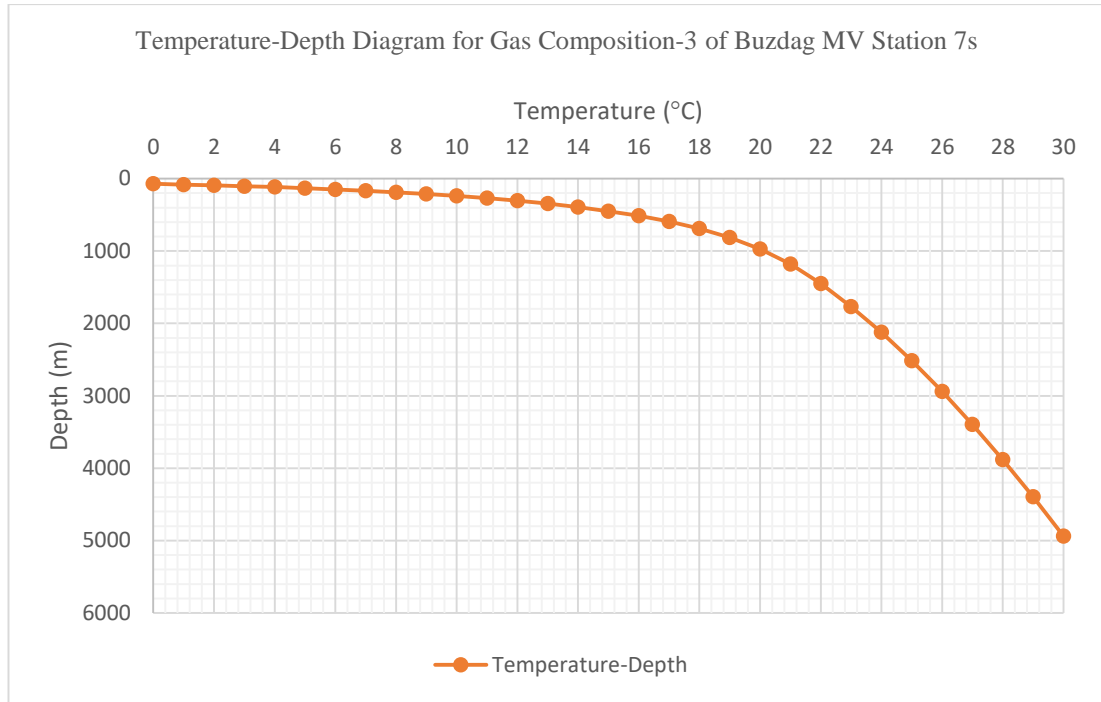
Figure 6.15: Temperature-depth diagram for gas composition-3 of Buzdag mud volcano, station 7s

6.2.3. Thickness of GHSZ

Low and high geothermal gradients obtained from investigations are listed in Table 6.4. These data are only available for Buzdag and Elm mud volcanoes. Still, the same data is used for unnamed mud volcano on Abikha bank.

Table 6.4: Data of geothermal gradient measurements from six stations of Buzdag and Elm mud volcanoes (adapted from Ginsburg et al., 1992)

Mud volcano	Station no.	Depth of probe (m)	Temperature (°C)	Geothermal Gradients (°C/100 m)	
				Low	High
Buzdag	7-1	~1	5.97	120	129
	7-2	1.4	6.20	7	15
Elm	17-1	~1	5.93	12.9	22.6
	17-1	~1	5.98	34.1	35.3
	46	~1	5.96	7.8	10.5
	47	~1	5.97	1.1	4.4

As a sample, temperature-depth diagram of gas composition-3 for Buzdag mud volcano, station 7s, according to low (7 °C/100 m) and high (15 °C/100 m) geothermal gradient values is shown in Figure 6.16. The other temperature-depth diagrams are displayed in Appendix B from Figure B-19 to Figure B-45.
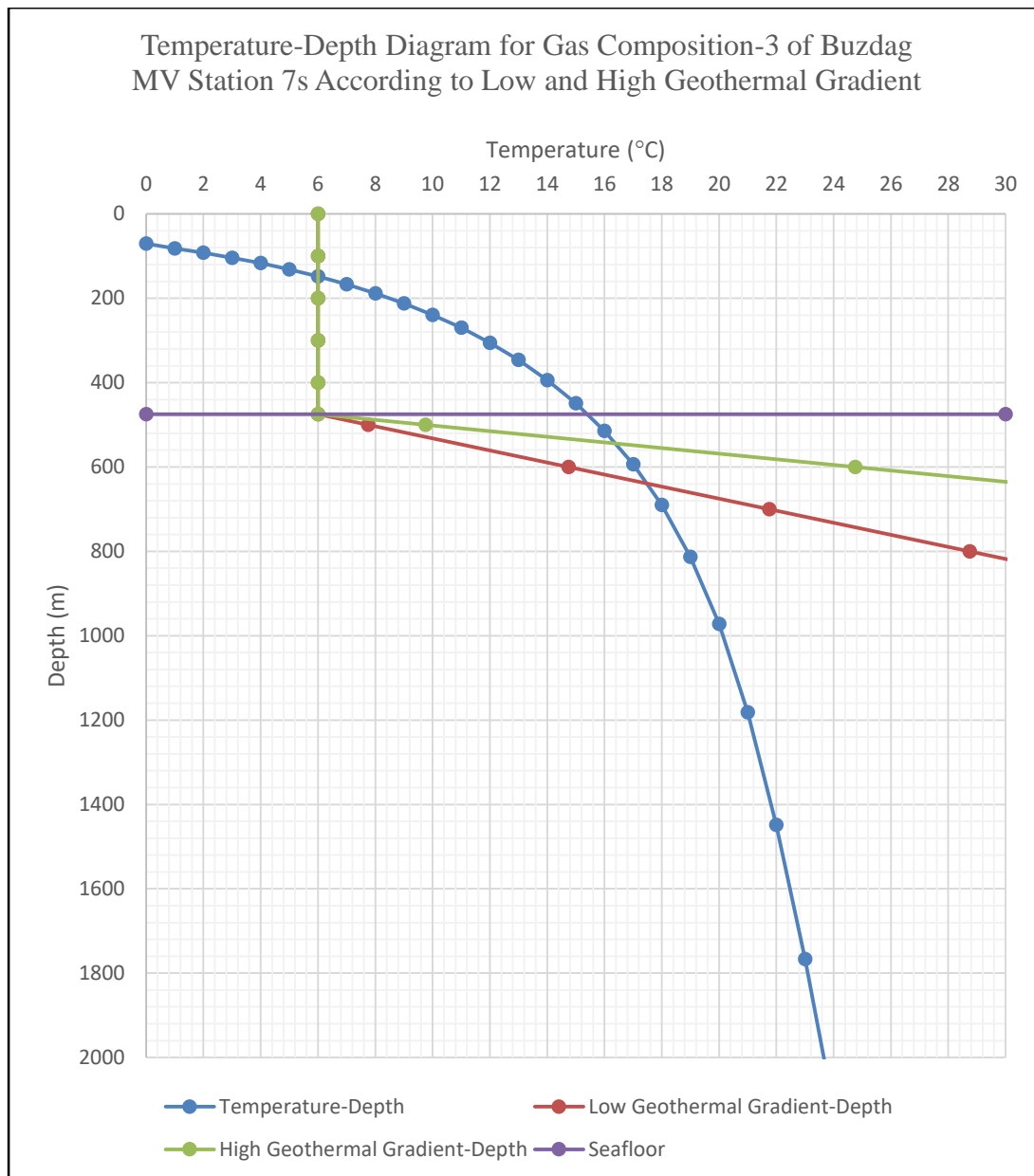
Figure 6.16: Temperature-depth diagram for gas composition-3 of Buzdag mud volcano, station 7s, according to low and high geothermal gradient. Low GG = 7 °C/100 m; High GG = 15 °C/100 m

6.3. Monte Carlo Application For The South Caspian Sea

Using Monte Carlo simulation, 10,000 iterations are run in @RISK. Concentrated, bearing and mud volcanoes zones are calculated separately. The obtained results are presented in the following sections.

6.3.1. Concentrated Zones

The minimum, mean, and maximum estimations of parameters for gas hydrate concentrated zones are listed in Table 6.5.

Table 6.5: List of the minimum, mean, and maximum estimations of input results for gas hydrate concentrated zones

| | Gas Hydrate Concentrated Zones | | | | | |
	Area A (m²)	Thickness h (m)	Hydrate Saturation S_h (%)	Porosity ϕ (%)	Volume Ratio VR (%)	Cage Occupancy CO (%)
Minimum	5.84×10^8	200	0.45	0.1	166	0.96
Mean	7.30×10^8	865.4	0.6	0.2	-	0.98
Maximum	8.76×10^8	1,400	0.9	0.4	172	0.99

The estimated methane amount in concentrated zones where BSRs are observed is calculated according to these parameters. The minimum, mean, and maximum estimation for accessible resource volume is calculated by @RISK. Sand content of the area is taken as 10% (Bagirov et al., 1999). The results from @RISK are multiplied by sand content and following findings are obtained:

- Minimum: 2.05×10^{11} Sm³
- Mean: 1.50×10^{12} Sm³
- Maximum: 5.80×10^{12} Sm³

Frequency of probable values is displayed on the related histogram, in Figure 6.17.
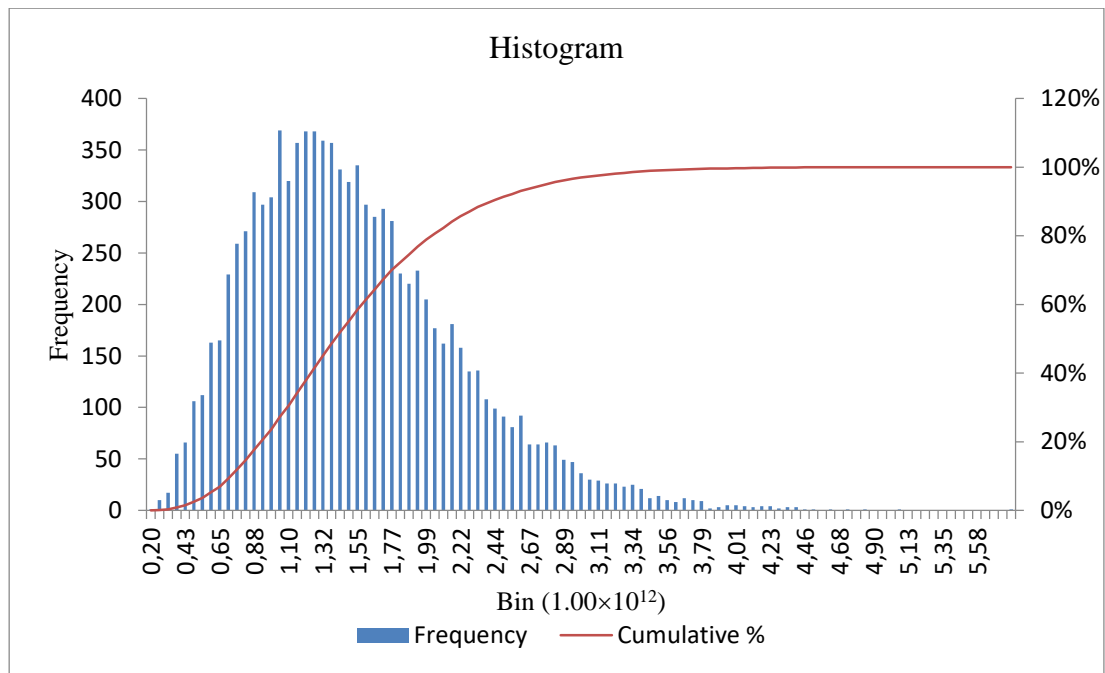
Figure 6.17: Histogram of gas hydrate concentrated zones

Probability-estimated accessible resource volume diagram for concentrated zones is shown in Figure 6.18.
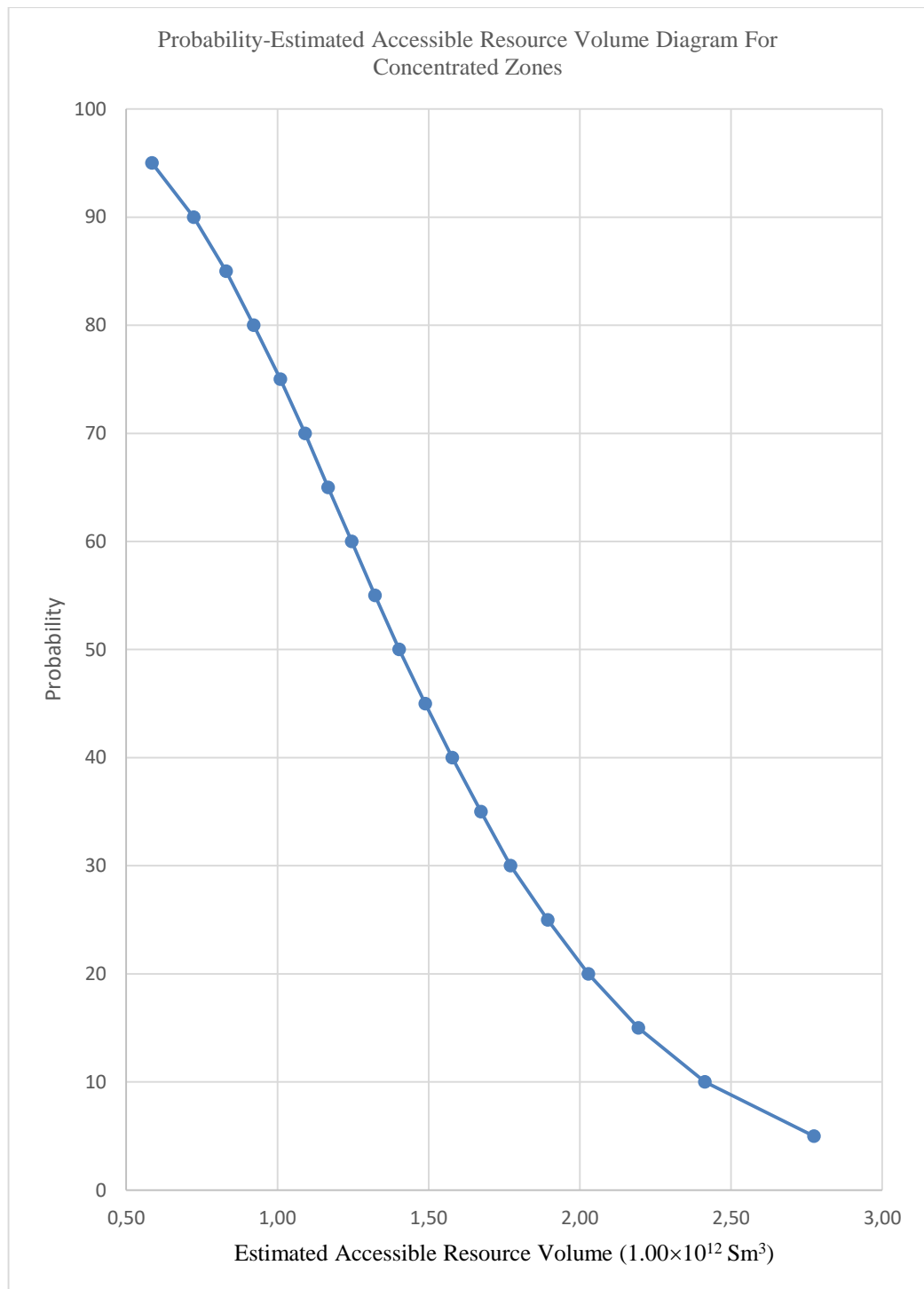
Figure 6.18: Probability-estimated accessible resource volume diagram for concentrated zones

6.3.2. Bearing Zones

The minimum, mean, and maximum estimations of parameters for gas hydrate bearing zones are listed in Table 6.6.

Table 6.6: List of the minimum, mean, and maximum estimations of input results for gas hydrate bearing zones

	Gas Hydrate Bearing Zones					
	Area A (m^2)	**Thickness H (m)**	**Hydrate Saturation S_h (%)**	**Porosity ϕ (%)**	**Volume Ratio VR (%)**	**Cage Occupancy CO (%)**
Minimum	1.34×10^{10}	200	0.21	0.1	166	0.96
Mean	1.68×10^{10}	830	0.29	0.2	-	0.98
Maximum	2.01×10^{10}	1400	0.35	0.4	172	0.99

The estimated methane amount in bearing zones where suitable temperature and pressure conditions are available for generation of gas hydrates is calculated. Sand content is taken as 10% (Bagirov et al., 1999). The results from @RISK are multiplied by sand content and following findings are obtained:

The minimum, mean, and maximum estimation for accessible resource volume is found as follow:

- Minimum: 2.09×10^{12} Sm^3
- Mean: 1.48×10^{13} Sm^3
- Maximum: 4.74×10^{13} Sm^3

Frequency of probable values is displayed on the related histogram, in Figure 6.19.
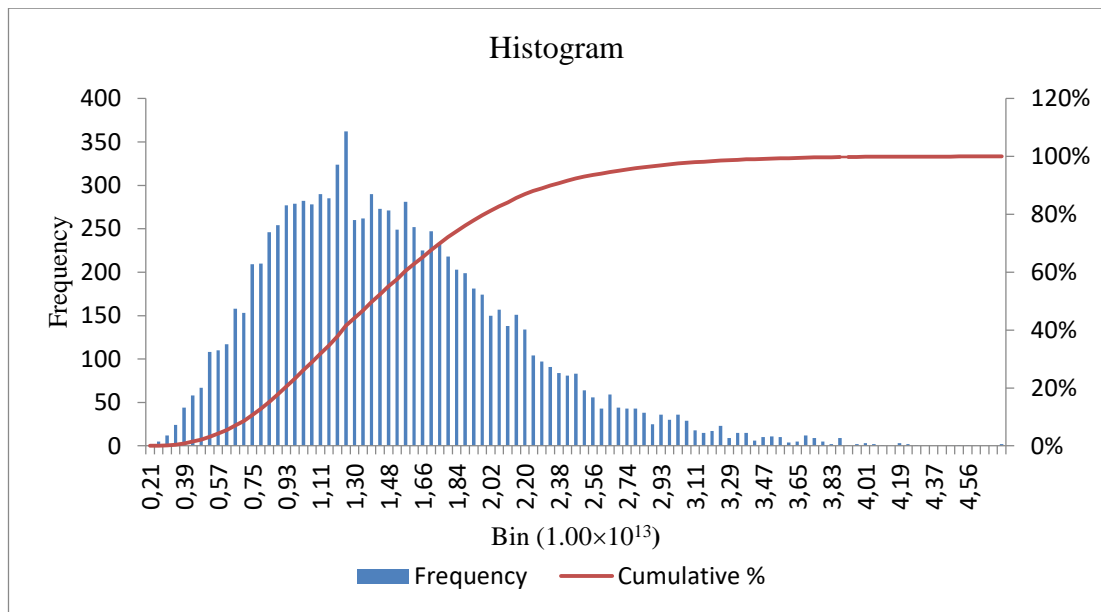
Figure 6.19: Histogram of gas hydrate bearing zones

Probability-estimated accessible resource volume diagram for bearing zones is shown is Figure 6.20.
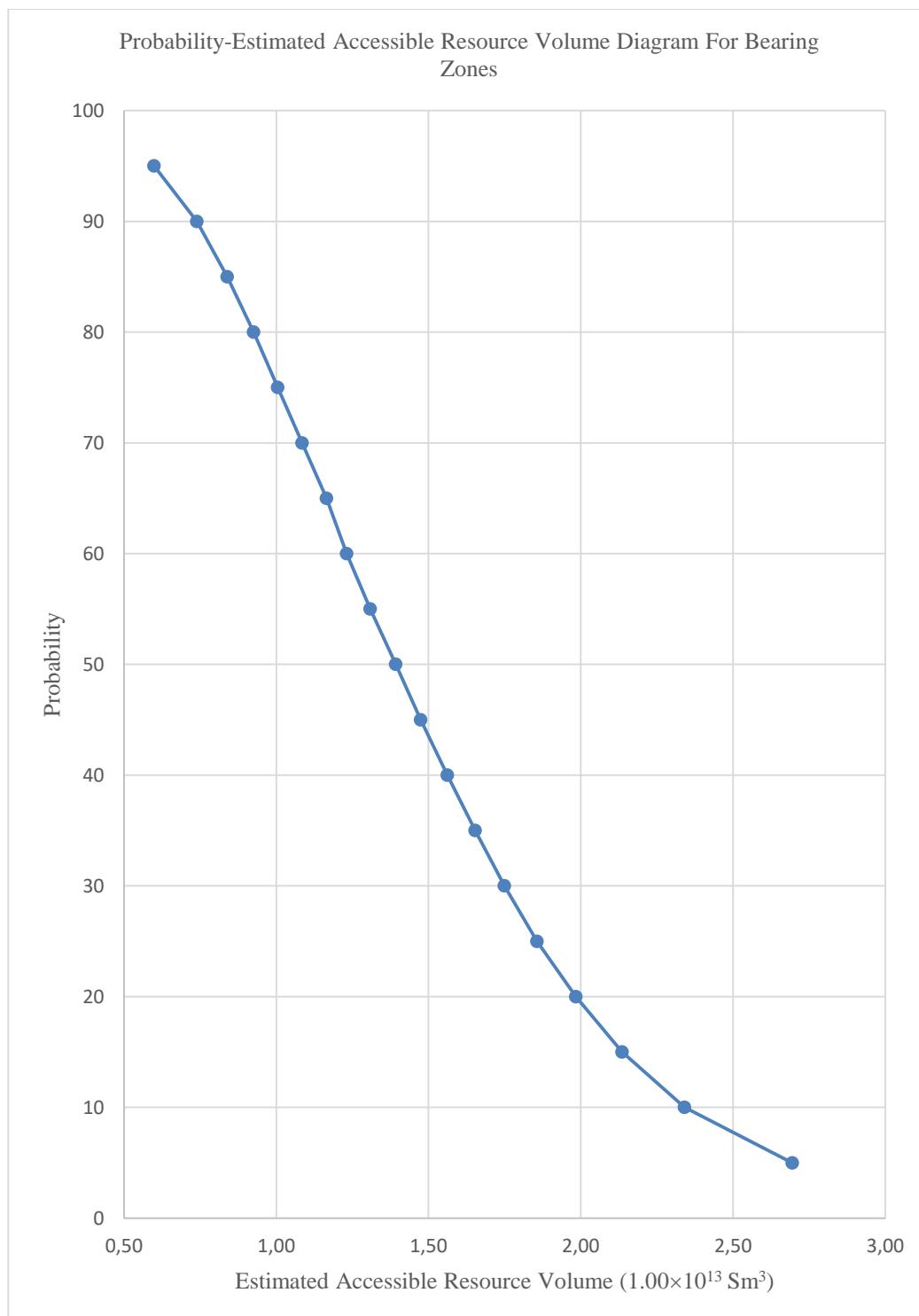
Figure 6.20: Probability-estimated accessible resource volume diagram for bearing zones

6.3.3. In and Around of Craters of Mud Volcanoes

The minimum, mean, and maximum estimations of parameters for mud volcanoes are listed in Table 6.7.

Table 6.7: List of the minimum, mean, and maximum estimations pf input results for gas hydrate in and around of craters of mud volcanoes

	Gas Hydrate In and Around of Craters of Mud Volcanoes					
	Area A (m^2)	Thickness H (m)	Hydrate Saturation S_h (%)	Porosity ϕ (%)	Volume Ratio VR (%)	Cage Occupancy CO (%)
Minimum	4.75×10^{07}	15	0.15	0.1	166	0.96
Mean	5.94×10^{07}	20	0.35	0.2	-	0.98
Maximum	7.12×10^{07}	30	0.5	0.4	172	0.99

The estimated amount of methane in and around of craters of mud volcanoes where intensively gas seepages are occurred near surface area is calculated.

The minimum, mean, and maximum estimation for accessible resource volume is found as follow:

- Minimum: 3.59×10^{09} Sm^3
- Mean: 1.65×10^{10} Sm^3
- Maximum: 5.04×10^{10} Sm^3

Frequency of probable values is displayed on the related histogram, in Figure 6.21.
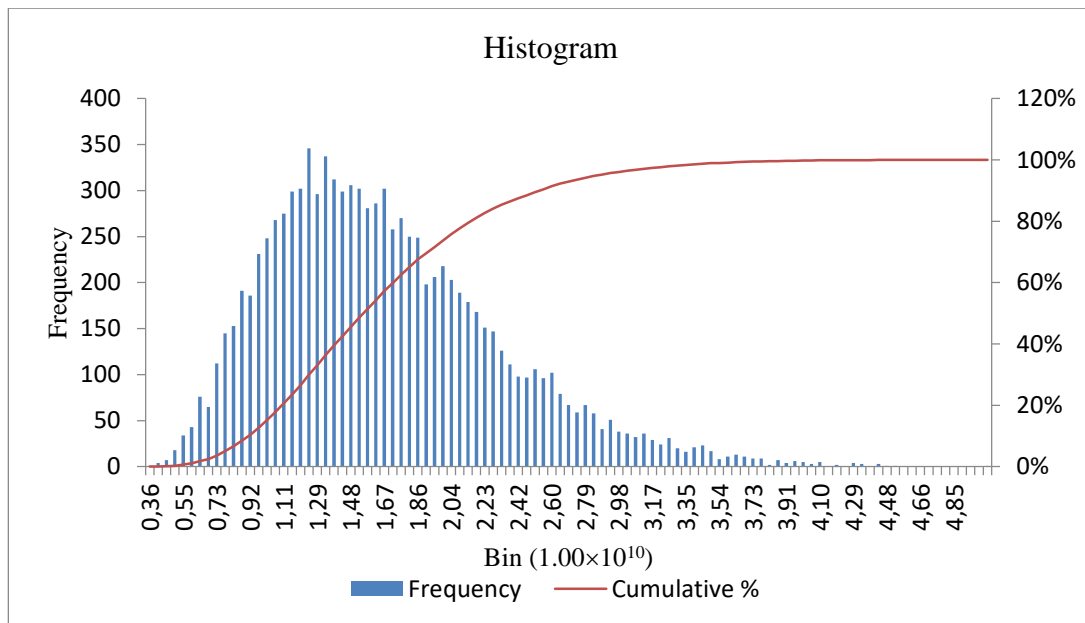
Figure 6.21: Histogram for mud volcanoes

Probability-estimated accessible resource volume diagram for mud volcanoes is shown is Figure 6.22.
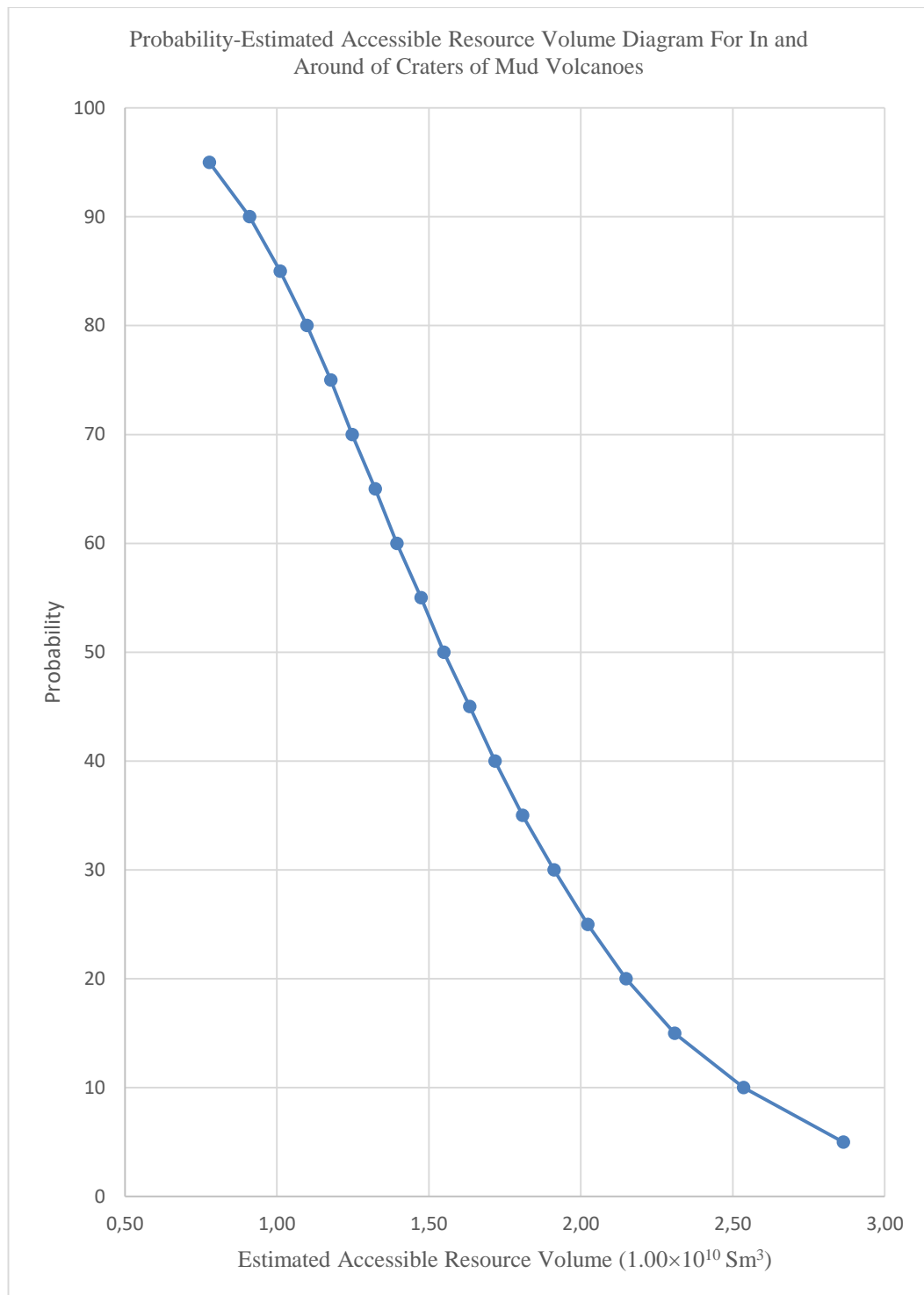
Figure 6.22: Probability-estimated accessible resource volume diagram for mud
volcanoes

The minimum, mean and maximum of total accessible resource volume is given in Table 6.8.

Table 6.8: Estimated amount of methane in gas hydrates

		Minimum	Mean	Maximum
Concentrated Zone	Accessible Resource Volume (Sm^3)	$2{,}05\times10^{11}$	$1{,}50\times10^{12}$	$5{,}80\times10^{12}$
Bearing Zone	Accessible Resource Volume (Sm^3)	$2{,}09\times10^{12}$	$1{,}48\times10^{13}$	$4{,}74\times10^{13}$
Mud Volcanoes	Accessible Resource Volume (Sm^3)	3.59×10^{09}	1.65×10^{10}	5.04×10^{10}
	Total Accessible Resource Volume (Sm^3)	**2.30×10^{12}**	**1.64×10^{13}**	**5.32×10^{13}**

According to an estimation done by Gerivani and Gerivani, 2015, GHSZ in Apsheron region, Azerbaycan, with thickness of 200 m extending for 10 km and only 5% of the sediments volume being composed of gas hydrates is assumed. The volume of methane hydrate is estimated around 1 billion cubic meters. The volume of methane is nearly 160 times more than hydrate volume. Therefore, regarded hydrate zone probably has around 160 billion cubic meter of hydrocarbon gas. When mud volcanoes are the case, in the study of Muradov, 2002 it is stated that gas hydrates, almost 100 m beneath the seafloor, contains $0.2\cdot10^{15}$–$8\cdot10^{15}$ m^3 volume of hydrocarbon gases in gas hydrates (Huseynov and Guliyev, 2004). The consensus value for methane in gas hydrates is estimated as 2.1×10^{16} m^3 by Kvenvolden, 1999 for the world's gas hydrates reserves. When these values are considered, although, estimations are done under lots of uncertainties in this work; total accessible resource volume is as expected and comparable with the data from literature. Results emphasize that together with all data from literature and useful tools used in this study, the South Caspian Sea is a gas hydrate province with quite large amount of methane encapsulated in gas hydrates.

CHAPTER 7

CONCLUSION

In this study, gas hydrate potential of the South Caspian Sea is carried out through Monte Carlo method. Estimations are run by @RISK.

The study area is divided by three according to special characteristics of each part.

Concentrated zone show strong evidence of BSRs. Bearing zones has suitable conditions for generation of gas hydrates (Knapp et al., 2005). In and around of craters of mud volcanoes, intensive gas seepage is observed (Ginsburg et al., 1992).

Three gas compositions known from literature are studied for concentrated and bearing zones (Diaconescu and Knapp, 2000). Pure and saline water cases for the environment is considered and compared. For calculations in and around of craters of mud volcanoes, gas compositions from literature (Ginsburg et al., 1992) are applied only in pure water environment. The following remarks are obtained from calculations.

For concentrated and bearing zones:

- Both in concentrated and bearing zones, for composition-1, only sI hydrate structure is formed; for compositon-2, sI and sII hydrate structures are formed; and for composition-3, only sII hydrate structure is formed.
- For all three gas compositions, salinity shrinks the GHSZ both in concentrated and bearing zones.
- GHSZ enlarges as heavier hydrocarbons are present.

- Thickness of GHSZ changes from 200 to 1,400 mbsf in concentrated zones. In bearing zones, it changes between 190 and 1,420 mbsf.
- In concentrated zones, minimum- 2.05×10^{11} Sm^3, mean- 1.50×10^{12} Sm^3, and maximum- 5.80×10^{12} Sm^3 of methane is estimated. While in bearing zones, 2.09×10^{12} Sm^3, 1.48×10^{13} Sm^3, and 4.74×10^{13} Sm^3 of methane is estimated for the minimum, mean, and maximum values, respectively.

For in and around of craters of mud volcanoes:

- Both sI and sII hydrates are observed from calculations using CSMHYD. However, sII hydrates are most likely to occur since sI type is observed at high temperature values (from 23 °C to 27 °C) (note: calculations are done up to 30 °C) and high pressure.
- Thickness of GHSZ for mud volcanoes extends for a few tens of meter
- In and around of carters of mud volcanoes, minimum- 3.59×10^9 Sm^3, mean- 1.65×10^{10} Sm^3, and maximum- 5.04×10^{10} Sm^3 of methane is estimated.
- The minimum, mean, and maximum values of total accessible resource volume are estimated as 2.30×10^{12}, 1.64×10^{13}, and 5.32×10^{13}.

This study shows that there is a great gas hydrate potential in the South Caspian Sea. However, it is highly recommended to carry out geophysical surveys targetting the shallow sediments in deep waters of the region.

REFERENCES

Akarsu, E. (2012). Gaz hidrat arama ve araştırma yöntemleri. MTA Doğal Kaynaklar ve Ekonomi Bülteni 14, 35-46. Retrieved on August 8, 2017, from http://www.mta.gov.tr/v3.0/sayfalar/hizmetler/kutuphane/ekonomi-bultenleri/2012_14/MTA_Dogal_Kaynaklar_EmineAKARSU.pdf _EmineAKARSU.pdf.

Aladin, N. & Plotnikov, I. (2004). *The Caspian Sea.* Lake Basin Management Initiative Thematic Paper.

Allahdadi, M. N., Chegini, V., Fotouhi, N. & Golshani, A. (2004). *Wave modeling and hindcast of the Caspian Sea*. 6th International Conference on Coasts, Ports, and Marine Structures.

Amundsen, L., Landra, M. & Reichel, T. (2013). *Gas hydrates part IV: Where are gas hydrates found?*. Retrieved on June 16, 2017, from https://www.geoexpro.com/articles/2013/05/gas-hydrates-part-iv-where-are-gas-hydrates-found.

Arpe, K., Bengtsson, L., Golitsyn, G. S., Mokhov, I. I., Semenov, V. A. & Sporyshev, P. V. (2000). Connection between Caspian Sea level variability and ENSO. *Geophysical Research Letters,* 27(17), 2693-2696. doi:10.1029/1999GL002374.

Ayres, D., Schmutte, J. & Stanfield, J. (2017). Expect the unexpected: Risk assessment using Monte Carlo simulations. *Journal of Accountancy*, 224(5), 42-48.

Bagirov, E. & Lerche, I. (1997). Hydrates represent gas source, drilling hazard, *Oil and Gas Journal,* 95 (48), 99-101.

Bagirov, E., Lerche, I., Bagirov, B. & Mamedova, S. (1999). *Reservoir characteristics for South Caspian oil fields*. Offshore Technology Conference.

Bily, C. & Dick, J. W. L. (1974). Naturally occurring gas hydrates in the Mackenzie Delta, N.W.T. *Bulletin of Canadian Petroleum Geology,* 22(3),340-352.

Birchwood, R., Dai, J., Shelander, D., Boswell, R., Collett, T., Cook, A. & ... Saeki, T. (2010). Developments in gas hydrates. *Oilfield Review,* 22(1), 18-33.

Boswell, R. & Collett, T. S. (2011). Current perspectives on gas hydrate resources. *Energy & Environmental Science,* 4(4), 1206-1215.

Boswell, R., Collett, T., Frye, M., Shedd, W., McConnell, D. R. & Shelander, D. (2012). Subsurface gas hydrates in the Northern Gulf of Mexico. *Marine and Petroleum Geology,* 34(1), 4-30. doi:10.1016/j.marpetgeo.2011.10.003.

Buryakovsky, L. A., Chilingar, G. V. & Aminzadeh, F. (2001). *Petroleum geology of the South Caspian Basin.* [electronic resource]. Boston: Gulf Professional Pub., c2001.

Chatti, I., Delahaye, A., Fournaison, L. & Petitet, J. (2005). Benefits and drawbacks of clathrate hydrates: a review of their areas of interest. *Energy Conversion and Management,* 46(9-10), 1333-1343.

Chong, Z. R., Yang, S. H. B., Babu, P., Linga, P. & Li, X. S. (2016). Review of natural gas hydrates as an energy resource: Prospects and challenges. *Applied Energy,* 162, 1633-1652.

Christie, S., Dubois, R., Zaworotko, M., Rogers, R. & White, P. (1991). Air stable liquid clathrates: Solid state structure and hydrocarbon solubility of organic cation triiodide salts. *Journal of Inclusion Phenomena and Molecular Recognition in Chemistry,* 11(2), 103-114. doi:10.1007/BF01153294.

Clathrate Compound. In Wikiwand. Retrieved on July 20, 2017, from https://www.wikiwand.com/en/Clathrate_compound.

Collett, T. S. (2001). *A review of well-log analysis techniques used to assess gas-hydrate-bearing reservoirs, in natural gas hydrates: Occurrence, distribution, and detection* (eds C. K. Paull and W. P. Dillon), American Geophysical Union, Washington, D. C. doi: 10.1029/GM124p0189.

Collett, T. S., Johnson, A. H., Knapp, C. C. & Boswell, R. (2009). Natural gas hydrates: A review. Natural gas hydrates. A. H. Johnson and C. C. Knapp, Eds. *Energy resource potential and Associated Gelogic Hazards*, 89(1), 146–219.

Collett, T., Lee, M., Zyrianova, M., Mrozewski, S., Guerin, G., Cook, A. & Goldberg, D. (2012). Gulf of Mexico Gas Hydrate Joint Industry Project Leg II logging-while-drilling data acquisition and analysis. *Marine and Petroleum Geology,* 34(1), 41-61. doi:10.1016/j.marpetgeo.2011.08.003.

Croissant, M. P. & Aras, B. (1999). *Oil and geopolitics in the Caspian Sea Region.* Westport, Conn.: Praeger.

CSMHYD. In Centre for Hydrate Research - Colorado School of Mines. Retrieved on December 27, 2017 from http://hydrates.mines.edu/CHR/Software.html.

Dai, J., Snyder, F., Gillespie, D., Koesoemadinata, A. & Dutta, N. (2008). Exploration for gas hydrates in the deepwater, northern Gulf of Mexico: Part I. A seismic approach based on geologic model, inversion, and rock physics principles. *Marine and Petroleum Geology*, 25(9), 830-844.

Devlin, W., Cogswell, J., Gaskins, G., Pitcher, D., Puls, D., Wall, G., Isaksen, G. & Stanley, K. (1999). South Caspian Basin: Young, cool, and full of promise. *GSA Today,* 9(7), X-9.

Diaconescu, C. C. & Knapp, J. H. (2000). Buried gas hydrates in the deepwater of the South Caspian Sea, Azerbaijan: Implications for geo-hazards. *Energy Exploration & Exploitation,* 18(4), 385-400.

Diaconescu, C. C. & Knapp, J. H. (2002). *Gas hydrates of the South Caspian Sea, Azerbaijan: Drilling hazards and sea floor destabilizers*. Proceedings of the Annual Offshore Technology Conference, 393-399.

Diaconescu, C., Knapp, J. & Kieckhefer, R. (2001). Geophysical evidence for gas hydrates in the deep water of the South Caspian Basin, Azerbaijan. *Marine and Petroleum Geology,* 18(2), 209-221. doi:10.1016/S0264-8172(00)00061-1.

Dimitrov, L. I. (2003). Mud volcanoes—a significant source of atmospheric methane. *Geo-Marine Letters,* 23(3-4), 155-161.

Dyadin, Y., Terekhova, I., Rodionova, T. & Soldatov, D. (1999). Half-century history of clathrate chemistry. *Journal of Structural Chemistry,* 40(5), 645-653.

Esin, N., Yanko-Hombach, V. & Esin, N. I. (2016). *Evolutionary mechanisms of the Paratethys Sea and ıts separation into the Black Sea and Caspian Sea*. Quaternary International, doi:10.1016/j.quaint.2016.06.019.

Fathi, K. (2016). *Optimisation of a novel micro-calorimeter through Monte Carlo simulations and thermal analysis for use in particle therapy* (Doctoral Dissertation University of Surrey (United Kingdom)). (Accession No:edsoai.995784967).

Finney, R. L., Giordano, F. R., Thomas, G. B. & Weir, M. D. (2003). *Thomas' calculus.* Boston ; London : Addison-Wesley, c2003.

Fujii, T., Saeki, T., Kobayashi, T., Inamori, T., Hayashi, M., Takano, O., Takayama, T., Kawasaki, T., Nagakubo, S., Nakamizu, M. & Yokoi, K. (2008). *Resource assessment of methane hydrate in the eastern Nankai Trough, Japan.* In Offshore technology conference. Offshore Technology Conference.

Gerivani, H. & Gerivani, B. (2015). Potential map of gas hydrate formation in Caspian Sea based on physicochemical stability evaluation of methane hydrate. *Marine Georesources and Geotechnology,* 35(1), 136-142. doi:10.1080/1064119X.2015.1118581.

Ginsburg, G.D., Ivanov, V.L., Soloviev, V.A. (1984). Natural gas hydrates of the World's Oceans. In: Oil and gas content of the World's Oceans. PGO Sevmorgeologia, pp. 141–158 (in Russian).

Ginsburg, G. D. & Soloviev, V. A. (1994). Mud volcano gas hydrates in the Caspian Sea. *Bulletin of the Geological Society of Denmark*, 41(95), 100.

Ginsburg, G. D., Guseynov, R. A., Dadashev, A. A., Ivanova, G. A., Kazantsev, S. A., Solov'yev, V. A., ... & Mashirov, Y. G. (1992). Gas hydrates of the southern Caspian. *International Geology Review,* 34(8), 765-782.

Guerin, G., Goldberg, D., & Meltser, A. (1999). Characterization of in situ elastic properties of gas hydrate-bearing sediments on the Blake Ridge. Journal of Geophysical Research: Solid Earth, 104(B8), 17781-17795.

Herbstein, F. (2005). Crystalline molecular complexes and compounds: Structures and principles. Oxford University Press. doi:10.1093/acprof:oso/9780198526605.001.0001.

Hesse, R., & Harrison, W. E. (1981). Gas hydrates (clathrates) causing pore-water freshening and oxygen isotope fractionation in deep-water sedimentary sections of terrigenous continental margins. Earth and Planetary Science Letters, 55(3), 453-462.

Huseynov, D. A. & Guliyev, I. S. (2004). Mud volcanic natural phenomena in the South Caspian Basin: geology, fluid dynamics, and environmental impact. *Environmental Geology,* 46(8), 1012-1023.

Hyndman, R. & Spence, G. (1992). A seismic study of methane hydrate marine bottom simulating reflectors. *Journal of Geophysical Research-Solid Earth,* 97(B5), 6683-6698.

Hyndman, R.,Yuan, T. & Moran, K. (1999). The concentration of deep sea gas hydrates from downhole electrical resistivity logs and laboratory data. *Earth and Planetary Science Letters,* 172(1-2), 167-177. doi:10.1016/S0012-821X(99)00192-2.

Ibrayev, R. A., Özsoy, E., Schrum, C. & İ.Sur, H. (2009). Seasonal variability of the Caspian Sea three-dimensional circulation, sea level and air-sea interaction. *Ocean Science Discussions,* 6(4), 1913.

IUPAC. (1997).Compendium of Chemical Terminology, 2nd ed. (the "Gold Book"). Compiled by A. D. McNaught and A. Wilkinson. Blackwell Scientific Publications, Oxford.

Jeffrey, G. (1984). Hydrate inclusion compounds. *Journal of Inclusion Phenomena,* 1(3), 211-222. doi:10.1007/BF00656757.

Kakroodi, A. A., Leroy, S. A. G., Kroonenberg, S. B., Lahijani, H. A. K., Alimohammadian, H., Boomer, I. & Goorabi, A. (2015). Late Pleistocene and Holocene sea-level change and coastal paleoenvironment evolution along the Iranian Caspian shore. *Marine Geology*, 361, 111-125.

Kastner, M., Kvenvolden, K. A. & Lorenson, T. D. (1998). Chemistry, isotopic composition, and origin of a methane-hydrogen sulfide hydrate at the Cascadia subduction zone. *Earth and Planetary Science Letters,* 156(3), 173-183.

Kim, D., Park, Y. & Lee, H. (2007). Tuning clathrate hydrates: Application to hydrogen storage. *Catalysis Today,* 120(3-4 SPEC. ISS.), 257-261. doi: 10.1016/j.cattod.2006.09.001.

Kioka, A. & Ashi, J. (2015). Episodic massive mud eruptions from submarine mud volcanoes examined through topographical signatures. *Geophysical Research Letters,* 42(20), 8406-8414.

Khitarov, N. I. and Pugin, V. A. (1966). Montmorillonite under conditions of increased temperature and pressure: Moscow, Geochemistry, No. 7, pp. 790-795.

Klige, R. K. & Myagkov, M. S. (1992). Changes in the water regime of the Caspian Sea. *Geojournal*, (3), 299.

Knapp, C. C., Knapp, J. H. & Duff, P. (2005). *South Caspian Sea: A unique setting to evaluate proposed mechanisms for Late-Pleistocene large-scale submarine slope failure.* AGU, Dec.

Kosarev, A. N. (2005). *Physico-geographical conditions of the Caspian Sea.* In, The Caspian Sea Environment (pp. 5-31). Springer Berlin Heidelberg.

Krey, V., Canadell, J. G., Nakicenovic, N., Abe, Y., Andruleit, H., Archer, D., ... & Lamarque, J. F. (2009). Gas hydrates: entrance to a methane age or climate threat?. *Environmental Research Letters,* 4(3), 034007.

Kvenvolden, K. (1988a). A primer on the geological occurrence of gas hydrate. doi:10.1144/GSL.SP.1998.137.01.02 .

Kvenvolden, K. A (1988b). Methane hydrate - a major reservoir of carbon in the shallow geosphere?. *Chemical Geology, 71*(1-3), 41-51. doi:10.1016/0009-2541(88)90104-0.

Kvenvolden, K. A (1993). Gas hydrates—geological perspective and global change. *Reviews of Geophysics,* 31(2), 173-187. doi:10.1029/93RG00268.

Kvenvolden K. A (1999). Potential Effects of Gas Hydrate on Human Welfare. Proceedings Of The National Academy Of Sciences Of The United States Of America, (7), 3420.

Kvenvolden, K. A. (2002). Methane hydrate in the global organic carbon cycle. *Terra Nova,* 14(5), 302-306.

Kvenvolden, K. A. & Claypool, G. E. (1988). *Gas hydrates in oceanic sediment.* Department of the Interior U.S. Geological Survey. Open-File Report, 88-216.

Kvenvolden, K. A. & Lorenson, T. D. (2001). *The global occurrence of natural gas hydrate.* Natural Gas Hydrates: Occurrence, Distribution, and Detection, 3-18.

Laherrere, J. (2000). Oceanic hydrates: More questions than answers. *Energy Exploration & Exploitation*, 18(4), 349-383.

Lognormal Distribution (a). In Statistics How To. Retrieved on November 27, 2017, from http://www.statisticshowto.com/lognormal-distribution.

Lognormal Distribution (b). In Wikiwand. Retrieved on November 27, 2017, from https://www.wikiwand.com/en/Log-normal_distribution.

MacDonald, G. J. (1990). The future of methane as an energy resource. *Annual Review of Energy*, 15(1), 53-83.

Mackay, M., Jarrard, R., Westbrook, G. & Hyndman, R. (1994). Origin of bottom simulating reflectors - geophysical evidence from the Cascadia accretionary prism. *Geology,* 22(5), 459-462.

Magara, K. (1982). Compaction of Rocks and Migration of Fluids. Applied Petroleum Geology (translated from English): Moscow, Nedra Publishing House, 296 pp.

Mahajan, D., Taylor, C. & Mansoori, G. (2007). An introduction to natural gas hydrate/clathrate: The major organic carbon reserve of the Earth. *Journal of Petroleum Science and Engineering*, 56(1-3), 1-8. doi:10.1016/j.petrol.2006.09.006.

Makogon, I. F. (1997). *Hydrates of hydrocarbons*. Tulsa, Okla.: PennWell Books, c1997.

Map of the Caspian Sea with the Neighboring States. Retrieved on December 4, 2017, from http://www.alamy.com/stock-photo-map-of-the-caspian-sea-with-the-neighboring-states-99511038.html.

Masuda, Y., Yamamoto, K., Tadaaki, S., Ebinuma, T. & Nagakubo, S. (2018). Japan's methane hydrate R&D program progresses to phase 2. *Natural Gas & Oil,* 304(2018), 285-4541.

Mathews, M. (1986). Logging characteristics of methane hydrate. *The Log Analyst*, 27(3), 26-63.

Max, M. D. (2003). *Natural gas hydrate. [electronic resource]: in oceanic and permafrost environments*. Dordrecht; Boston: Kluwer Academic Publishers, c2003.

Mayes, D. S. (1963). *Use of Werner complexes for the clathration-separation of organic mixtures*. 6th World Petroleum Congress.

Merey, S. & Sinayuc, C. (2016). Investigation of gas hydrate potential of the Black Sea and modelling of gas production from a hypothetical Class 1 methane hydrate reservoir in the Black Sea conditions. *Journal of Natural Gas Science and Engineering,* 2966-79. doi:10.1016/j.jngse.2015.12.048.

Milkov, A. V. & Sassen, R. (2002). Economic geology of offshore gas hydrate accumulations and provinces. *Marine and Petroleum Geology,* 19(1), 1-11.

Milkov, A. V. (2000). Worldwide distribution of submarine mud volcanoes and associated gas hydrates. Marine Geology, 167(1-2), 29-42.

Milkov, A. V. (2004). Global estimates of hydrate-bound gas in marine sediments: How much is really out there?. *Earth-Science Reviews, 66*(3), 183-197.

Millero, F., Chen, C., Bradshaw, A. and Schleicher, K. (1980). A new high pressure equation of state for seawater. Deep Sea Research Part I: *Oceanographic Research Papers,* 27, 255–264.

Monte Carlo Method. In Wikiwand. Retrieved on November 21, 2017, from https://www.wikiwand.com/en/Monte_Carlo_method#/Definitions.

Moudrakovski, I., Sanchez, A., Ratcliffe, C. & Ripmeester, J. (2001). Nucleation and growth of hydrates on ice surfaces: New insights from 129Xe NMR experiments with hyperpolarized xenon. *Journal of Physical Chemistry B,* 105(49), 12338-12347. doi:10.1021/jp012419x.

Muradov, ChS (2002) Estimation of resources of gas in gas hydrate accumulations of Southern Caspian Sea. In: Abstract book of 7th International Conference ''Gas in Marine Sediments'', October 7–12. Nafta-Press, Baku, pp 149–150

Normal Distribution (a). In Engineering Statistics Hanbook. Retrieved on November 26, 2017, from http://www.itl.nist.gov/div898/handbook/eda/section3/eda3661.htm.

Normal Distribution (b). In Online Statistics Education: A Multimedia Course of Study. Retrieved on November 27, 2017, from http://onlinestatbook.com.

Normal Distribution (c). In Wikiwand. Retrieved on November 26, 2017, from.

Ocean Water Density Calculator. In CSGNetwork. Retrieved on December 10, 2017, from http://www.csgnetwork.com/water_density_calculator.html.

Ors, O. (2012). *Investigation of the interaction of the CO_2 and CH4 Hydrate for the Determination of Feasibility of CO_2 Storage in the Black Sea Sediments (MSc Thesis).* Retrieved from METU Library Database (Accession No: metu.b2206803).

Parlaktuna, M. & Erdogmus, T. (2001). Natural Gas Hydrate Potential of the Black Sea. *Energy Sources*, 23(3), 203. doi:10.1080/00908310151133861.

Popescu, I., De Batist, M., Lericolais, G., Nouzé, H., Poort, J., Panin, N., Versteeg, W. & Gillet, H. (2006). Multiple bottom-simulating reflections in the Black Sea: Potential proxies of past climate conditions. *Marine Geology,* 227(3), 163-176.

Probability Density Function. In Stat Trek. Retrieved on November 25, 2017, from http://stattrek.com/statistics/dictionary.aspx?definition=Probability%20density%20function.

Riedel, M., Spence, G., Chapman, N. & Hyndman, R. (2002). Seismic investigations of a vent field associated with gas hydrates, offshore Vancouver Island. *Journal of Geophysical Research B: Solid Earth,* 107(9), 5-1.

Ripmeester, J. A., Tse, J. S., Ratcliffe, C. I. & Powell, B. M. (1987). A new clathrate hydrate structure. *Nature,* 325(6100), 135-136. doi:10.1038/325135a0.

Rodionov, S. N. (1994). *Global and regional climate interaction: The Caspian Sea experience.* Dordrecht; Boston: Kluwer Academic, c1994.

Ryu, B., Riedel, M., Kim, J., Hyndman, R. D., Lee, Y., Chung, B. & Kim, I. (2009). *Gas hydrates in the western deep-water Ulleung Basin, East Sea of Korea.* Marine and Petroleum Geology, 261483-1498. doi: 10.1016/j.marpetgeo.2009.02.004.

Senger, K., Bünz, S. & Mienert, J. (2010). First-order estimation of in-place gas resources at the Nyegga gas hydrate prospect. *Norwegian Sea. Energies,* 3(12), 2001-2026.

Sha, Z., Liang, J., Zhang, G., Yang, S., Lu, J., Zhang, Z., ... & Humphrey, G. (2015). A seepage gas hydrate system in northern South China Sea: Seismic and well log interpretations. Marine Geology, 366, 69-78.

Sloan, E. D. & Koh, C. A. (2008). *Clathrate hydrates of natural gases*. Boca Raton, FL: CRC Press, c2008.

Sloan, E. D. (1991). Natural Gas Hydrates. *Society of Petroleum Engineers*. doi:10.2118/23562-PA.

Sloan, E. D. (2003). Fundamental principles and applications of natural gas hydrates. *Nature,* 426(6964), 353-359. doi:10.1038/nature02135.

Sloan, E.D. (1990). *Clathrate hydrates of natural gases,* Marcel Dekker, NY, 641 pp.

Statistical Concepts in Risk Analysis. In Petrowiki. Retrieved on November 25, 2017, from http://petrowiki.org/Statistical_concepts_in_risk_analysis.

Strobel, T., Hester, K., Koh, C., Sum, A. & Sloan, E. D. (2009). Properties of the clathrates of hydrogen and developments in their applicability for hydrogen storage. *Chemical Physics Letters,* 478(4-6), 97-109. doi: 10.1016/j.cplett.2009.07.030.

Sum, A. K., Koh, C. A. & Sloan, E. D. (2009). Clathrate hydrates: From laboratory science to engineering practice. *Industrial and Engineering Chemistry Research,* 48(16), 7457-7465. doi:10.1021/ie900679m.

Tamura-Wicks, H. M. (2015). *Sensitivity study of Caspian Sea ice* (Doctoral dissertation). Retrieved from METU Library Database (Accession No: edsble.682089).

Tohidi, B., Anderson, R., Chapoy, A., Yang, J. & Burgass, R. W. (2012). Do we have new solutions to the old problem of gas hydrates?. *Energy & Fuels*, 26(7), 4053-4058.

Triangular Distribution (a). In Statistics Learning Centre. Retrieved on November 28, 2017, from https://learnandteachstatistics.files.wordpress.com/2013/07/notes-on-triangle-distributions.pdf.

Triangular Distribution (b). In Wikiwand. Retrieved on November 27, 2017, from https://www.wikiwand.com/en/Triangular_distribution.

Trofimuk, A., Chersky, N. & Tsaryov, V. (1977). Chapter 52: *The role of continental glaciation and hydrate formation on petroleum occurrence.* The Future Supply of Nature-Made Petroleum and Gas Technical Reports, 919-926. doi:10.1016/B978-0-08-021735-2.50062-8.

Tsuji, Y. (2003). *Assessment of the resource potential of methane hydrate in the Nankai Trough, offshore Central Japan, Fire in ice: Implications for energy development and the carbon cycle?*. Workshop Proceedings.

Tuzhilkin, V. S. & Kosarev, A. N. (2005). *Thermohaline structure and general circulation of the caspian sea waters*. In, The Caspian Sea Environment (p. 33). doi:10.1007/698_5_003.

Uchida, T., Takeya, S., Wilson, L., Tulk, C., Ripmeester, J., Nagao, J., Ebinuma, T. & Narita, H. (2003). Measurements of physical properties of gas hydrates and in situ observations of formation and decomposition processes via Raman spectroscopy and X-ray diffraction. *Canadian Journal of Physics*, 81(1-2), 351-357.

Uniform Distribution (a). In Engineering Statistics Handbook. Retrieved on April 3, 2018, from.

Uniform Distribution (b). In Investopedia. Retrieved on April 3, 2018, from https://www.investopedia.com/terms/u/uniform-distribution.asp.

Urea. In Wikiwand. Retrieved on July 20, 2017, from https://www.wikiwand.com/en/Urea.

Woller, J. (1996). *The basics of Monte Carlo simulations. Physical Chemistry Lab, Spring:* University of Nebraska–Lincoln.

Yamamoto, K. (2014). *Overview and introduction: Pressure core sampling and analyses in the 2012e2013 MH21 offshore test of gas production from methane hydrates in the eastern Nankai Trough*. Marine and Petroleum Geology, 6614p. doi: 10.1016/j.marpetgeo.2015.02.024.

Ye, Y., & Liu, C. (2013). *Natural Gas Hydrates*. [electronic resource]: Experimental techniques and their applications. Berlin, Heidelberg: Springer Berlin Heidelberg: Imprint: Springer, 2013.

Yusifov, M. & Rabinowitz, P. D. (2004). Classification of mud volcanoes in the South Caspian Basin, offshore Azerbaijan. *Marine and Petroleum Geology*, 21(8), 965-975.

Yusifov, M., & Rabinowitz, P. (2003). *Seismic interpretation and classification of mud volcanoes of the South Caspian Basin,* offshore Azerbaijan. Offshore Technology Conference.

Zou, C. (2014). *1.9 Unconventional petroleum geology*. In, Unconventional Petroleum Geology Elsevier.

@RISK. In Palisade. Retreived on April 5, 2018 from http://www.palisade.com/risk/.

APPENDICES

Appendix A

A: 1 Thickness of GHSZ for Concentrated and Bearing Zones

Temperature-depth diagrams of composition-1, 2, and 3 according to low and high geothermal gradient are displayed in Figure A.1 to Figure A.18 for pure and saline water environments.
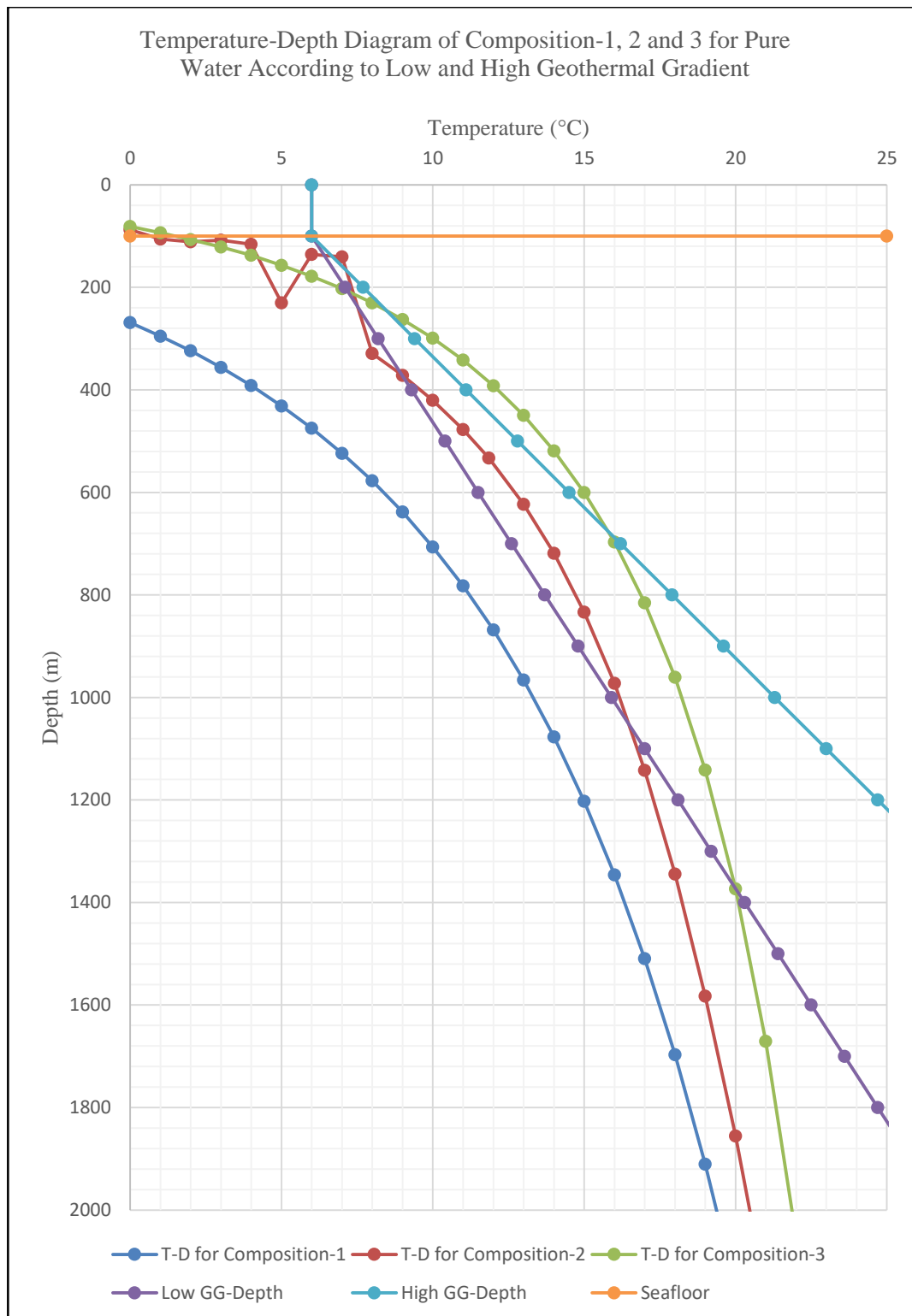
Figure A-1: Temperature-depth diagram of Composition-1, 2, and 3 for pure water case according to low and high geothermal gradient. Seafloor is at 100 m.
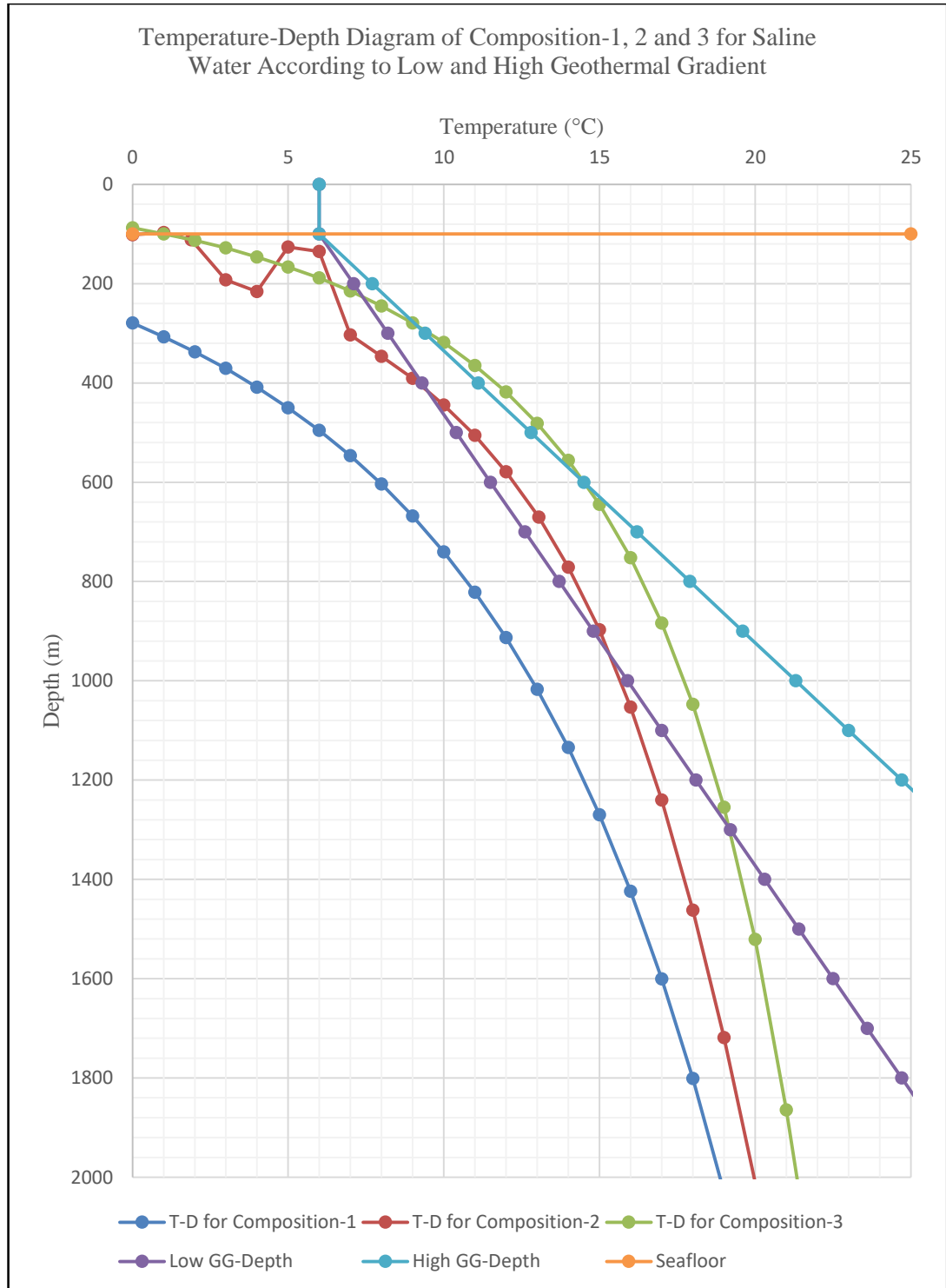
Figure A-2: Temperature-depth diagram of Composition-1, 2, and 3 for saline water case according to low and high geothermal gradient. Seafloor is at 100 m.
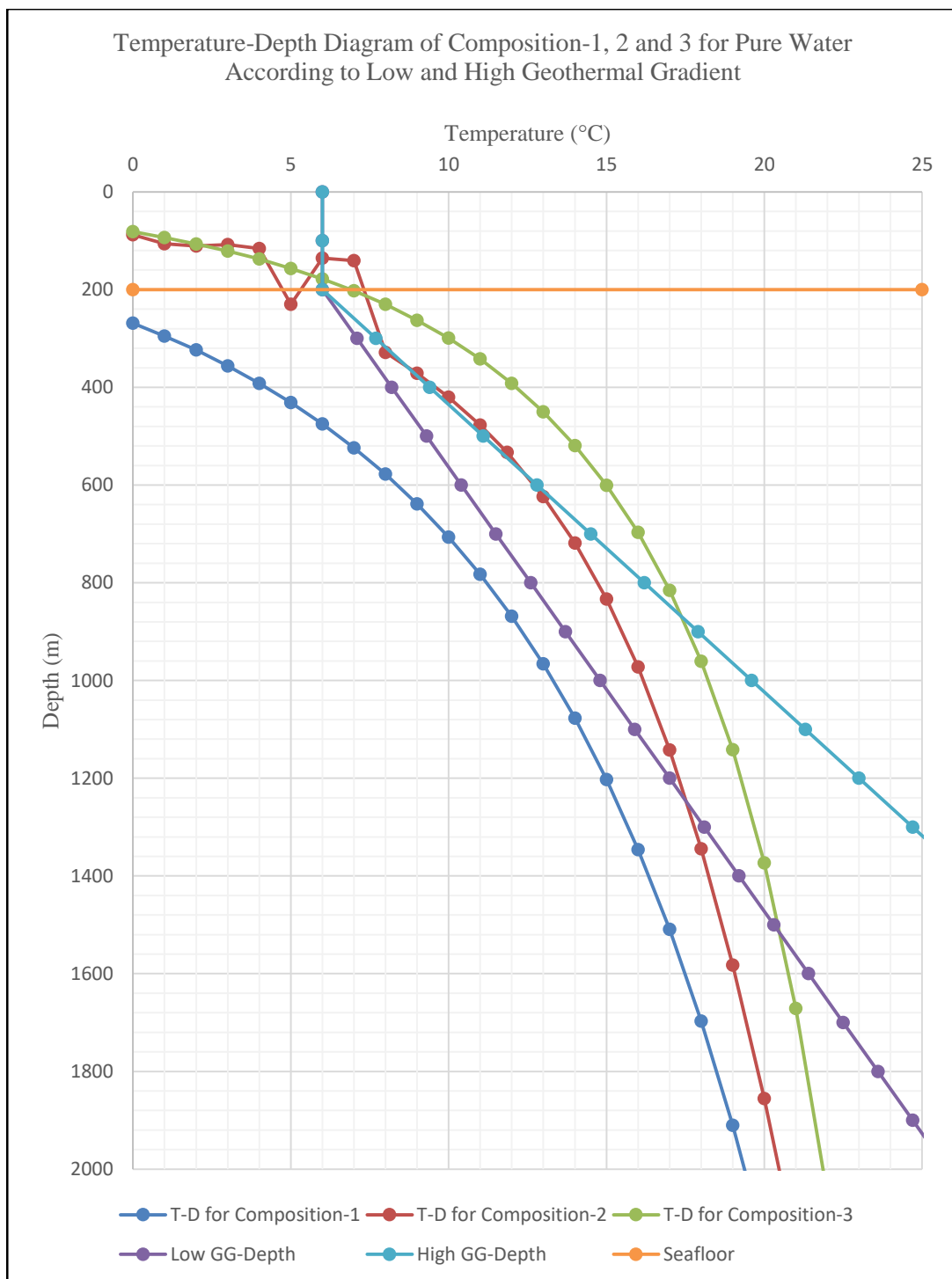
Figure A-3: Temperature-depth diagram of Composition-1, 2, and 3 for pure water case according to low and high geothermal gradient. Seafloor is at 200 m.
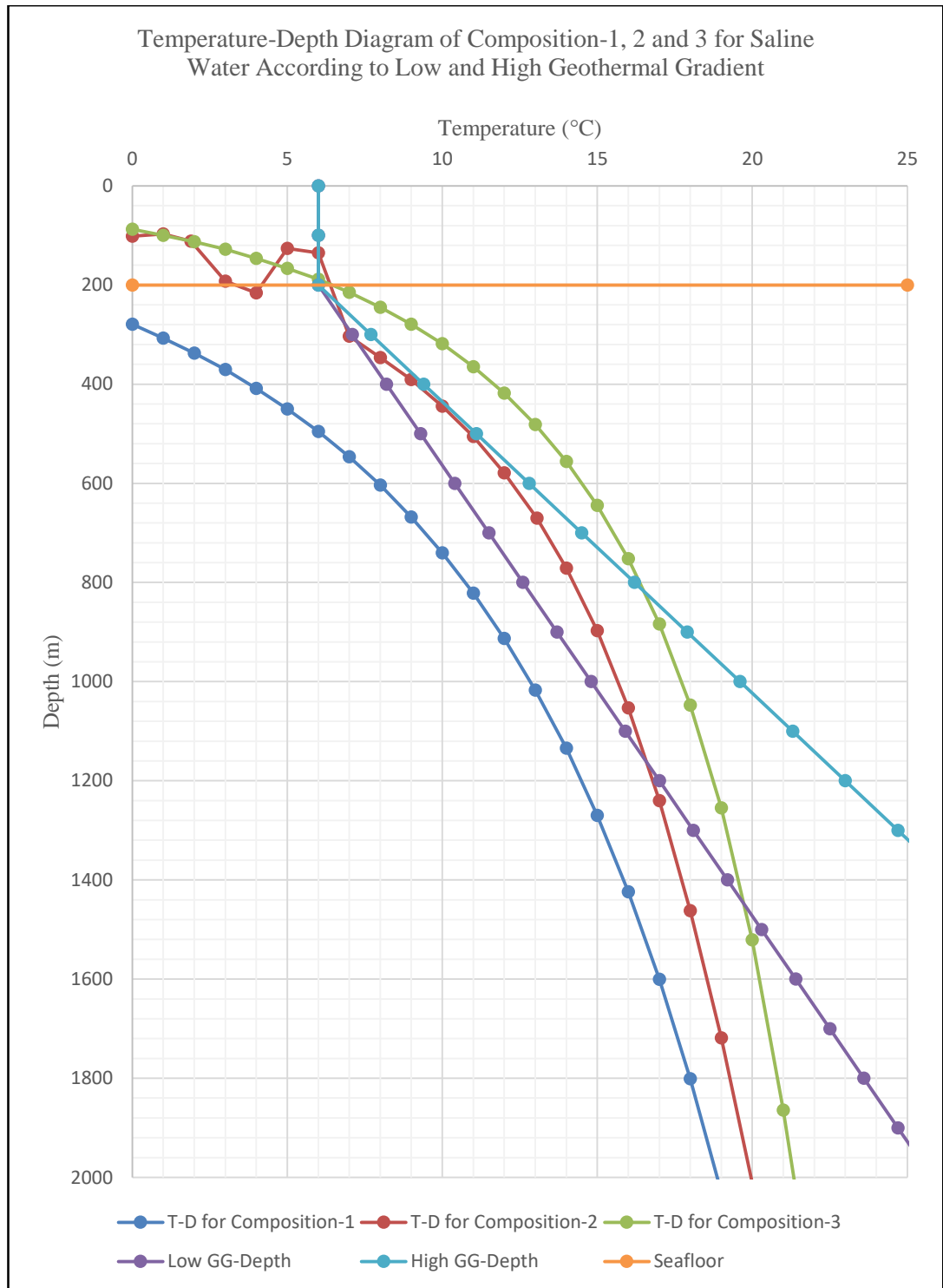
Figure A-4: Temperature-depth diagram of Composition-1, 2, and 3 for saline water case according to low and high geothermal gradient. Seafloor is at 200 m.
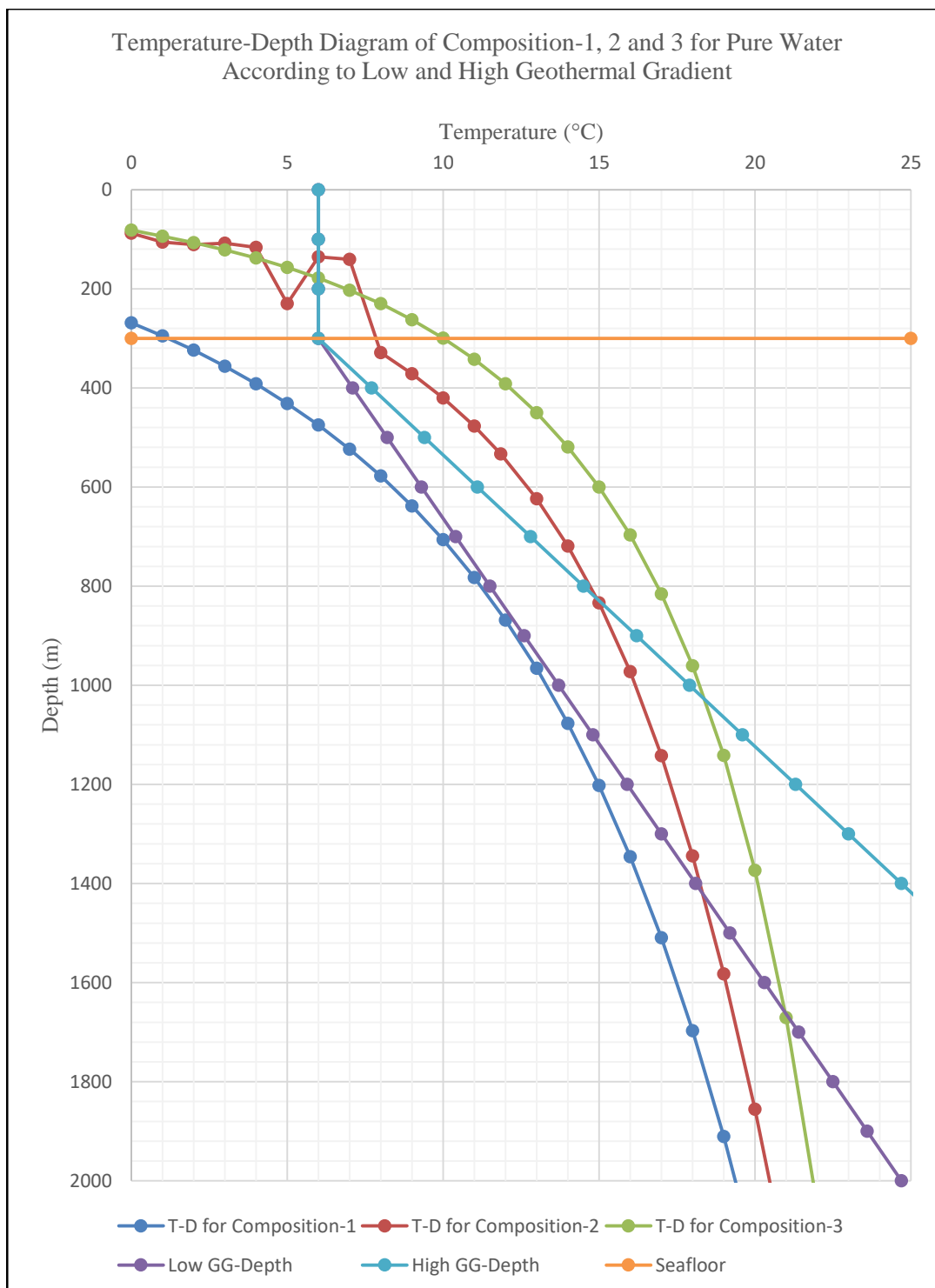
Figure A-5: Temperature-depth diagram of Composition-1, 2, and 3 for pure water case according to low and high geothermal gradient. Seafloor is at 300 m.
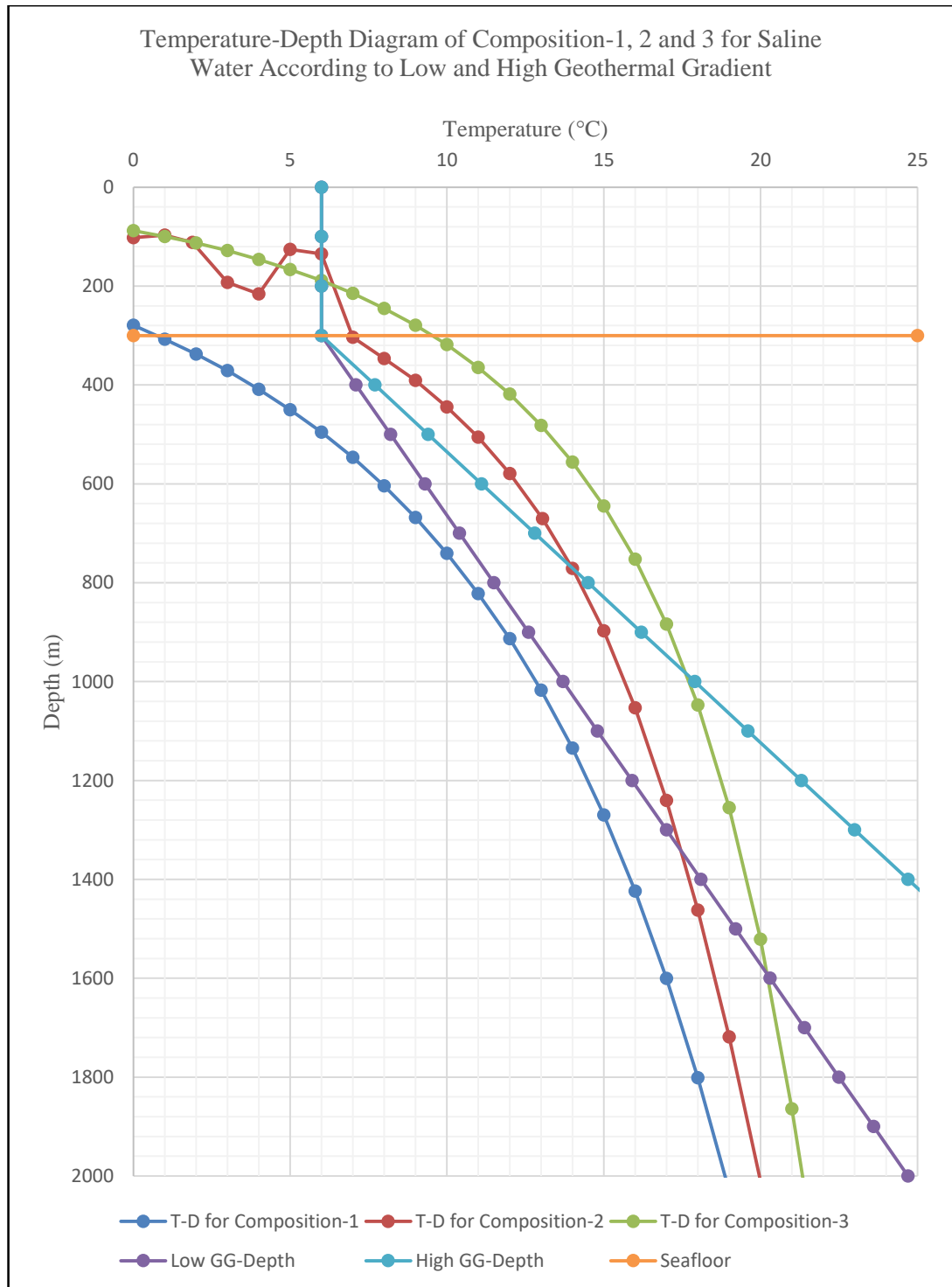
Figure A-6: Temperature-depth diagram of Composition-1, 2, and 3 for saline water case according to low and high geothermal gradient. Seafloor is at 300 m.
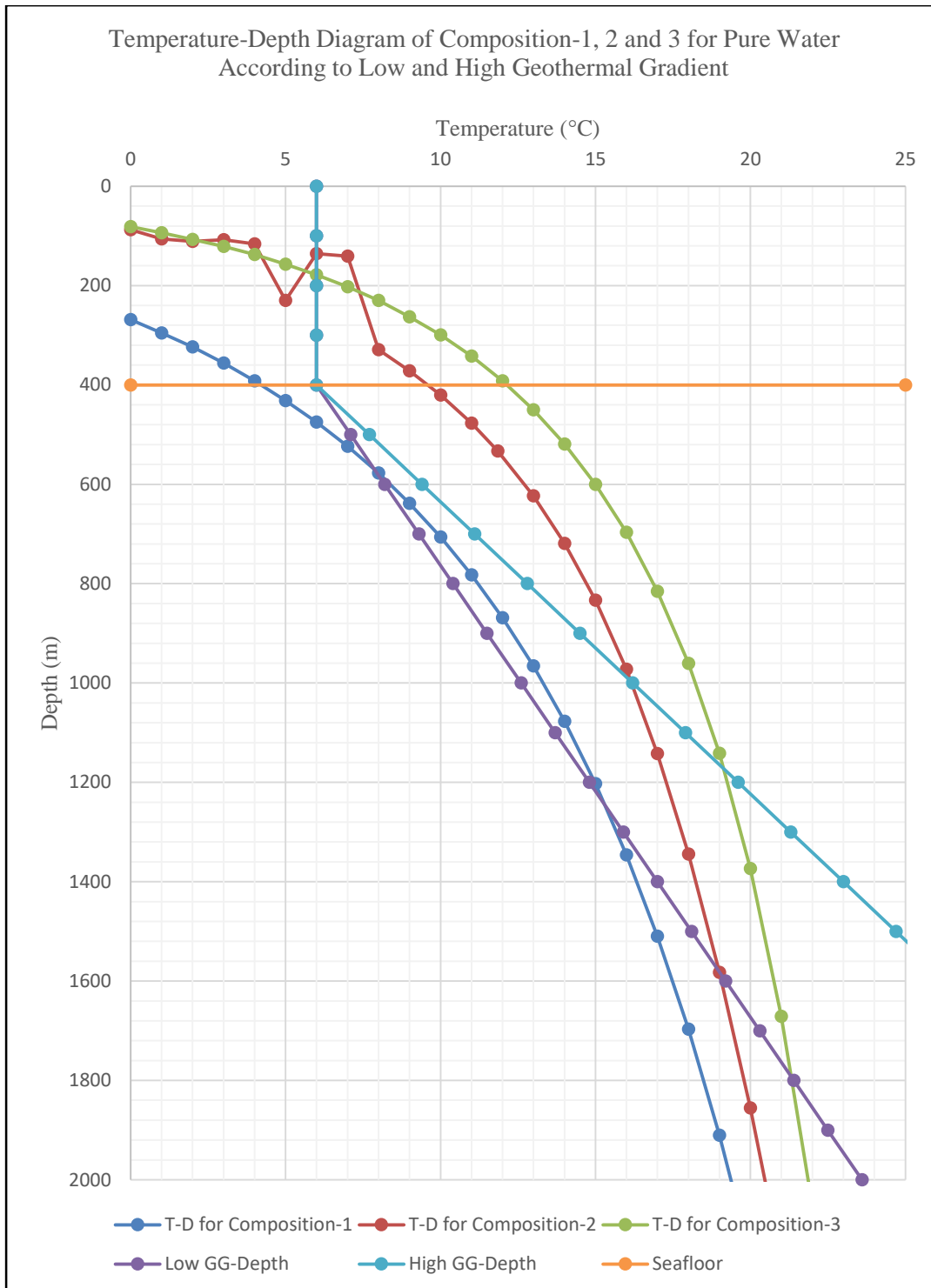
Figure A-7: Temperature-depth diagram of Composition-1, 2, and 3 for pure water case according to low and high geothermal gradient. Seafloor is at 400 m.
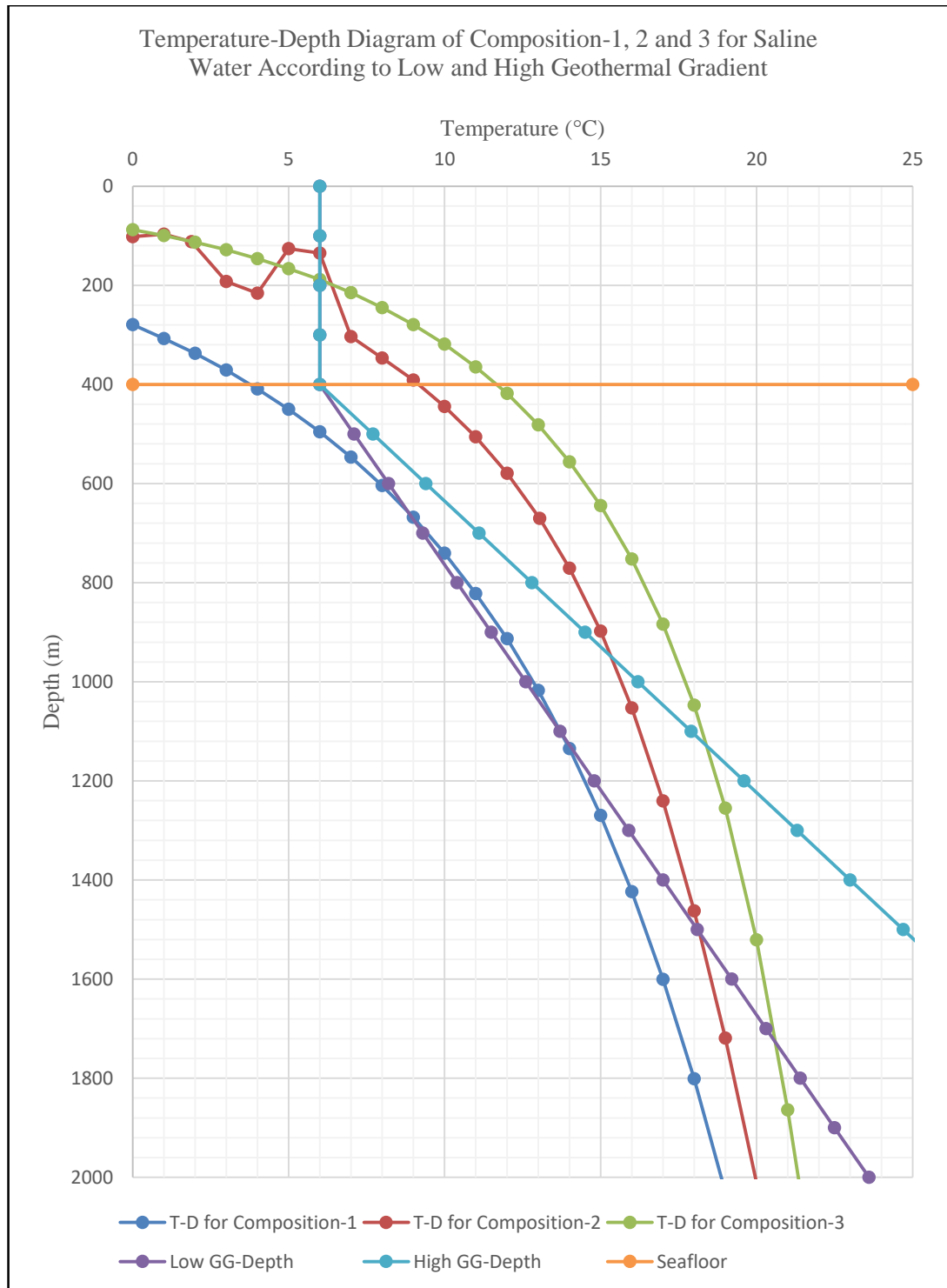
Figure A-8: Temperature-depth diagram of Composition-1, 2, and 3 for saline water case according to low and high geothermal gradient. Seafloor is at 400 m.
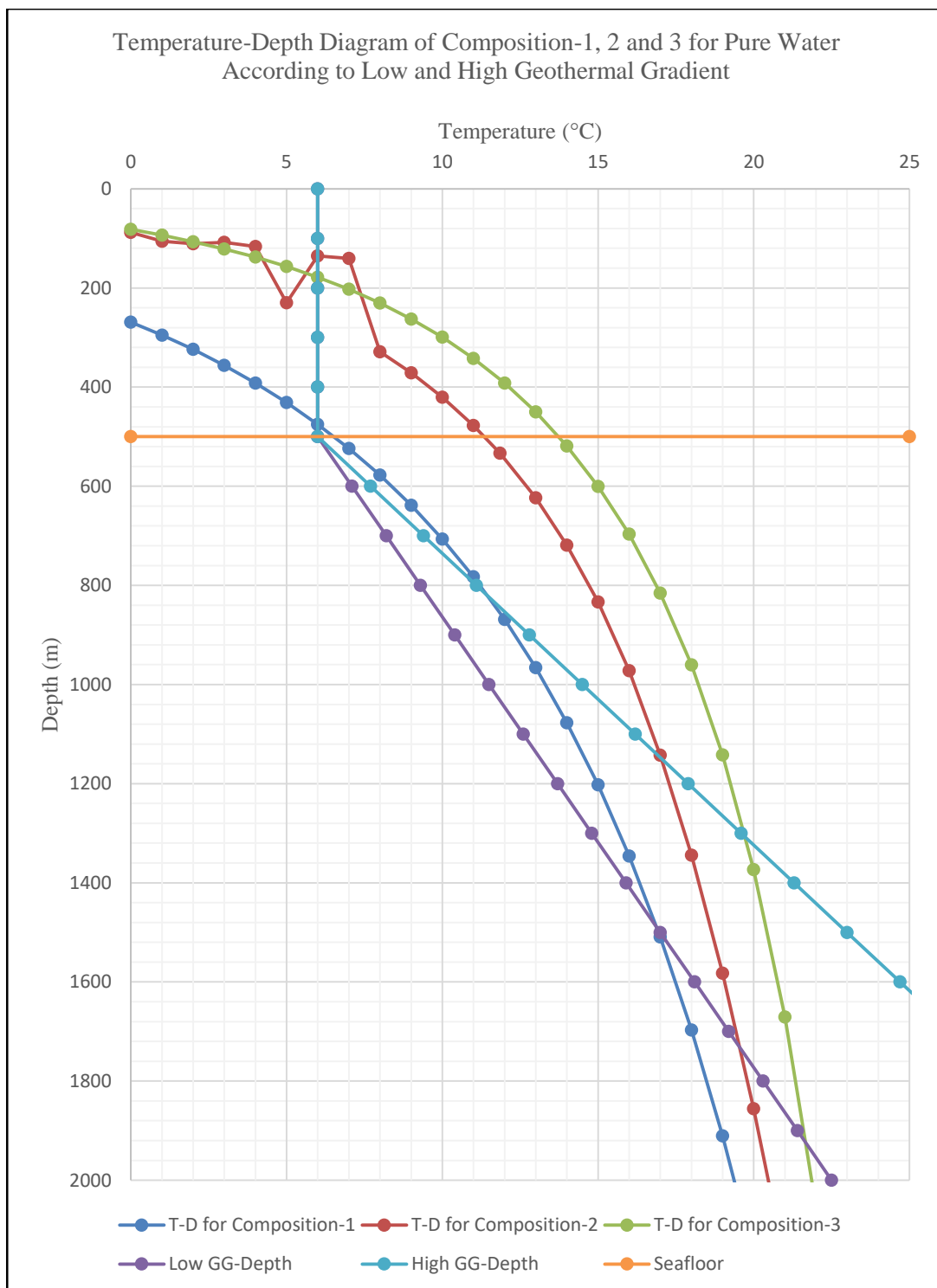
Figure A-9: Temperature-depth diagram of Composition-1, 2, and 3 for pure water case according to low and high geothermal gradient. Seafloor is at 500 m.
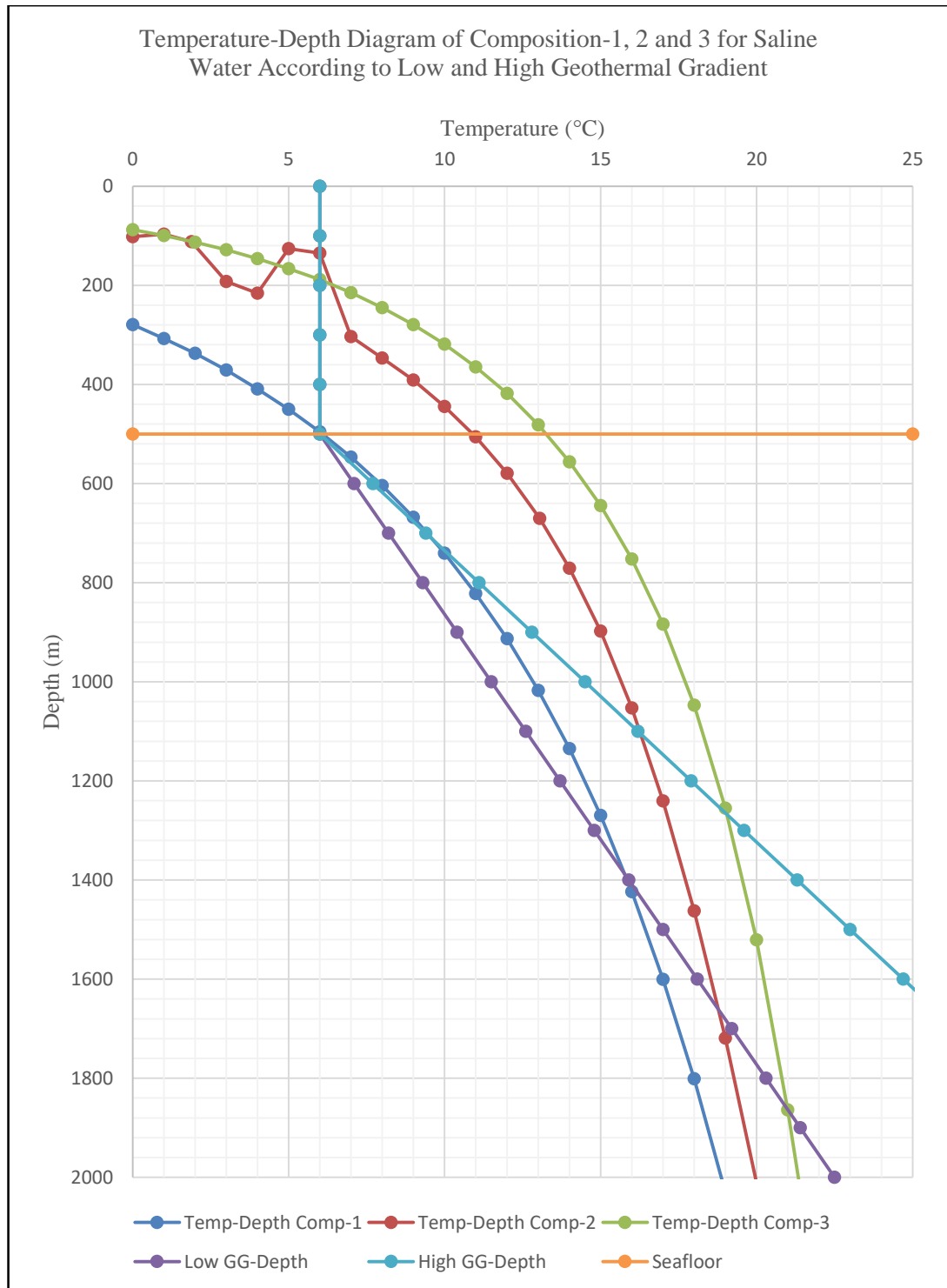
Figure A-10: Temperature-depth diagram of Composition-1, 2, and 3 for saline water case according to low and high geothermal gradient. Seafloor is at 500 m.
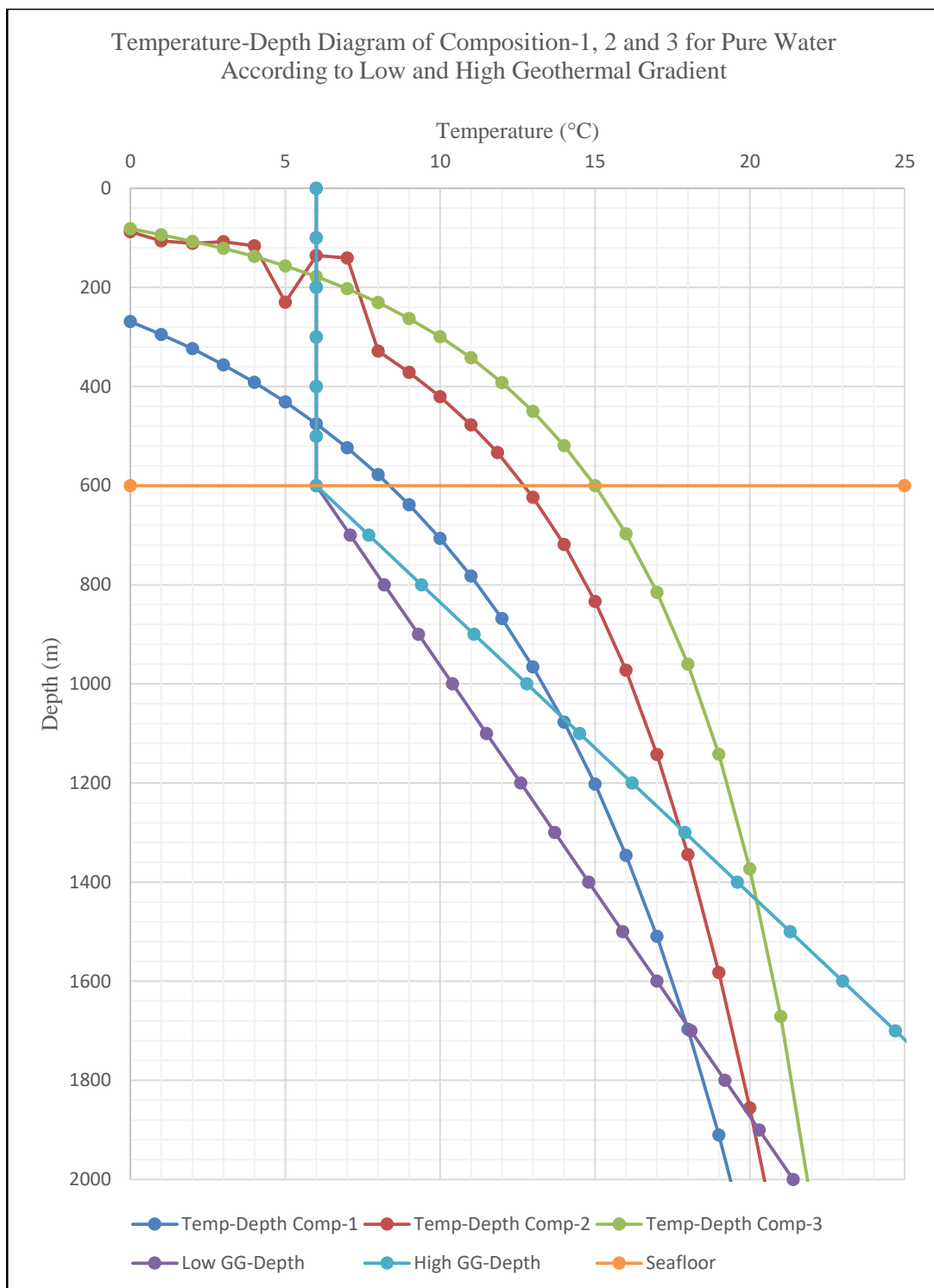
Figure A-11: Temperature-depth diagram of Composition-1, 2, and 3 for pure water case according to low and high geothermal gradient. Seafloor is at 600 m.
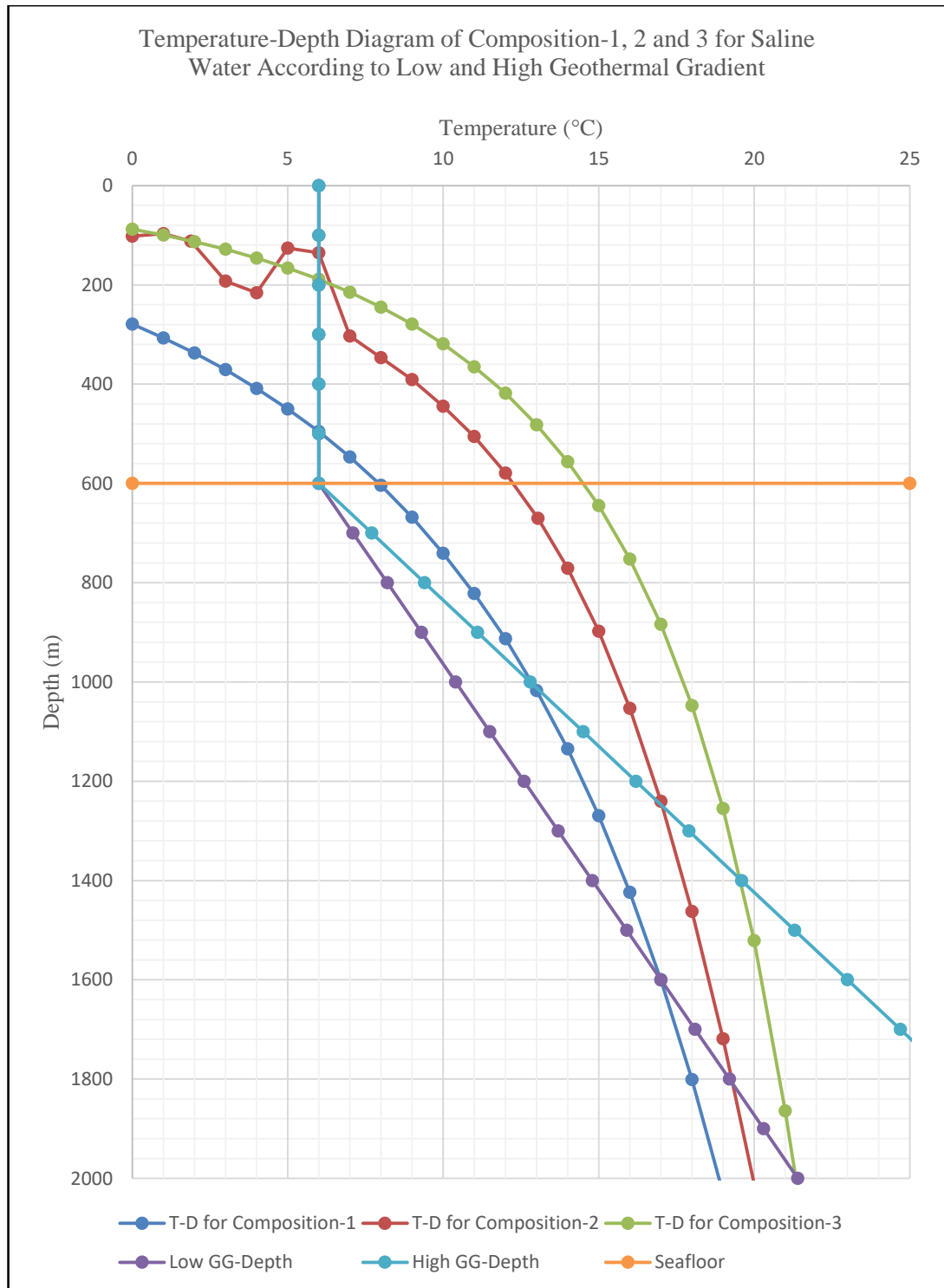
Figure A-12: Temperature-depth diagram of Composition-1, 2, and 3 for saline water case according to low and high geothermal gradient. Seafloor is at 600 m.
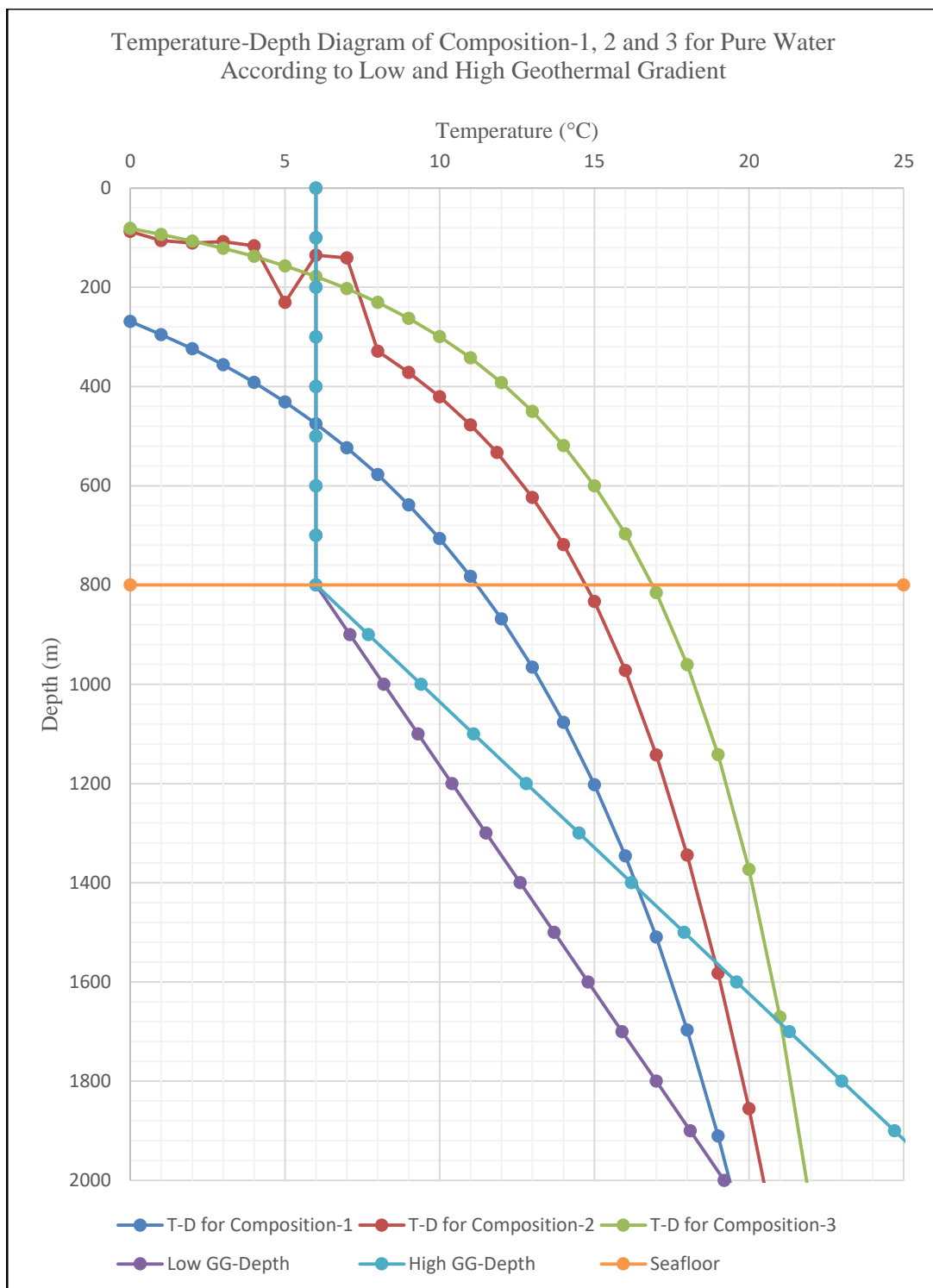
Figure A-13: Temperature-depth diagram of Composition-1, 2, and 3 for pure water case according to low and high geothermal gradient. Seafloor is at 800 m.
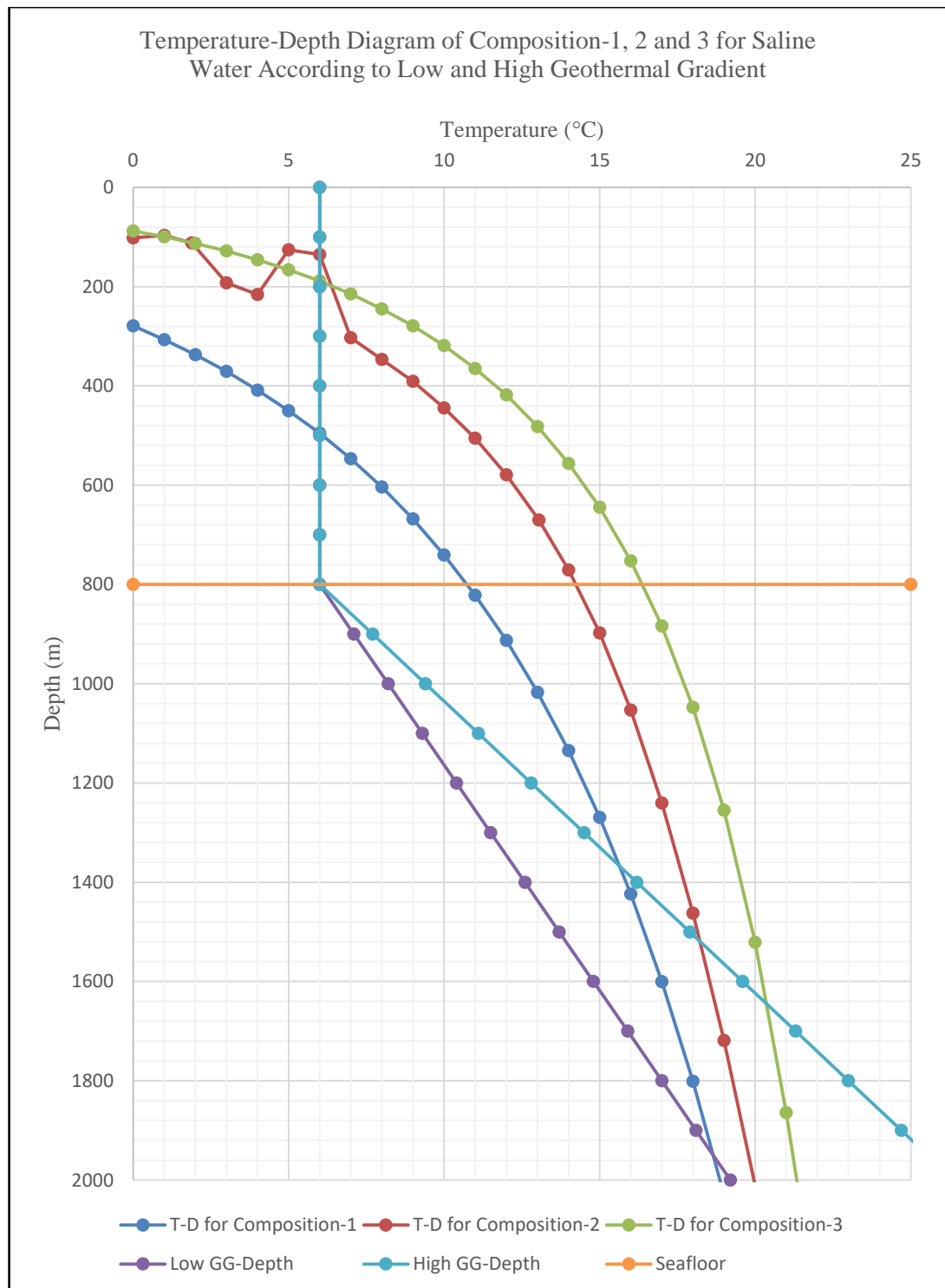
Figure A-14: Temperature-depth diagram of Composition-1, 2, and 3 for saline water case according to low and high geothermal gradient. Seafloor is at 800 m.
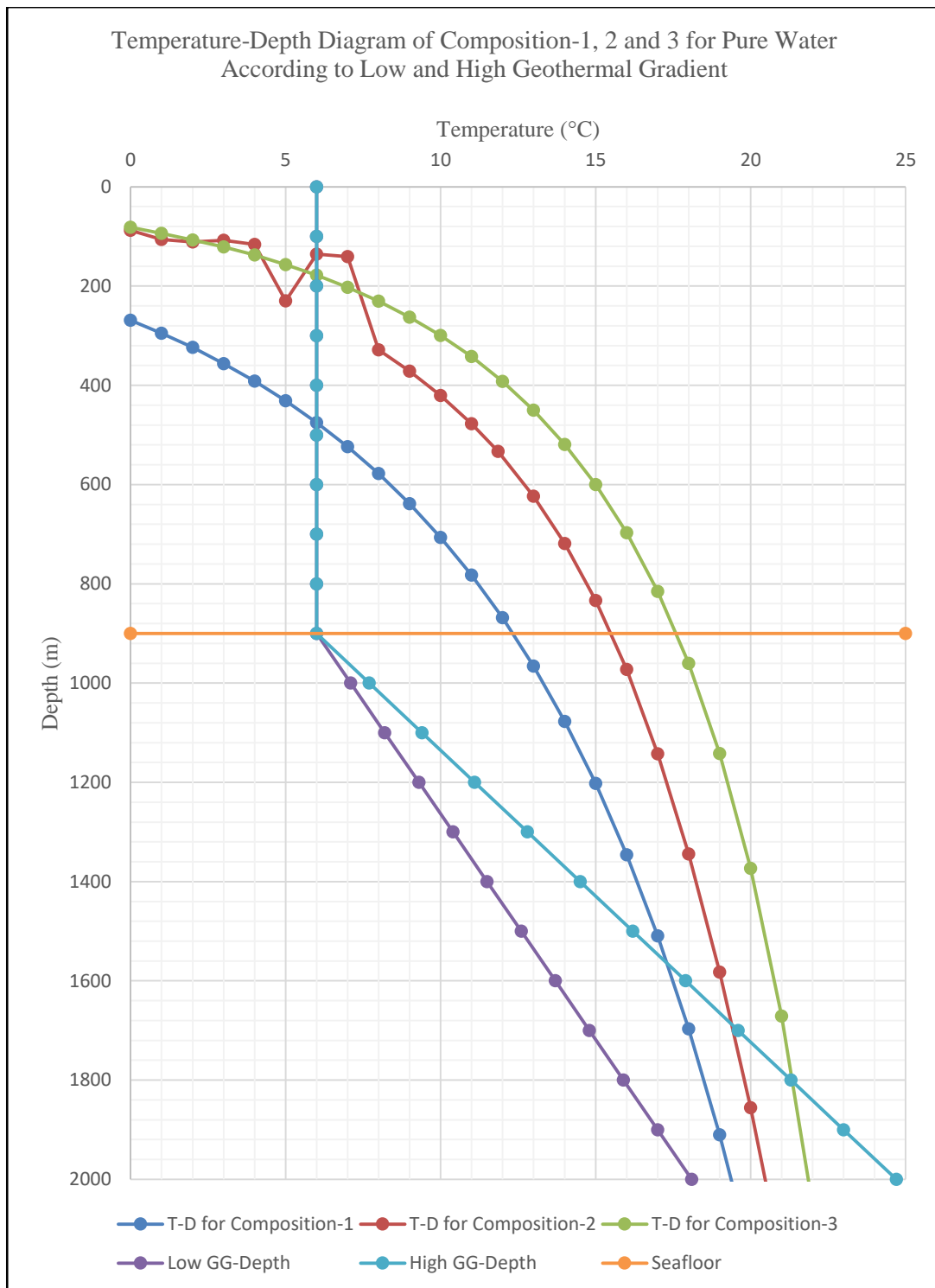
Figure A-15: Temperature-depth diagram of Composition-1, 2, and 3 for pure water case according to low and high geothermal gradient. Seafloor is at 900 m.
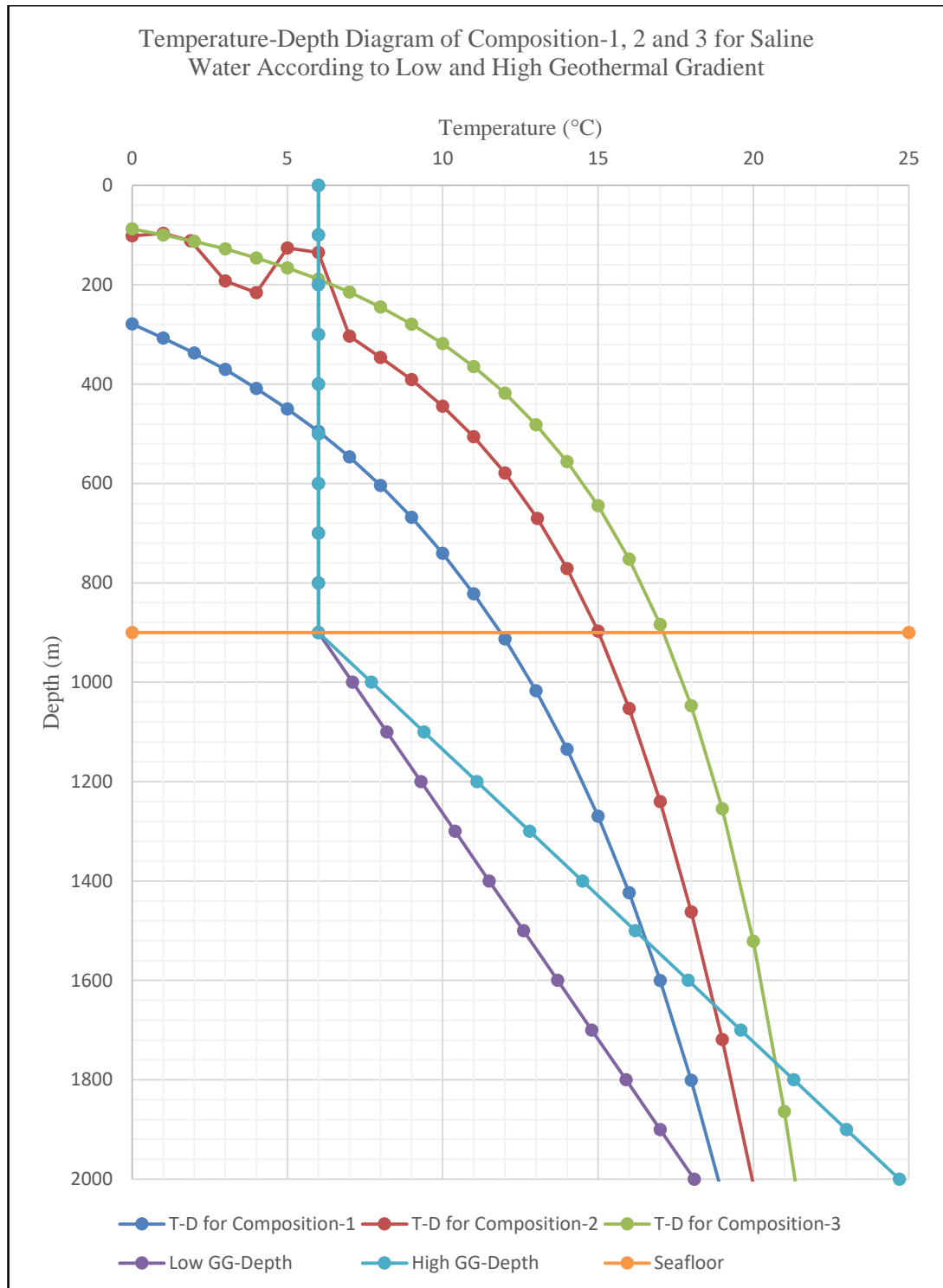
Figure A-16: Temperature-depth diagram of Composition-1, 2, and 3 for saline water case according to low and high geothermal gradient. Seafloor is at 900 m.
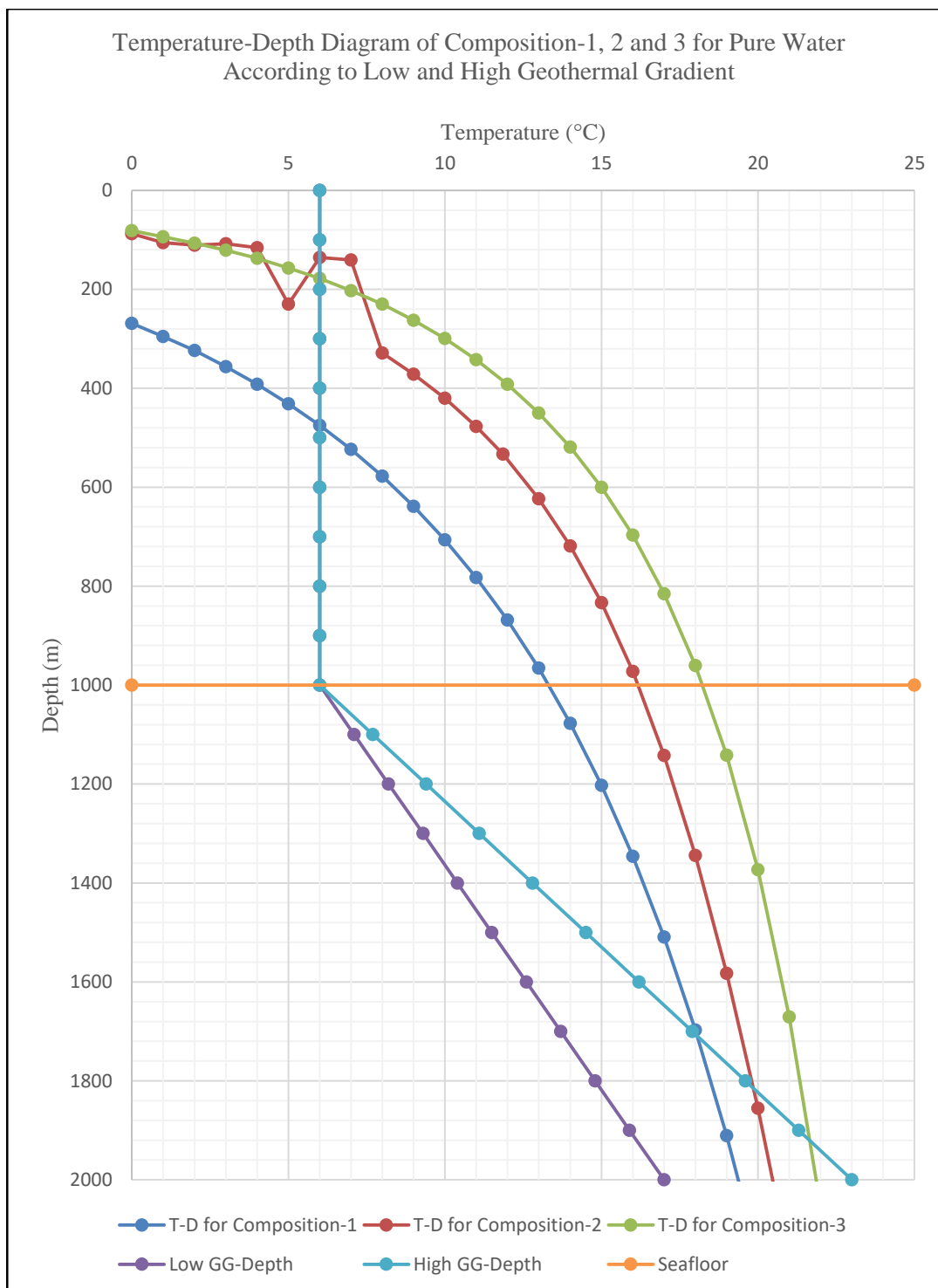
Figure A-17: Temperature-depth diagram of Composition-1, 2, and 3 for pure water case according to low and high geothermal gradient. Seafloor is at 1,000 m.
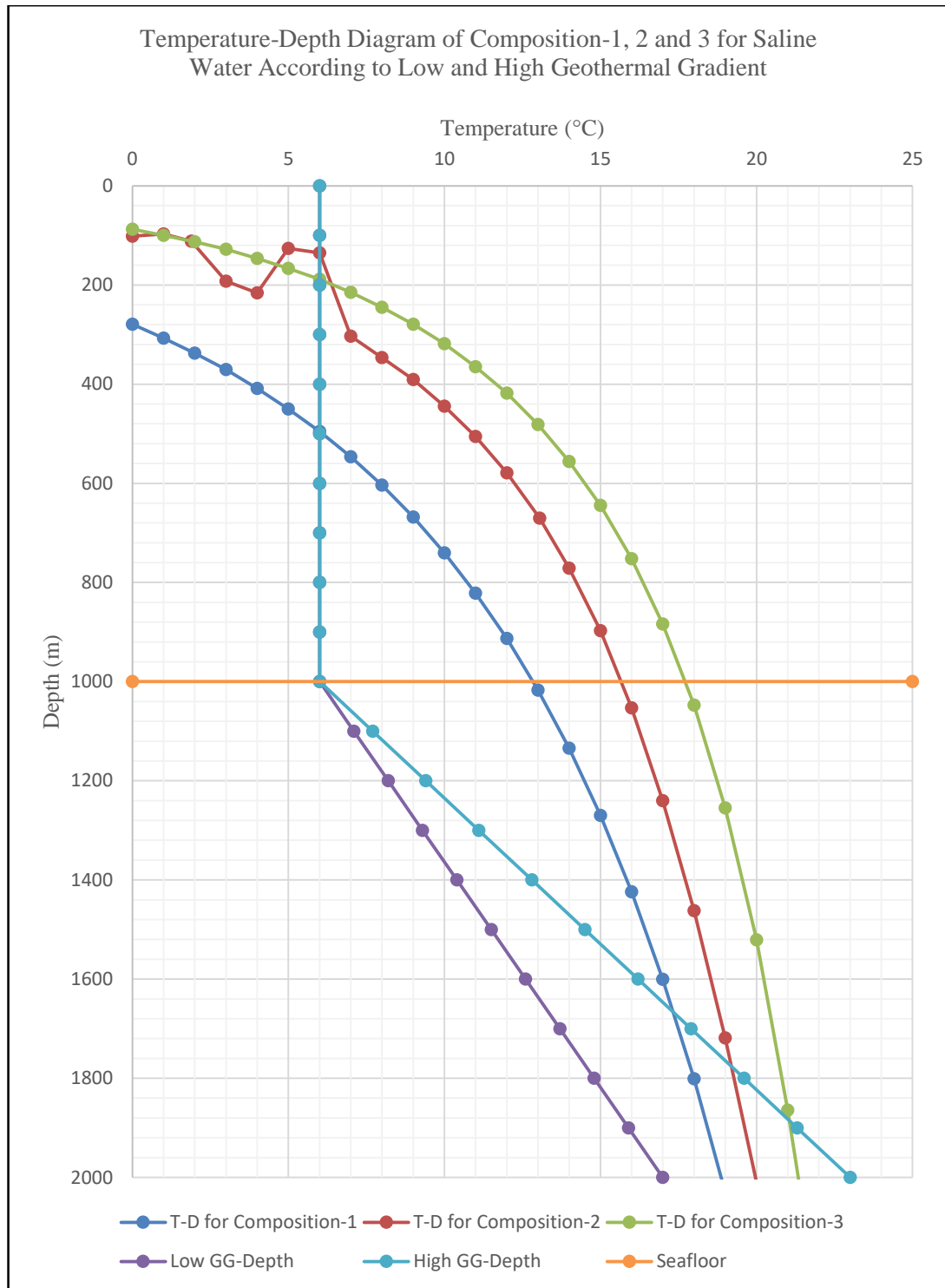
Figure A-18: Temperature-depth diagram of Composition-1, 2, and 3 for saline water case according to low and high geothermal gradient. Seafloor is at 1,000 m.

Appendix B

Appendix B: 1 Pressure Temperature Diagrams for Mud Volcanoes

Pressure temperature diagrams for Buzdag, Elm and unnamed mud volcano on Abikha bank are displayed in Figure B-1 to Figure B-9.
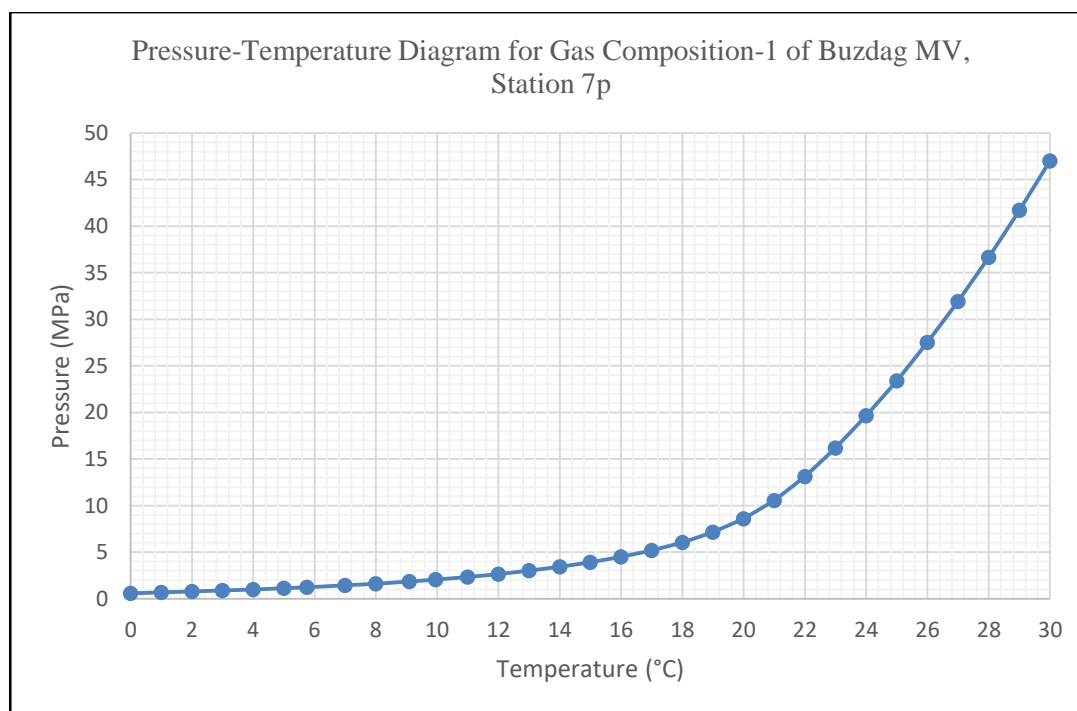
Figure B-1: Pressure-temperature diagram for gas composition-1 of Buzdag mud volcano, station 7p.
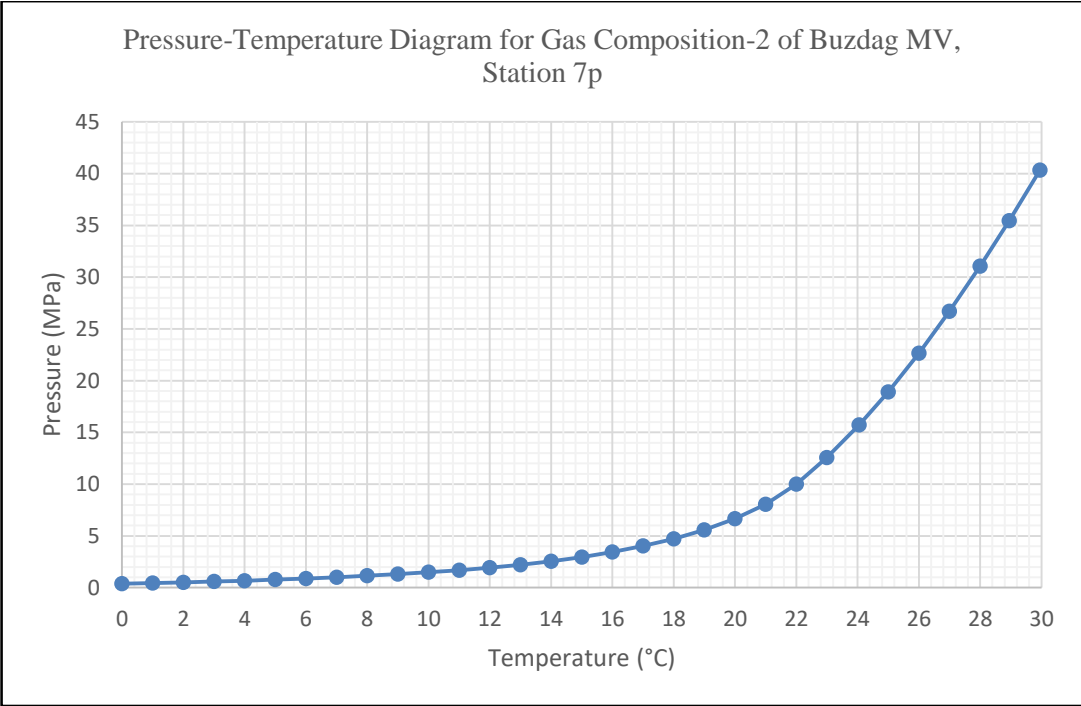
Figure B-2: Pressure-temperature diagram for gas composition-2 of Buzdag mud volcano, station 7p
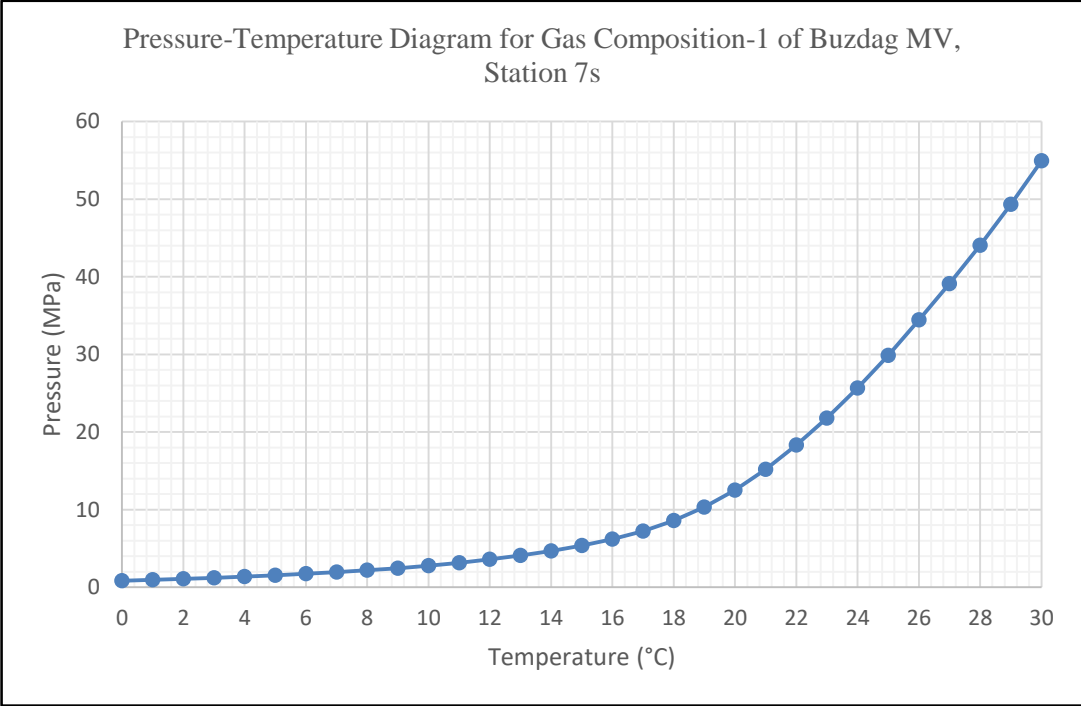
Figure B-3: Pressure-temperature diagram for gas composition-1 of Buzdag mud volcano, station 7s
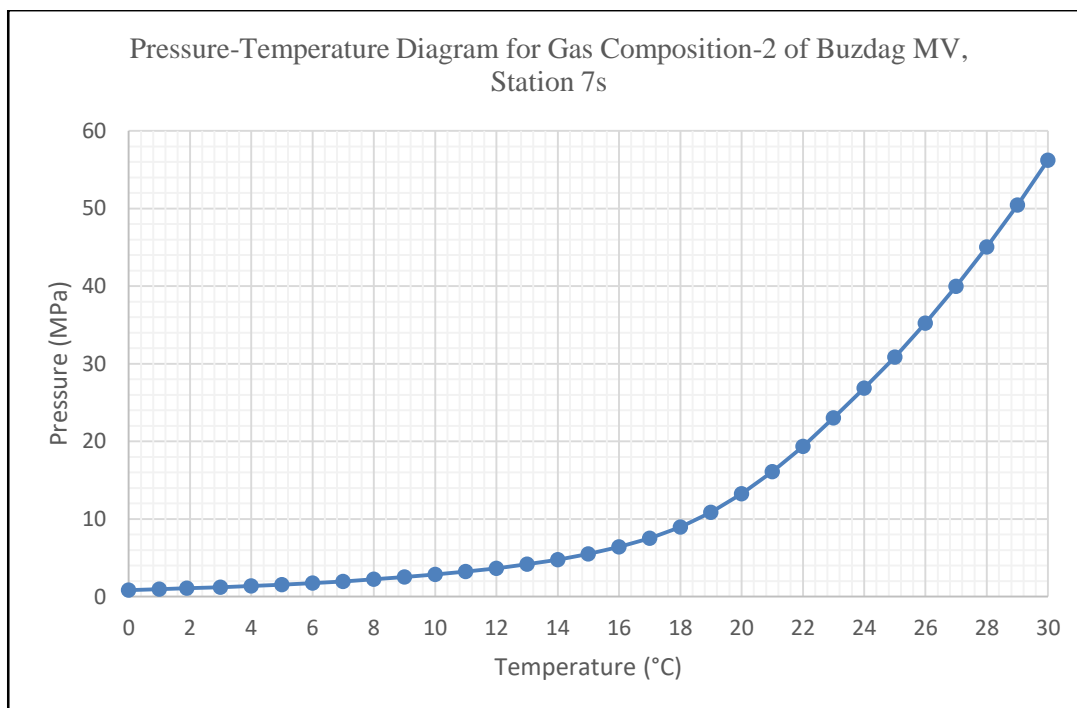
Figure B-4: Pressure-temperature diagram for gas composition-2 of Buzdag mud volcano, station 7s
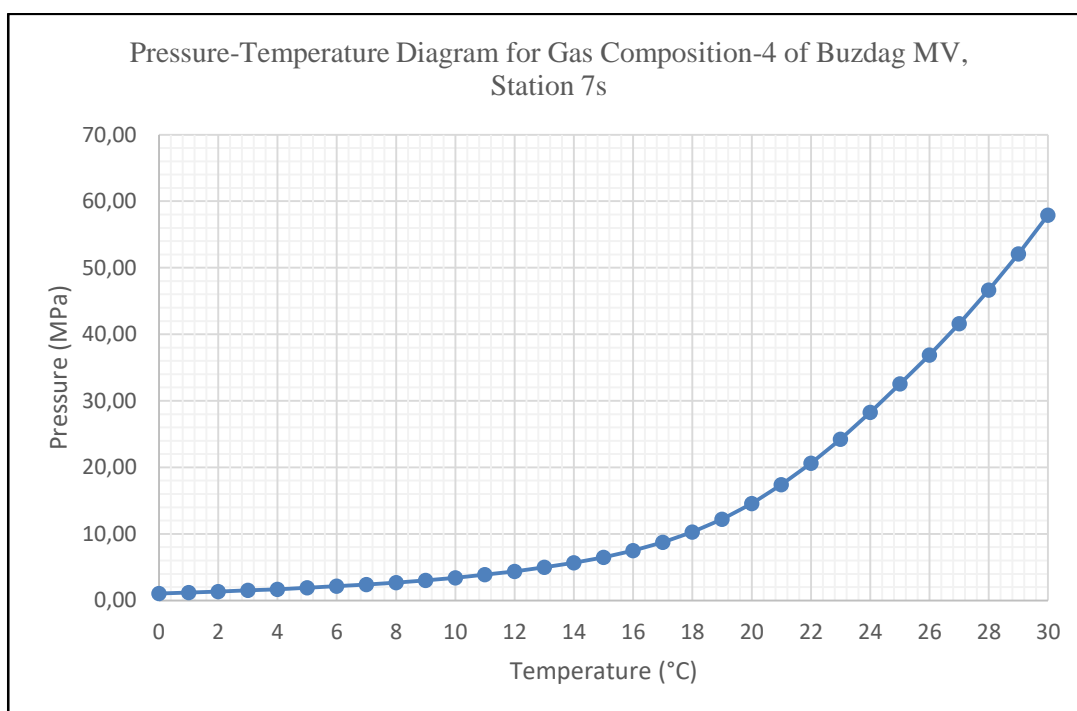
Figure B-5: Pressure-temperature diagram for gas composition-4 of Buzdag mud volcano, station 7s
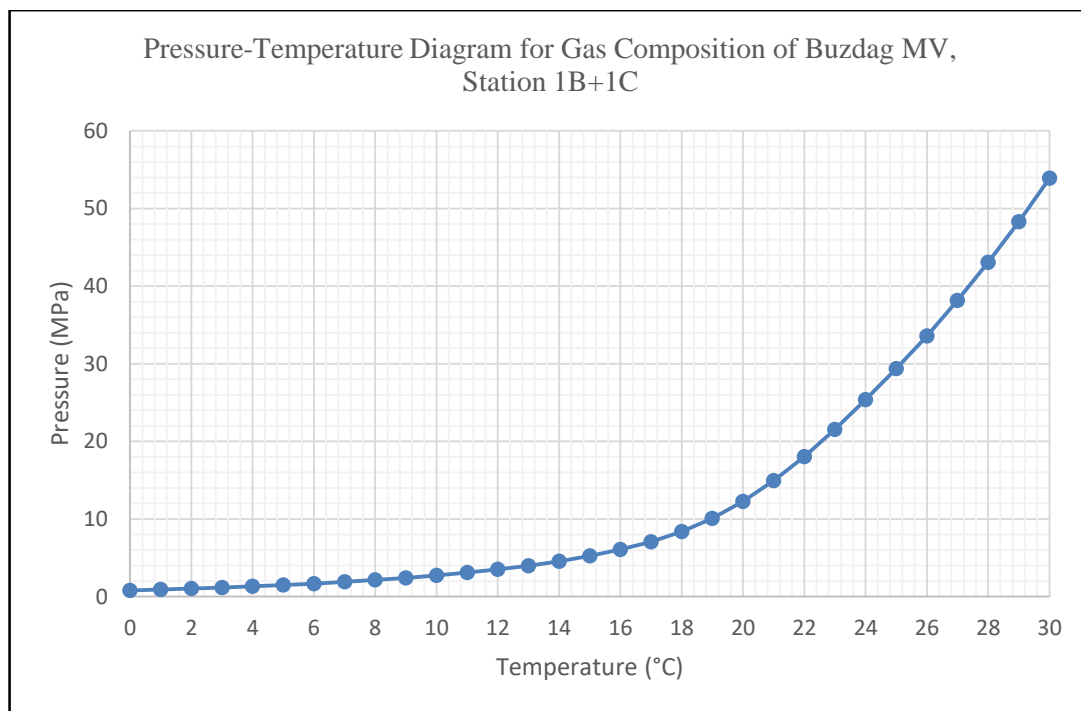
Figure B-6: Pressure-temperature diagram for gas composition of Buzdag mud volcano, station 1B+1C
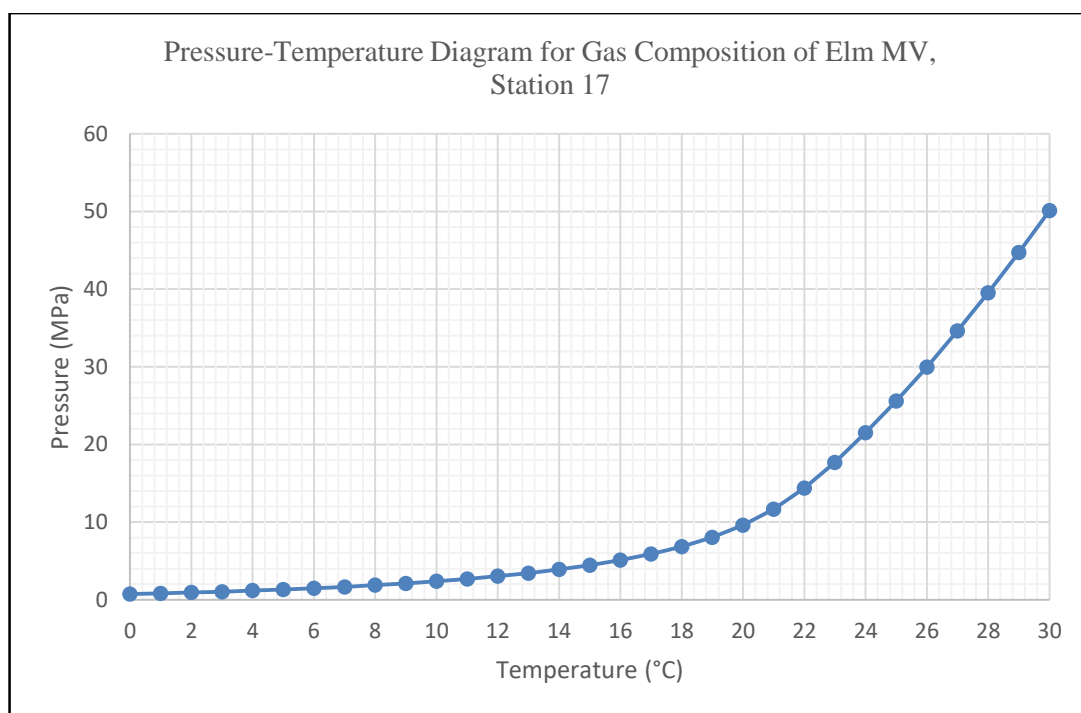
Figure B-7: Pressure-temperature diagram for gas composition of Elm mud volcano, station 17
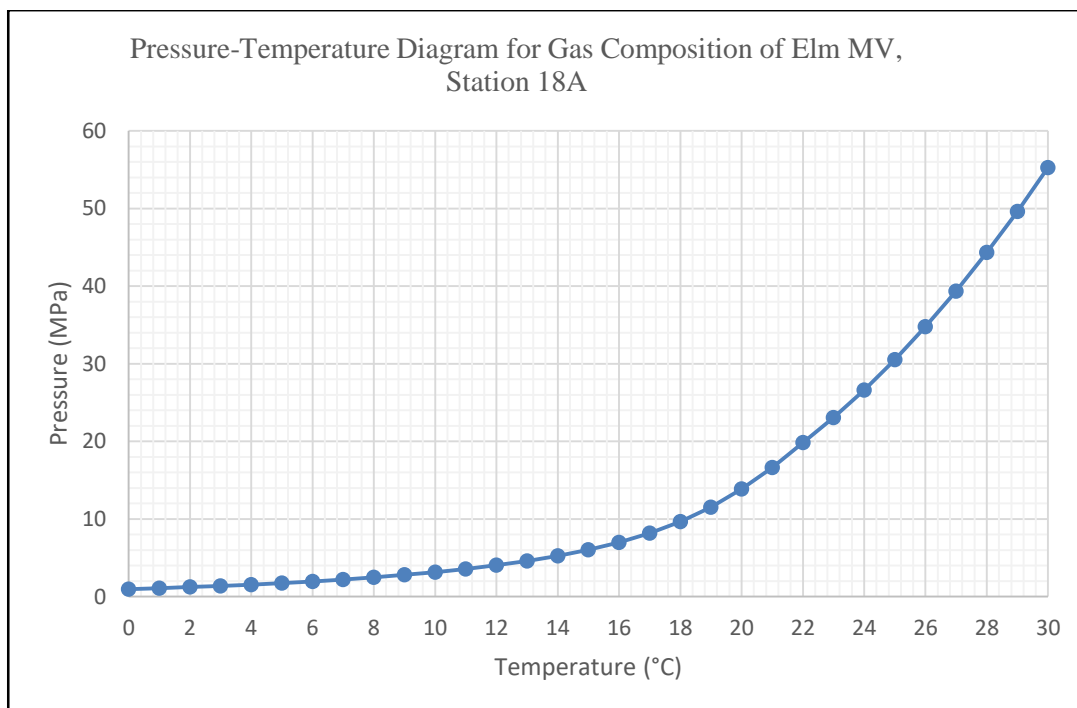
Figure B-8: Pressure-temperature diagram for gas composition of Elm mud volcano, station 18A
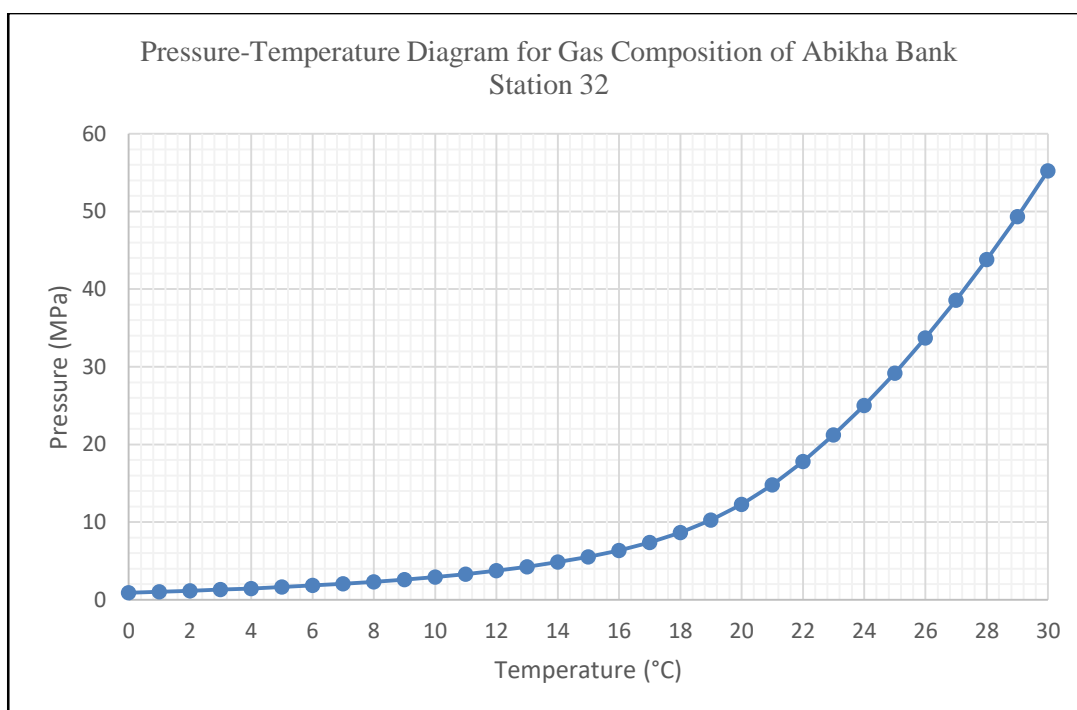
Figure B-9: Pressure-temperature diagram for gas composition of unnamed mud volcano on Abikha bank, station 32

Appendix B: 2 Temperature-Depth Diagrams for Mud Volcanoes

Temperature-depth diagrams for Buzdag, Elm and unnamed mud volcano on Abikha bank are displayed in Figure B-10 to Figure B-18.
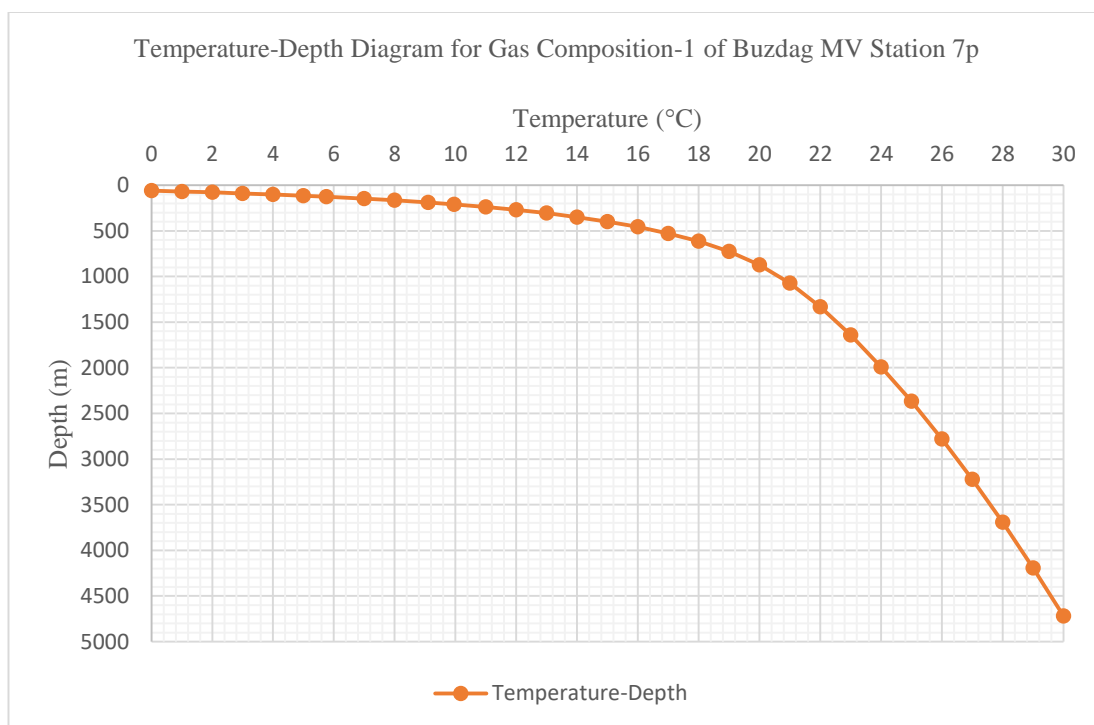
Figure B-10: Temperature-depth diagram for gas composition-1 of Buzdag mud volcano, station 7p
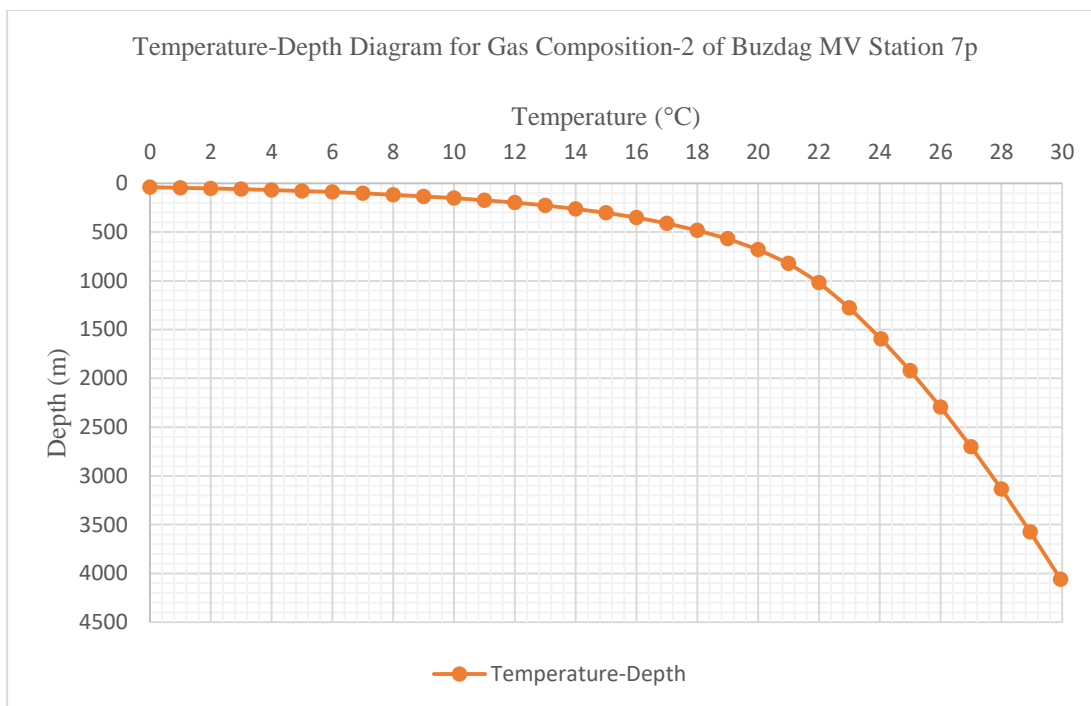
Figure B-11: Temperature-depth diagram for gas composition-2 of Buzdag mud volcano, station 7p
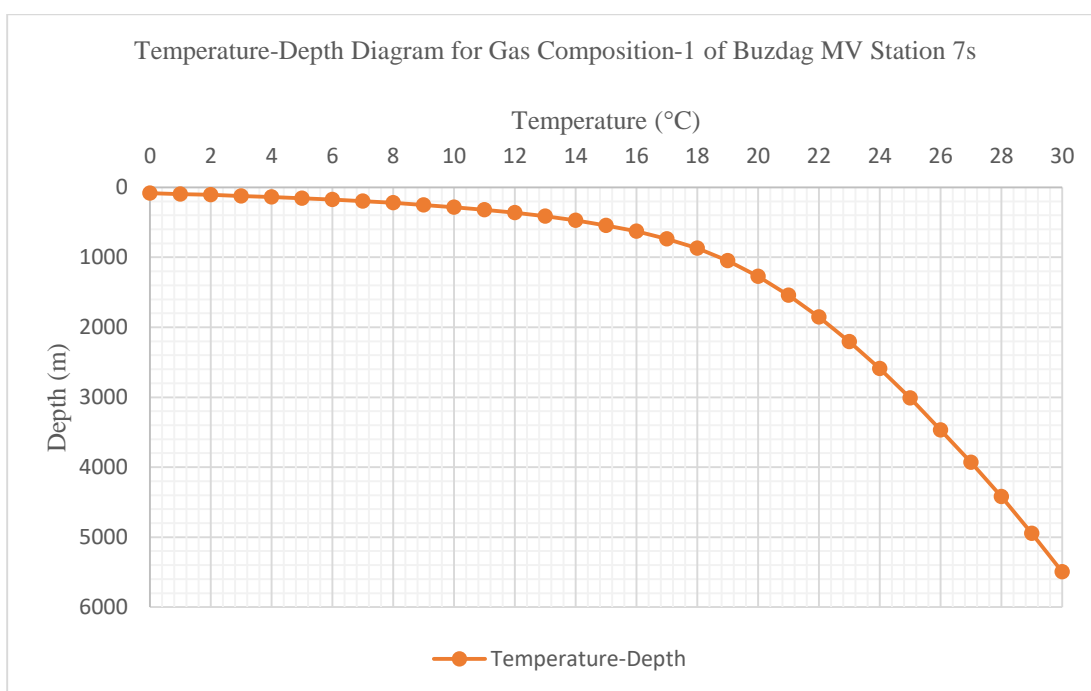
Figure B-12: Temperature-depth diagram for gas composition-1 of Buzdag mud volcano, station 7s
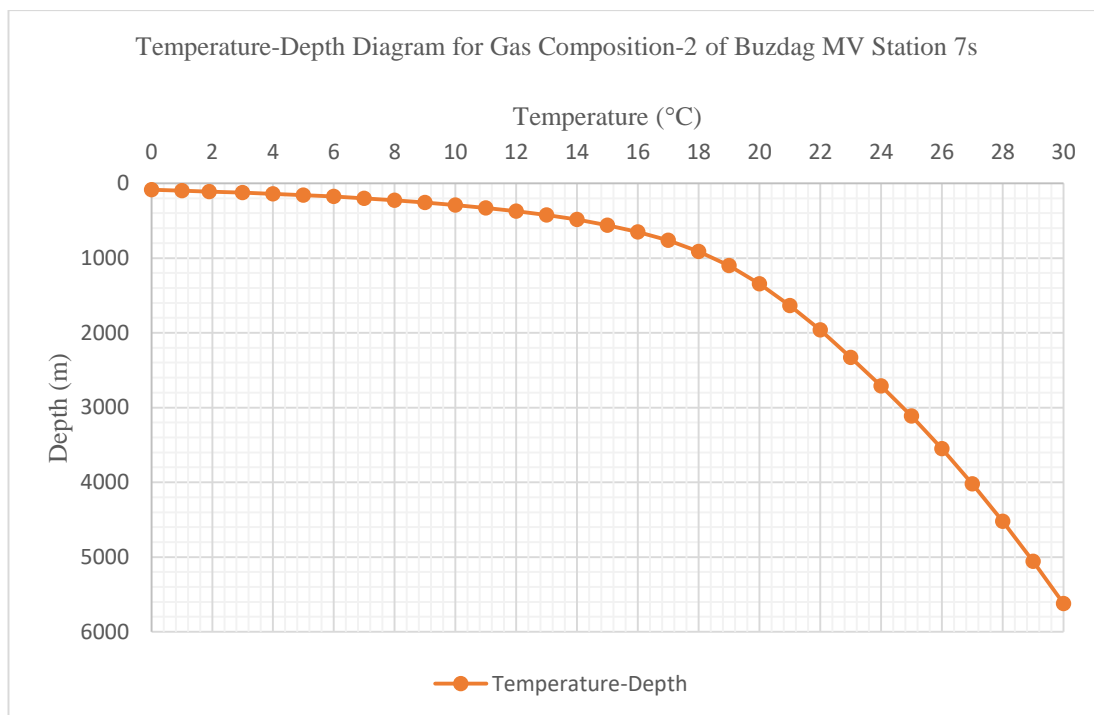
Figure B-13: Temperature-depth diagram for gas composition-2 of Buzdag mud volcano, station 7s
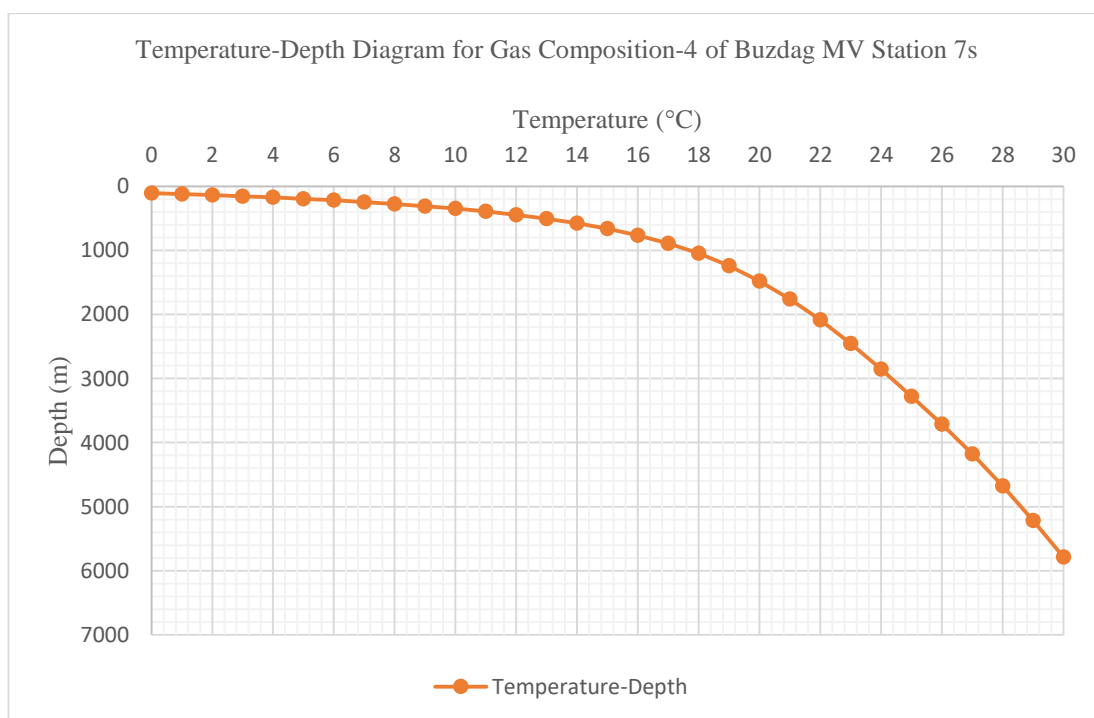
Figure B-14: Temperature-depth diagram for gas composition-4 of Buzdag mud volcano, station 7s

147

Figure B-15: Temperature-depth diagram for gas composition of Buzdag mud volcano, station 1B+1C

Figure B-16: Temperature-depth diagram for gas composition of Elm mud volcano, station 17

148
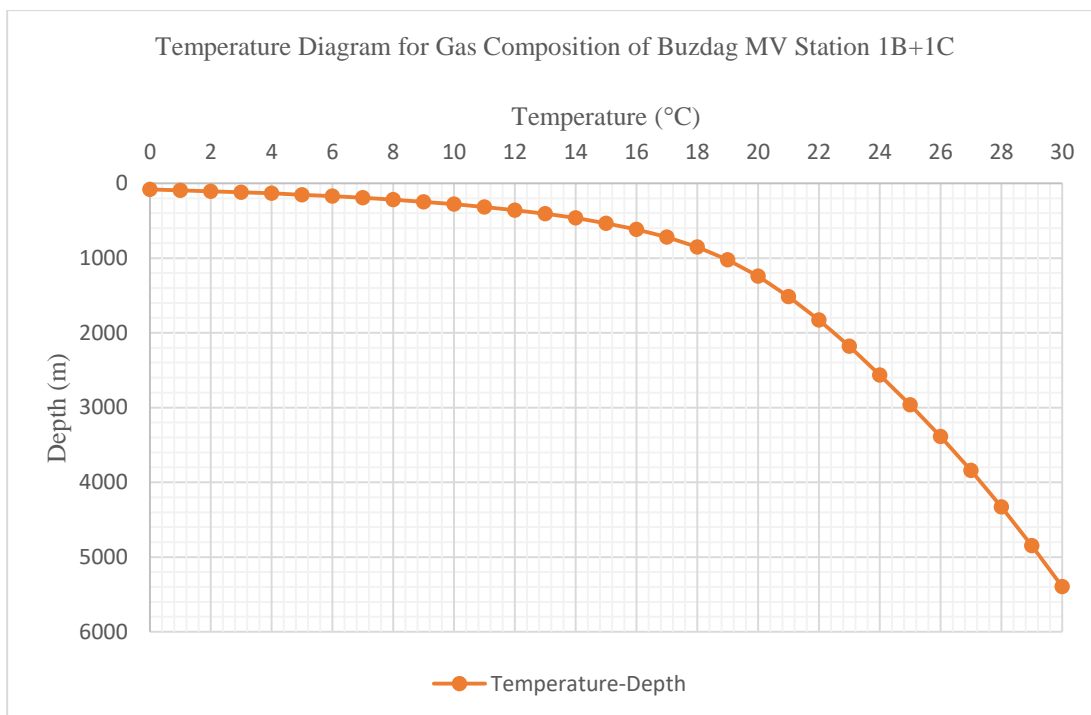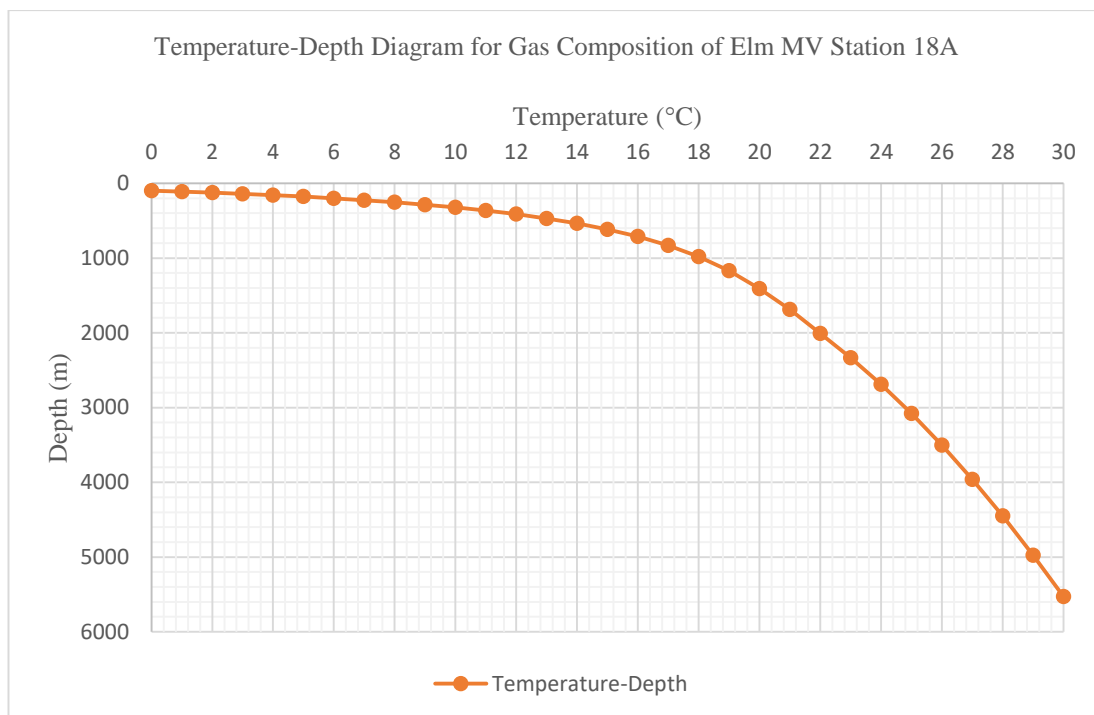
Figure B-17: Temperature-depth diagram for gas composition of Elm mud volcano, station 18A
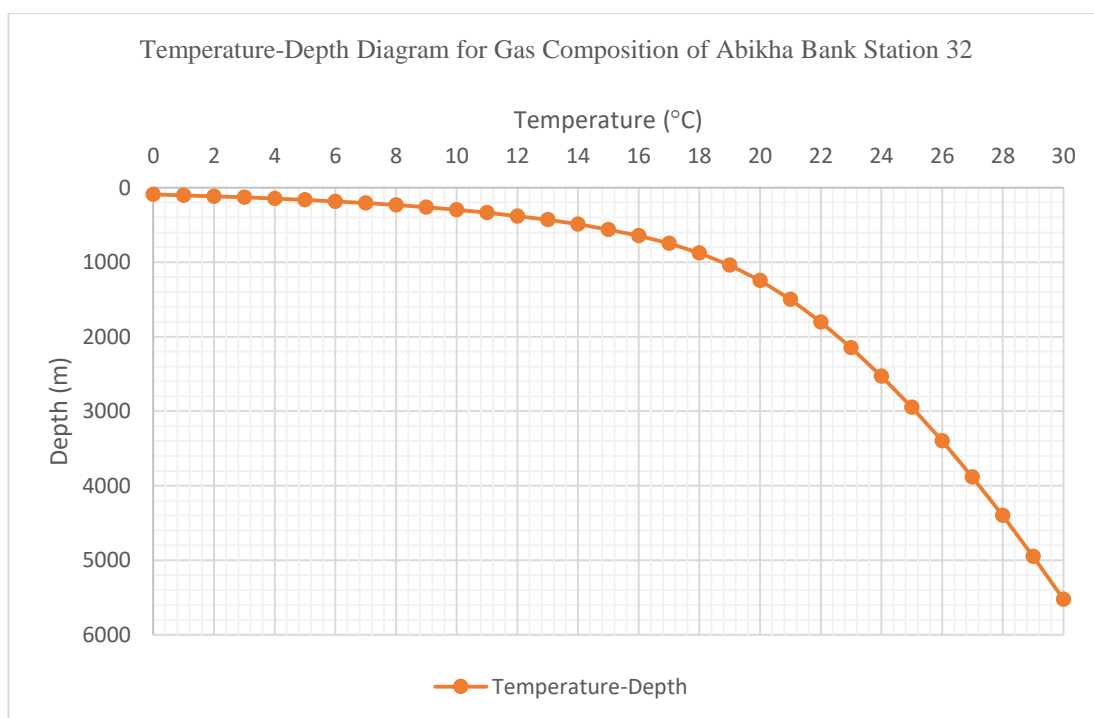
Figure B-18: Temperature-depth diagram for gas composition of unnamed mud volcano on Abikha bank, station 32

Appendix B: 3 Temperature-Depth Diagrams According to Low and High Geothermal Gradients for Mud Volcanoes

Temperature-depth diagrams of different compositions (see Table 6.3) according to different low and high geothermal gradients (see Table 6.4) are displayed in Figure B-19 to Figure B-45. Diagrams are made for Buzdag, Elm, and unnamed mud volcano on Abikha bank.
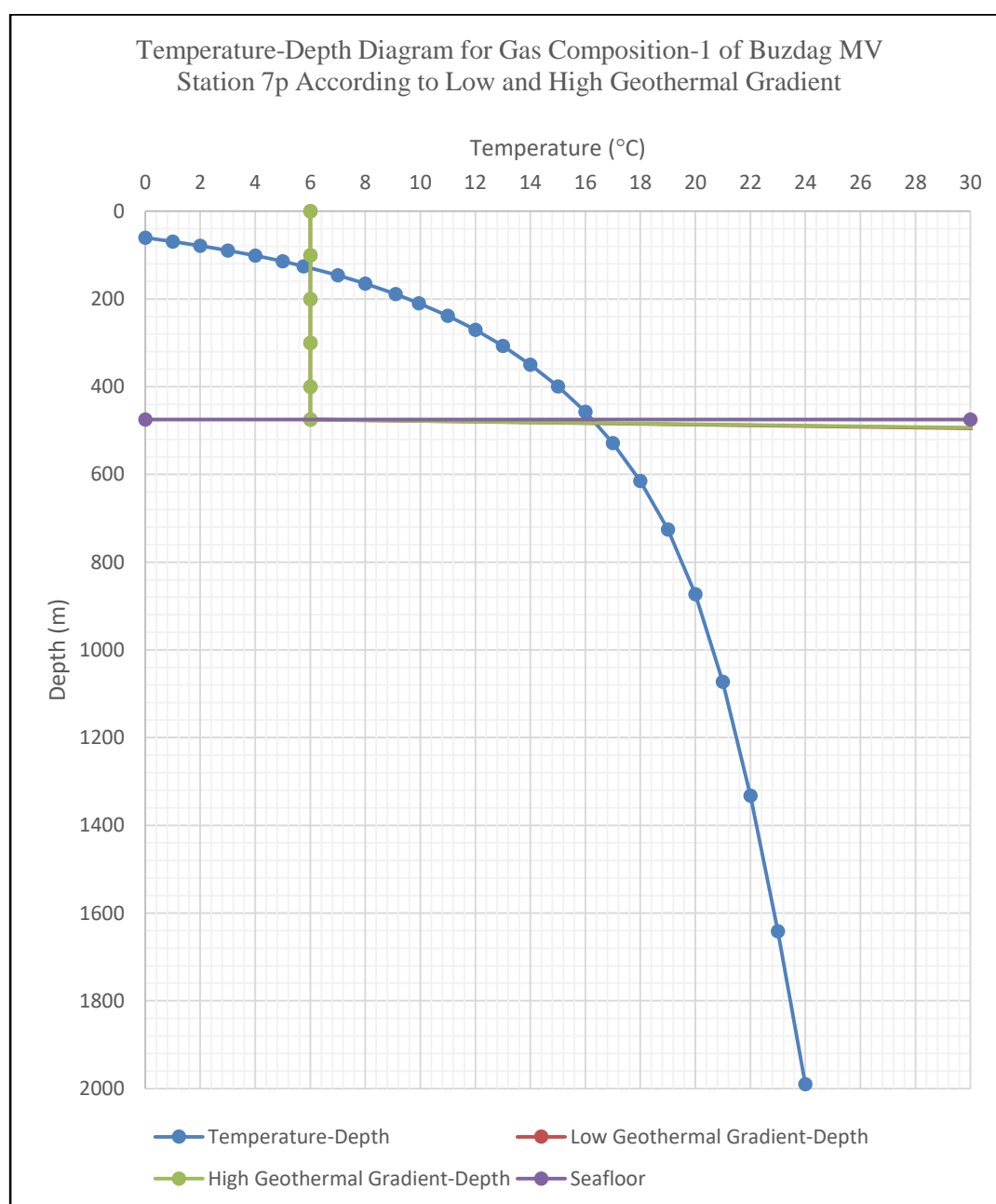
Figure B-19: Temperature-depth diagram for gas composition-1 of Buzdag mud volcano, station 7p, according to low and high geothermal gradient. Low GG = 120 °C/100 m; High GG = 129 °C/100 m.
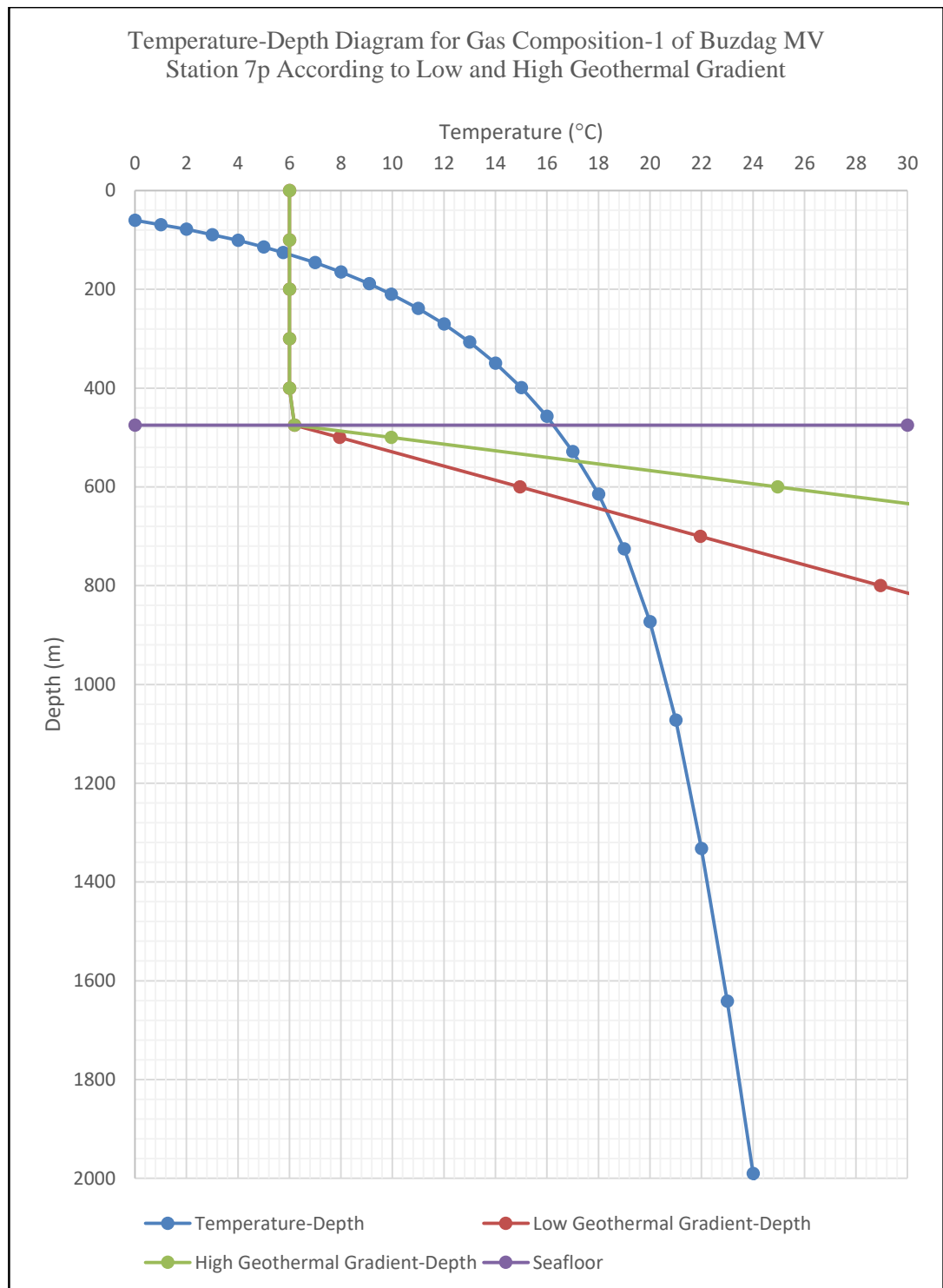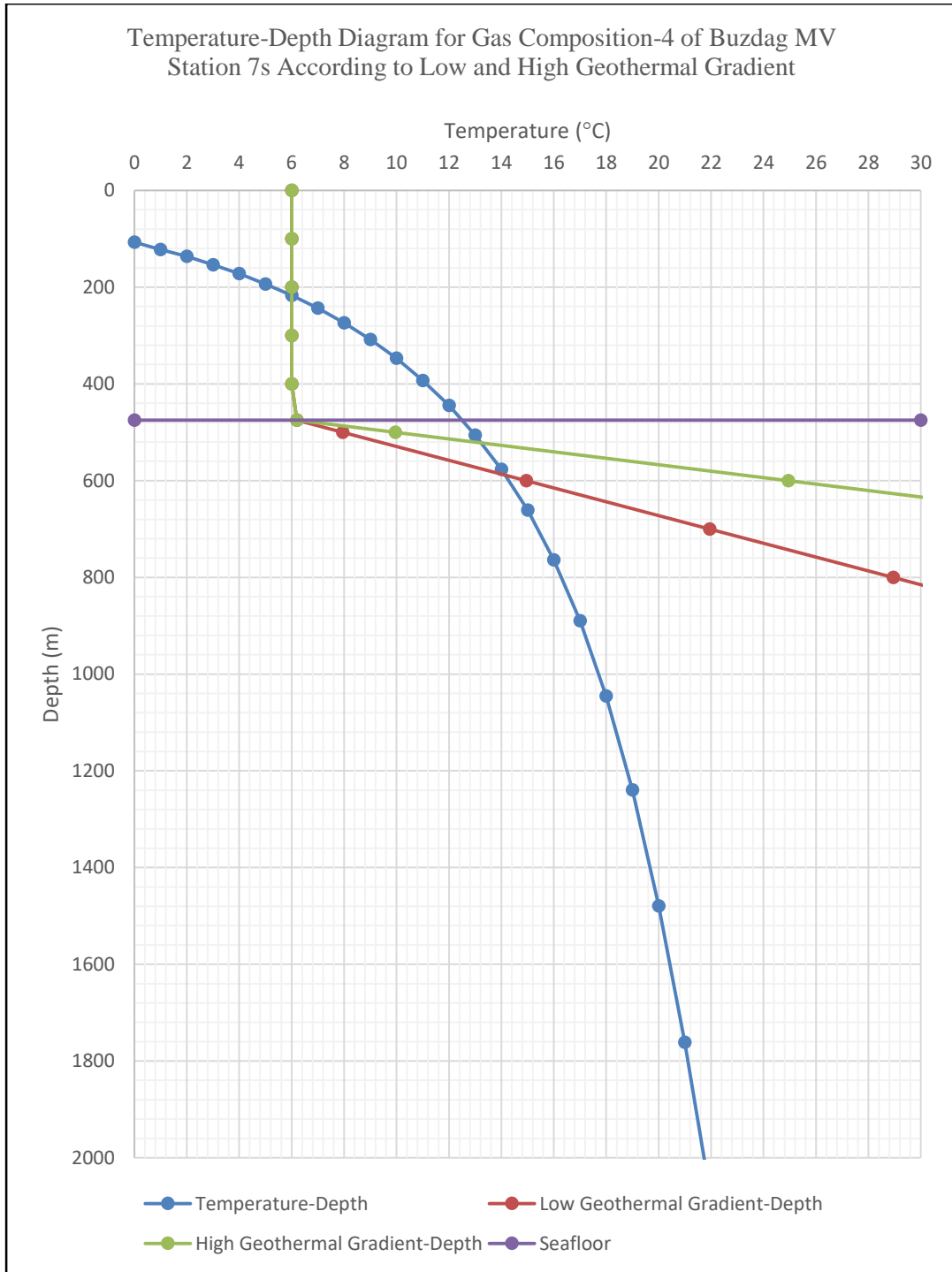
Figure B-20: Temperature-depth diagram for gas composition-1 of Buzdag mud volcano, station 7p, according to low and high geothermal gradient. Low GG = 7 °C/100 m; High GG = 15 °C/100 m.
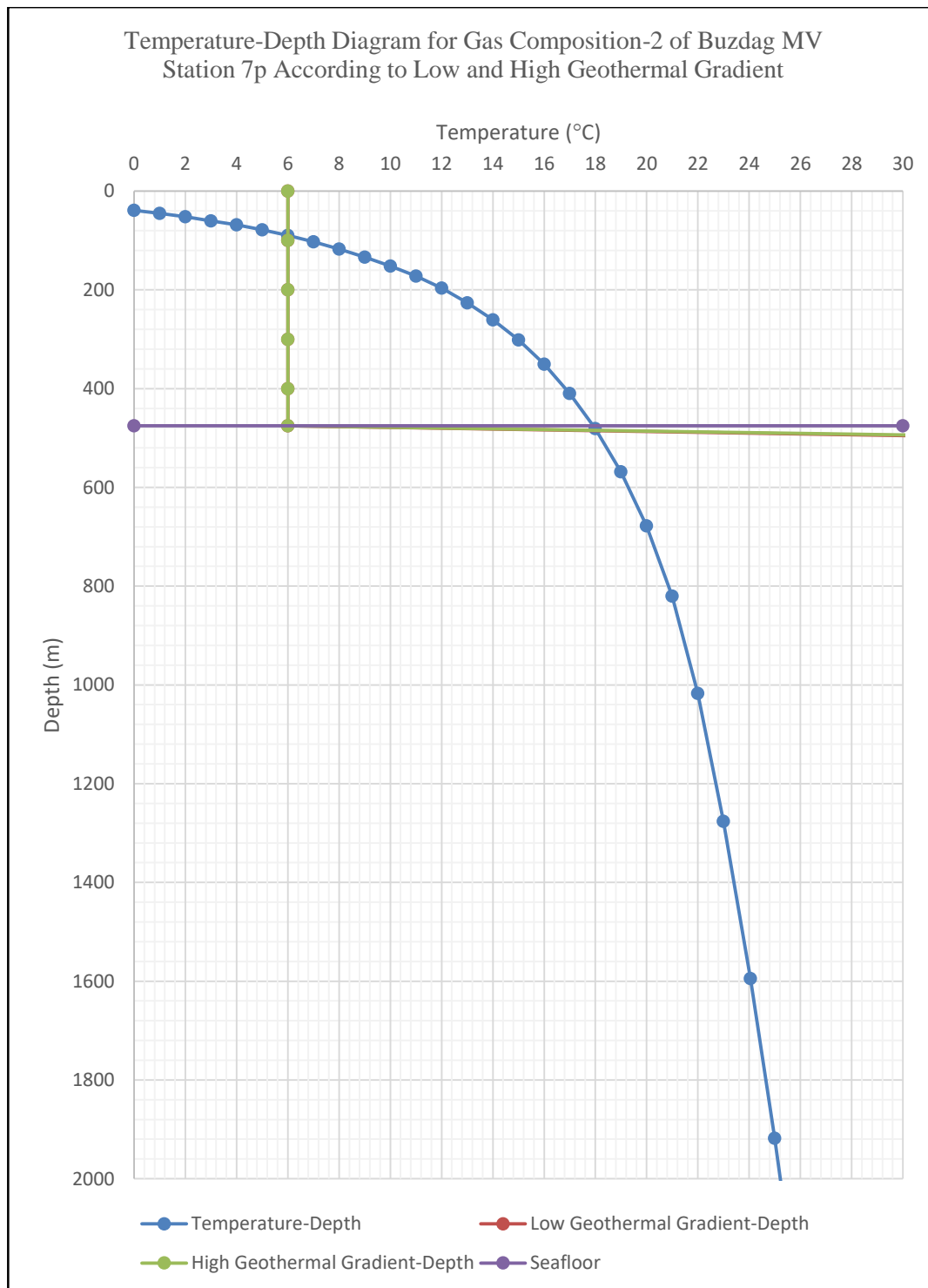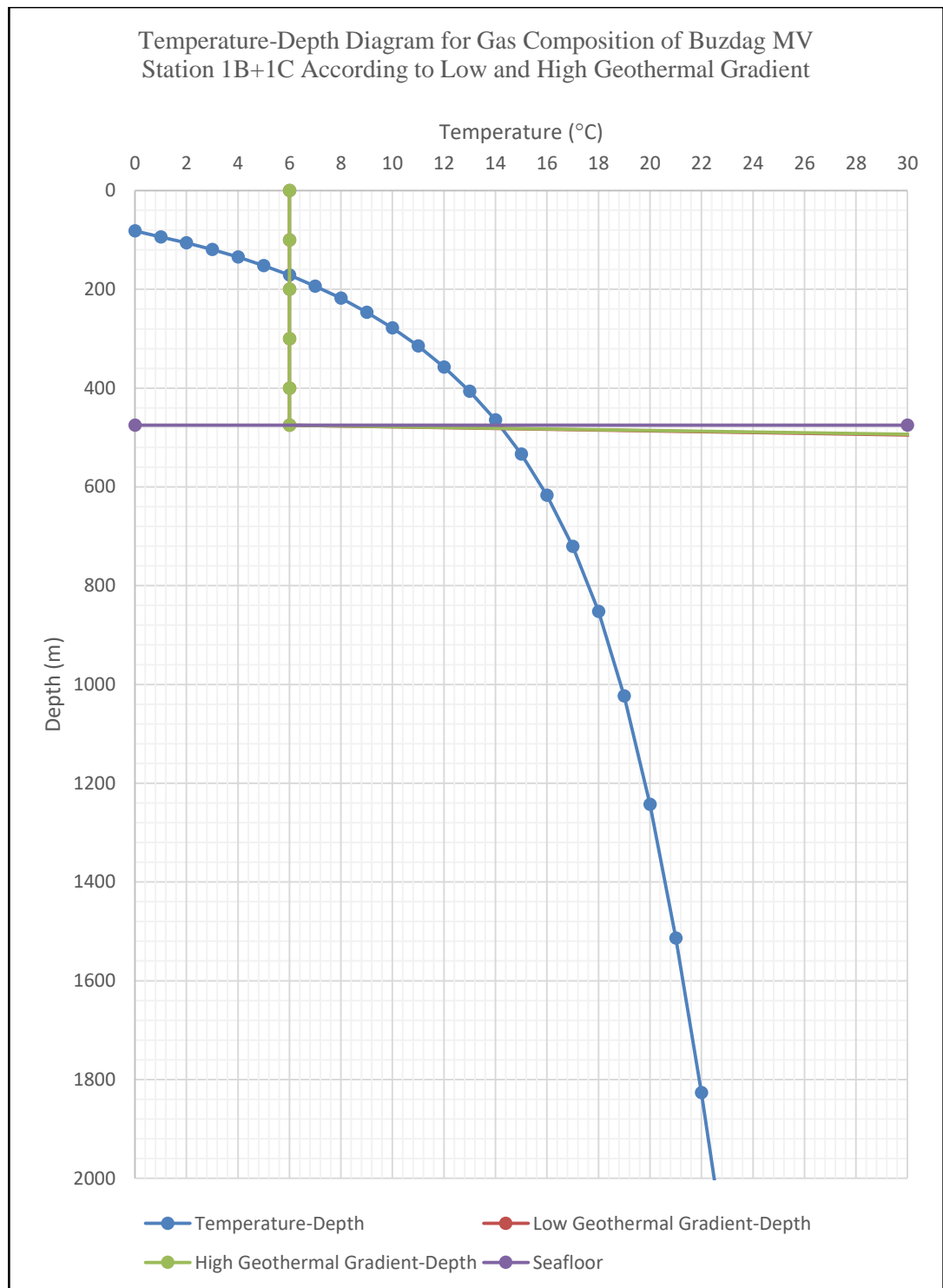
Figure B-21: Temperature-depth diagram for gas composition-2 of Buzdag mud volcano, station 7p, according to low and high geothermal gradient. Low GG = 120 °C/100 m; High GG = 129 °C/100 m.
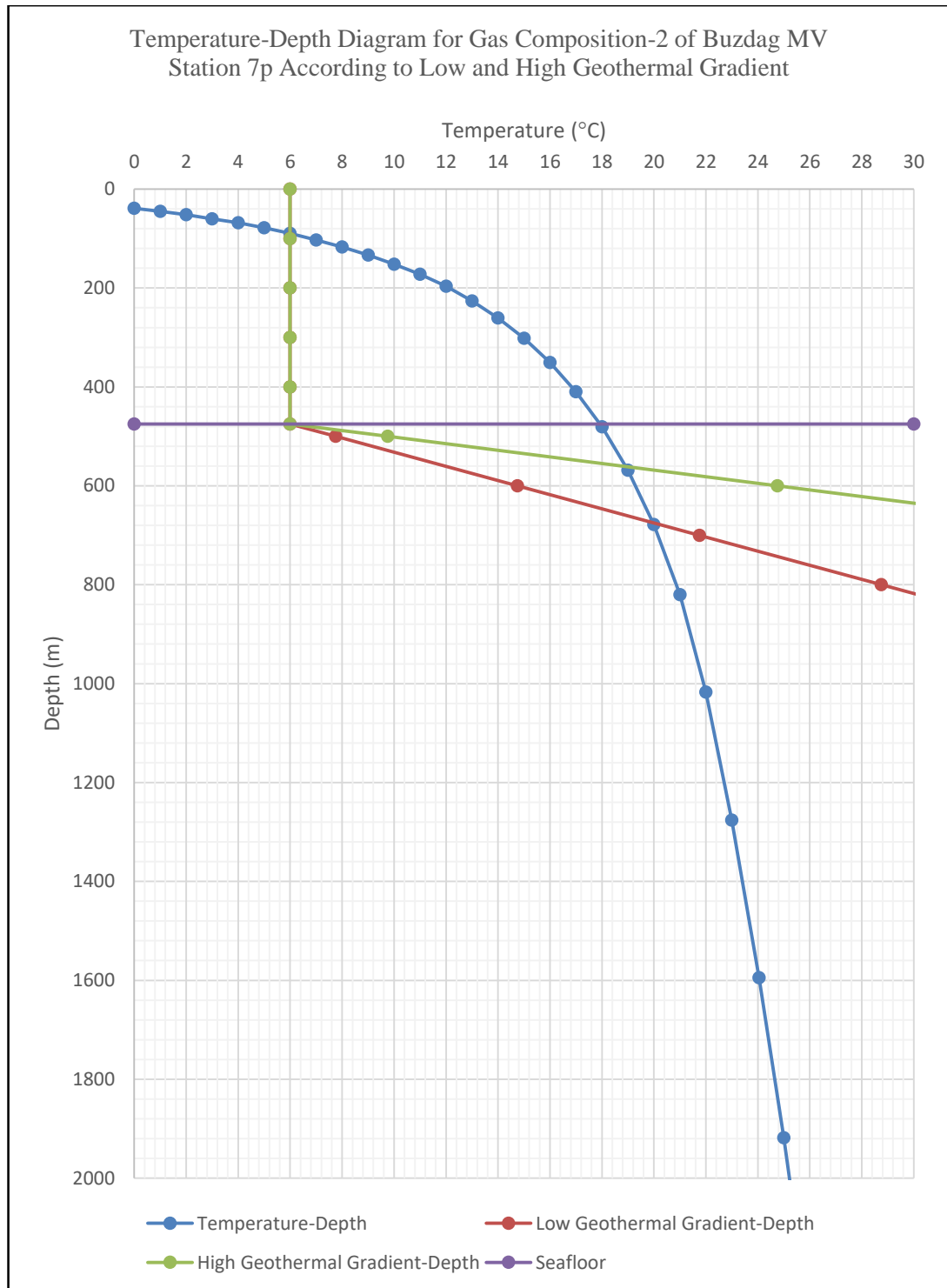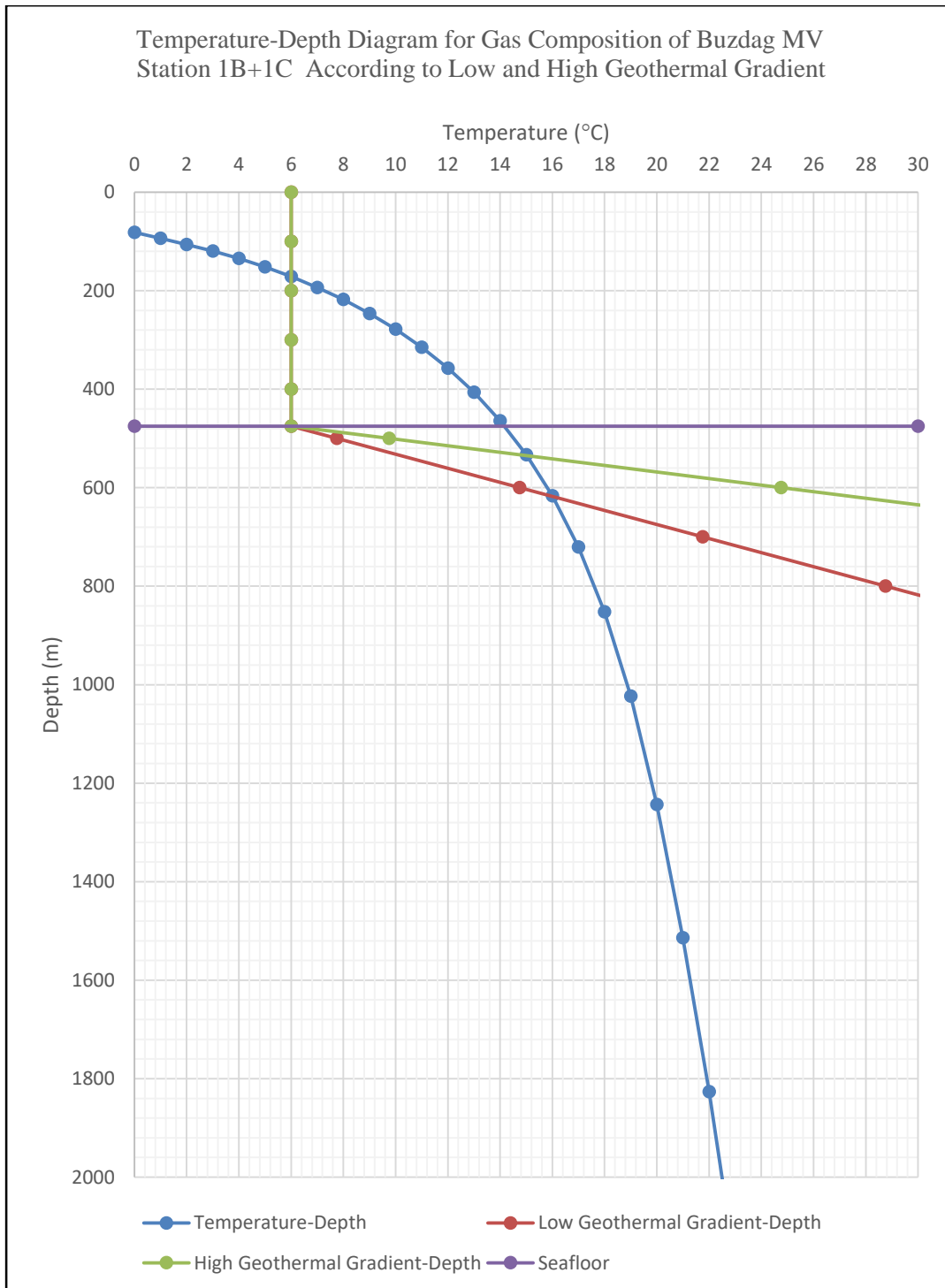
Figure B-22: Temperature-depth diagram for gas composition-2 of Buzdag mud volcano, station 7p, according to low and high geothermal gradient. Low GG = 7 °C/100 m; High GG = 15 °C/100 m.
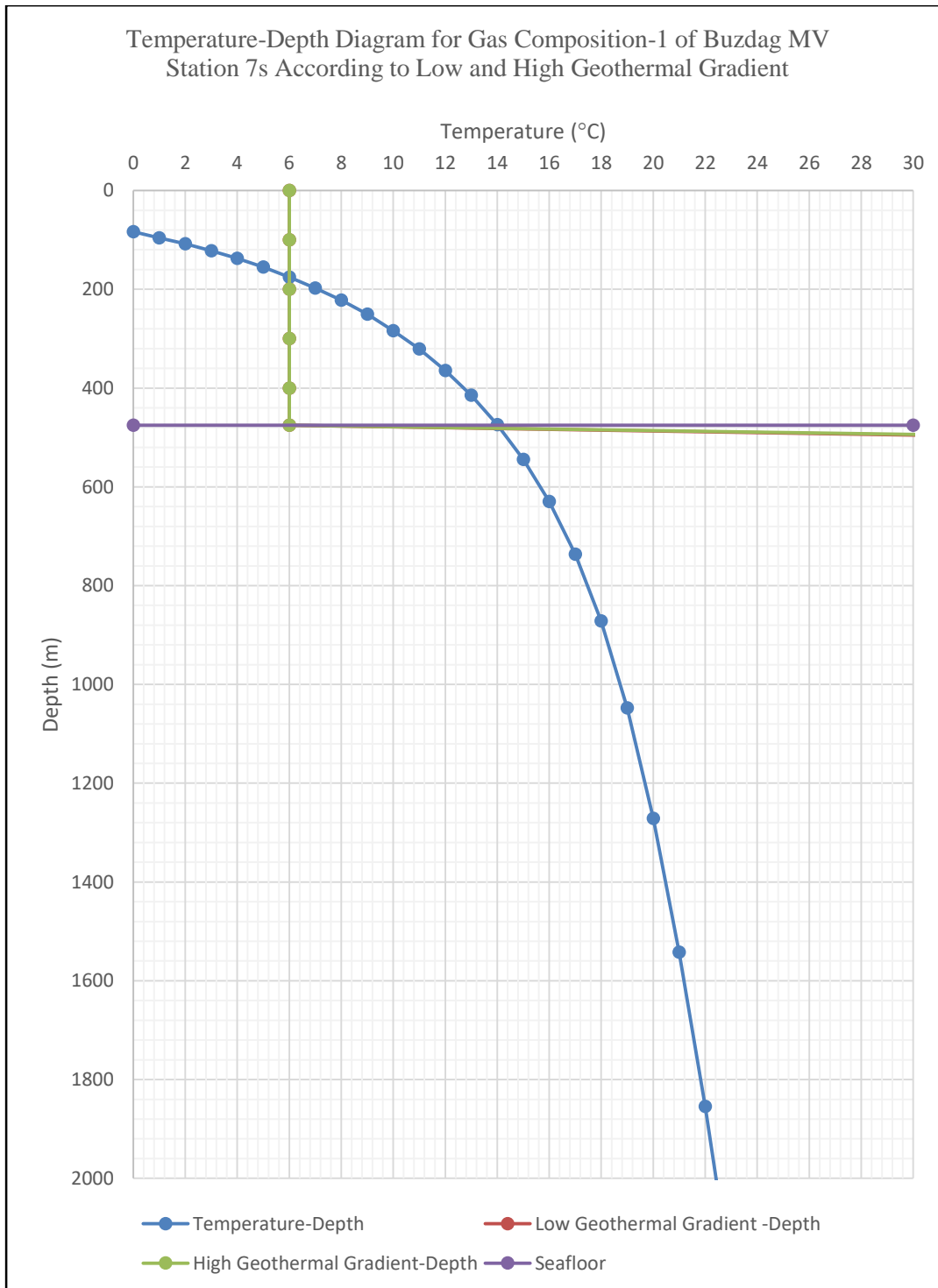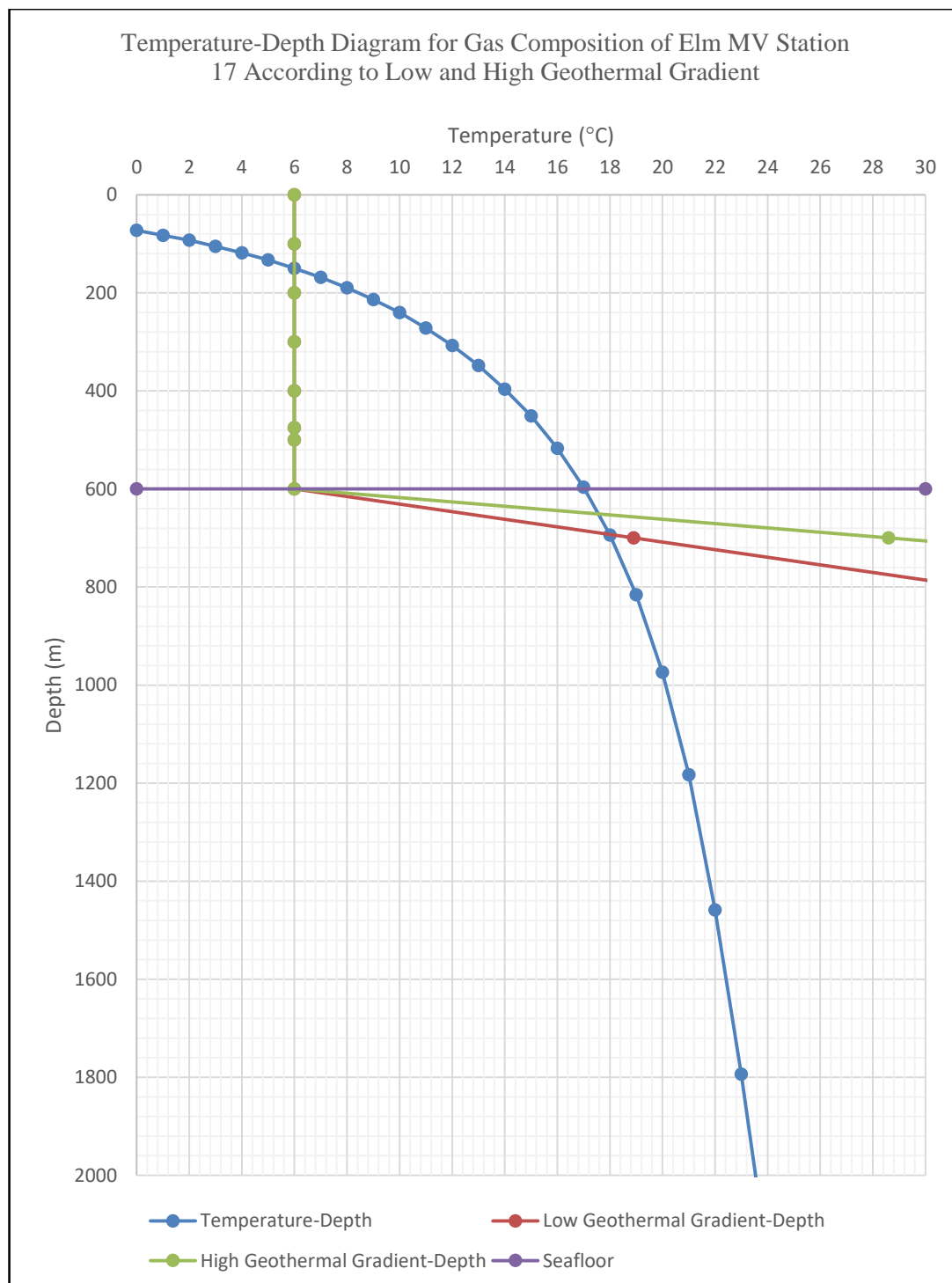
Figure B-23: Temperature-depth diagram for gas composition-1 of Buzdag mud volcano, station 7s, according to low and high geothermal gradient. Low GG = 120 °C/100 m; High GG = 129 °C/100 m.
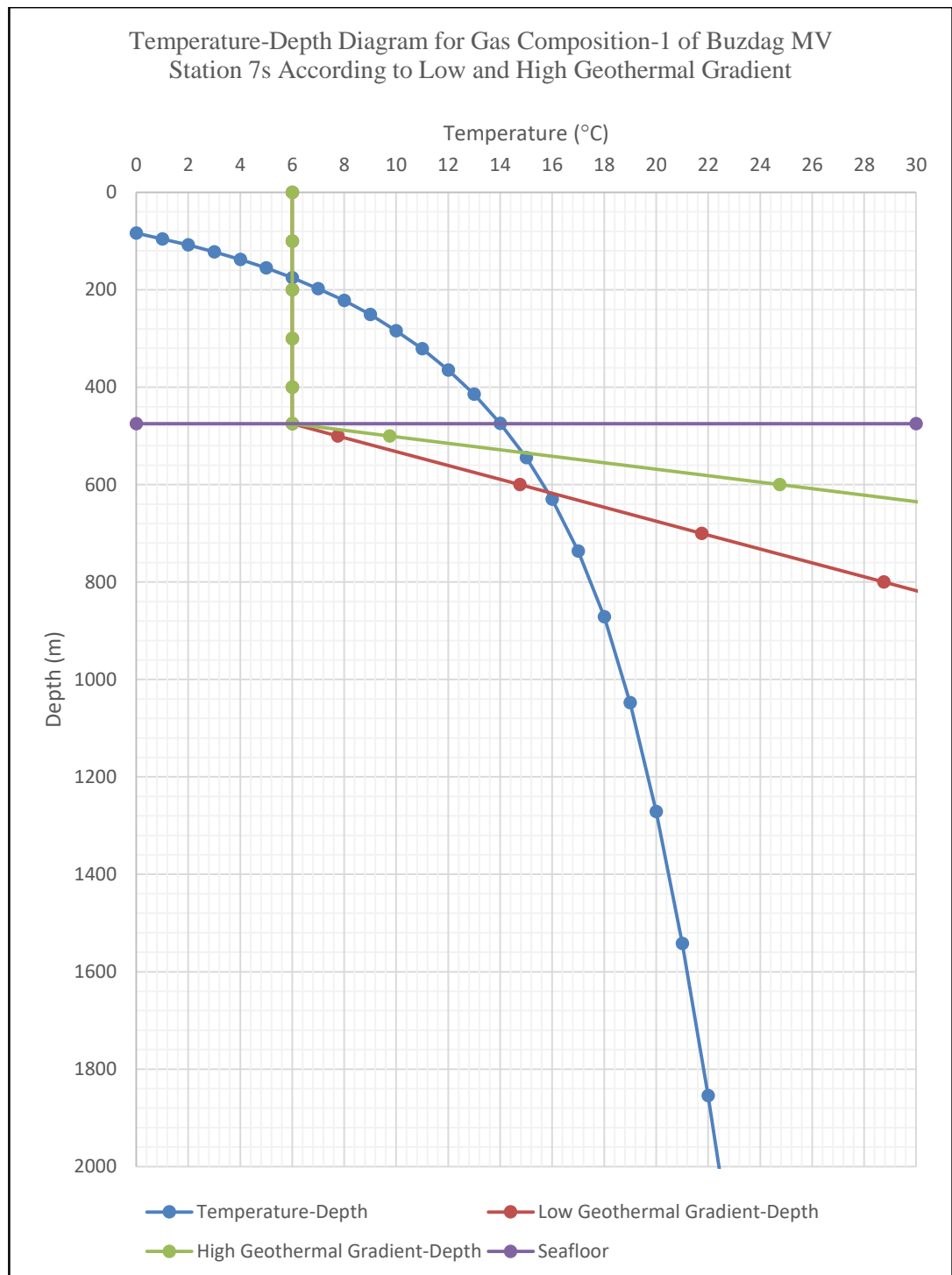
Figure B-24: Temperature-depth diagram for gas composition-1 of Buzdag mud volcano, station 7s, according to low and high geothermal gradient. Low GG = 7 °C/100 m; High GG = 15 °C/100 m.
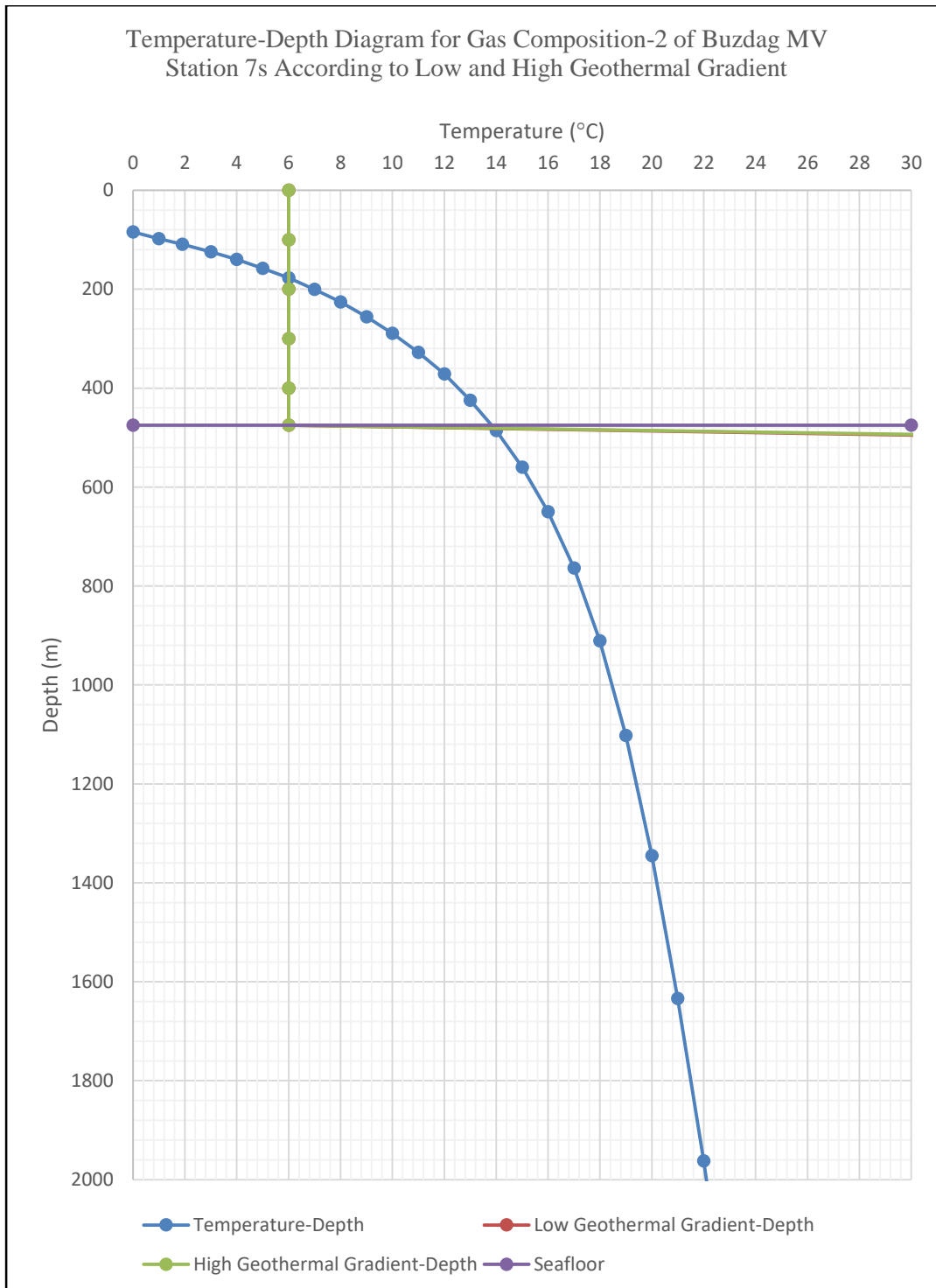
Figure B-25: Temperature-depth diagram for gas composition-2 of Buzdag mud volcano, station 7s, according to low and high geothermal gradient. Low GG = 120 °C/100 m; High GG = 129 °C/100 m.
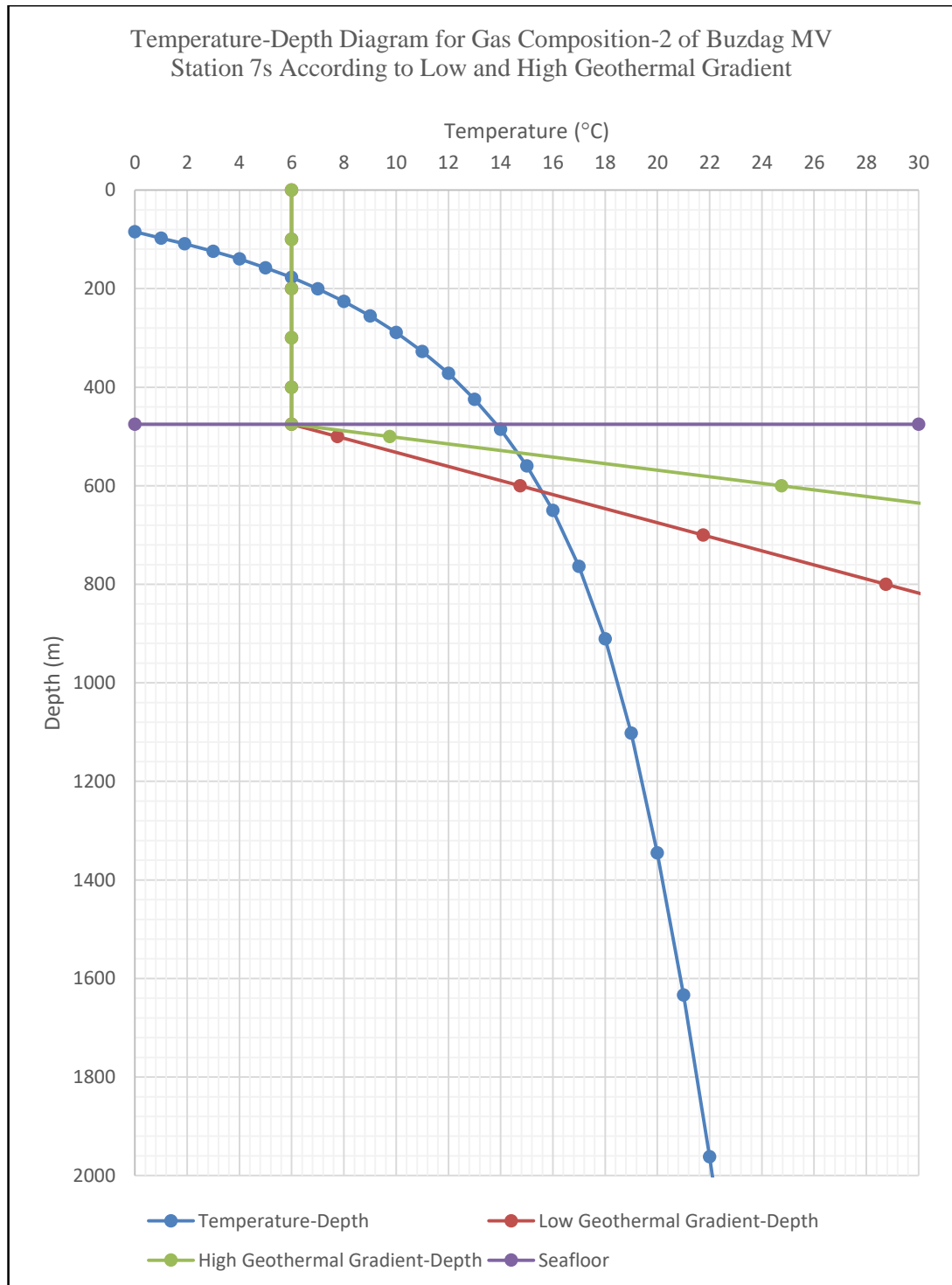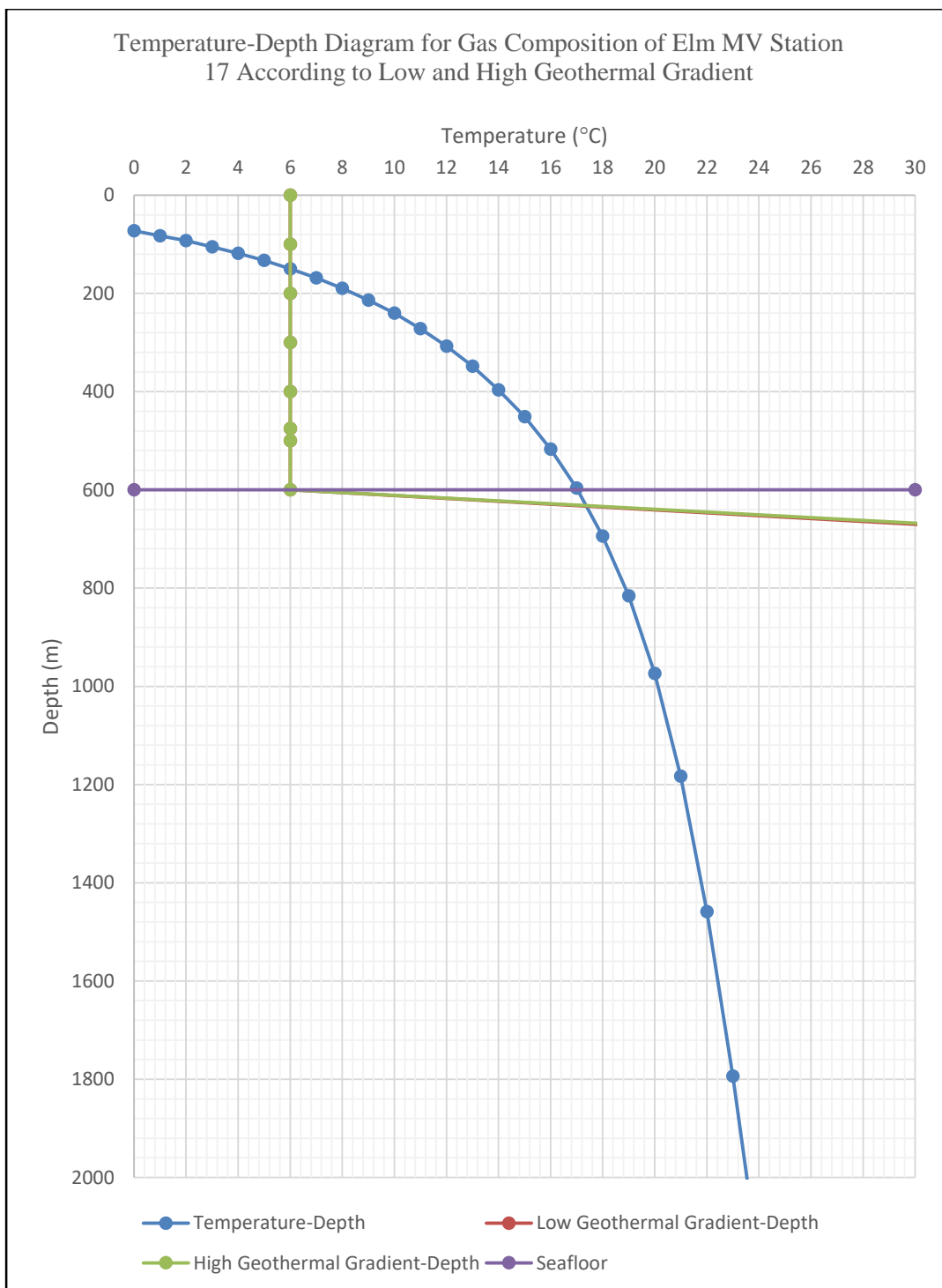
Figure B-26: Temperature-depth diagram for gas composition-2 of Buzdag mud volcano, station 7s, according to low and high geothermal gradient. Low GG = 7 °C/100 m; High GG = 15 °C/100 m.
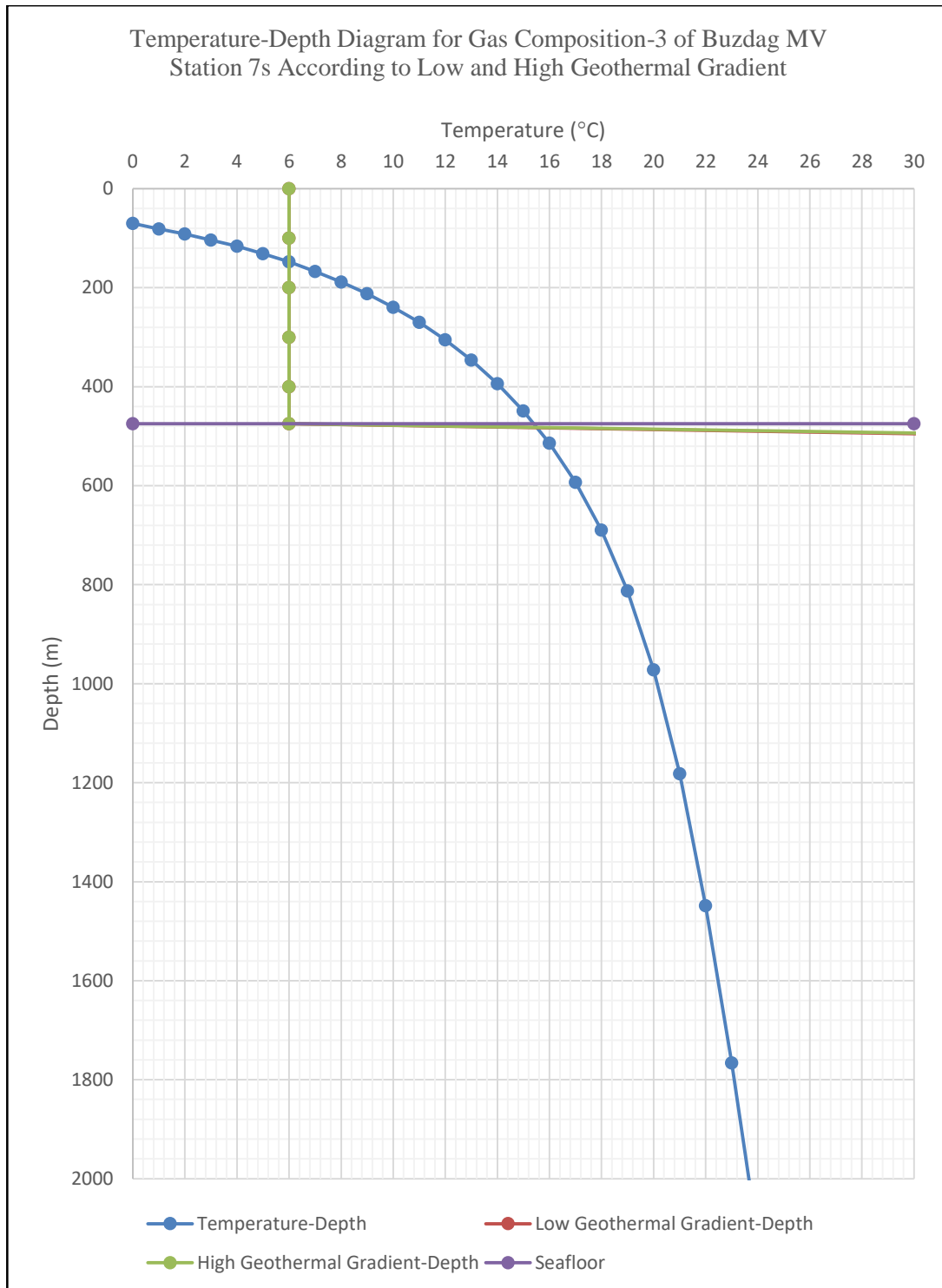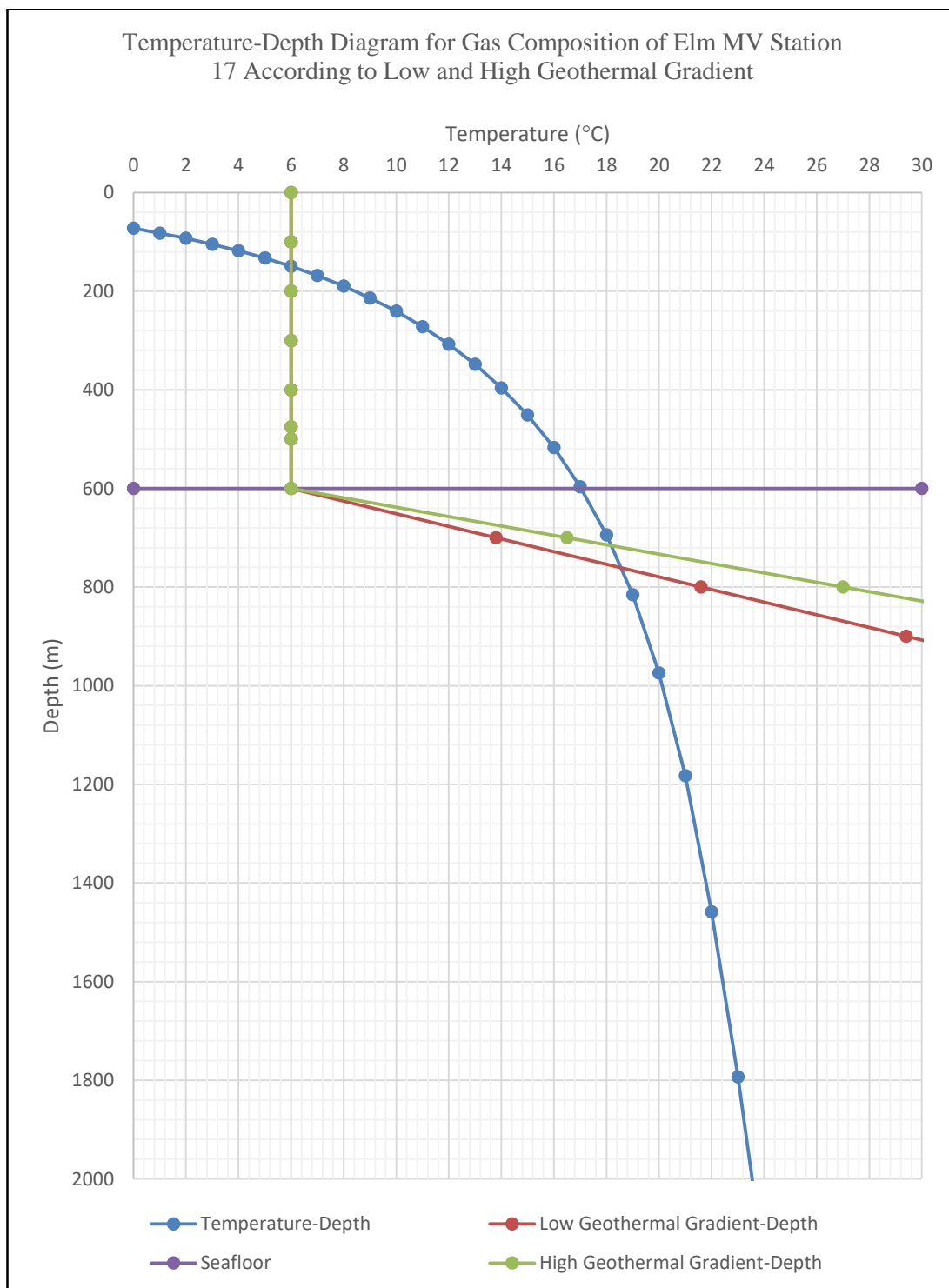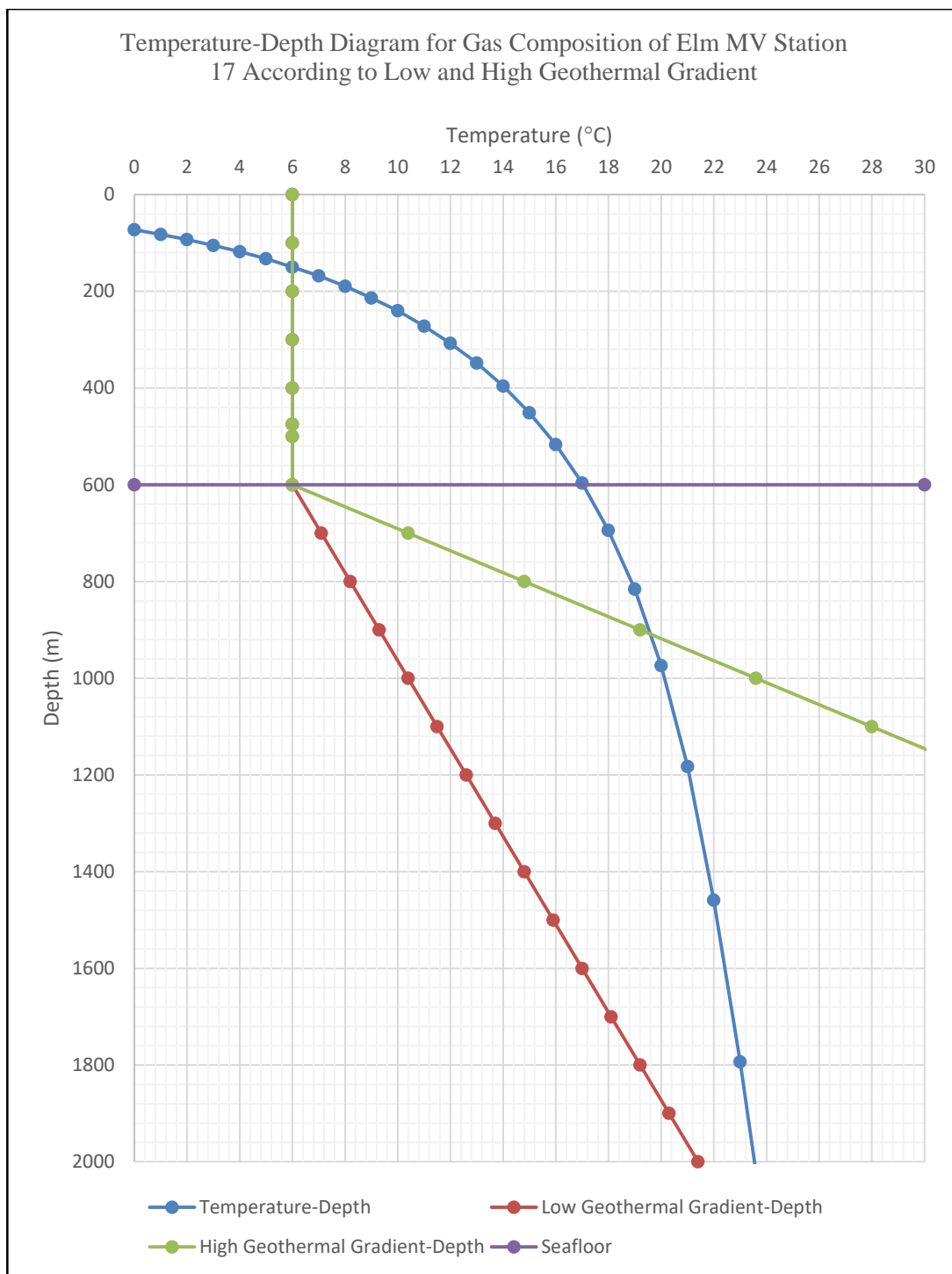
Figure B-27: Temperature-depth diagram for gas composition-3 of Buzdag mud volcano, station 7s, according to low and high geothermal gradient. Low GG = 120 °C/100 m; High GG = 129 °C/100 m.
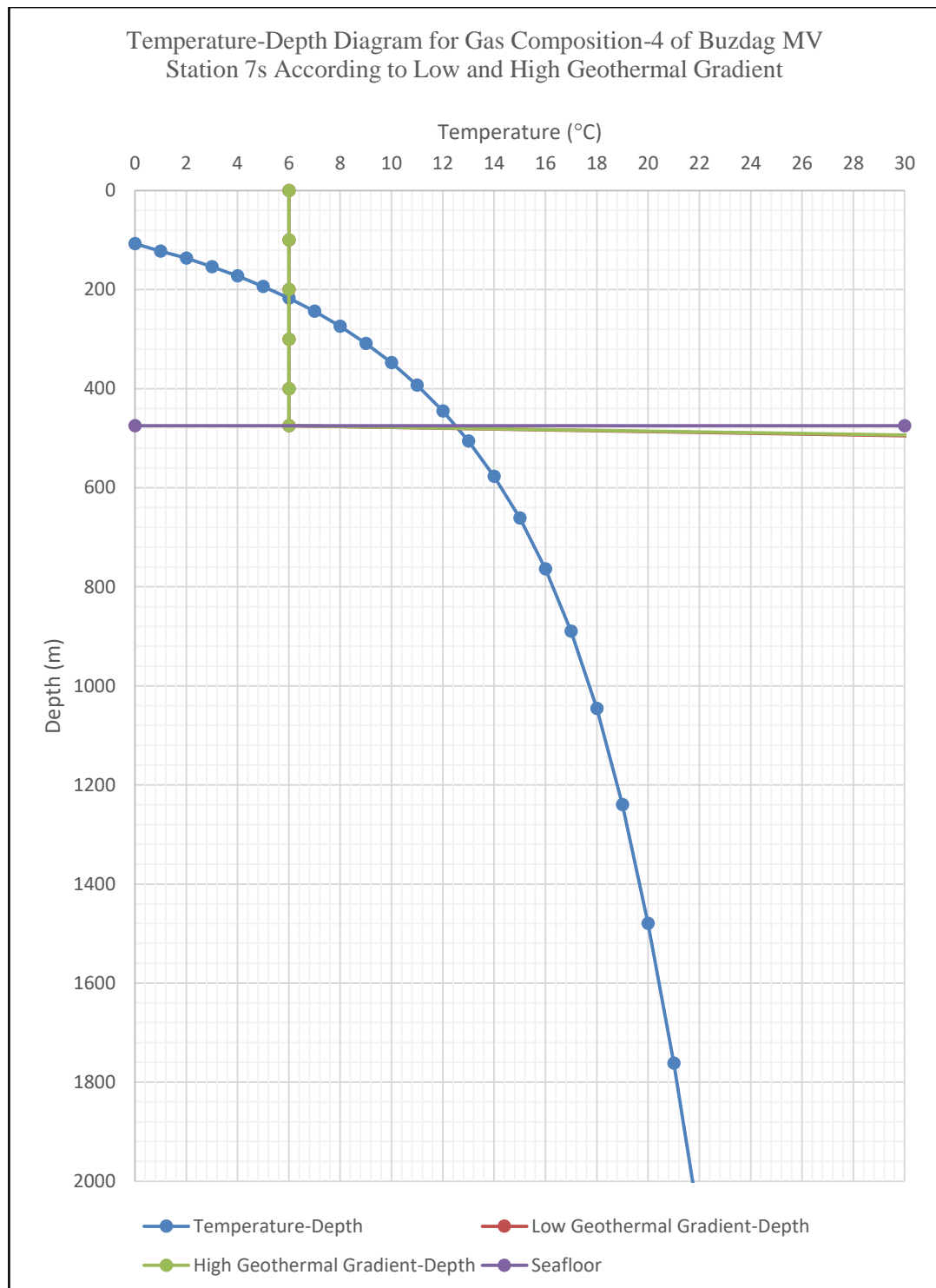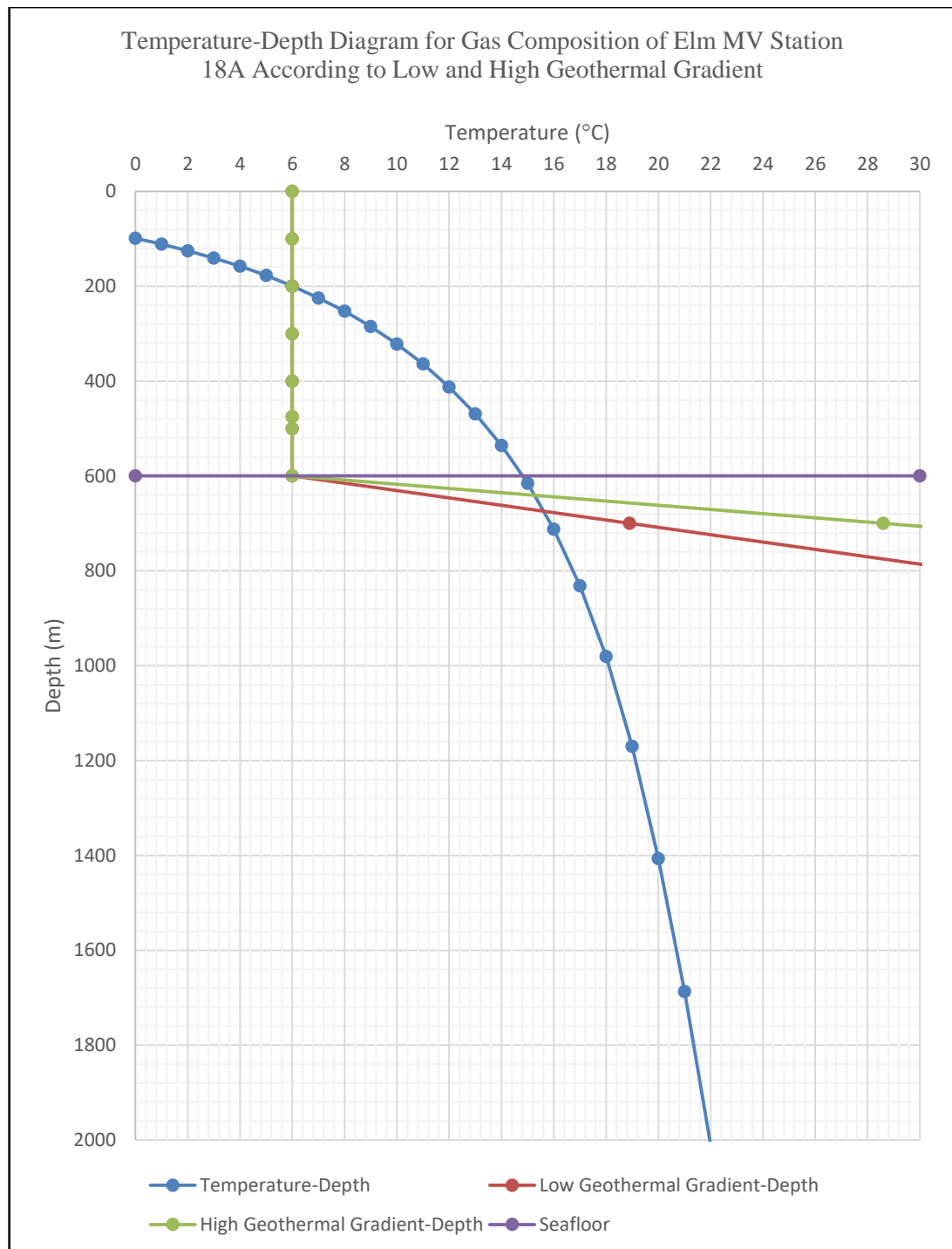
Figure B-28: Temperature-depth diagram for gas composition-4 of Buzdag mud volcano, station 7s, according to low and high geothermal gradient. Low GG = 120 °C/100 m; High GG = 129 °C/100 m.

Figure B-29: Temperature-depth diagram for gas composition-4 of Buzdag mud volcano, station 7s, according to low and high geothermal gradient. Low GG = 7 °C/100 m; High GG = 15 °C/100 m.
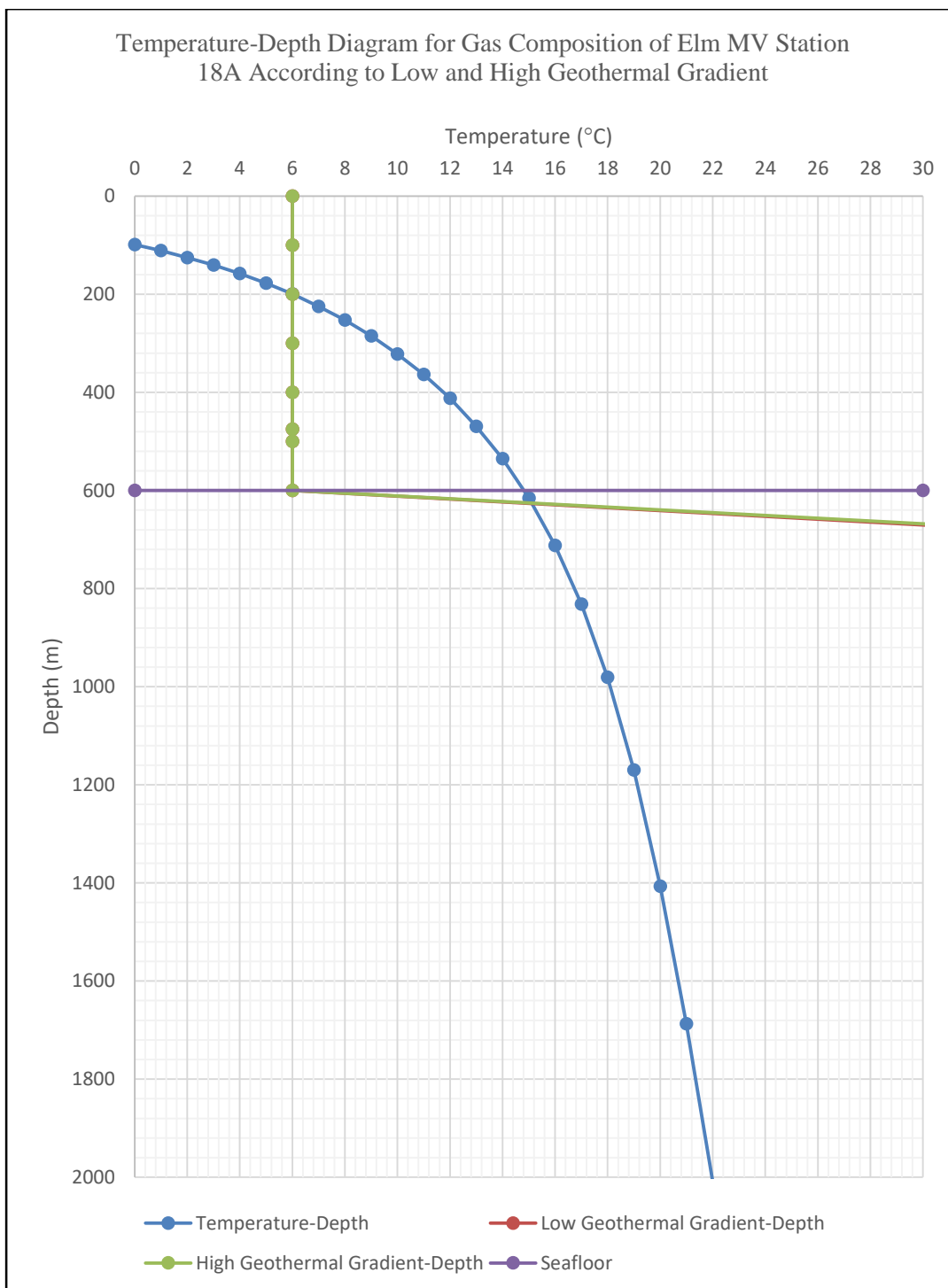
Figure B-30: Temperature-depth diagram for gas composition of Buzdag mud volcano, station 1B+1C, according to low and high geothermal gradient. Low GG = 120 °C/100 m; High GG = 129 °C/100 m.

Figure B-31: Temperature-depth diagram for gas composition of Buzdag mud volcano, station 1B+1C, according to low and high geothermal gradient. Low GG = 7 °C/100 m; High GG = 15 °C/100 m.
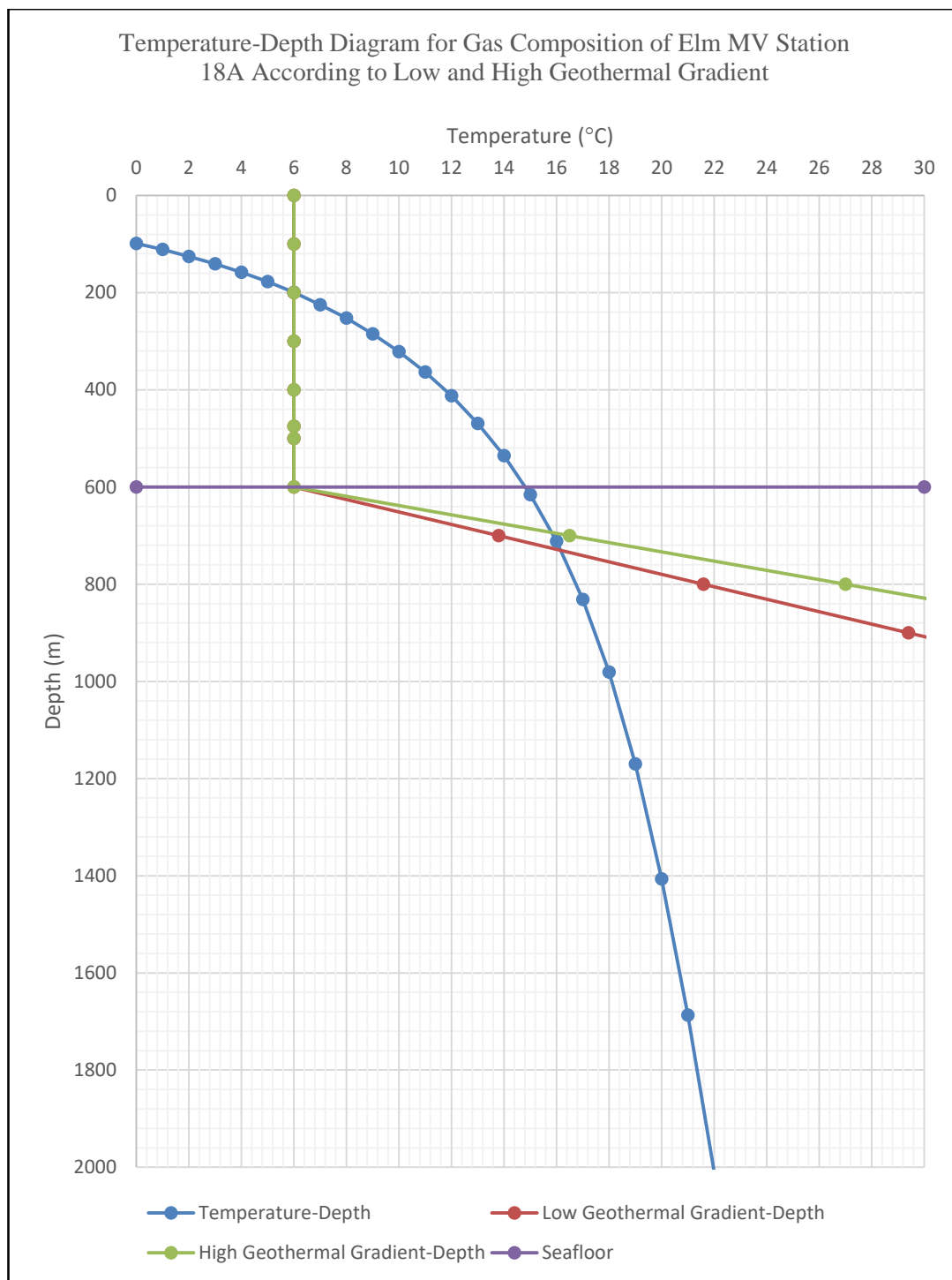
Figure B-32: Temperature-depth diagram for gas composition of Elm mud volcano, station 17, according to low and high geothermal gradient. Low GG = 12.9 °C/100 m; High GG = 22.6 °C/100 m.
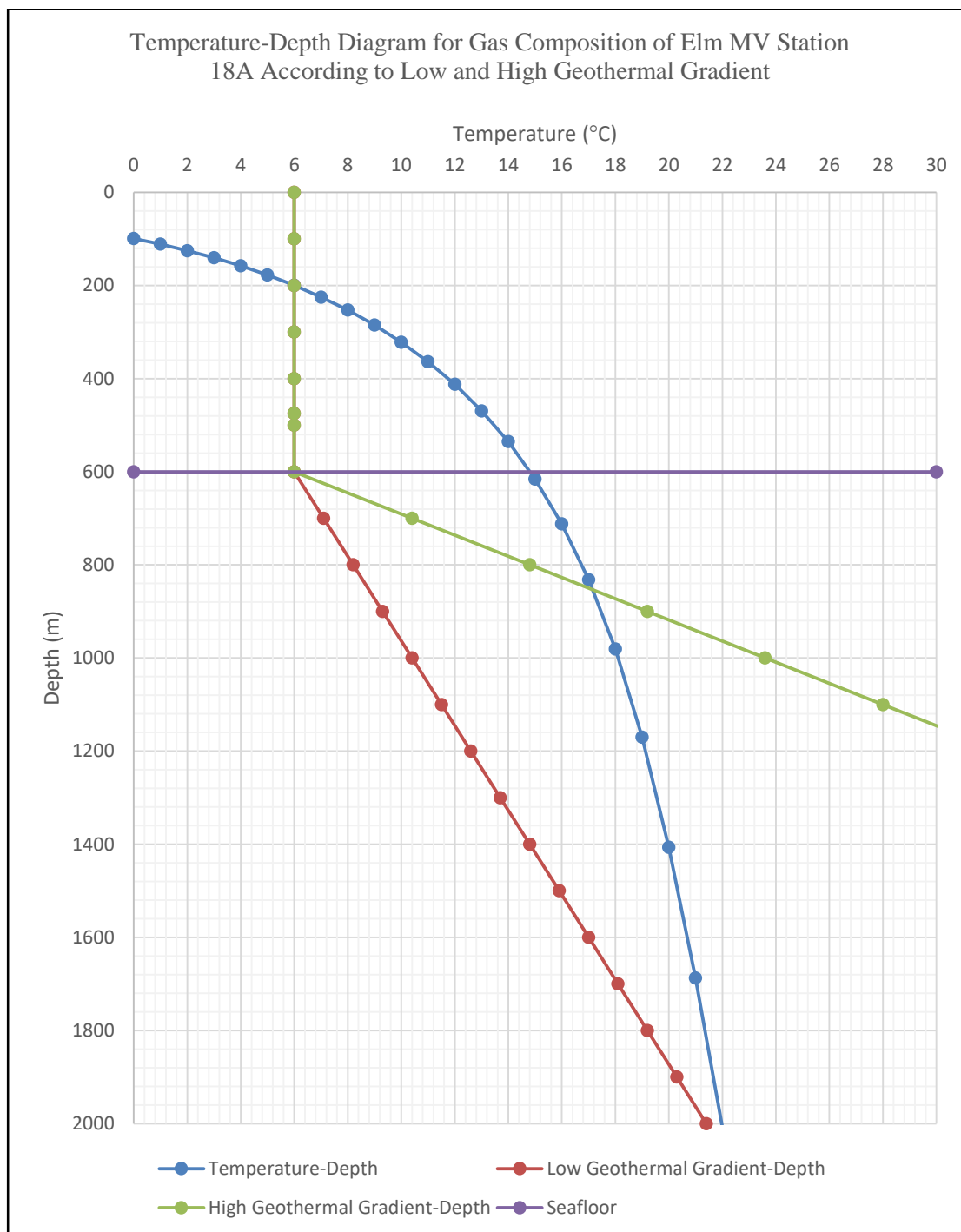
Figure B-33: Temperature-depth diagram for gas composition of Elm mud volcano, station 17, according to low and high geothermal gradient. Low GG = 34.1 °C/100 m; High GG = 35.3 °C/100 m.

Figure B-34: Temperature-depth diagram for gas composition of Elm mud volcano, station 17, according to low and high geothermal gradient. Low GG = 7.8 °C/100 m; High GG = 10.5 °C/100 m.

Figure B-35: Temperature-depth diagram for gas composition of Elm mud volcano, station 17, according to low and high geothermal gradient. Low GG = 1.1 °C/100 m; High GG = 4.4 °C/100 m.

Figure B-36: Temperature-depth diagram for gas composition of Elm mud volcano, station 18A, according to low and high geothermal gradient. Low GG = 12.9 °C/100 m; High GG = 22.6 °C/100 m.

Figure B-37: Temperature-depth diagram for gas composition of Elm mud volcano, station 18A, according to low and high geothermal gradient. Low GG = 34.1 °C/100 m; High GG = 35.3 °C/100 m.
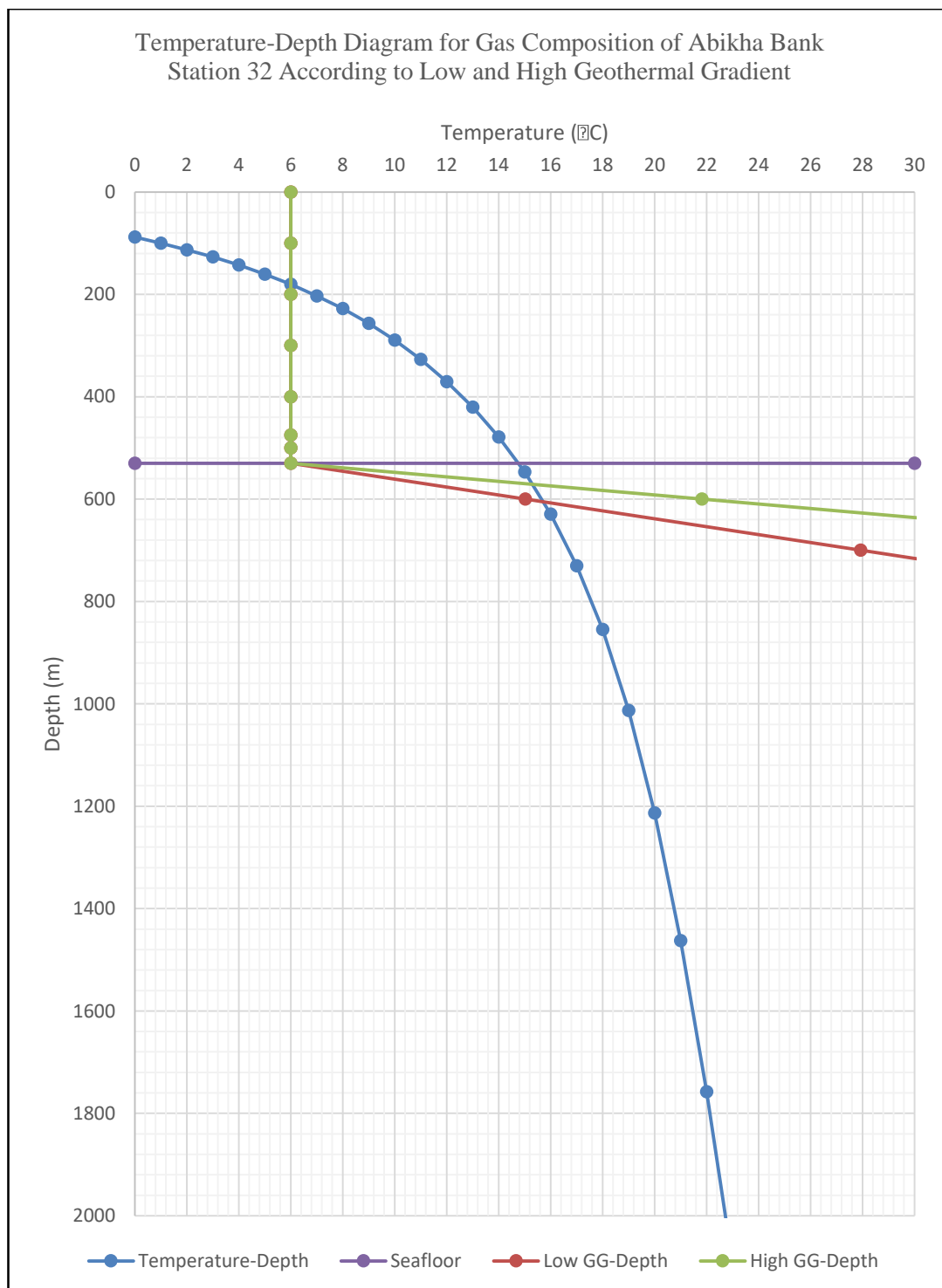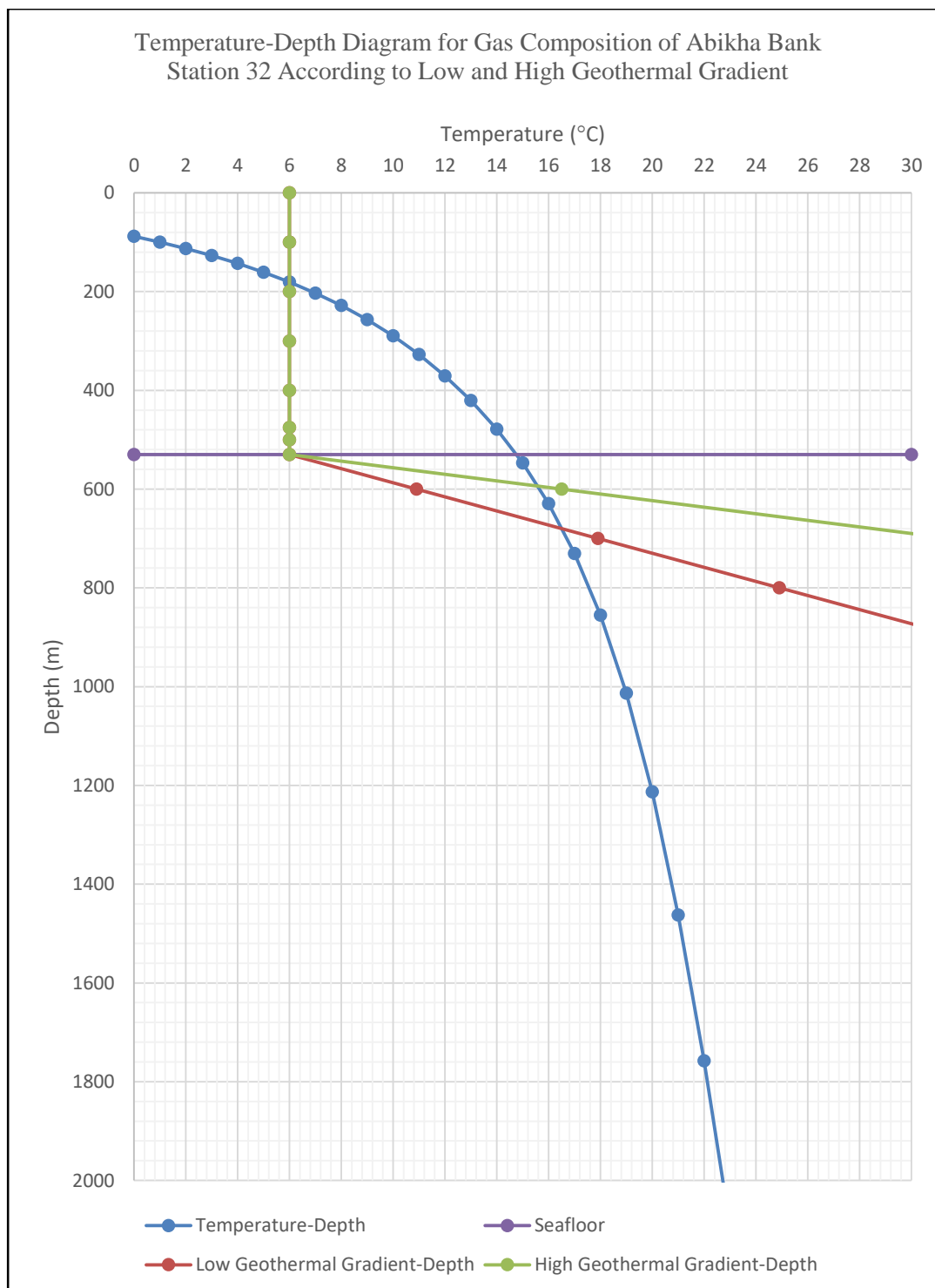
Figure B-38: Temperature-depth diagram for gas composition of Elm mud volcano, station 18A, according to low and high geothermal gradient. Low GG = 7.8 °C/100 m; High GG = 10.5 °C/100 m.

Figure B-39: Temperature-depth diagram for gas composition of Elm mud volcano, station 18A, according to low and high geothermal gradient. Low GG = 1.1 °C/100 m; High GG = 4.4 °C/100 m.
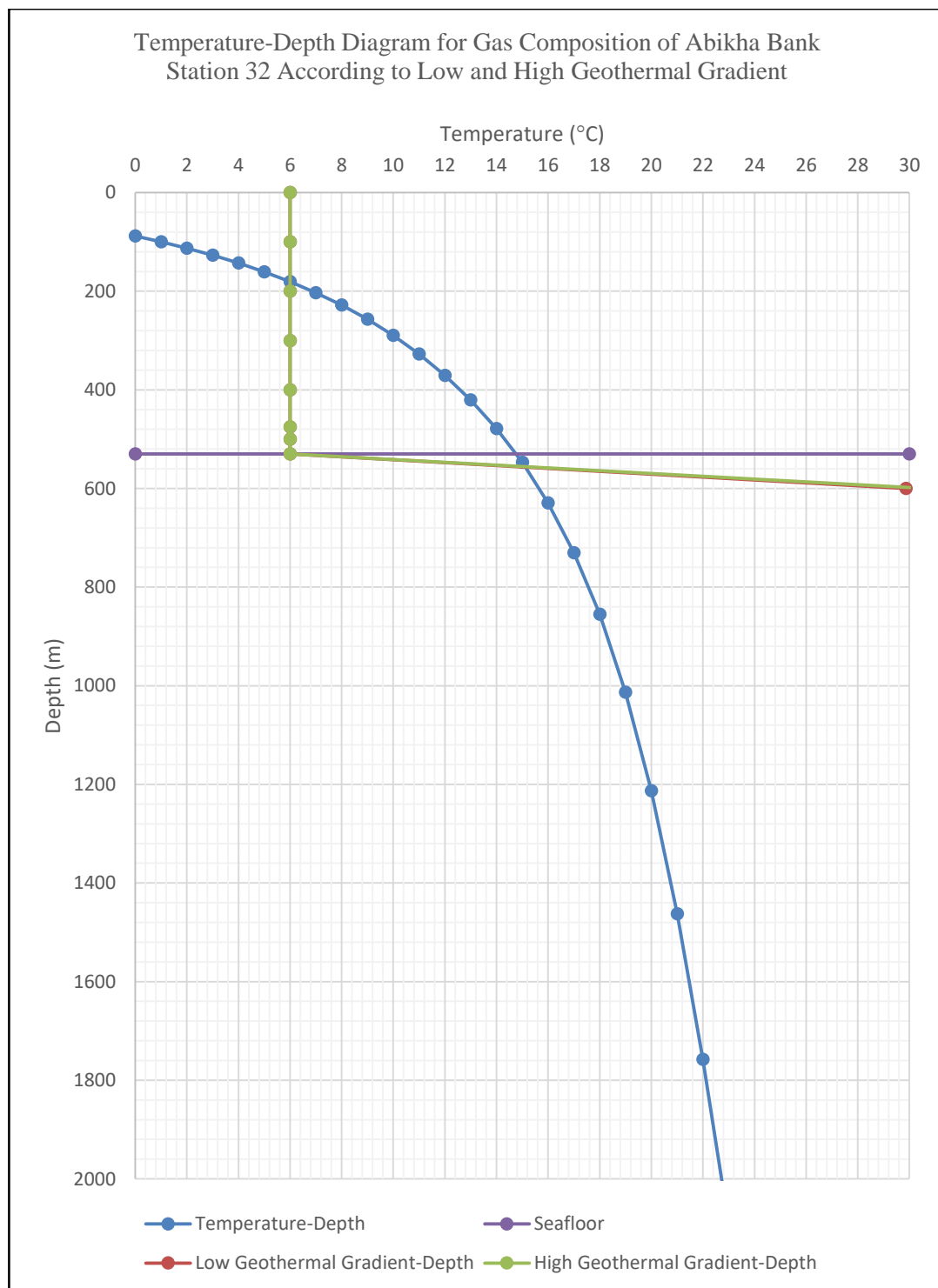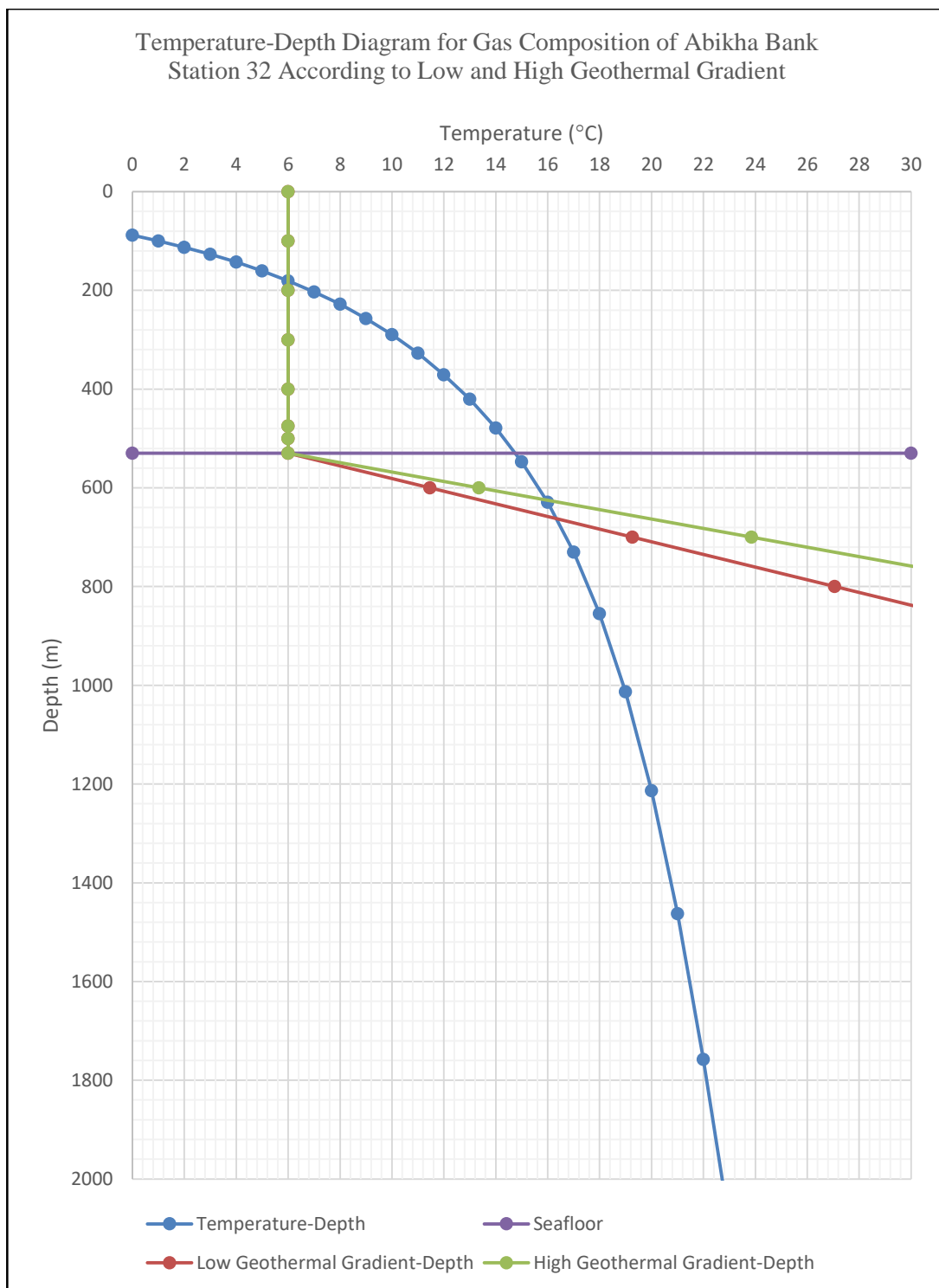
Figure B-40: Temperature-depth diagram for gas composition of unnamed mud volcano on Abikha bank, station 32, according to low and high geothermal gradient. Low GG = 12.9 °C/100 m; High GG = 22.6 °C/100 m.
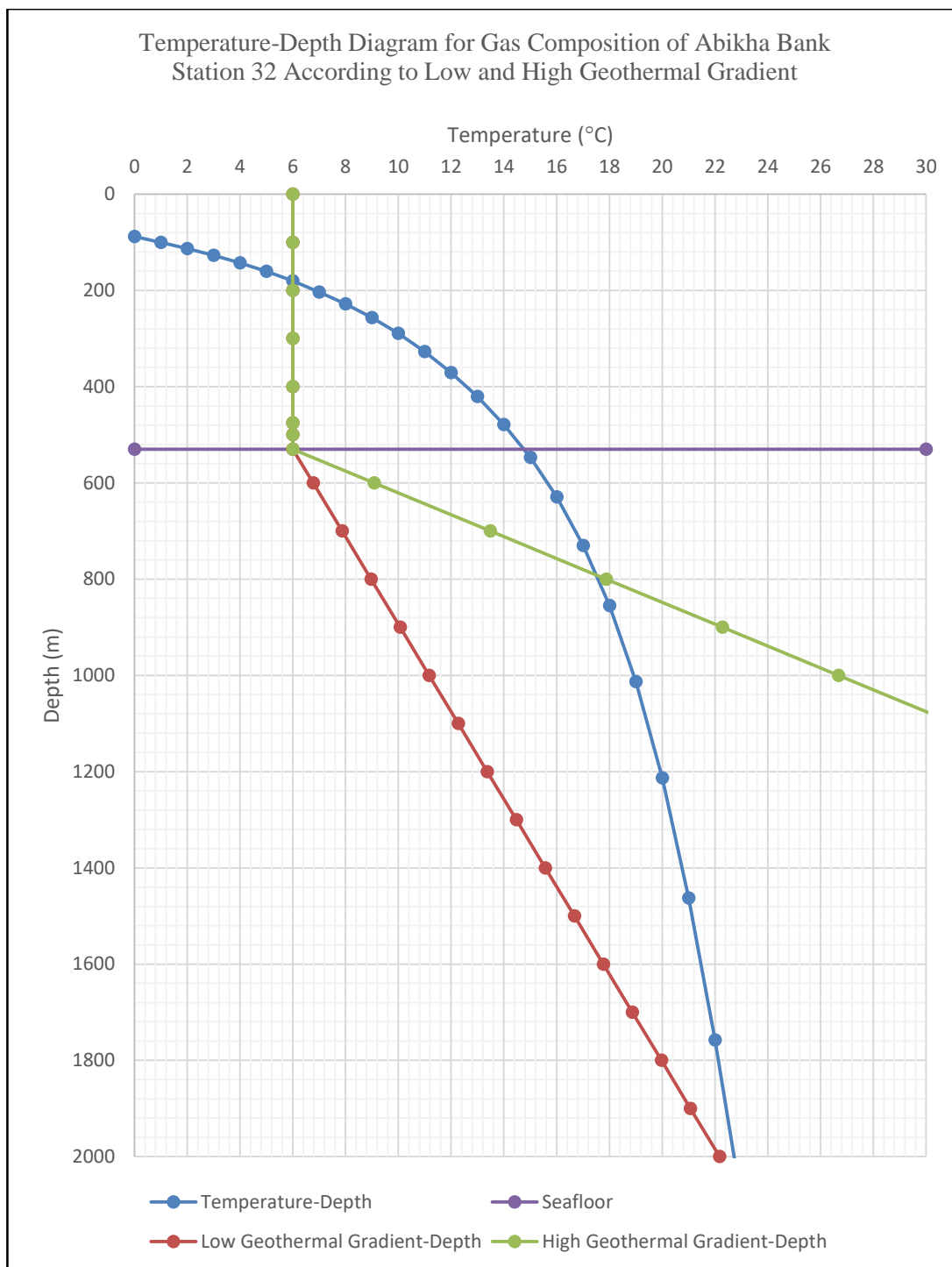
Figure B-41: Temperature-depth diagram for gas composition of unnamed mud volcano on Abikha bank, station 32, according to low and high geothermal gradient. Low GG = 7 °C/100 m; High GG = 15 °C/100 m.
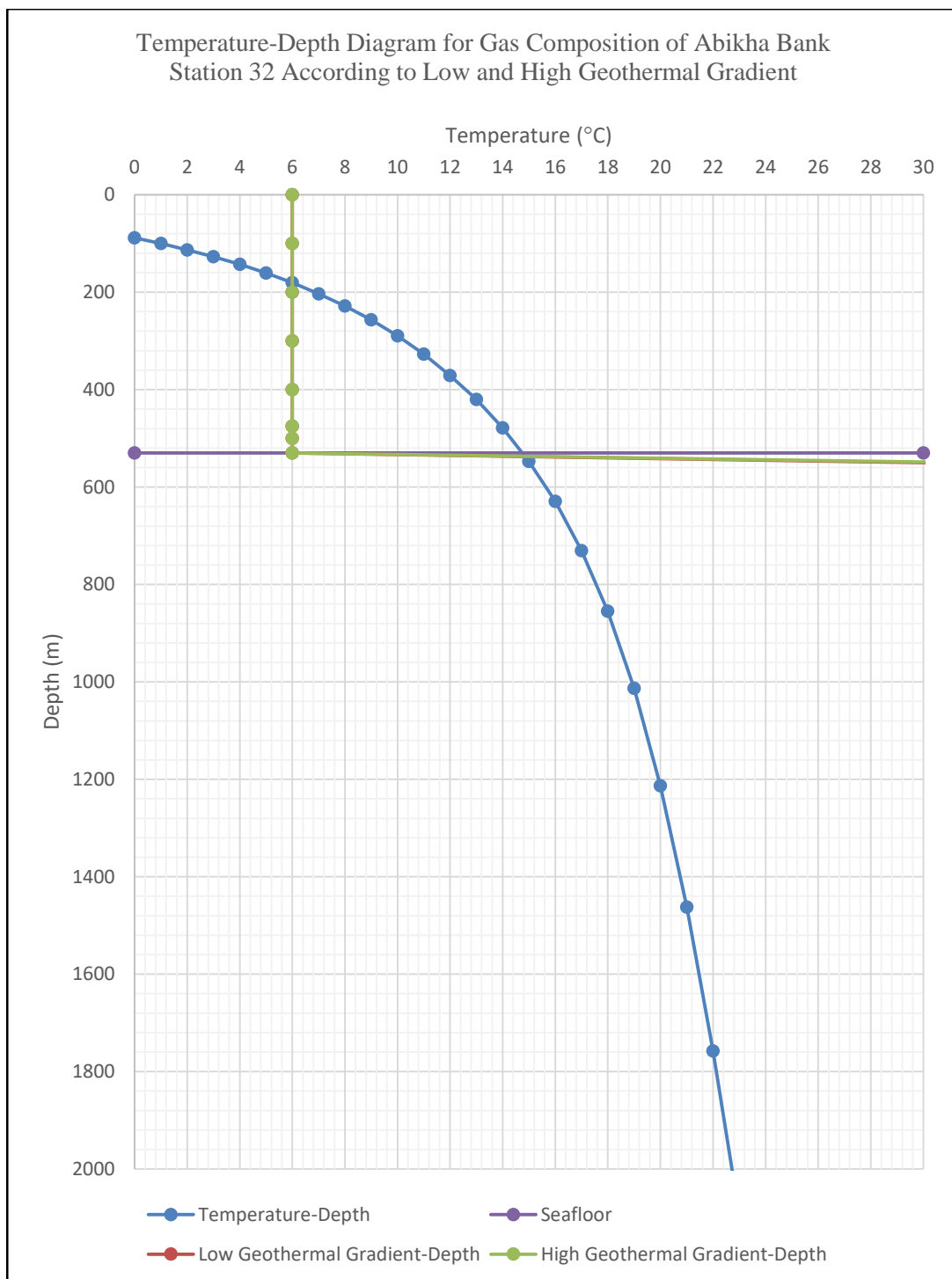
Figure B-42: Temperature-depth diagram for gas composition of unnamed mud volcano on Abikha bank, station 32, according to low and high geothermal gradient. Low GG = 34.1 °C/100 m; High GG = 35.3 °C/100 m.

Figure B-43: Temperature-depth diagram for gas composition of unnamed mud volcano on Abikha bank, station 32, according to low and high geothermal gradient. Low GG = 7.8 °C/100 m; High GG = 10.5 °C/100 m.

Figure B-44: Temperature-depth diagram for gas composition of unnamed mud volcano on Abikha bank, station 32, according to low and high geothermal gradient. Low GG = 1.1 °C/100 m; High GG = 4.4 °C/100 m.

Figure B-45: Temperature-depth diagram for gas composition of unnamed mud volcano on Abikha bank, station 32, according to low and high geothermal gradient. Low GG = 120 °C/100 m; High GG = 129 °C/100 m.